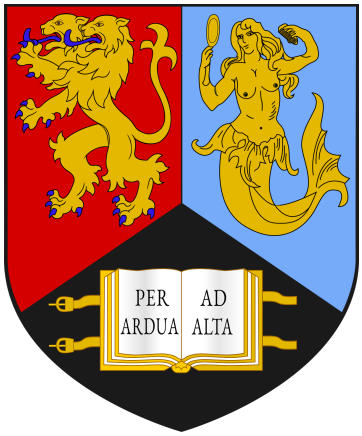


LUMINESCENT GOLD NANOPARTICLES FOR DETECTION AND LOCALIZATION IN CANCER CELLS

by

IRENE THEOFILOU

A thesis submitted to the University of Birmingham

for the degree of

DOCTOR OF PHILOSOPHY

School of Chemistry

College of Engineering and Physical Sciences

University of Birmingham

March 2021

UNIVERSITY OF
BIRMINGHAM

University of Birmingham Research Archive

e-theses repository

This unpublished thesis/dissertation is copyright of the author and/or third parties. The intellectual property rights of the author or third parties in respect of this work are as defined by The Copyright Designs and Patents Act 1988 or as modified by any successor legislation.

Any use made of information contained in this thesis/dissertation must be in accordance with that legislation and must be properly acknowledged. Further distribution or reproduction in any format is prohibited without the permission of the copyright holder.

Abstract

Conventional imaging agents and chemotherapeutic drugs are highly associated with reduced systematic bioavailability, induced by their inefficient delivery and imprecise localization within subcellular compartments. In recent years, gold nanoparticles have attracted considerable scientific interest for potential applications in the diagnosis and treatment of cancer, due to their ability to selectively deliver imaging and therapeutic moieties to the tumor site. The multifunctionality and unique physiochemical properties of gold nanoparticles provide countless opportunities for selectively targeting tumor cells and monitoring biological processes, both at a cellular and subcellular level.

In this thesis, luminescent gold nanoparticles are presented for enhanced detection and intracellular delivery in cancer cells. Through the attachment of luminescent metal complexes to the gold surface, multifunctional nanoprobes were developed that exhibit the characteristic photophysical properties of the molecular probes. The favorable optical properties offered by the metal complex and the gold scaffold provided enhanced detection in cancer cells using multimodal imaging. Confocal luminescence imaging and transmission electron microscopy revealed the highly efficient uptake and subcellular localization of the functionalized nanoparticles in cancer cells. The ability of transition metal complexes to be easily tuned through modifying the type of ligand attached to the metal core, allowed the efficient accumulation of nanoparticles in different subcellular organelles, including mitochondria and nucleus.

The use of gold nanoparticles to improve the valency of antibodies towards antigen receptors expressed on the surface of malignant cells is also presented. The antibody coated nanoparticles were further modified with luminescent complexes to allow detection. The enhanced cellular uptake and binding affinity of the functionalized nanoparticles was evident through flow cytometry and confocal microscopy.

The detection sensitivity offered by the luminescent signal, along with the improved delivery provided by the gold scaffold, offer opportunities for monitoring biological responses upon selectively targeting cancer cells in *in vivo* models.

Acknowledgments

It's no secret that completing a PhD thesis is a hard, long road with many obstacles along the way. I wouldn't be able to reach the finish line if it wasn't for the enormous support I received from a long list of people who were there for me, encouraged me and pushed me to achieve my goals.

First of all, I would like to express my gratitude to my supervisor, Prof. Zoe Pikramenou, for her valuable comments, guidance and support throughout my time in the lab and while writing up my PhD thesis. I would also like to thank my supervisors, Prof. Michael Hannon and Prof. Paul Murray, for their insightful comments and encouragement during my PhD study.

I wish to thank all the Pikramenou, Hannon and Murray research group members for their immense support and for making this journey pleasant and memorable. I wish to extend my special thanks to Menisha Manhota, Sajni Haria, and Tasha Chauhan for always being there for me, supporting and encouraging me every step of the way.

I am extremely grateful to my parents and my grandparents for their infinite love and continuous support, without whom I would have not been able to complete this PhD.

(Είμαι εξαιρετικά ευγνώμων στους γονείς μου και στους παππούδες μου για την απέραντη αγάπη και τη συνεχή στήριξή τους από την αρχή μέχρι την ολοκλήρωση του διδακτορικού μου)

I would also like to thank all my friends and family, both in Cyprus and Birmingham, for their love, care and support during my studies.

To my beloved parents and grandparents

"I am among those who think that science has
great beauty. A scientist in his laboratory
is not only a technician: he is also a child
placed before natural phenomena which
impress him like a fairy tale."

~ Marie Curie

Table of contents

Declaration of originality

Abstract

Acknowledgements

Table of contents

List of Figures

List of Schemes

List of Tables

Nomenclature and Abbreviations

Chapter 1: Introduction **1**

1.1 Current challenges in cancer treatment 1

1.2 Nanomaterials for cancer therapy 2

1.3 Clinically approved cancer nanomedicines 9

1.4 Gold nanoparticles for cancer theranostics 11

1.4.1 Gold nanoparticles for the delivery of therapeutic agents 16

1.4.2 Gold nanoparticles in clinical studies 19

1.5 Cellular uptake mechanisms of gold nanoparticles 24

1.6 Gold nanoparticles for biomedical imaging 27

1.6.1 Luminescent gold nanoparticles for multimodal imaging 31

1.7 Conjugation of antibodies to gold nanoparticles 35

1.8 Thesis aims 41

1.9 References 43

Chapter 2: Luminescent iridium gold nanoparticles to target mitochondria in cancer cells 58

2.1 Introduction 58

2.2 Chapter outline 65

2.3 Results and Discussion 66

2.3.1 Synthesis and Characterization of AuNPs 66

2.3.2 Synthesis and Characterization of IrS1 67

2.3.3 Photophysical Characterization of IrS1 67

2.3.4 Preparation of IrS1·Z·AuNP25 and characterization 70

2.3.5 Cytotoxicity of IrS1·Z·AuNP25 in HeLa cells 75

2.3.6 Cellular uptake efficacy of IrS1·Z·AuNP25 in HeLa cells 78

2.3.7 Luminescence lifetime detection of IrS1·Z·AuNP25 in HeLa cells 81

2.3.8 Circular Dichroism (CD) of IrS1 and IrS1·Z·AuNP25 85

2.3.9 Cellular uptake and subcellular localization of IrS1·Z·AuNP25 in HeLa cells by Confocal Microscopy 87

2.3.10 Cellular uptake and subcellular localization of IrS1·Z·AuNP25 in HeLa cells by TEM 91

2.3.11 Cellular uptake and subcellular localization of IrS1·Z·AuNP25 in HeLa cells by ICP-MS 94

2.3.12 Targeting Mitochondria in HeLa cells through inducing elevation of ROS levels 99

2.4 Conclusion 102

2.5 Acknowledgments 104

2.6 Experimental 105

2.6.1 Synthesis of IrS1 and Ir1 105

2.6.2 Preparation of IrS1·Z·AuNP25 105

2.6.3 MTT Cell Viability Assay 106

2.6.4 Cellular uptake by FACS 107

2.6.5 Live cell imaging by Confocal Microscopy 107

2.6.6 Cellular uptake and subcellular localization by ICP-MS 108

2.6.7 Cellular uptake and subcellular localization by TEM 109

2.6.8 DCFDA/H_2DCFDA Assay for detection of ROS 109

2.7 References 111

Chapter 3: Development of luminescent iridium gold nanoparticles with optimal cellular uptake to study subcellular localization in cancer cells 121

3.1 Introduction 121

3.2 Chapter outline 125

3.3 Results and Discussion 126

3.3.1 Synthesis and Characterization of IrC_{12} 126

3.3.2 Photophysical Characterization of IrC_{12} 126

3.3.3 Synthesis and Characterization of AuNPs 127

3.3.4 Preparation and Characterization of IrC_{12}·Z·AuNP25 128

3.3.5 Photophysical Characterization of IrC_{12}·Z·AuNP25 133

3.3.6 Cytotoxicity of IrC_{12}·Z·AuNP25 in HeLa cells 135

3.3.7 Cellular uptake efficacy of IrC_{12}·Z·AuNP25 in HeLa cells 137

3.3.8 Luminescence lifetime detection of IrC_{12}·Z·AuNP25 146

3.3.9 Circular Dichroism (CD) of IrC_{12} and IrC_{12}·Z·AuNP25 148

3.3.10 Cellular uptake and subcellular localization of IrC_{12}·Z·AuNP25 in HeLa cells by Confocal Microscopy 150

3.3.11 Cellular uptake and subcellular localization of IrC_{12}·Z·AuNP25 in HeLa cells by ICP-MS 154

3.4 Conclusion 158

3.5 Acknowledgments 160

3.6 Experimental 161

3.6.1 Synthesis of iridium complexes 161

3.6.2 Preparation of IrC_{12}·Z·AuNP25 and IrbpySS·Z·AuNP25 161

3.6.3 MTT Cell Viability Assay 162

3.6.4 Cellular uptake by FACS 163

3.6.7 Live cell imaging by Confocal microscopy 164

3.6.8 Cellular uptake and subcellular localization by ICP-MS 164

3.7 References 166

Chapter 4: Antibody conjugated luminescent gold nanoparticles for enhanced detection of tumor biomarkers

174

4.1 Introduction 174

4.2 Chapter outline 182

4.3 Results and Discussion 184

4.3.1 Synthesis and characterization of AuNP100 184

4.3.2 Preparation and characterization of RuphenS12·CD20·AuNP100 187

4.3.3 Cellular uptake of RuphenS12·CD20·AuNP100 in CD20 positive cells by FACS 194

4.3.4 Cellular uptake of RuphenS12·CD20·AuNP100 in Karpas 422 cells by Confocal microscopy 199

4.3.5 Synthesis and Characterization of AuNP 206

4.3.6 Preparation of Rituximab with nanoparticle linker 207

4.3.7 Conjugation of Rituximab-linker to AuNP 209

4.3.8 Conjugation or IrS1 to Rituximab-linker•PEG•AuNP 211

4.3.9 Characterization of IrS1·Rituximab-linker·PEG·AuNP by DLS 214

4.3.10 Gel electrophoresis to evaluate the size and surface charge of IrS1·Rituximab-linker·PEG·AuNP 217

4.3.11 Binding affinity of IrS1·Rituximab-linker·PEG·AuNP in tonsil tissue samples by Confocal luminescence microscopy 220

4.4 Conclusion 224

4.5 Acknowledgments 227

4.6 Experimental 228

4.6.1 Synthesis of AuNP100 228

4.6.2 Synthesis of RuphenS12 229

4.6.3 Preparation of RuphenS12·CD20·AuNP100 229

4.6.4 Preparation of RuphenS12·Z·AuNP100 230

4.6.5 Cellular uptake by FACS 231

4.6.6 Cell imaging by Confocal microscopy 231

4.6.7 Synthesis of AuNP 232

4.6.8 Preparation of Rituximab-linker complex 232

4.6.9 Preparation of IrS1·Rituximab-linker·PEG·AuNP 233

4.6.10 Preparation of IrS1·PEG·AuNP 235

4.6.11 Gel Electrophoresis of AuNP samples 235

4.6.12 Preparation of tonsil tissue specimens and imaging by confocal microscopy 236

4.7 References 238

Chapter 5: General Conclusions and Future work 248

Chapter 6: General Experimental 256

6.1 Synthesis of AuNP25 256

6.2 Photophysical Characterization 257

6.3 Dynamic Light Scattering (DLS) and Zeta Potential measurements 257

6.4 Circular Dichroism (CD) Spectroscopy 258

6.5 Preparation of nanoparticle samples for TEM 258

6.6 Cell Culture conditions 259

6.6.1 HeLa and HEK293 cell lines 259

6.6.2 Karpas 422 and SU-DHL-4 cell lines 259

6.7 References 260

Appendix A 262

Appendix B 273

Appendix C 277

Appendix D 279

Appendix E 288

List of Figures

Figure 1-1. Main types of organic and inorganic nanoparticles used for diagnostic and therapeutic purposes in the nanomedicine field. **4**

Figure 1-2. The impact of "protein corona" formation on the surface of a nanomaterial. **8**

Figure 1-3. TEM and SEM images of gold nanoparticles of different shapes and sizes. **12**

Figure 1-4. Schematic representation of the SPR effect on AuNPs. **14**

Figure 1-5. Multifunctionalized AuNP for theranostic applications. **15**

Figure 1-6. (a) Schematic illustration of doxorubicin conjugated AuNPs. (b) Schematic illustration of the delivery of doxorubicin on AuNPs. **18**

Figure 1-7. Schematic illustration of drug distribution in a human body subsequent to injecting with drug conjugated on AuNPs and free drug. **20**

Figure 1-8. Schematic illustration of the basic mechanisms of PDT and PTT using functionalized AuNPs to target cancer cells. **22**

Figure 1-9. Schematic representation of the different endocytic mechanisms by which AuNPs internalize into cells. **25**

Figure 1-10. Schematic illustration of AuNPs accumulation in tumor cells via EPR effect for use in NIR-mediated imaging guided by PDT. **28**

Figure 1-11. Imaging analysis of nuclear localization of ruthenium coated 100 nm AuNPs in A549 lung cancer cell. **32**

Figure 1-12. Two-photon luminescence lifetime imaging of 13, 25 and 100 nm iridium coated AuNPs in HeLa cells. **34**

Figure 1-13. Structure of an IgG antibody. **36**

Figure 1-14. Comparative bioluminescence imaging of tumor growth in mice after treatment with (a) gemcitabine and cetuximab (control group) and (b) gemcitabine on cetuximab-functionalized AuNPs (experimental group). **38**

Figure 1-15. Physical interactions between antibodies and AuNPs. **39**

Figure 2-1. Intracellular ROS levels in normal and cancer cells. **59**

Figure 2-2. Confocal microscopy images of HeLa cells showing subcellular localization of cyclometalated iridium(iii) complexes in mitochondria and lysosomes. **60**

Figure 2-3. Characterization of AuNP25 by DLS, TEM and SPR. **66**

Figure 2-4. UV-Vis absorption spectra of IrS1 at concentrations of 10 to 40 μM. Molar extinction coefficient (ε) of IrS1 in water and methanol. **68**

Figure 2-5. Phtophysical characterisation of 30 μM IrS1 in water. **69**

Figure 2-6. UV-Vis titration of 1.13 mM IrS1 on 2 nM Z·AuNP25 in water. **71**

Figure 2-7. UV-Vis of AuNP25, Z·AuNP25 and IrS1·Z·AuNP25 in water. **71**

Figure 2-8. DLS size and zeta potential distributions of Z·AuNP25 and IrS1·Z·AuNP25 **72**

Figure 2-9. TEM images of Z·AuNP25 and IrS1·Z·AuNP25 **73**

Figure 2-10. Photophysical characterisation of 2 nM IrS1·Z·AuNP25 in water. **74**

Figure 2-11. Cytotoxicity in HeLa cells determined using the MTT cell viability assay after treatment for 24 h. **77**

Figure 2-12. Cytotoxicity in HEK293 cells determined using the MTT cell viability assay after treatment for 24 h. **78**

Figure 2-13. Cellular uptake efficacy in HeLa cells by FACS analysis after treatment with AuNP25 samples, IrS1 and Ir1 for 24 h. **80**

Figure 2-14. Overlay of emission spectra of IrS1·Z·AuNP25 in water (dashed line) and in HeLa cells (solid line). **81**

Figure 2-15. Fitted luminescence lifetime decays of IrS1·Z·AuNP25 in HeLa cells and sub-cellular organelles. **82**

Figure 2-16. Fitted luminescence lifetime decays of Ir1 in HeLa cells and sub-cellular organelles. **84**

Figure 2-18. Circular dichroism spectra of BSA (0.1 μM) with sequential additions of (a) IrS1 solution (100 μM) and (b) IrS1·Z·AuNP25 in water (2 nM). **86**

Figure 2-19. Confocal microscopy of live HeLa cells after treatment with 0.2 nM IrS1•Z•AuNP25 for 24 h. **88**

Figure 2-20. Confocal microscopy of HeLa cells after treatment with 0.5 μM IrS1 for 24 h. **88**

Figure 2-21. Confocal microscopy of HeLa cells after treatment with 0.5 μM Ir1 for 24 h. **89**

Figure 2-22. Transmission Electron Microscopy in HeLa cells after treatment with 0.2 nM IrS1•Z•AuNP25 for 24 h. **92**

Figure 2-23. Transmission Electron Microscopy of endosomal vesicles in HeLa cells after treatment with 0.2 nM IrS1•Z•AuNP25 for 24 h. **92**

Figure 2-24. Transmission Electron Microscopy of mitochondria in HeLa cells after treatment with 0.2 nM IrS1•Z•AuNP25 for 24 h. **93**

Figure 2-25. Transmission Electron Microscopy of mitochondria in HeLa cells after treatment with (a) Control (H_2O), (b) 0.5 μM Ir1 and (c) 1 μM Ir1 for 24 h. **94**

Figure 2-26. ICP-MS Analysis of the number of AuNPs per cell in HeLa and HEK293 cells after treatment with 0.2nM IrS1·Z·AuNP25 for 24 h. **96**

Figure 2-27. ICP-MS Analysis of iridium concentration in whole cell lysates of HeLa and HEK293 cells after treatment with 0.2 nM IrS1·Z·AuNP25, 0.5 μM IrS1 and 0.5 μM Ir1 for 24 h. **98**

Figure 2-28. Intracellular ROS levels as evaluated by FACS analysis in the presence of H_2DCFDA probe after treatment for 24 h with 0.2 nM Z·AuNP25, 0.2 nM IrS1·Z·AuNP25, 0.5 μM Ir1 and 1 μM Ir1. **100**

Figure 3-1. Photophysical characterization of 30 μM IrC_{12} in water. **127**

Figure 3-2. UV-Vis titration of 1 mM IrC_{12} on 2 nM Z·AuNP25 in water. **129**

Figure 3-3. UV-Vis absorption spectra of AuNP25, Z·AuNP25 and IrC_{12}·Z·AuNP25. **129**

Figure 3-4. Functionalized AuNP25 with the zonyl fluorosurfactant and the IrbpySS complex. **130**

Figure 3-5. UV-Vis titration of 1 mM IrbpySS on 2 nM Z·AuNP25 in water. **131**

Figure 3-6. DLS intensity distributions of IrC_{12}·Z·AuNP25 and IrbpySS·Z·AuNP25. **132**

Figure 3-7. TEM images of IrC_{12}·Z·AuNP25 and IrbpySS·Z·AuNP25. **132**

Figure 3-8. Photophysical characterization of 2 nM IrC_{12}·Z·AuNP25 in water. **133**

Figure 3-9. Emission spectra of 30 μM IrC_{12} in water (solid line) and 30 μM IrC_{12} with 2 μM of 2.5 % zonyl FSA in water (dashed line). **134**

Figure 3-10. Cytotoxicity in HeLa cells determined using the MTT cell viability assay after treatment for 24 h. **136**

Figure 3-11. (a) UV-Vis absorption spectra of IrC_{12}·Z·AuNP25 and IrbpySS·Z·AuNP25 in water. (b) Emission spectra of IrC_{12}·Z·AuNP25 and IrbpySS·Z·AuNP25 in water. (c) Fold difference in AUC of the emission intensity of IrC_{12}·Z·AuNP25 and IrbpySS·Z·AuNP25 in water. **139**

Figure 3-12. Cellular uptake efficacy in HeLa cells by FACS analysis after treatment with IrC_{12}·Z·AuNP25 and IrbpySS·Z·AuNP25 for 24 h. **140**

Figure 3-13. (a) Chemical structures of IrC_{12}, IrbpySS, IrC_{12}bpy and Irbpy. (b) UV-Vis absorption spectra of IrC_{12}, IrbpySS, IrC_{12}bpy and Irbpy in water. (c) Emission spectra of IrC_{12}, IrbpySS, IrC_{12}bpy and Irbpy in water. (d) Fold difference in the AUC of the emission intensity of IrC_{12}, IrbpySS, IrC_{12}bpy and Irbpy. **141**

Figure 3-14. Cellular uptake efficacy in HeLa cells by FACS analysis after treatment with IrC_{12}, IrbpySS, IrC_{12}bpy and Irbpy for 24 h. **143**

Figure 3-15. (a) Cellular uptake efficacy in HeLa cells by FACS analysis after treatment with IrC_{12}·Z·AuNP25, IrbpySS·Z·AuNP25, IrC_{12}, IrbpySS, IrC_{12}bpy and Irbpy for 24 h. **145**

Figure 3-16. Circular dichroism spectra of BSA (0.1 μM) with sequential additions of (a) IrC_{12} solution (100 μM) and (b) IrC_{12}·Z·AuNP25 in water (4 nM). **150**

Figure 3-17. Confocal microscopy of live HeLa cells after treatment with 0.4 nM IrC_{12}•Z•AuNP25 for 4 and 24 h. **151**

Figure 3-18. Confocal microscopy of live HeLa cells after treatment with 0.3 μM IrC_{12} for 4 and 24 h. **152**

Figure 3-19. Confocal microscopy of live HeLa cells after treatment with 0.4 nM IrC_{12}•Z•AuNP25 for 24 h. **153**

Figure 3-20. ICP-MS Analysis of the number of AuNPs per cell in HeLa cells in fractionated and whole cell lysates after treatment with 0.4 nM IrC_{12}·Z·AuNP25 for 24 h. **155**

Figure 3-21. ICP-MS Analysis of iridium concentration per cell in HeLa cells in fractionated and whole cell lysates after treatment with 0.3 μM IrC_{12} for 24 h. **156**

Figure 4-1. Schematic representation of the two different functionalization methods used to attach antibodies to the surface of AuNPs. (a) Adsorption and (b) Directional conjugation using intermediary PEG linker **177**

Figure 4-2. DLS intensity distributions of AuNP13, AuNP25, AuNP50 and AuNP100. **185**

Figure 4-3. (a) UV-Vis absorbance of AuNP100 in water. (b) Zeta potential distribution of AuNP100. **186**

Figure 4-4. UV-Vis absorption spectra of AuNP100, CD20·AuNP100 and RuphenS12·CD20·AuNP100. **188**

Figure 4-5. DLS intensity distributions of AuNP100, CD20·AuNP100 and RuphenS12·CD20·AuNP100. **189**

Figure 4-6. TEM image of RuphenS12·CD20·AuNP100. **189**

Figure 4-7. DLS zeta potential distributions of AuNP100, CD20·AuNP100 and RuphenS12·CD20·AuNP100. **192**

Figure 4-8. Phtophysical characterisation of RuphenS12 and RuphenS12·CD20·AuNP100 in water. **193**

Figure 4-9. Cellular uptake efficacy in Karpas 422 and SU-DHL-4 cells by FACS analysis after treatment with 10 pM of AuNP100 samples for 24 h. **195**

Figure 4-10. Cellular uptake efficacy in Karpas 422 by FACS analysis after treatment with 10 pM of AuNP100 samples for 24 h. . **197**

Figure 4-11. Dot plots of side scatter versus fluorescence of Karpas 422 cells after treatment with CD20 (negative control), 10 pM of AuNP100, CD20·AuNP100, RuphenS12·Z·AuNP100 and RuphenS12·CD20·AuNP100. **199**

Figure 4-12. Confocal microscopy images of Karpas 422 cells after treatment with 10 pM RuphenS12·CD20·AuNP100 for 24 h. **200**

Figure 4-13. Confocal microscopy images of Karpas 422 cells after treatment with 10 pM RuphenS12·CD20·AuNP100 for 24 h. **201**

Figure 4-14. Confocal microscopy images of Karpas 422 cells after treatment with 10 pM RuphenS12·CD20·AuNP100 for 24 h. **203**

Figure 4-15. Confocal microscopy images of SU-DHL-4 cells after treatment with 10 pM RuphenS12·CD20·AuNP100 for 24 h. **203**

Figure 4-16. Confocal microscopy images of Karpas 422 cells after treatment with 10 pM RuphenS12·CD20·AuNP100 for 24 h. **204**

Figure 4-17. Confocal microscopy images of SU-DHL-4 cells after treatment with 10 pM RuphenS12·CD20·AuNP100 for 24 h. **204**

Figure 4-18. (a) DLS number distribution of AuNP, (b) DLS intensity distribution of AuNP, (c) TEM image of AuNP (d) UV-Vis absorbance of AuNP in water. **206**

Figure 4-19. Colorimetric assay using Purpald regaent to confirm the oxidation of the carbohydrate to aldehydes on Rituximab. **208**

Figure 4-20. UV-Vis absorption spectra of Rituximab (1 mg/ml) and Rituximab-linker in PBS. **208**

Figure 4-21. UV-Vis absorption spectra of AuNP and attempted attachment of Rituximab-linker•AuNP in water. **209**

Figure 4-22. UV-Vis titration of 1 mM Rituximab-linker complex to 1 nM PEG•AuNP in water. **210**

Figure 4-23. UV-Vis titration of 1.17 mM IrS1 to 1 nM of Rituximab-linker•PEG•AuNP in water. **212**

Figure 4-24. UV-Vis absorption spectra of AuNP, PEG·AuNP, Rituximab-linker·PEG·AuNP and IrS1·Rituximab-linker·PEG·AuNP after purification. **212**

Figure 4-25. UV-Vis absorption spectra of PEG·AuNP, IrS1·PEG·AuNP and IrS1·Rituximab-linker·PEG·AuNP after purification. **213**

Figure 4-26. DLS Intensity distributions of AuNP, PEG·AuNP, IrS1·PEG·AuNP, Rituximab- linker·PEG·AuNP and IrS1·Rituximab-linker·PEG·AuNP. **214**

Figure 4-27. TEM image of IrS1·Rituximab-linker·PEG·AuNP. **215**

Figure 4-28. DLS zeta potential distri8utions of PEG·AuNP, IrS1·PEG·AuNP, Rituximab- linker·PEG·AuNP and IrS1·Rituximab-linker·PEG·AuNP. **216**

Figure 4-29. Phtophysical characterisation of IrS1·Rituximab-linker·PEG·AuNP in water. **217**

Figure 4-30. Gel electrophoresis of AuNP samples on a 1% agarose gel, run for 1 h at 100 V in 0.5x TBE. **219**

Figure 4-31. Confocal microscopy images of tonsil tissue after treatment with 1 nM IrS1·Rituximab-linker·PEG·AuNP for 90 min. **221**

Figure 4-32. Confocal microscopy images of tonsil tissue after treatment with 1 nM IrS1·Rituximab-linker·PEG·AuNP for 90 min. **222**

Figure 4-33. Confocal microscopy images of tonsil tissue after treatment with 1 nM IrS1·PEG·AuNP for 90 min. **222**

Figure A-1. ^{1}H NMR of Ir1 (acetone-d_6). **268**

Figure A-2. ^{1}H NMR of IrS1 (acetone-d_6). **269**

Figure A-3. Fitted luminescence lifetime decays of IrS1 in water and PBS. **270**

Figure A-4. (a) Fitted luminescence lifetime decay of Ir1 in water. (b) Fitted luminescence lifetime decay of IrS1·Z·AuNP25 in water. **271**

Figure B-1. ^{1}H NMR of IrC_{12} (acetone-d_6). **274**

Figure B-2. ^{1}H NMR of IrC_{12}bpy in (acetone-d_6). **274**

Figure B-3. (a) Fitted luminescence lifetime decay of IrC_{12} in water. (b) Fitted luminescence lifetime decay of IrC_{12}·Z·AuNP25 in water. **275**

Figure B-4. (a) Fitted luminescence lifetime decay of IrC_{12} in HeLa cells. (b) Fitted luminescence lifetime decay of IrC_{12}·Z·AuNP25 in HeLa cells. **276**

Figure C-1. ^{1}H NMR of RuphenS12 (δ_4-CD_3OD). **277**

Figure C-2. DLS intensity distributions of AuNP100, RuphenS12·Z·AuNP100 and RuphenS12·CD20·AuNP100**.** **278**

Figure C-3. DLS zeta potential distributions of AuNP100, RuphenS12·Z·AuNP100 and RuphenS12·CD20·AuNP100. **278**

List of Schemes

Scheme 1-1. Schematic representation of the AuNPs syntesis method first reported by Turkevich et al. in 1951. **13**

Scheme 2-1. Schematic of coating AuNPs with zonyl fluorosurfactant and the iridium(III) complex, IrS1. **63**

Scheme 3-1. Schematic of coating AuNPs with zonyl fluorosurfactant and the luminescent iridium(III) complex, IrC_{12}. **124**

Scheme 4-1. Schematic of coating AuNPs with CD20 antibody and the ruthenium(II) complex, RuphenS12. **180**

Scheme 4-2. Schematic of coating AuNPs with Rituximab and the iridium (III) complex, IrS1. **181**

Scheme 4-3. Schematic representation of the AuNP synthesis and the growth procedure to form 100 nm AuNPs. **184**

Scheme A-1. Schematic of the synthesis of $[Ir(pq)_2Cl]_2$. **263**

Scheme A-2. Schematic of the synthesis of 5,5'-Bis(bromomethyl)-2,2'-bipyridine. **264**

Scheme A-3. Schematic of the synthesis of 5,5′-Bis(mercaptomethyl)-2,2′-bipyridine. **264**

Scheme A-4. Schematic of the synthesis of $[Ir(2\text{-}pq)_2bpy]Cl$ (Ir1). **266**

Scheme A-5. Schematic of the synthesis of $[Ir(2\text{-}pq)_2bpySH]Cl$ (IrS1). **267**

Scheme B-1. Synthetic scheme for IrC_{12} and $IrC_{12}bpy$. The final structure is the general structure for the iridium complexes, where R=dodecyl. **273**

Scheme C-1. Schematic of the synthesis of RuphenS12**.** **277**

List of Tables

Table 1-1. Clinically approved nanoparticle-based therapies. **11**

Table 2-1. DLS for AuNP25, Z·AuNP25 and IrS1·Z·AuNP25 in water. **73**

Table 2-2. Luminescence lifetimes of IrS1·Z·AuNP25 in water, with BSA, HeLa cells and subcellular organelles. **84**

Table 2-3. Luminescence lifetimes of Ir1 in water, HeLa cells, subcellular organelles and upon addition of BSA, along with the percentage of each component fitted using three-component analysis. **84**

Table 3-1. DLS for AuNP25, Z·AuNP25, IrC_{12}·Z·AuNP25 and IrbpySS·Z·AuNP25. **132**

Table 3-2. Luminescence lifetimes of IrC_{12} in water, with BSA, HeLa cells and subcellular organelles. **148**

Table 4-1. DLS for AuNP13, AuNP25, AuNP50 and AuNP100 in water. **185**

Table 4-2. DLS for AuNP100, CD20·AuNP100, RuphenS12·CD20·AuNP100 and RuphenS12·Z·AuNP100 in water. **191**

Table 4-3. DLS for AuNP, PEG·AuNP, IrS1·PEG·AuNP, Rituximab-linker·PEG·AuNP and IrS1·Rituximab-linker·PEG·AuNP in water. **214**

Nomenclature and Abbreviations

Nomenclature

Symbol	Definition	Units
ε	Molar Extinction Coefficient	M^{-1} cm^{-1}
ζ	Zeta Potential	mV
λ	Wavelength	nm
τ	Luminescence Lifetime	ns
A	Absorbance	A.U
d	Diameter	nm
M	Molar Concentration	Mole per liter
RPM	Revolutions per minute	r min^{-1}

List of Abbreviations

A

A549	Human Adenocarcinoma cell line
ABCN	Azobis(cyclohexanecarbonitrile)
ADCC	Antibody-Dependent Cell-mediated Cytotoxicity
ADCP	Antibody-Dependent Cell-mediated Phagocytosis
AUC	Area Under the Curve
AuNP13	13 nm Gold Nanoparticles
AuNP25	25 nm Gold Nanoparticles
AuNPs	Gold Nanoparticles

B

Bcl-2	B-cell Lymphoma 2
bpy	2,2'-bipyridne
BSA	Bovine Serum Albumin

C

CCl_4	Carbon Tetrachloride
CD	Circular Dichroism
CDC	Complement-Dependent Cytotoxicity
$CDCl_3$	Deuterated chloroform
CLL	Chronic Lymphocytic Leukaemia
cm	Centimeter
CO_2	Carbon Dioxide
CT	Computed Tomography

D

DAPI	4′,6- diamidino-2-phenylindole
DCF	Dichlorofluorescein
DCFDA	2′,7′-dichlorofluorescein diacetate
DCM	Dichloromethane
DLBCL	Diffuse Large B-cell Lymphoma
DLS	Dynamic Light Scattering
DMEM	Dulbecco's Modified Eagle Medium
DMSO	Dimethyl Sulfoxide
DNA	Deoxyribonucleic Acid

E

ECM	Extracellular Matrix
EDTA	Ethylenediaminetetraacetic acid
EGFR	Epidermal Growth Factor Receptor
EMA	European Medicines Agency
EPR	Enhanced Permeability and Retention
ES	Electrospray
EtOH	Ethanol

F

Fab region	Fragment antigen-binding region
FACS	Fluorescence-Activated Cell Sorting
FBS	Fetal Bovine Serum
Fc region	Fragment crystallisable region
FDA	Food and Drug Administration
FISH	Fluorescence In Situ Hybridization

G

GLOBOCAN	Global Cancer Observatory
g	Grams

H

H_2O	Water
$HAuCl_4 \cdot 3H_2O$	Gold Chloride Trihydrate
HCL	Hydrochloric Acid
HEK293	Human embryonic kidney 293 cells
HeLa	Human Cervical carcinoma cell line
HepG2-R	Human Hepatocellular carcinoma cell line
HER2	Herceptin-2
HNO_3	Nitric Acid

I

ICP-MS	Inductively Coupled Plasma Mass Spectrometry
IgG	Immunoglobulin G
$IrCl_3$	Iridium(iii) Chloride

L

LC	Ligand-centred
LLCT	Ligand-to-ligand charge transfer

M

MCF-7	Breast Cancer cell line (Michigan Cancer Foundation-7)
MDR	Multi Drug Resistance
MeOH	Methanol
MFI	Mean Fluorescent Intensity
mg	Milligram
Mg_2SO_4	Magnesium Sulfate
ml	Milliliter
MLCT	Metal-to-ligand charge transfer
µl	Microliter
mM	Millimolar (Millimoles per liter)
µm	Micrometer
µM	Micromolar (Micromoles per litre)
MMP	Mitochondrial Membrane Potential
MRI	Magnetic Resonance Imaging
MS	Mass Spectrometry
MSNPs	Mesoporous Silica Nanoparticles
MTT	3-(4,5-dimethylthiazol-2-yl)-2,5-diphenyl tetrazolium bromide
MTR	MitoTracker Red

N

N_2	Nitrogen
Na_2HPO_4	Disodium Hydrogen Phosphate
$Na_2S_2O_3$	Sodium thiosulfate
Na_2SO_4	Sodium Sulfate
$NaIO_4$	Sodium Periodate

NaOH	Sodium Hydroxide
NBS	N-bromosuccinimide
NH_4PF_6	Ammonium Hexafluorophosphate
NHL	Non-Hodgkin Lymphoma
NIR	Near-Infrared
NIRF	Near-Infrared Fluorescence
nm	Nanometer
nM	Nanomolar (Nanomoles per liter)
NMR	Nuclear Magnetic Resonance
ns	Nanosecond

O

OD	Optical Density

P

PBS	Phosphate-Buffered Saline
PCD	Programmed Cell Death
PCR	Polymerase Chain Reaction
PDCs	Peptide Drug Conjugates
PDI	Polydispersity Index
PDT	Photodynamic Therapy
PE	Phycoerythrin
PEG	Polyethylene Glycol
PEG-SH	Thiol-terminated polyethylene glycol
PET	Positron Emission Tomography
PF_6	Hexafluorophosphate
P-gp	P-glycoprotein

phen	1,10-phenanthroline
pHLIP	pH-low-insertion peptide
pM	Picomolar (Picomoles per litre)
PMT	Photomultiplier tube
ps	Picosecond
PSMA	Prostate-specific membrane antigen
PTT	Photothermal Therapy

Q

QDs	Quantum Dots

R

RBCs	Red Blood Cells
RNA	Ribonucleic Acid
ROS	Reactive Oxygen Species
RT	Room Temperature

S

SD	Standard Deviation
SEM	Scanning Electron Microscopy
siRNA	Small interfering RNA
SOP	Standard Operating Procedure
SPR	Surface Plasmon Resonance
SSC	Side Scatter
ssDNA	Single-stranded DNA

T

TBE	Tris-borate-EDTA
TBS-T	Tris-buffered saline with 0.1 % Tween-20
TEM	Transmission Electron Microscopy
TNF	Tumor Necrosis Factor
TOF-MS	Time-of-Flight Mass Spectrometry

U

UV	Ultraviolet
US	Ultrasound

V

Vis	Visible

Chapter 1:

1. Introduction

1.1 Current challenges in cancer treatment

Cancer is one of the leading causes of death globally[1]. Even though carcinogenesis related risk factors have been alleviated in the recent years, the prevalence of cancer cases still continues to grow worldwide. According to the GLOBOCAN 2018, 18.1 million new cancer cases and 9.6 million deaths from cancer were estimated worldwide in 2018[2]. These numbers show a significant increase in both new cases of cancer and cancer related deaths when compared to the previously reported estimated numbers by GLOBOCAN in 2012, confirming the increase in cancer incidence and mortality rate worldwide over the years[3].

Current approaches of cancer treatment include surgical resection, chemotherapy and radiotherapy, depending on the stage at which the cancer is diagnosed and the different parts of the body affected. Even though, chemotherapy and radiotherapy are considered as the most common cancer treatment approaches, their use in the clinic is hindered due to the development of severe side effects. These severe adverse effects result from targeting non-specifically rapidly diving cells regardless of whether they are tumor or healthy cells, thereby, compromising the quality of life in cancer patients that often leads to treatment discontinuation[4, 5].

Many anticancer drugs that are currently used in the clinic show poor pharmacokinetic characteristics as a result of low stability, solubility and metabolism, leading to inefficacy, limited bioavailability and high levels of toxicity[6, 7]. Another major drawback of current treatment approaches is the ineffective delivery of drugs to the tumor site, as it has been previously reported that only between 1 to 10 parts out of 100 000 of clinically approved monoclonal antibodies that are administered intravenously can actually reach their target of interest in *vivo*[8]. Similar limitations also apply to the use of contrast agents for imaging applications in cancer theranostics.

Therefore, it is essential to develop effective diagnostic and treatment approaches in order to address the aforementioned challenges and achieve a more selective targeting of tumor sites, while sparing significant damage to healthy cells and tissues. In order to increase the efficacy per dose of a therapeutic or imaging contrast agent, a novel formulation with enhanced targeting selectivity and the ability to overcome biological barriers that prevent the agent from reaching its target is required[8-10].

1.2 Nanomaterials for cancer therapy

The fundamental limitations of conventional cancer treatment approaches have led to the development of more effective and safer nanotechnology approaches, which are referred to as cancer nanomedicine[11]. A nanomaterial is described as a material that contains nano-scale particles, meaning that either itself or its essential components contain at least 50% of the particles within the range of 1 to 100 nm[12]. The two major subfields of nanomedicine are nanovectors, which are used for the administration and delivery of targeting and imaging agents, and the precise functionalization of nanomaterials through surface modifications using nanoprobes. The use of nanomaterials in cancer theranostics aids in directing targeting complexes and therapeutic drugs specifically to the tumor site, ensuring that treatments act locally rather than systematically and therefore provide an improved anti-tumor efficacy while preventing damage to healthy cells and tissues[13-15].

Diagnostic and therapeutic nanoparticles are usually divided into two categories, organic nanoparticles, including polymeric, micelles, dendrimers and liposomes, and inorganic, such as quantum dots (QDs), iron oxide, silica and gold[16] (Figure 1-1). The use of both organic and inorganic nanoparticles in the clinic has been successful with many systems being developed for a wide range of applications. For instance, organic nanoparticles have been successfully used for long-acting drug delivery, vaccination and systematic administration of topical agents through the skin[17-19], while inorganic nanoparticles have been used for applications including diagnosis through identification of

tumor biomarkers, imaging of intra-operative sentinel lymph nodes as well as thermal ablation of solid tumors[20-22].

The majority of the nanomaterials currently approved for therapeutic purposes are organic nanoparticles, with most of the systems that have reached clinical trials including polymer-based nanoparticles, such as dendrimers and micelles, and lipid-based nanoparticles such as liposomes[23]. The wide use of dendrimers in clinical applications is mainly attributed to their highly branched structure and the formation of cavities within the dendrimer molecules, which allow high drug entrapment efficacy for the delivery of therapeutic agents[24]. The encapsulation capacity of dendrimers provides opportunities for improved drug solubility and delivery of bioactive molecules such as vaccines, genes and drugs to the target site. Currently, a variety of polymers, including poly(propyleneimine), poly(amidoamine) and poly-L-lysine, are used in the form of dendrimers for therapeutic purposes[24, 25].

The use of polymeric nanopaticles provides an alternative system in the oncology field for improving conventional treatment approaches due to their high biocompatibility and biodegradability as well as their low cytotoxicity and immunogenicity[26]. The unique polymer membrane of polymer-based nanoparticles allows entrapment of therapeutic agents, which are directly dispersed within their polymeric matrix and are released in a controlled manner upon targeting[27]. This allows high concentrations of the therapeutic agents to be delivered to the target site. What is more, the ability of polymeric nanoparticles to undergo surface functionalization with cancer-specific ligands promotes the specific delivery of the encapsulated therapeutic agents to the target site, thereby, improving the therapeutic outcome[28].

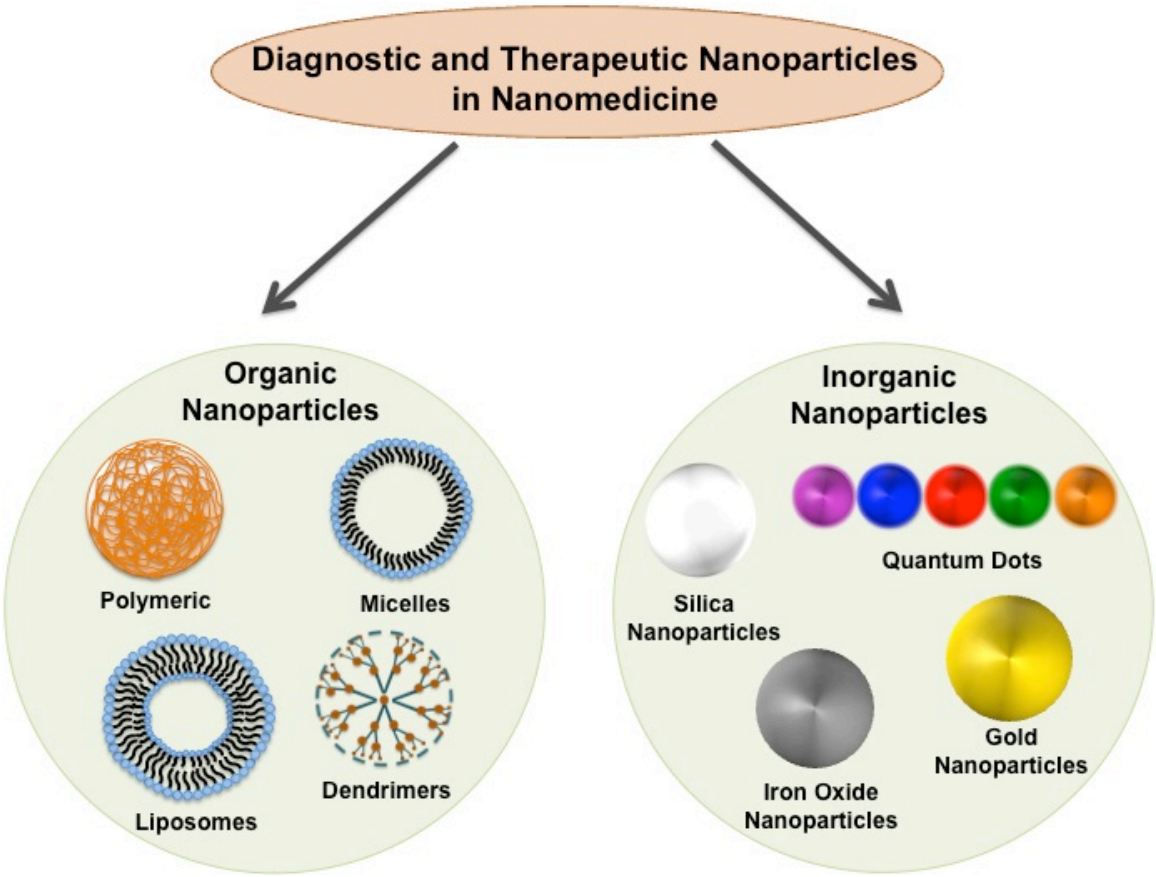


Figure 1-1. Main types of organic and inorganic nanoparticles used for diagnostic and therapeutic purposes in the nanomedicine field.

Polymeric micelles are currently used in the nanotechnology field for the systematic delivery of water-insoluble drugs. The spheroidal structure of the molecular components of polymeric micelles is formed through the surrounding of the hydrophobic cores by hydrophilic groups[29]. This enables entrapment of water-insoluble therapeutic agents within the hydrophobic matrix, while the hydrophilic groups provide protection against micelle aggregation, and thus, prolong blood circulation time[29, 30]. Therefore, the dynamic structure of polymeric micelles provides an advantageous system for the delivery of therapeutic agents with high loading capacity and reduced dissolution rate[31].

The broad use of liposomal vesicles in cancer treatment is mainly attributed to their distinct structure and ability to fuse with the cell surface membrane or lyse upon interaction with intracellular organelles, which induces the release of encapsulated drugs in the

cytoplasm[32]. Liposomes consist of either a single bilayer that surrounds the enclosed aqueous space or multiple lipid bilayers, which are separated by aqueous compartments[33]. Their characteristic structural properties allow them to deliver both hydrophilic and hydrophobic molecules to the target site, as hydrophilic molecules can be loaded in the aqueous matrix, whereas hydrophobic molecules can be dissolved in the lipid bilayer[34]. Consequently, more than one type of therapeutic agents can be incorporated within the liposomal structure, allowing different drug molecules to be released in a controlled manner[35]. Besides their favorable structure, the surface of liposomes can be easily modified using functionalized polymer chains in order to improve targeted drug delivery and prolong circulation time within biological environments[36].

As discussed earlier, inorganic nanoparticles have also been investigated in the nanotechnology field as cancer diagnostic and therapeutic nanoplatforms. When compared to organic nanoparticles, inorganic nanoparticles exhibit significantly lower cytotoxicity and higher stability in biological systems[37]. Moreover, they possess unique physiochemical properties, including optical and magnetic properties, and they have high surface area to volume ratio, which allows their surface to be multifunctionalized with various types of ligands to improve their affinity towards target molecules and cells[38]. The use of inorganic nanoparticles as nanovectors prevents drug degradation, which reduces administration frequency and allows considerably lower dosing concentrations to be administered, thus eliminating off-target toxicity associated with conventional cancer therapies[39].

Metallic nanoparticles, such as gold, nickel, cobalt and iron, can be synthesized easily into different sizes and functionalized with a variety of functional chemical groups to allow attachment of different molecules including peptides, proteins, nucleic acids, drugs and imaging agents[40]. The unique magnetic properties of metallic nanoparticles can be used for targeting specific locations in complex biological systems using an external magnetic field that can induce heat production and thereby, tumor ablation[41, 42].

Quantum dots (QDs) are tiny nanoparticles, usually between 2 to 10 nm, and consist of an aqueous organic coated shell, like zinc sulfide, and a semiconducting inorganic core such cadmium seledine[43]. The inorganic core of QDs is responsible for the distinctive fluorescence color emitted, whereas the organic aqueous shell is used for attachment of biological molecules such as proteins, peptides and nucleic acids[44]. The strong fluorescence and narrow emission of QDs make them ideal as therapeutic and imaging agents in biological systems. QDs are investigated in the nanomedicine field for theranostic purposes including, photodynamic therapy (PDT), tracking biodistribution of drugs and *in vivo* imaging[45, 46]. Even though the high photostability and unique photophysical properties of QDs indicate that they are superior over conventional fluorescent imaging agents, the high cytotoxicity they exhibit both in *in vitro* and *in vivo* applications hinders their approval for clinical use[47].

Inorganic silica nanoparticles have received considerable attention in the nanotechnology field due to their easily regulated pore sizes for encapsulation of drugs, incorporation of metal complexes for cancer theranostics and their rapid degradation in *in vivo* systems[48-50]. The development of mesoporous silica nanoparticles (MSNs) has provided opportunities for overcoming challenges associated with other organic and inorganic nanomaterials, such as their biodegradability, biocompatibility and drug release rates[51, 52]. Both the diameter and pore size of MSNs can be easily tuned during synthesis using different surfactant concentrations, temperature, pH and solvents, in order to achieve high drug loading[53]. Several stimuli-responsive drug release systems have been developed using different chemical moieties to functionalize the surface of MSNPs in order to trigger the release of encapsulated drugs[54, 55]. Besides their use as nanovectors for the controlled delivery of targeting agents, MSPNs can be modified using antibodies and nucleic acids in order to improve their biodistribution and reduce cytotoxicity in biological environments[56].

Even though, considerable success has been achieved in the field of nanomedicine in the past few years, the high complexity and heterogeneity of tumors as well as the nano-bio interactions are the main obstacles for the field to become the novel paradigm in cancer theranostics[11]. In order to be able to translate the use of nanomaterials in the clinic

and promote their commercialization, a better understanding of the interactions between nanomaterials and biological systems is required. This will aid in overcoming the challenges present in the field regarding the chemistry and manufacturing of nanomaterials.

When a nanomaterial enters a biological environment, such as intracellular fluid, extracellular matrix (ECM) or bloodstream, several biomolecules like proteins immediately interact and get adsorbed or bound on its surface forming a layer known as “protein corona”[57, 58]. The adsorption of proteins on the surface of nanomaterials can induce alterations in the material’s size, stability, crystallinity, hydrophobicity / hydrophilicity, electronic and surface properties, determining their biological identity and thus, the physiological responses they educe such as cytotoxicity, cellular uptake, intracellular trafficking and biodiversity (Figure 1-2)[11]. Furthermore, a corona rich in proteins can induce inhibition of phagocytic cellular uptake and internalization mechanisms, resulting to the stealth effect of nanomaterials[59]. Although nanomaterials might lack effectiveness and targeting capability upon the formation of a protein corona, surface functionalization using different proteins, ligands and targeting complexes can aid in improving their cellular internalization and their delivery in specific organs[60, 61].

Therefore, identifying the gaps in the current nanotherapy approaches through better comprehending the current grasp of nano-bio interactions, as well as tumour complexity and heterogeneity, will allow the development of novel nanomedicines with maximal patient response and prolonged patient survival.

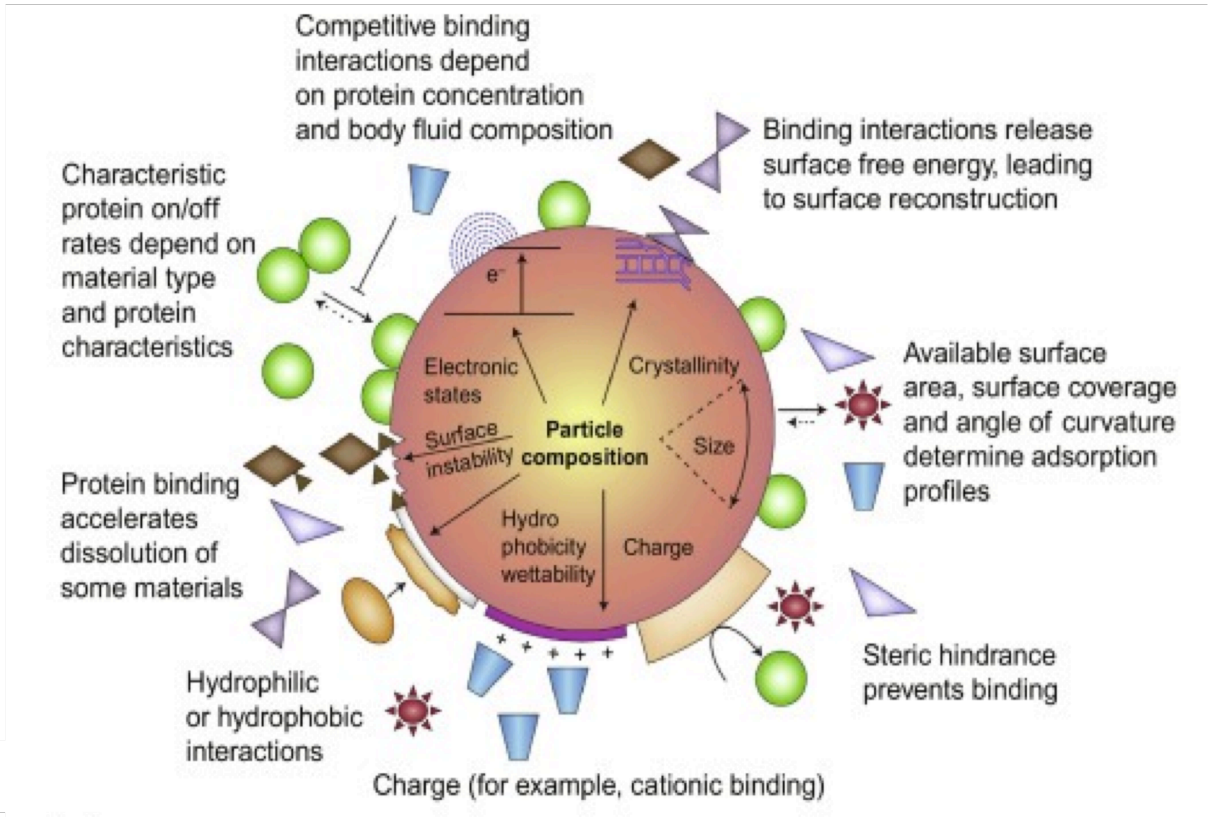


Figure 1-2. The impact of "protein corona" formation on the surface of a nanomaterial. The initial characteristics of nanomaterial determine the formation of the protein corona within a biological environment. The protein corona is mainly comprised from a primary nano-bio interface, which defines the materials fate in a biological system and can dramatically damage interactive proteins. Protein corona can result to competitive binding interactions based on the concentration of proteins and composition of body fluid, protein attachment / detachment depending on proteins characteristics and accelerated dissolution of materials on the surface due to binding of proteins. These can lead to surface reconstruction that alters the shape and surface area of the material, changes in hydrophilicity / hydrophobicity due to different hydrophilic or hydrophobic interactions, steric hindrance induced from molecules adsorbed on the material's surface and different overall charge of the material. (*Figure adapted from Nel et al. 2009[58], Copyright © 2009, with permission from Springer Nature*)

1.3 Clinically approved cancer nanomedicines

Over the last few decades, the nanomedicine field has been rapidly evolving, aiming to overcome limitations associated with conventional cancer therapeutic approaches. The use of nanoparticles can radically improve drug bioavailability at the target site, eliminate off-target toxicity and enhance drug solubility. Within the past two decades, the Food and Drug Administration (FDA) has approved various nanomaterial-based systems for safe use in the clinic (Summarized in Table 1-1), while over 200 new systems are currently undergoing clinical studies[30, 62].

Numerous nanoparticle formulations have been clinically approved for the treatment of different types of cancers at different stages. Doxil, a polyethylene glycol (PEG) fucntionalized liposomal nanoparticle encapsulated with doxorubicin, was the first cancer nanomedicine that received approval by the FDA and EMA in 1995 and 1996, respectively, for the treatment of Karposi's sarcoma and ovarian cancer[63]. The same formulation received approval by the FDA in 2007 for the treatment of multiple myeloma[64]. Not long after the approval of Doxil, many other liposomal formulations including DaunoXome, a liposomal nanoparticle encapsulating daunorubicin (FDA approval: 1996)[65], and DepoCyt, a liposomal nanoparticle encapsulating Cytarabine (FDA approval: 1999)[66], also received FDA approval, for the treatment of Karposi's sarcoma and lymphomatous meningitis, respectively. Another two liposomal systems that have been approved by the FDA are Marqibo a liposomal nanoparticle encapsulating vincristine (FDA approval: 2012)[67], and Onivyde, a PEG modified liposomal nanoparticle encapsulating irinotecan (FDA approval: 2015)[68], approved for the treatment of acute lymphoblastic leukemia and metastatic pancreatic cancer, respectively. What is more, two liposomal formulations received approval by the European Medicines Agency (EMA), Myocet, a liposomal nanoparticle encapsulating doxorubicin (EMA approval: 2000) for the treatment of metastatic breast cancer and MEPACT (EMA approval: 2009), a liposomal nanoparticle encapsulating mifamurtide, for the treatment of osteosarcoma[69, 70].

Besides liposomal formulations, other nanoparticle systems have also received approval for treating solid tumors and haematologcal malignancies. For instance,

Abraxane, an albumin-bound nanoparticle with paclitaxel, received approval both by the FDA (2005) and EMA (2008) for the treatment of advanced non-small cell lung cancer, metastatic breast and pancreatic cancer[71]. A recently approved formulation that has received approval both by the FDA (2017) and EMA (2018) is VYXEOS, which is a combination chemotherapy liposomal nanoparticle, encapsulating cytarabine and daunorubicin for a synergistic effect in acute myeloid leukemia[72].

The latest formulation that has been approved for safe use in the clinic is NBTXR3, crystalline hafnium oxide nanoparticles, which has received European market approval (CE mark) in 2019 for the local treatment of advanced squamous cell carcinoma. This nanoparticle-based system is used to enhance radiotherapy treatment through generating a higher number of electrons at the target site and thereby, increases radiation-mediated cell death when compared to standard radiation procedures[73, 74].

With the rapid expansion of nanotechnology, it is expected that in the near future the number of approved nanomedicines for safe use in the clinic will rise. Even though extensive research is currently carried out on the discovery of novel drug targets and the development of nanomaterials for combination therapy, immunotherapy, and cancer screening, there are is still a translational gap between experimental work and *in vivo* applications, hindering the fast entry of nanoparticle formulations to clinical trials. Consequently, there is currently a growing need for developing novel nanomaterials with well-established nano-bio interactions, in order to enhance the therapeutic efficacy in *in vivo* studies and achieve successful clinical translation.

Name	Particle type / Active agent	Approved application	Approval (year)
Doxil	PEG modified liposomal / Doxorubicin	Kaposi's sarcoma and ovarian cancer Multiple Myeloma	FDA (1995), EMA (1996) FDA (2007)
DaunoXome	Liposomal / Daunorubicin	Kaposi's sarcoma	FDA (1996)
DepoCyt	Liposomal / Cytarabine	Lymphomatous meningitis	Accelerated: FDA (1999) Full: FDA (2007)
Myocet	Liposomal / Doxorubicin	Metastatic breast cancer	EMA (2000)
Abraxane	Albumin-particle / Paclitaxel	Advanced non-small cell lung cancer Metastatic breast cancer Metastatic pancreatic cancer	FDA (2005), EMA (2008)
MEPACT	Liposomal / Mifamurtide	Osteosarcoma	EMA (2009)
Marqibo	Liposomal / Vincristine	Acute Lymphoblastic Leukemia	FDA (2012)
Onivyde	Liposomal / Irinotecan	Metastatic pancreatic cancer	FDA (2015)
VYXEOS	Liposomal / Cytarabine and daunorubicin	Acute Myeloid Leukemia	FDA (2017), EMA (2018)
NBTXR3	Hafnium oxide nanoparticles	Locally advanced squamous cell carcinoma	CE mark (2019)

Table 1-1. Clinically approved nanoparticle-based therapies.

1.4 Gold nanoparticles for cancer theranostics

Gold nanoparticles, AuNPs, have recently caught the attention of researchers in the cancer nanomedicine field due to their ease of synthesis and size tunable properties, which allow a broad range of sizes to be synthesised[12, 75]. AuNPs of various shapes and sizes have been previously synthesized through chemical, physical and biological methods[76, 77]. Interestingly, several types of AuNPs, including nanospheres, nanostars, nanorods and nanocages, have successfully become valuable tools in the cancer and cell biology research fields (Figure 1-3).

The extensive application of AuNPs in the development of cancer theranostics is attributed to their advantageous properties over other nanomaterials. In particular, their unique physiochemical properties, including their surface plasmon resonance (SPR), chemical stability, unique optical properties, surface multifunctionality and biocompatibility, provide countless opportunities for both drug delivery and imaging applications in biological systems[78-80].

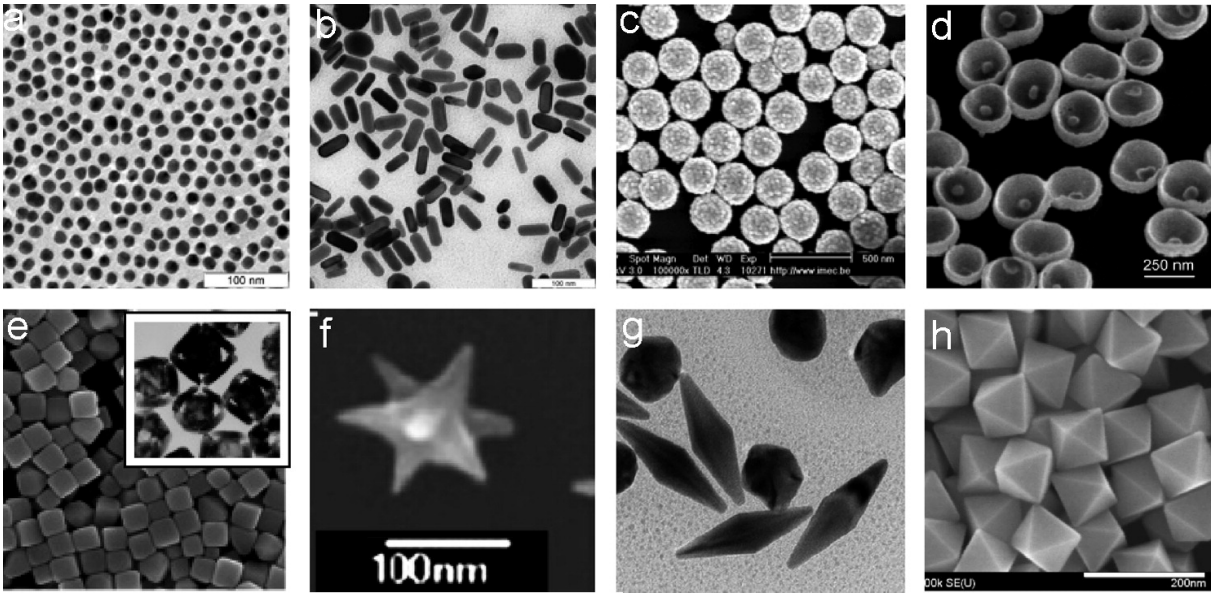
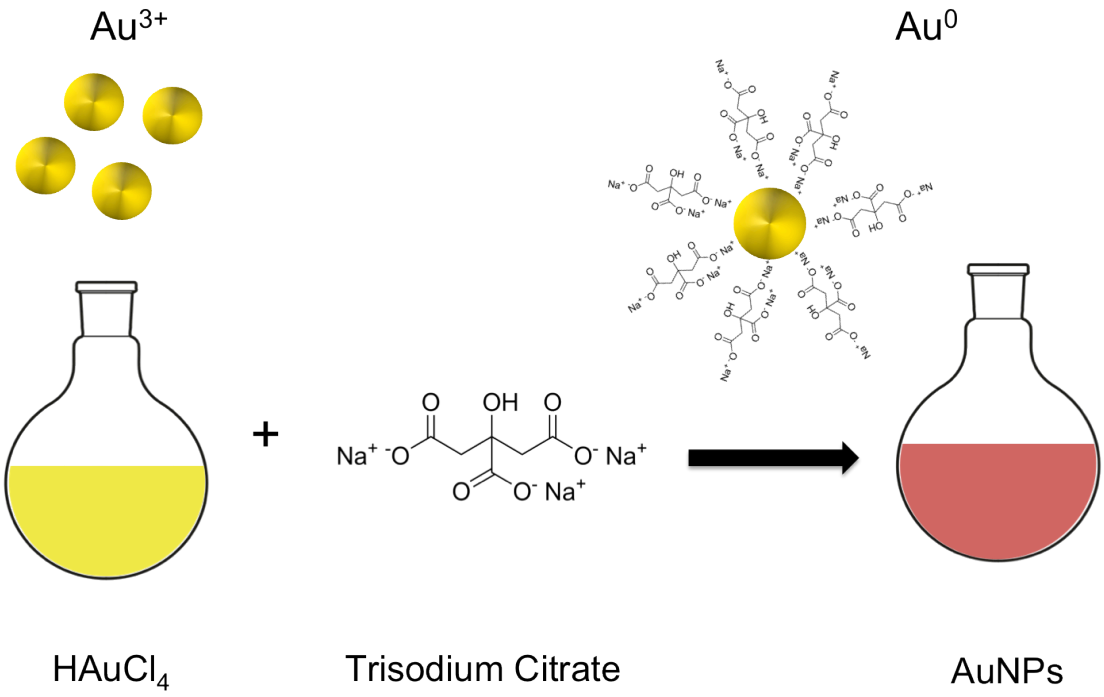


Figure 1-3. Gold nanoparticles of different shapes and sizes. Transmission electron microscopy (TEM) images of (a) 15 nm colloidal AuNPs, (b) 15 x 50 nm gold nanorods, Scanning electron microscopy (SEM) image of (c) 160 (core) / 17 (shell) nm silica / gold nanoshells and TEM images of (d) 250 nm gold nanobowls with 55 nm gold seeds in their inside, (e) gold nanocages and silver cubes, (f) 100 nm gold nanostars, (g) gold bipyramids and (h) gold octahedrals. (*Figure adapted from Khlebtsov and Dykman 2010 [78, 81], Copyright © 2010, with permission from Elsevier*)

The synthesis of AuNPs is relatively simple, with several synthetic routes being available, which mainly rely on the reduction of the gold salt into a gold metal using citrate. Through reduction of the gold salt by citrate, stabilization of the citrate nanoparticles is achieved through electrostatic or steric interactions[82]. The majority of the synthetic procedures currently used for the synthesis of AuNPs are based on a method first described by Turkevitch et al. in 1951[83], which involves the addition of a citrate solution to a boiling solution of $HAuCl_4$ in order to reduce the gold salt from Au^{3+} to form A^0 (Scheme 1-1).



Scheme 1-1. Schematic representation of the AuNPs syntesis method first reported by Turkevich et al. in 1951.

The favourable optical properties of AuNPs rely on their SPR, a process by which electrons of the gold surface layer resonate as a result of an incoming radiation, which allows them to both absorb and emit light[84] (Figure 1-4). The combination of SPR with an imaging system allows high throughput and label free biosensing, while biomolecular interactions can be monitored at the same time[84]. The size and shape tunable properties of AuNPs allow the synthesis of nanoparticles with a surface plasmonic resonance within the range of 500 to 1200 nm[85]. Another advantageous property of AuNPs is the surface area they offer, which is inversely proportional to their small size[86]. Therefore, they have a large surface area to volume ratio for high loading of drugs, targeting complexes and biological moieties. The large surface area of AuNPs along with their negatively charged citrate surface allow them to be easily multifunctionalised with a various types of ligands and biomolecules through conjugation of amine and thiol groups to the gold surface.

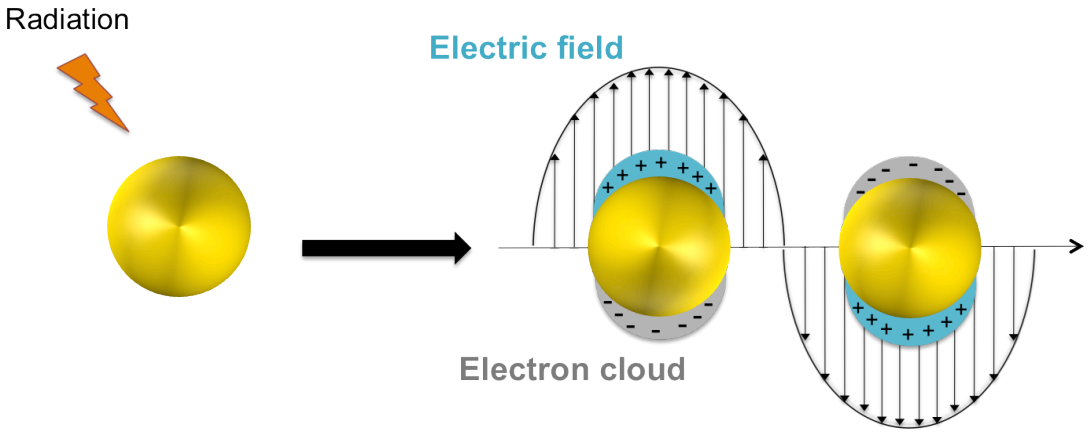


Figure 1-4. Schematic representation of the SPR effect on AuNPs. Upon irradiation of AuNPs with a light of a specific wavelength, the free electrons on the gold surface collectively oscillate. This effect is described as the surface plasmon resonance (SPR) effect. The SPR of AuNPs is highly dependent on their size and shape.

The favourable physiochemical properties of AuNPs along with their ability to be loaded with different types of bioactive molecules offer opportunities for use in a wide range of medical applications including diagnostics, localised drug delivery, imaging and sensing[87] (Figure 1-5). For example, AuNPs can be functionalized with nucleic acids and oligonucleotides for silencing of genes and applications in colorimetric assays[88]. Attachment of carbohydrates to the gold surface can also be used enhancing the detection sensitivity of colorimetric bioassays[89]. What is more, attachment of polymers, like PEG, can improve drastically the solubility and stability of AuNPs, which is essential for the successful development of theranostic nanoprobes suitable for both *in vitro* and *in vivo* applications[90]. Conjugation of chemotherapeutic drugs, aptamers and dendrimers to AuNPs can also be used to improve the targeted delivery of therapeutic agents to the tumor site, and thereby induce an enhanced therapeutic effect[91]. Furthermore, the attachment of tumor biomarkers, antibodies and peptides to the gold surface can lead to optimal cellular uptake in biological samples and provide high selectivity upon treatment[91, 86]. The use of fluorescent molecules to coat AuNPs is also investigated in the nanotechnology field for the development of fluorescent nanoprobes, which can be used in biomedical imaging applications. For instance, fluorescent AuNPs can be used in biological specimens for diagnostic purposes, probing of the tumor microenvironment as well as monitoring therapeutic response[92].

The large surface are to volume ratio provided by small AuNPs plays a major role in their biological responses within an intracellular environment, as smaller in size nanoparticles tend to exhibit more interactions with cellular proteins when compared to larger nanoparticles with smaller surface area to volume ratio[93]. Consequently, the large surface area of AuNPs provides a favourable pharmacokinetic profile, with enhanced stability and solubility, which is essential to maintain high bioavailability of targeting agents in biological systems[94, 95]. The high stability that AuNPs exhibit against oxidation in physiological conditions, such as variable pH, temperature and ionic strength, reduces considerably toxicity levels in biological environments, thereby, providing a promising approach for site-specific targeting[96, 97].

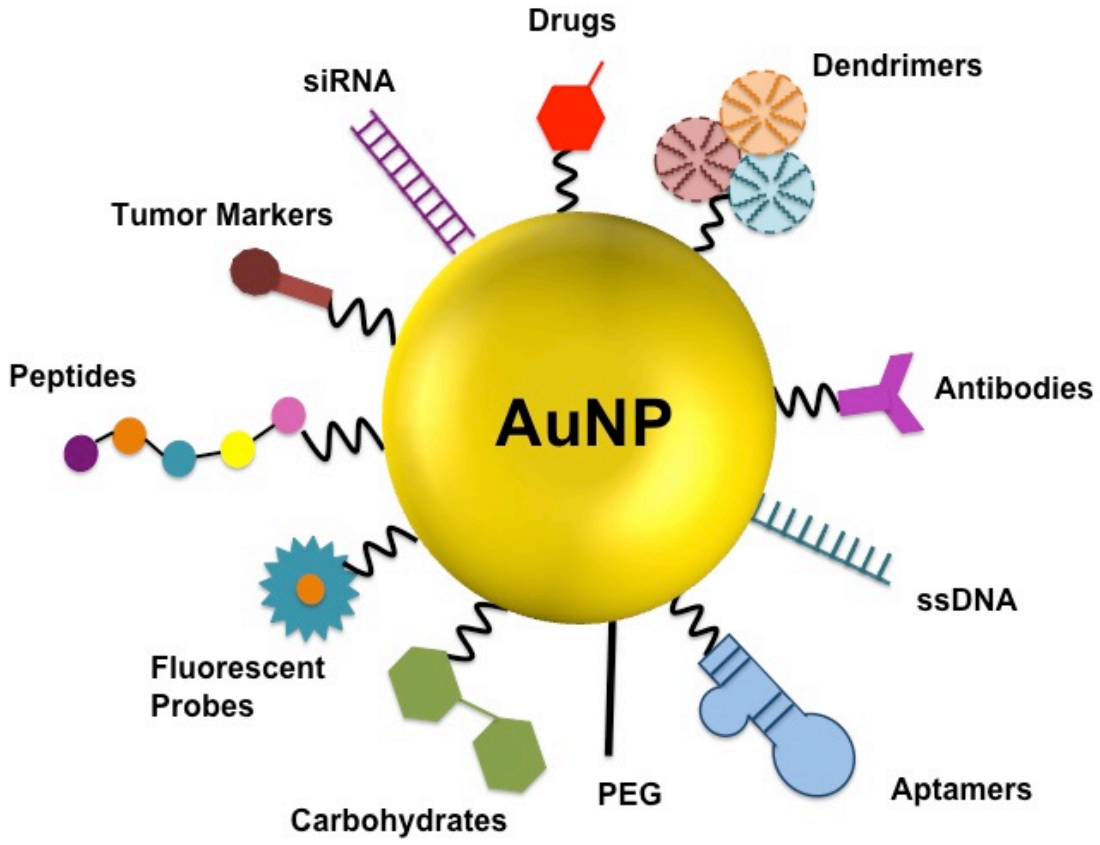


Figure 1-5. Multifunctionalized AuNP for theranostic applications. AuNPs can be functionalized with nucleic acids like DNA and RNA for use in colorimetric assays and gene silencing. Carbohydrates also serve as sensitive colorimetric molecules. Aptamers, anticancer drugs and dendrimers can be attached for improved drug delivery to the target site. PEG can be used to enhance stability and solubility. Tumor biomarkers, antibodies and peptides can be attached to provide selectivity and improve cellular uptake in biological samples. Fluorescent probes can be used for imaging applications.

Besides the beneficial properties of citrate AuNPs in biomedical applications discussed in this section, the extensive evaluation of the *in vitro* biocompatibility of functionalized AuNPs subsequent to cellular internalization is crucial prior to proceeding to *in vivo* applications and clinical studies. Even though AuNPs exhibit an inert nature that makes them highly biocompatible, upon surface modification they can still display cellular cytotoxicity due to the formation of a "protein corona" formation on their functionalized surface[93]. The "corona" formation impacts the biodistribution and pharmacokinetics profiles of AuNPs in an intracellular environment, and therefore, defines their fate within a large living organism, such as the human body.

1.4.1 Gold nanoparticles for the delivery of therapeutic agents

The recent advances in nanomedicine have led to the development of various gold nanoparticle-based systems for the delivery of chemotherapeutic drugs that are currently approved for use in the clinic. The use of AuNPs as nanovectors has demonstrated improved delivery efficacy and enhanced bioavailability of chemotherapeutic drugs at the target site, as the high complexity of the tumor vasculature provides favourable conditions for accumulation of AuNPs.

Previously reported formulations include the attachment of methotrexate, a chemotherapy agent and an immune-system suppressant, to the surface of AuNPs, in order to achieve higher and faster accumulation of the drug in cancer cells[98]. Upon conjugation to the gold surface, methotrexate displayed higher levels of cytotoxicity in numerous cancer cell lines when compared to free methotrexate in solution. Multiple studies have reported similar results after treatment of cancer cells with the fluorescent chemotherapeutic agent doxorubicin in the presence and absence of the gold scaffold. Due to the fluorescent nature of doxorubicin, drug release can be easily monitored upon entry of the drug into the intracellular environment. When doxorubicin was conjugated to AuNPs, the drug demonstrated higher cytotoxicity in a resistant breast cancer cell line, through overcoming multi drug resistance (MDR) via inhibition of P-glycoprotein (P-gp)-

mediated drug efflux[99] (Figure 1-6). A similar study reported that the development of a drug delivery system using PEG to attach doxorubicin to the surface of AuNPs resulted to highly efficient cellular uptake and high drug accumulation in the resistant hepatocellular carcinoma cell line hepG2-R.[100]. The high efficacy of AuNPs as nanovectors to deliver doxorubicin in cancer cells was further confirmed through another study, which reported that the use of AuNPs to deliver doxorubicin to human lung cancer cells results to enhanced cellular uptake and up-regulation of tumor suppressor genes, leading to intrinsic apoptosis[101].

AuNPs have also been used for delivering doxorubicin in combination with another chemotherapeutic drug, bleomycin, in cervical carcinoma cells, HeLa, aiming to develop a simple nanohybrid drug delivery system. The simultaneous delivery of the two anticancer agents upon attachment to AuNPs induced an enhanced therapeutic effect while using significantly reduced drug concentration, through blocking progression of the cell cycle[102].

Several platinum-based drugs, including oxaliplatin, carboplatin and cisplatin have been used widely as chemotherapeutic agents for treating cancer, but their therapeutic efficacy in the clinic is hindered by their ability to induce resistance and sever, dose-limiting side effects. Similarly to the chemotherapeutic agents discussed in this section, the effectiveness of platinum-based drugs can also be improved using AuNPs as drug carries, through targeting cancer cells in either a passive or active manner. It has been previously reported that conjugation of the active component of oxaliplatin to AuNPs, improves radically the site-specific delivery of the drug. More specifically, the results of the study indicated that the platinum conjugated AuNPs have improved cytotoxicity and higher penetration of the nuclear membrane when compared to the free drug in solution[103].

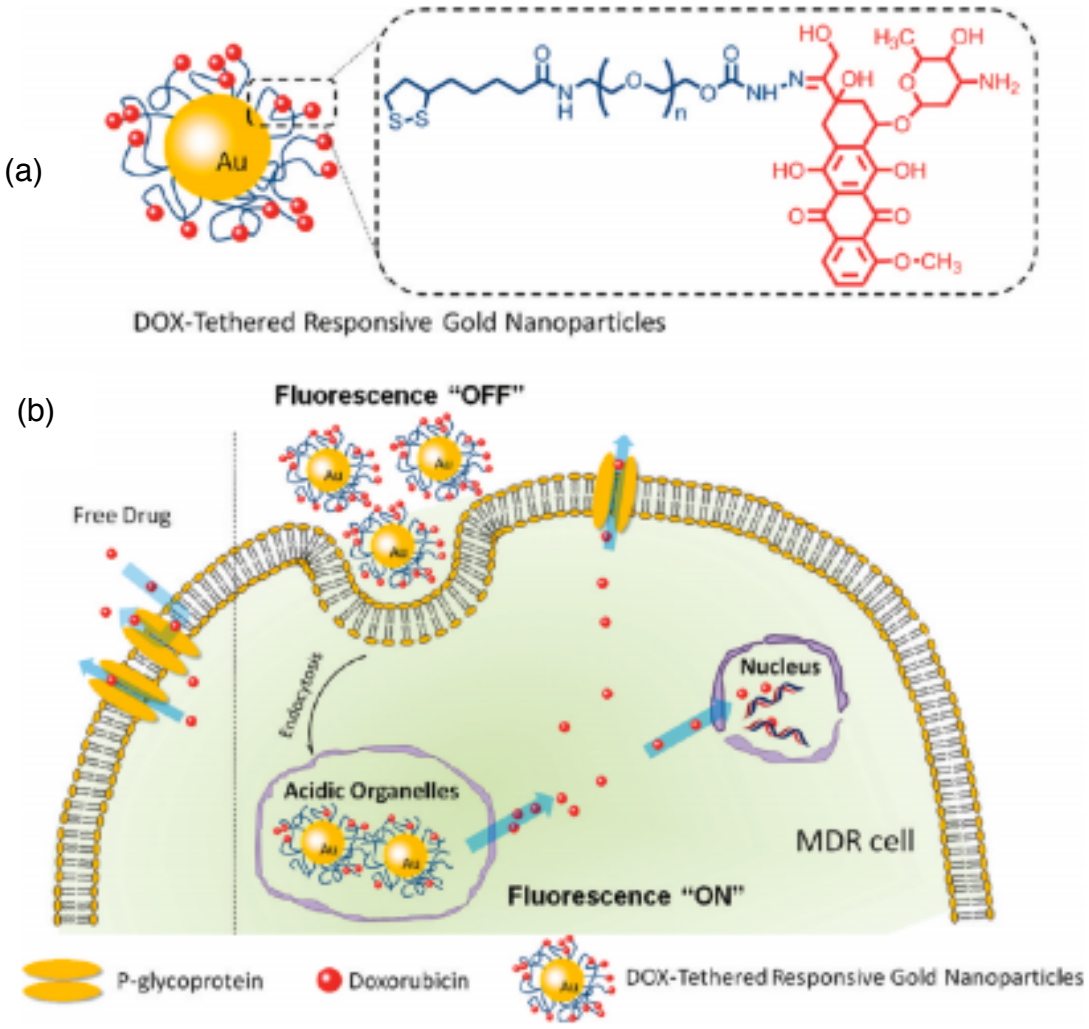


Figure 1-6. **(a) Schematic illustration of doxorubicin conjugated AuNPs. (b) Schematic illustration of the delivery of doxorubicin on AuNPs showing enhanced entry in MDR cell with an intracellular release of the drug overcoming resistance. Conjugation of doxorubicin to the gold surface quenches fluorescence of the drug. Upon release from the surface of AuNPs within intracellular conditions, the fluorescence of the drug is recovered, aiding in tracking intracellular release and trafficking. (*Figure adapted from Wang et al. 2011[99], Copyright © 2011, with permission from American Chemical Society*)**

Peptide-drug-conjugates (PDCs) have been previously investigated as potential anti-cancer agents, but their success in clinical applications was compromised by their low solubility and stability within the bloodstream and several organs, including kidneys and liver[104]. However, it was recently suggested that the solubility and stability related issues of PDCs can be overcome in the presence of AuNPs, as an increase in the half-life of PDCs was observed upon conjugation to the gold surface, while cytotoxicity was

maintained at relatively high levels[105]. Besides synthetic drugs, phytochemicals have also been studied as potential cancer therapeutic agents, but it was suggested that they are lacking specificity, have low cell penetration and short half-life. However, when the effect of a phytochemical, kaempferol, was investigated upon attachment to AuNPs in the breast cancer cell line MCF-7, it was able to promote apoptosis and inhibition of angiogenesis[106].

The findings of the aforementioned studies indicate that AuNPs provide advantageous properties as drug carriers, as they have the ability to overcome the therapeutic limitations of conventional anticancer agents, such as reduced solubility, inefficient drug delivery and multi drug resistance. Hence, they represent a promising approach, with favourable elements, for the development of novel, nanoparticle-based systems to improve drug bioavailability and site-specific delivery of therapeutic agents in biological systems.

1.4.2 Gold nanoparticles in clinical studies

As discussed earlier, the use of gold nanoparticle-based systems for the systematic delivery of drugs demonstrates significant advantages over the delivery of free drugs in solution, as such systems are able to deliver drugs to targeting sites that free drugs cannot successfully reach[16] (Figure 1-7). Consequently, AuNPs are widely investigated as delivery and imaging systems in both preclinical and clinical settings.

The use of nanoparticle formulations for drug delivery in the clinic begun in the early 1990s and since then, research has evolved drastically to adapt to the growing needs of the nanotechnology field, aiming to improve the delivery of conventional therapeutic agents. Over the past few decades, various generations of nanoparticles with the ability to perform improved delivery functions have emerged in the field, enabling the development of novel therapeutic modalities[62]. Currently, many of these generations of nanoparticles have successfully reached the clinical trial stage and have been approved for different applications.

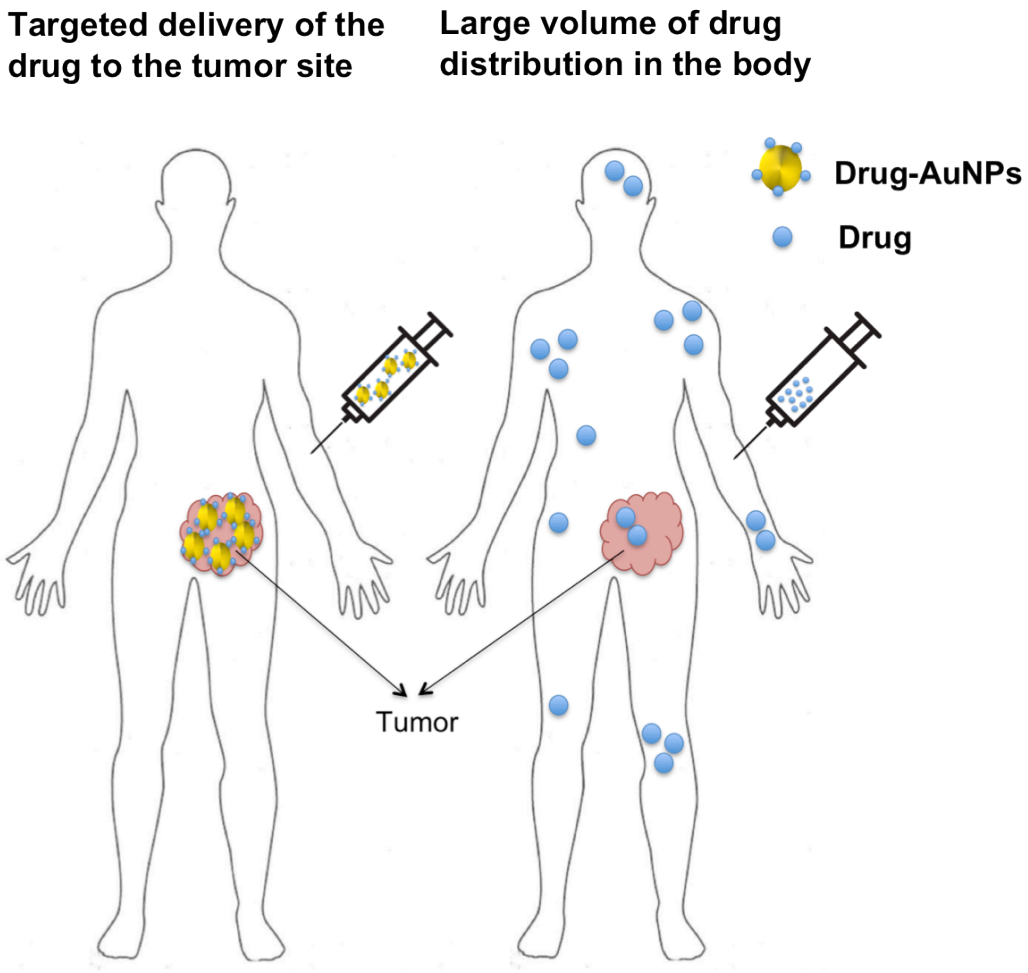


Figure 1-7. Schematic illustration of drug distribution in a human body subsequent to injection with drug conjugated on AuNPs and free drug.

There is a currently a large number of trials that are actively carried out investigating the use of nanomaterials in the clinic. Even though there are only a few clinical trials carried out for the approval of AuNPs in cancer treatment, there are already some gold nanoparticle-based systems that have been approved by FDA for both diagnostic and therapeutic purposes[107]. One of the clinical trials carried out for the approval of AuNPs as therapeutic nanoprobes involved the use of thiolated PEG coated AuNPs to deliver the tumor necrosis factor alpha (TNF) to cancer cells. The results indicated the safe delivery of TNF to malignant cells at doses three times higher than the usual dose of administration, without any adverse toxic effects[108]. The delivery of TNF into tumors upon attachment to

AuNPs resulted to disruption of blood vessels, allowing chemotherapeutic agents to penetrate the tumor site and destroy cancer cells[108].

Due to the favorable property of gold to absorb near-infrared (NIR) light, there is a growing interest in the use of AuNPs in both photodynamic and photothermal therapy (PDT and PTT) approaches[109-111]. PDT involves the use of NIR-light to activate functionalized AuNPs, resulting to generation of free radicals or reactive oxygen species (ROS), usually singlet oxygen ($^1O_2$), which leads to cellular toxicity[112]. In PTT, the use of NIR-light to irradiate functionalized AuNPs results to enhanced tissue penetration, leading to heat-induced cell death[113] (Figure 1-8).

Scientists are currently focusing on the development of photothermal approaches using gold nanomaterials in order to improve *in vivo* bioavailability and at the same time, selectively target cancer cells and promote their destruction[114]. For instance, PEG coated silica-gold nanoshells have been developed that can be stimulated with a source of NIR light to induce an increase in temperature and thus, thermally ablate solid tumors[16, 115, 116]. Numerous clinical trials have been carried out for the approval of these nanoaprticle formulations in the clinic for treating different types of cancer. More specifically, clinical studies have been performed for locally treating both primary and metastatic tumors in lungs, refractory and recurrent tumors of head and neck cancer as well as prostate tumors[86, 20]. Due to the fact there is no active drug used in these delivery systems, the coated nanoshells are activated through an external stimulus at the target site, eliminating damage to healthy tissues and thereby, avoid off-target toxicity in normal cells. Therefore, the use of gold nanomaterials is a promising tumor ablation therapeutic approach, aiming to maximize the treatment efficacy and prevent undesirable side effects[86, 20].

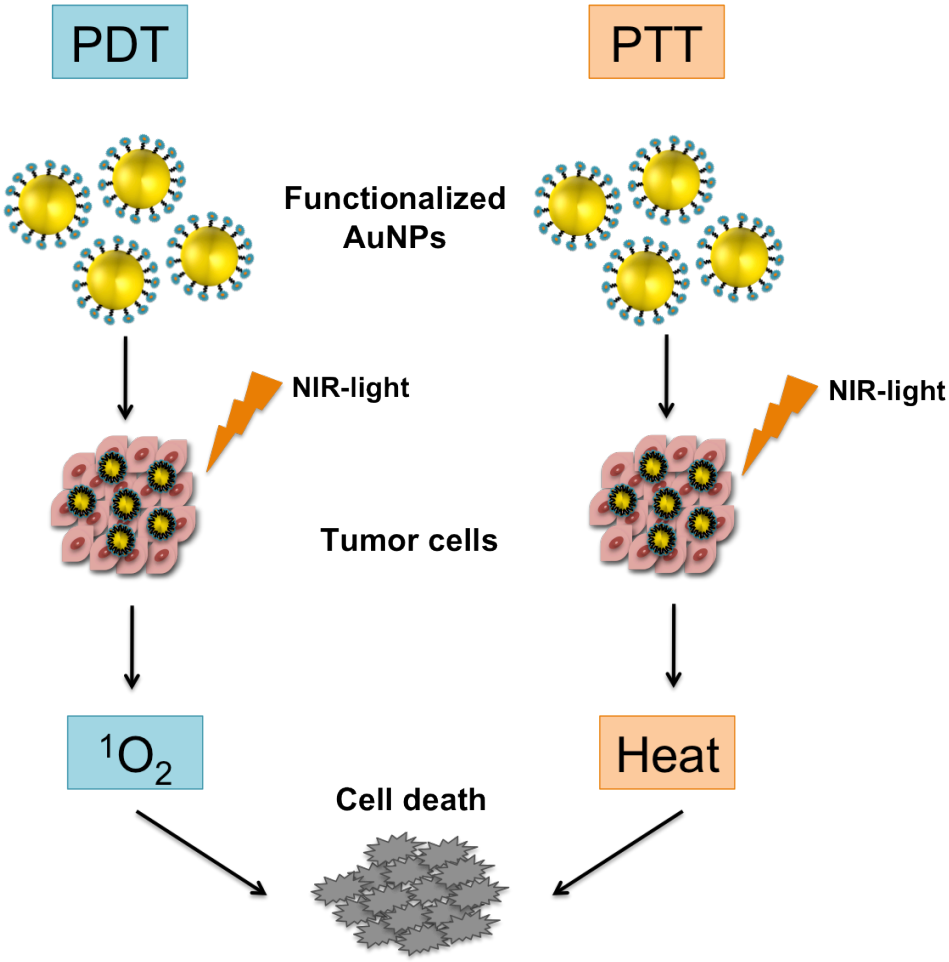


Figure 1-8. **Schematic illustration of the basic mechanisms of PDT and PTT using functionalized AuNPs to target cancer cells. PDT uses NIR-light to activate functionalized AuNPs, resulting to generation of singlet oxygen that leads to cell death. PTT uses NIR-light to activate functionalized AuNPs, leading to heat-induced cell destruction.**

Besides the use of gold nano-based systems for therapeutic purposes, many formulations have been developed in the presence of AuNPs for cancer theranostic applications and have advanced to the clinical trial stage. Due to the ability of nanomaterials to penetrate various biological barriers, such as blood-brain and blood-tumor barriers, AuNPs are considered as ideal permeable anticancer conjugates for delivering various proteins, drugs and nucleic acids to suppress oncogene expression[117, 118] The efficacy of a spherical nucleic acid formulation has been previously investigated in clinical trials and involved the covalent conjugation of siRNAs to AuNPs, aiming to target the Bcl-2-L12 gene in patients with glioblastoma[117, 118].

In a different clinical trial, the appropriateness of a novel at the time method based on AuNPs was evaluated, which involved breathing analysis using a nanosensor array to detect gastric diseases. The results of the study suggested that a nanosensor array can be successfully used in the clinic for non-invasive screening to differentiate precancerous lesions and benign tumors from malignant tumors and gastric carcinoma[119].

Apart from the clinical evaluation of gold nanoparticle-based systems for cancer theranostics, the use of AuNPs as therapeutic nanoprobes for treating cardiovascular diseases was also evaluated in a clinical setting. For example, the efficacy of a PTT approach using silica-gold nanoparticles was investigated as a treatment for the ablation of plaques in arteries, with the findings of the study indicating an acceptable safety level for clinical use and a significant regression of coronary atherosclerosis[120].

Even though the use of AuNPs in the current clinical landscape shows promising results for the clinical translation of cancer nanomedicines, there are still numerous issues that need to be addressed, prior to designing and developing novel nanoparticle formulations for *in vivo* applications. Such issues include the reproducibility of the manufacturing method, the nanoparticles stability, cellular responses and the long-term effects on human health. Therefore, there is a growing need in the nanotechnology field for sustained research in order to develop novel systems that focus on the precise localization of nanoparticles in a biological system, related immune responses and excretion from the human body.

1.5 Cellular uptake mechanisms of gold nanoparticles

The multifunctionality of AuNPs and their ability to be synthesized into a variety of different shapes and sizes allow them to penetrate the cell surface membrane with high efficiency[79]. The interaction of modified AuNPs with biological membranes is greatly impacted by their size, shape, surface coating and charge[121]. Therefore, for the effective design of AuNPs with optimal uptake, a cautious consideration of nanoparticles properties is fundamental, as they determine cellular interactions in living systems and thus, the appropriateness of the functionalized nanoparticles to be used in biomedical applications[122].

The cellular uptake mechanism by which AuNPs enter a cell and their intracellular fate is highly dependent on their physiochemical characteristics[123, 124]. Other factors, such as the concentration of nanoparticles and the incubation time used during treatment of the cells can also influence both the uptake of nanoparticles and their intracellular fate[125, 126]. Since physiochemical properties are essential in determining intracellular fate, surface functionalization of AuNPs with targeting moieties can greatly impact their trafficking behavior and subcellular localization inside cells[127]. For example, binding of biomolecules that are conjugated to the surface of AuNPs against cellular targets inside the cells can enhance nanoparticle accumulation within the intracellular environment and thereby, decrease the processes of exocytosis[128, 129]. Conjugation of biological moieties such as antibodies and peptide ligands to AuNPs has previously shown to increase cellular uptake as a result of interactions between the nanoparticles and cell surface membrane[130]. Enhanced cellular uptake through different ligand modifications can improve cellular signaling and lead to long-term tracking of molecular targets inside the cell[131].

There are several cellular uptake mechanisms by which AuNPs internalize within a cellular environment, such as clathrin- and caveolae-dependent endocytosis, clathrin- and caveolae-independent endocytosis, macropinocytosis and phagocytosis[132] (Figure 1-9). Cellular uptake of AuNPs by endocytosis involves the formation of membrane-enclosed vesicles formed from the cell surface membrane that contain the nanoparticles along with extracellular fluids and different proteins[133].

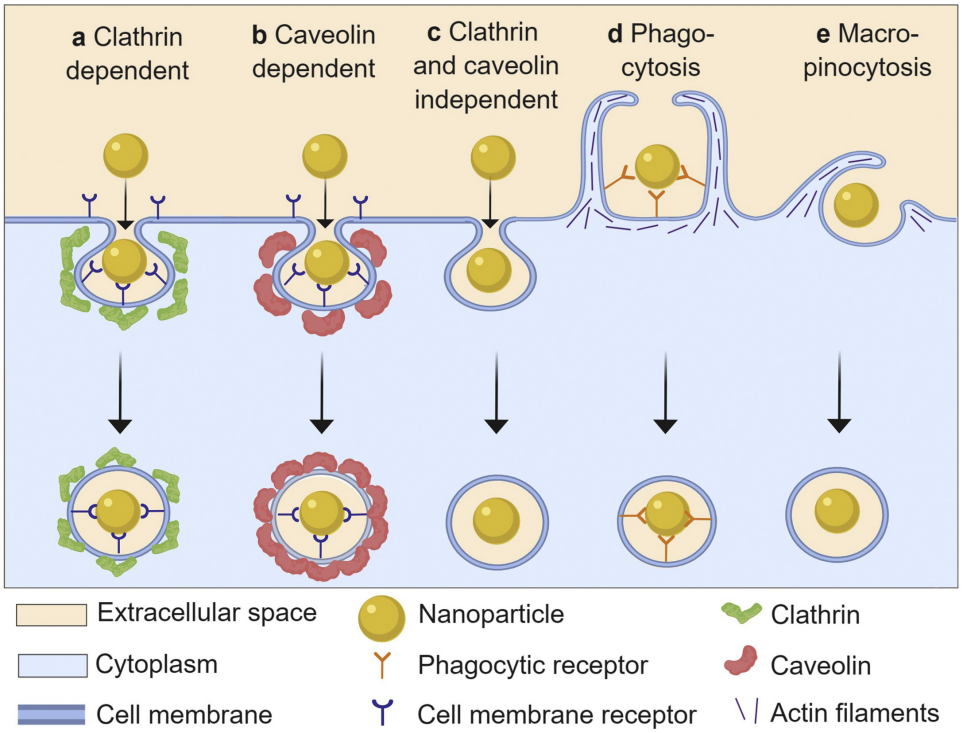


Figure 1-9. Schematic representation of the different endocytic mechanisms by which AuNPs internalize into cells. Cellular uptake of AuNPs results in the entrapment of AuNPs into vesicles, which are transported within the cellular environment with the aid of actin filaments. (a) Clathrin-dependent endocytosis – Major pathway of AuNPs cellular entry that involves binding of ligands on the surface of AuNPs on corresponding receptors on the cell membrane. (b) Caveolin-dependent endocytosis – Receptor specific internalization pathway of AuNPs that depends on caveolin coated cell membrane invaginations, described as caveolae. (c) Clathrin- and caveolin-independent endocytosis – Cellular internalization of AuNPs relies on lipid rafts like sphingolipid and cholesterol rich domains found on the cell membrane. (d) Phagocytosis – Cellular uptake through binding of ligands on the surface of AuNPs on phagocytic receptors on the surface of cell membrane. (e) Macropinocytosis – Non-specific cellular uptake mechanism that is characterized by engulfment of extracellular material along with the AuNPs by actin-stabilized cell membrane extensions. (*Figure adapted from Donahue et al. 2019[134], Copyright © 2019, with permission from Elsevier*)

It has been previously discussed in literature that the main mechanisms that cells use to internalize nanoparticles are active processes, such as energy-dependent endocytosis mechanisms[135, 136]. The main cellular uptake mechanism by which functionalized AuNPs are internalized is known to be receptor-mediated endocytosis, through which molecules conjugated to the surface of AuNPs bind to and interact with receptors on the extracellular surface of the cell membrane. This results to fusion with the membrane followed by the formation of endosomal vesicles, which allows the cell to transport the AuNPs within the

cytosoplasmic region[137, 138]. The process of receptor-mediated endocytosis and the mechanism by which AuNPs are internalized involves proteins such as clathrin, a protein repoponsible for the formation of coated vesicles, and caveolae, which are small invaginations of the cell membrane[139, 140].

Although the different endocytosis mechanisms are widely recognized as the major pathways through which nanoparticles internalize within cells, other mechanisms of entry such as passive diffusion have also been discussed in the past[141]. Entry of nanomaterials by passive diffusion is regulated through proteins found on the cell membrane, including channel proteins, receptors and transporters[142]. It has been previously reported that nanoparticles of about 4 nm are able to internalize within red blood cells (RBCs) and penetrate their plasma membrane by a passive, non-endocytic process[143]. The interaction of the nanoparticles with the membrane results to a more flexible and soft bilayer structure, which allows the passive entry of nanoparticles without influencing the overall integrity of the cell membrane or producing any gaps in the phospholipid bilayer[143]. Moreover, various nanomaterials have also been shown to pass through cell membranes by passive processes like diffusion and adhesive interactions. Various types of both inorganic and organic nanoparticles have been reported in literature to be able to penetrate the cell membrane through disruption of the phospholipid bilayer and formation of nanosized holes[144, 145].

Even though the cellular uptake mechanisms and intracellular trafficking of nanomaterials have been well-exploited in the nanomedicine field within the past few years, a lot more progress is required to fully understand the full mechanisms of internalization and cellular interactions in different types of cells and tissues. New advances in the field are likely to lead to the development of new methods that will aid in the improved analysis of nano-bio interactions at subcellular level, through for example epigenetic or mitochondrial targeting[141]. Such methods include high content analytics, imaging cytometric techniques, cryo-electron and high-resolution microscopy. Through continuous advances in the chemical synthesis of nanomaterials, novel structures with precisely defined biochemical characteristics will soon be developed for both exploiting and treating complex human diseases, such as cancer[146].

1.6 Gold nanoparticles for biomedical imaging

Early detection and diagnosis is essential in clinical practice, especially for diseases like cancer. Cancer patients benefit from early detection and demonstrate a prolonged survival and mortality rate[147, 148]. Medical imaging based technologies are crucial for the early detection of malignant tumors and thus, for predicting the therapeutic response. Current imaging modalities include X-ray radiography, magnetic resonance imaging (MRI), computed tomography (CT), positron emission tomography (PET), photo-acoustic imaging, ultrasound (US) and fluorescence imaging[87, 149].

Even though imaging techniques such as MRI, CT, PET and US are widely used in the medical field for detecting cancerous lesions, their spatial resolution is only on a macroscopic level[150, 151]. Fluorescence imaging currently provides the highest resolution for detection and diagnosis of diseases at a microscopic level, particularly through the use of near-infrared light[149]. When compared to imaging approaches that use visible light, near-infrared fluorescence (NIRF) imaging provides deeper penetration and reduces non-specific autofluorescence in biological specimens. Although NIRF imaging is a powerful technique and significantly advantageous over other imaging applications, its depth penetration in various types of tissues and scattering properties sometimes still limit its use in the clinic[152]. Furthermore, poor detection sensitivity has also been previously observed with NIRF imaging due to low levels of fluorescence at the tumor site, which can induce photobleaching[152, 153].

The unique physiochemical properties of nanoparticles provide possibilities for overcoming the limitations of conventional imaging techniques. For instance, through their ability to be multi-functionalized, AuNPs can prevent potential quenching of NIRF[154], as nanoparticle-based systems for imaging applications can be designed to convert photons with low energy into higher energy photons, thereby aiding in reducing photobleaching[155].

What is more, the multifunctionality of AuNPs provides opportunities for high loading of imaging agents. For example, the use of nanoparticles in fluorescence imaging applications, allows a larger number of fluorescent molecules to be conjugated to the nanoparticles surface, providing an enhanced detection signal[156]. Also, the fact that

accumulation of nanoparticles in target lesions can be increased through both active and passive processes, suggests that high levels of fluorescence can be acquired upon imaging. More specifically, the vascular permeability of tumors driven by the enhanced permeability and retention effect (EPR) induces high accumulation of nanoparticles within cancer cells[157]. The high accumulation of AuNPs in tumors has led to the development of many nanoparticle-based multifunctional platforms for use in both NIR-based cancer imaging and PDT therapy[158] (Figure 1-10).

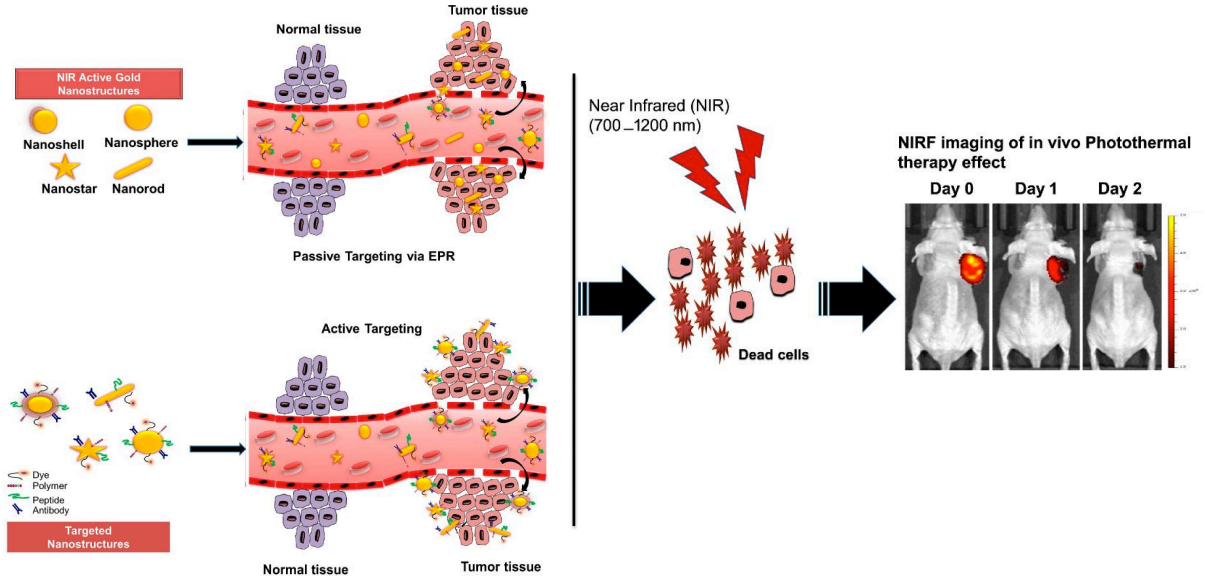


Figure 1-10. Schematic illustration of AuNPs accumulation in tumor cells via EPR effect for use in NIR-mediated imaging guided by PDT. (*Figure adapted from Vats et al. 2017*[158]*, Copyright © 2017, Open Access*)

Organic fluorophores have also been widely investigated for imaging biological samples, however, their use is hindered by their narrow excitation spectra and broad emission[159]. What is more, previously published studies have reported the fabrication of various NIR fluorophores with improved photophysical properties, but their intrinsic hydrophobicity prevented their direct use for *in vivo* applications[160, 161]. Even when NIR fluorophores were attached to nanoparticles in order to eliminate hydrophobicity related issues and achieve enhanced resolution in vasculature structures in *in vivo* models, their use in bioimaging was still an issue due to quenching upon transferring to aqueous solutions[162].

Besides fluorophores, quantum dots have also been investigated as alternative agents for biomedical imaging, but they also exhibit numerous limitations such as high cellular toxicity[163, 164]. In comparison to other inorganic nanoparticles and other gold nanosized materials, such as nanostars, nanorods and nanocages, AuNPs have been proven to have better properties for both *in vitro* and *in vivo* imaging applications due to their ability to be easily modified, tunable SPR and low cytotoxicity[165-169]. For example, the characteristic SPR wavelength of AuNPs can be easily tuned from the visible to the NIR region to eliminate photobleaching related issues during imaging[87, 168, 170]. The high electron density of gold is another advantageous property of AuNPs, as it provides enhanced contrast to study subcellular localization and nanoparticle-cell interactions using imaging techniques such as light and transmission electron microscopy[171]. What is more, the light scattering properties of AuNPs are superior over other inorganic nanoparticles, and thereby, allow them to appear brighter than the background in biological specimens due to enhanced contrast and detected easily by commercial microscopes using dark-field illumination[172-175].

Two-photon luminescence microscopy is another popular imaging system used widely in biomedical research, as it provides possibilities to overcome autofluorescence in biological samples and enables high spatial resolution 3D images, which are some of the most common problems that other optical imaging systems face[176]. Moreover, immuno-electron microscopy is another optical system that can be used to visualize functionalized AuNPs in cells and at the same time study cellular targets, such as proteins, at a

subcellular level using electron microscopy techniques[177, 178]. More specifically, this technique uses AuNPs labeled with antibodies in order to detect, quantify and localize a specific antigen in biological specimens[87, 178].

X-ray computed tomography is another biomedical imaging system that benefits from the advantageous properties of AuNPs. When compared to conventional contrast enhancing agents, AuNPs absorb X-rays with significantly higher efficiency and thus, allow improved contrast in computed tomography images[169, 179]. Also, the circulation time of AuNPs in the blood is considerably longer in comparison to the circulation time of conventional X-ray tomography agents, such as iodine-based contrast agents[180, 181].

MRI is a widely used imaging technique in the clinic, as with the use of contrast enhancement agents, such as gadolinium[182], it can noninvasively develop a well-defined 3D image with high resolution[87]. However, the use of AuNPs has been previously reported to enhance both the contrast as well as specificity in MRI scans. Gadolinium based contrast agents have relatively low specificity for tumors, as they are not able to differentiate between benign and malignant tumors[183]. The multifunctionality of AuNPs, allows the conjugation of cancer targeting moieties to their surface in order to direct them to the target site and achieve high accumulation of nanoparticles within tumor cells for cancer specific imaging[184].

Different surface functionalization approaches have been previously reported to successfully enhance the stability and biocompatibility of AuNPs in biological environments, which is essential for their use as nanoprobes in biomedical imaging applications. As discussed earlier, the favorable characteristics of AuNPs provide a lot of opportunities for their use in many imaging applications. However, their ability to combine multiple functional molecules on their surface provides further opportunities for the development of multimodal contrast imaging systems that can be used to unravel both the structural and functional complexity of a living system, such as the human body. Hence, the design of novel nanoparticle-based imaging systems is crucial for the continuous development of the nanotechnology field and the progress of biomedical imaging in the upcoming years.

1.6.1 Luminescent gold nanoparticles for multimodal imaging

Due to their unique optical and physiochemical properties, AuNPs have gained a lot of attention in the medical field for their ability to be used as multifunctional nanoprobes in cancer theranostics[95]. When compared to other molecular probes, AuNPs are capable of incorporating a high loading of multiple imaging and targeting moieties, thus providing high sensitivity with improved spatial resolution[185, 186].

The use of luminescent transition metal complexes has recently received significant interest in the nanotechnology field for the development of luminescent nanoparobes using AuNPs as a delivery vehicle, aiming to translate the attractive properties of the luminescent complexes to the gold nanoprobes[186-188]. Conjugation of transition metal complexes to the surface of AuNPs allows coating with hundreds to thousands metal complexes per nanoparticle, depending on the complex and nanoparticle size, which provided a strong luminescent signal during imaging[188, 189]. The luminescent AuNPs acquire the unique photophysical properties of luminescent transition metal complexes, including high photostability, large Stoke shifts and long-lived luminescence along with the favorable properties of gold[190, 191]. Therefore, luminescent AuNPs do not exhibit either the "blinking" effect previously reported with the use of other organic dyes[187] neither any unpredictable magnetic properties that can arise from the bulk material[192].

It has been previously reported that coating of AuNPs with a luminescent ruthenium complex, produces luminescent nanoparobes with longer luminescence lifetimes when compared to the molecular complex alone, which can be used for imaging cancer cells using confocal luminescence microscopy. More specifically, ruthenium coated AuNPs of 13 and 100 nm were developed and successfully used for luminescence imaging in lung cancer, A549 cells, revealing nuclear localization and biomolecular interactions of single, non-aggregated AuNPs with chromatin[187] (Figure 1-11). The appropriateness of such luminescent nanoprobes for imaging applications was evident through the high stability and long half-life that the ruthenium AuNPs exhibited, as luminescence was able to detected in the cells even three days after the chase experiment[187]. This was further confirmed by a recently published study, demonstrating that the high photostability of

ruthenium coated AuNPs in lung cancer cells allows quantification of the cellular uptake through tracking the ruthenium luminescent signal over time using confocal luminescence imaging[193].

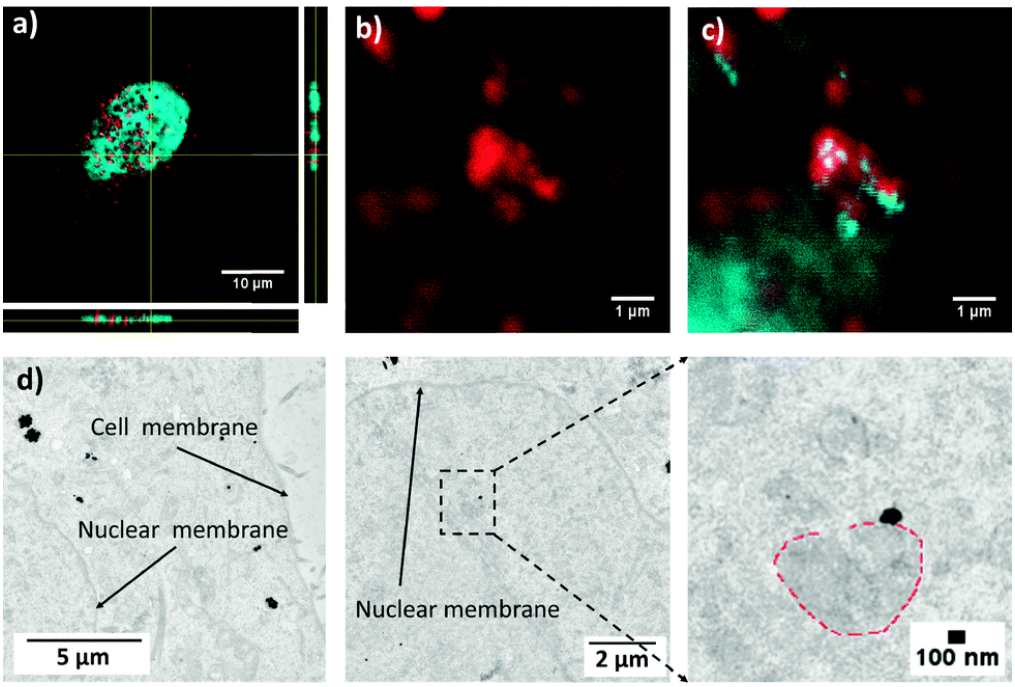


Figure 1-11. Imaging analysis of nuclear localization of ruthenium coated 100 nm AuNPs in lung cancer A549 cells, (a) Z-stack confocal image of a single cell showing ruthenium luminescence co-localized with Hoechst (nuclear stain) luminescence. (Scale bar: 10 µm) (b) Ruthenium luminescence image. (Scale bar: 1 µm) (c) Overlay image of (b) with Hoeschst. (Scale bar=1 µm) (d) TEM images of ruthenium coated 100 nm AuNPs in an A549 cell. Magnified inset shows interaction of condensed chromatin (red-dashed line) in the nucleus with the ruthenium coated nanoparticles. (Scale bars: 5 µm, 2 µm and 100 nm) (*Figure adapted from Rogers et al. 2014[187], Copyright © 2013, with permission from The Royal Society of Chemistry*)

Similarly to ruthenium molecular complexes, iridium complexes have also been reported to be suitable transition metal complexes for luminescence imaging, upon conjugation to AuNPs. Luminescent iridium coated AuNPs of 100 nm in size have been previously introduced for both visualization and tracking of blood flow in narrow vessels, with significantly enhanced resolution in comparison to conventional alternatives[189]. The luminescent iridium nanoprobes demonstrated visible emission and long-lived

luminescence lifetimes, allowing them to track blood flow. More specifically, subsequent to injecting mice, the iridium coated AuNPs were able to enter blood circulation and using luminescence imaging, the iridium signal was clearly detected in small blood vessels in lungs, mesentery and skeletal muscles with high resolution[189]. Also, the characteristic iridium signal detected was strong enough to eliminate any background autofluorescence, which is one of the most frequent issues in biomedical imaging applications. The luminescent AuNPs demonstrated efficient body clearance through the liver and the spleen[189], which is essential for the successful translation of novel nanoparticle-based systems in the clinic. Therefore, such systems can lead to the development of novel formulations for analyzing and tracking the flow of blood in *in vivo* models and aid to better understand the different functions and complexity of the human circulatory system.

The development of iridium coated AuNPs of different sizes, 13, 25 and 100 nm, has also been reported to be a successful system for luminescence imaging[188]. Besides emission within the visible region and long-lived lifetimes, the iridium nanoparticles demonstrated two-photon luminescence, allowing luminescence lifetime imaging of cancer cells, through detection in two different channels. A long signal, coming from the iridium complex, and a shorter signal from the AuNPs were able to be detected in HeLa cells after treatment with the luminescent nanoparticles[188]. The two-photon luminescence imaging approach used revealed a strong signal for both the iridium and the gold during imaging for all the different sizes of AuNPs studied (Figure 1-12). Through this system, the impact of the size of nanoparticles on subcellular localization was able to be determined, something that is rather challenging with other imaging systems, such as TEM[188]. Therefore, the results of the study further confirm that attachment of luminescent complexes to AuNPs provides opportunities for tracking nanoparticles in an intracellular environment and *in vivo* models using luminescence imaging.

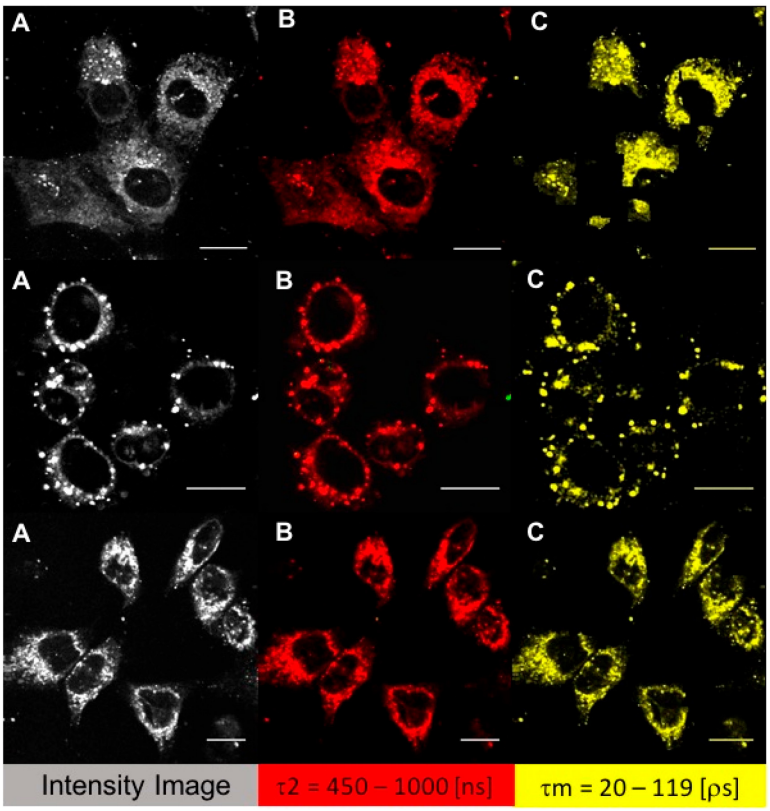


Figure 1-12. Two-photon luminescence lifetime imaging of 13 (bottom), 25 (top) and 100 (middle) nm iridium coated AuNPs in HeLa,cells through detection in two channels. (a) Intensity image (b) Iridium luminescene showing a lifetime of 450 to 1000 ns. (c) Lifetime imaging of short-lived signal from the gold with a lifetime of 20 to 119 ps. (Scale bar: 20 µm) (***Figure adapted from King et al. 2018[188], Copyright © 2018, with permission from the American Chemical Society***)

Besides transition metal complexes, lanthanide complexes have also been reported to be suitable candidates for the development of luminescent nanoprobes for imaging applications. Similarly to transition metal complexes, lanthanide complexes also exhibit intrinsic photophysical properties such as large Stoke shifts, narrow emission bands and long-lived luminescence lifetimes, which allow them to overcome issues associated with the use of organic dyes[191, 194]. In biological systems, lanthanide luminescence can be easily detected through the time-gating luminescence technique, which uses the long-lived luminescence signal of lanthanides and the time-delayed detection to enhance the signal-to-noise ratio and thereby, eliminate autofluorescence[191, 195].

The use of 13 nm AuNPs, coated with a europium luminescent complex, has been previously described for imaging of blood cells[190]. Through this system, europium coated AuNPs were internalized within human platelets with the help of a pH-dependent peptide ligand, pHLIP. The presence of the luminescent AuNPs in the intracellular environment was confirmed through detecting the signal of the europium complex in the treated cells using luminescence microscopy[190].

The development of luminescent nanoprobes has provided multiple possibilities for luminescence imaging, both for *in vitro* and *in vivo* settings. The use of transition metal complexes and lanthanides to coat AuNPs offers unique advantages over the use of conventional fluorescent molecules. One of the major benefits of using luminescent probes is that the luminescent signal can be easily detected over little to no background noise, thus, allowing long-term luminescence imaging to be performed without inducing phototoxicity. Therefore, the use of luminescent complexes for the design of novel nanoaprticle-based systems offers opportunities to further expand the use of multimodal luminescence imaging in biological systems and overcome limitations of conventional imaging approaches currently used in the clinic.

1.7 Conjugation of antibodies to gold nanoparticles

Antibody-conjugated AuNPs are fundamental in the development of emerging biosensing technologies in the nanomedicine field, as they combine the high specificity provided by the antibody for the selective recognition of antigens along with the unique properties of AuNPs[196, 197]. Due to the fact that the use of antibody-coated AuNPs results to significantly enhanced cellular uptake and intracellular stability, their use can vastly improve the sensitivity and multiplex analysis of conventional immunoassays[197].

Antibody-conjugated AuNPs are very popular in the nanomedicine field for their beneficial properties in cancer theranostic applications. The presence of antibodies on the gold surface can direct AuNPs to the tumor site through binding to antigens expressed on

the cell surface of malignant cells. When it comes to the development of cancer selective drug nanocarriers, the high specificity and affinity of an antibody towards an antigen receptor makes antibodies as an ideal targeting moiety[198]. There are many different types of antibodies, but usually the ones used for therapeutic purposes are Immunoglobulin G antibodies (IgG). An IgG antibody is the most abundant antibody in the human serum[199]. These antibodies have a Y-shaped structure, which is comprised from a constant region (Fc) that is the same in all IgG antibodies and a variable region (Fab), containing light and heavy chains, which is specific to each antibody. The upper part (Fab) and the lower part (Fc) of an antibody, are connected through disulfide bonds, known as hinge region[200] (Figure 1-13).

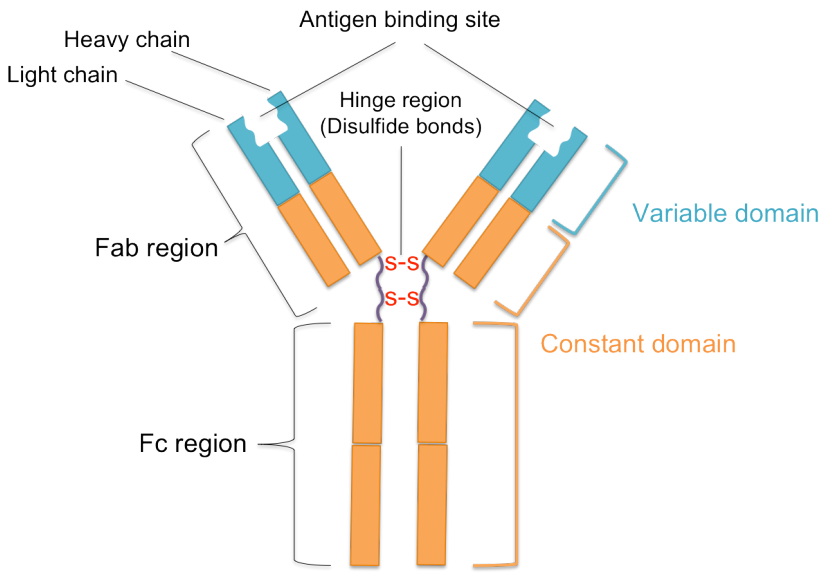


Figure 1-13. **Structure of an IgG antibody.**

The approval of antibodies for safe use in the clinic played a predominant role in the extensive research carried out on the development of antibody-conjugated AuNPs for cancer theranostic applications. Some of the antibodies that have been approved for use in the clinic include cetuximab, for the treatment of colorectal cancer with overexpression of epidermal growth factor receptor (EGFR) and trastuzumab, which is used for the treatment of breast cancer with herceptin-2 (HER2) overexpression[201, 202]. The clinical

success of these antibodies has been well established due to their high binding affinity against their targeting antigens and therefore, they have been widely used in the nanomedicine field for the development of antibody-conjugated AuNPs.

The ability of AuNPs to act as radiosensitizers and release electrons upon NIR radiation and X-ray irradiation, enhances significantly the effectiveness of conventional radiation therapy techniques[103]. Therefore, both cetuximab and transtuzumab have been previously used to develop antibody-conjugated AuNPs, in order to guide the nanoparticles to the tumor site and improve radiation therapy[203-205]. Antibody-conjugated AuNPs have been previously used to improve targeted PTT in many different types of cancer[206, 207]. Similarly to their successful use in radiation therapy, antibody-functionalized AuNPs exhibited selective cellular uptake by tumor cells and induced high cellular toxicity upon treatment.

The first antibody-conjugated AuNPs for cancer treatment were developed in 2008, aiming to enhance toxicity in cancer cells through the specific delivery of anticancer agents to the tumor site. More specifically, in 2008, the chemotherapeutic agent gemcitabine was conjugated to cetuximab-functionalized AuNPs for targeted drug delivery in pancreatic adenocarcinoma[208]. When compared to gemcitabine coated AuNPs, in the absence of the antibody, the cetuximab coated AuNPs demonstrated enhanced therapeutic efficacy both in *in vitro* and *in vivo* settings[208] (Figure 1-14).

The delivery of other widely used chemotherapeutic agents, including doxorubicin[209] and oxaliplatin[210], has also been investigated using antibody-functionalized AuNPs, with the results indicating that the presence of the antibody on the gold surface improves drastically the delivery of the chemotherapeutic agents to the target cells. These drugs are either adsorbed on the gold surface via hydrophobic interactions, through reversible Au-N bonds, or attached using PEG ligands along with the antibody[209-211].

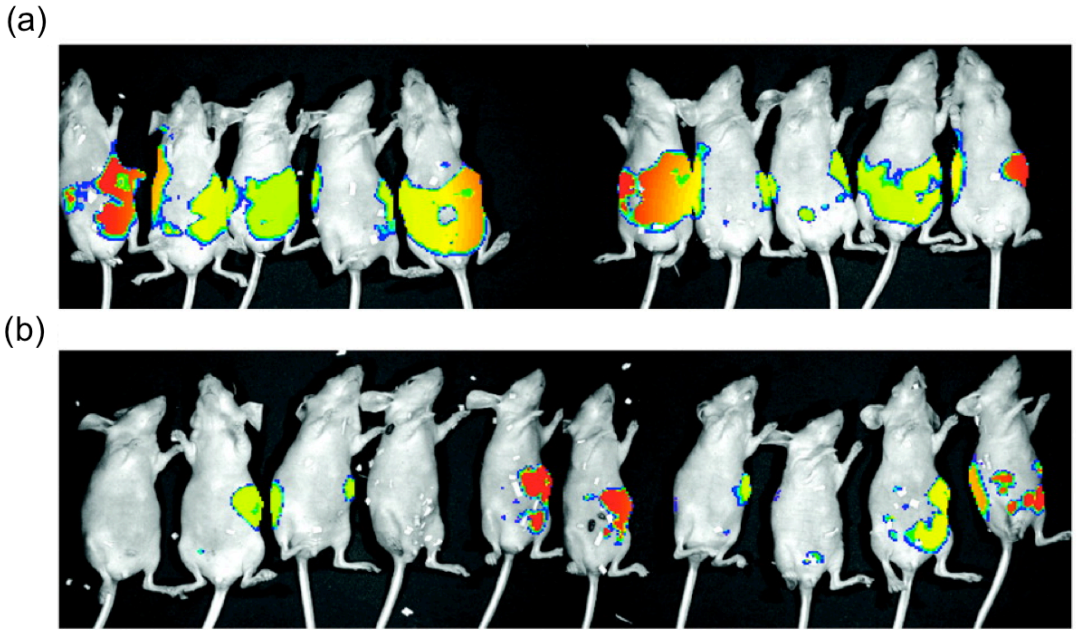


Figure 1-14. Comparative bioluminescence imaging of tumor growth in mice subsequent to treatment with (a) gemcitabine and cetuximab (control group) and (b) gemcitabine on cetuximab-functionalized AuNPs (experimental group). Experimental group shows significant inhibition in tumor growth. *(Figure adapted from Patra et al. 2008[208], Copyright © 2008, with permission from American Association of Cancer Research)*

The cellular uptake mechanism by which antibody-conjugated AuNPs are mainly internalized is receptor-mediated endocytosis[212]. Even though conjugation of an antibody to AuNPs can suggest that the antibody-antigen binding site is no longer available and can possibly hinder uptake, previously reported studies have shown that conjugation to the gold surface does not alter the pharmacokinetic profile of the antibody[212]. In fact, the use of AuNPs to deliver cetuximab was reported to induce considerably faster cellular uptake in pancreatic cancer cells when compared to free cetuximab[212]. This was attributed to the different endocytotic pathway used by the antibody upon conjugation to the gold surface, which altered the internalization process and thus, affected subcellular localization, intracellular trafficking and interactions at a molecular level[212].

Even though receptor-mediated endocytosis is the most common mechanism by which antibodies are internalized within a cellular environment, it has been previously discussed that not all antibodies are internalized upon binding to antigen receptors. For example, the internalization of trastuzumab upon binding to HER2 is still debated, as the antibody has a

high affinity towards the extracellular domain of HER2, but there is no evidence of targeting intracellular molecules[213, 214]. However, the use of AuNPs to deliver trastuzumab in HER2 overexpressing breast cancer cells has been reported to improve its cellular internalization in comparison to free trastuzumab at the same concentration[215].

The key to the successful development of antibody conjugated AuNPs in cancer theranostics, is the choice of the right targeting antibody along with the right strategy to conjugate it to the gold surface[216]. The conjugation of antibodies to the surface of AuNPs can be performed both through non-covalent and covalent immobilization, determined by physical and chemical interactions, respectively[217, 218]. The physical interactions between AuNPs and antibodies usually depend on hydrophobic attraction between the gold surface and the antibody, ionic interactions between the negatively charged surface of AuNPs and the positively charged antibody or dative binding between the conducting electrons on the gold surface and the sulfur atoms in the amino acids of the antibody[218, 219] (Figure 1-15). Chemical interactions between AuNPs and antibodies can be achieved through the use of bifunctional intermediary linkers, such as PEG, the use of adapter molecules such as Streptavidin anti-biotin or through adsorption of the antibody onto the gold surface using thiol groups[218, 220].

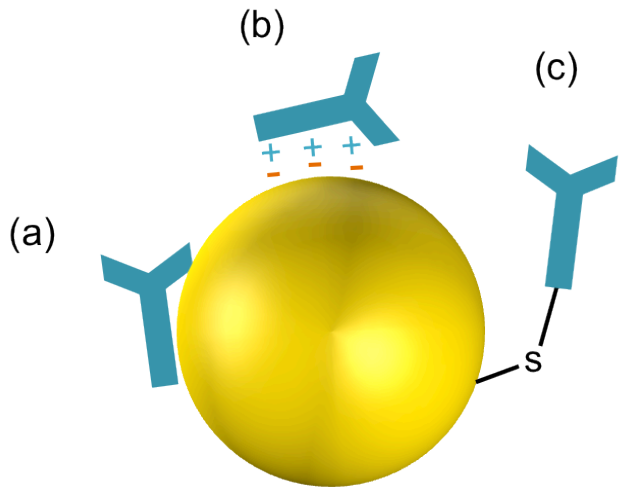


Figure 1-15. Physical interactions between antibodies and AuNPs. (a) hydrophobic interaction (b) ionic interaction and (c) dative binding.

Non-covalent immobilization is primarily based on both hydrophobic and electrostatic interactions between the surface of AuNPs and the antibodies[221] and is described as a conjugation strategy based on spontaneous adsorption of antibodies on the gold surface[218]. There are several issues associated with the use of non-covalent modes to conjugate antibodies to AuNPs, such as the need of a very high antibody concentration during preparation. Also, non-covalently conjugated antibodies are susceptible to changes in a biological environment, such as pH, and therefore, they can be easily replaced by other molecules in biological samples[217]. Another major disadvantage of non-covalent conjugation is the random orientation of antibodies on the gold surface, which results to loss of antibody-antigen binding activity and thus, compromises the high selectivity and affinity of the antibody-conjugated AuNPs[220, 217]. The fact that cellular uptake of antibody conjugated AuNPs relies vastly on receptor-mediated endocytosis[212], suggests that directional conjugation of antibodies to AuNPs can significantly improve cellular uptake as there are more binding sites available when compared to randomly oriented antibodies on the gold surface.

For directional conjugation of antibodies to the surface of AuNPs, covalent binding strategies are usually performed using biomolecules that contain thiol groups. For instance, antibodies can be covalently conjugated to AuNPs through the use of adapter molecules like biotin and avidin[217] and mediator linkers such as PEG, which are highly water soluble and approved for use in the medical field[198, 217]. Bioconjugation chemistry is an essential component of different conjugation strategies used for the directional conjugation of antibodies to the gold surface. Thiolated PEG linker (PEG-SH) is widely used to functionalize the surface of citrate AuNPs prior to antibody conjugation in order to eliminate non-specific binding[211, 218, 217]. PEG-SH chains are usually terminated with a carboxyl group, providing a binding site for the antibody through the formation of an amide bond[198, 203, 204, 222]. Even through not all antibodies can spontaneously bind to and form covalent bonds with carboxyl groups, the antibodies can be easily modified through coupling chemistry to bind without the need of a spacer molecule[217].

Therefore, a full understanding of the chemistry behind the bioconjugation of different antibodies to the gold surface is essential for the development of nanoparticle-based systems with high specificity towards antigen receptors. Such systems are presented as pioneering interventions in the nanomedicine field as they offer opportunities for improved delivery of conventional chemotherapeutic drugs and on-target specificity.

1.8 Thesis aims

Even though current advances in the oncology field have led to earlier detection of malignant tumors and more effective therapies, the successful delivery of theranostic agents to the tumor site and precise subcellular localization, still, present some of the most prevalent challenges in the diagnosis and treatment of cancer. Therefore, there is currently a growing interest in the development of novel formulations, which can intrude biological barriers that prevent therapeutic and imaging agents from successfully reaching their target of interest.

Recently, nanoparticles have gained significant scientific interest as vehicles to selectively deliver theranostic moieties to cancer cells due to their multifunctionality, unique physiochemical properties and ability to greatly accumulate within tumors. Hence, the main objective of the research work conducted in this thesis was to develop multifunctional gold nanoparticles with optimal cellular uptake to improve detection and intracellular localization in malignant cells.

Luminescent metal complexes were used to functionalize the gold surface, aiming to translate the attractive photophysical properties of the complexes onto the gold nanoprobes and achieve a strong luminescent signal for detection. What is more, in order to address the limitations of conventional imaging approaches, the favorable optical properties offered by both the metal complexes and the gold scaffold were used to investigate the appropriateness of the functionalized nanoprobes for use in multimodal imaging in biological specimens. The ability of metal complexes to be easily modified via changing the type of ligand attached to the metal core promotes subcellular localization in different organelles. Thus, different transition metal complexes were used to functionalize

the surface of gold nanoparticles, aiming to improve the systematic bioavailability of the complexes within a biological environment and achieve targeted intracellular delivery.

The improved intracellular bioavailability and localization of the luminescent complexes when attached to the gold scaffold are essential for promoting selective targeting of tumor cells and thus, reducing off-target cytotoxicity, which is highly related to severe adverse side effects. Therefore, the selectivity of the luminescent nanoprobes for targeting malignant over normal cells was also investigated in this thesis, aiming to determine their ability to overcome the limitations of conventional chemotherapeutic drugs and induce an improved therapeutic outcome through eliminating off-target toxicity.

When it comes to the development of cancer selective nanoprobes, the high specificity and affinity of antibodies against antigen receptors make them ideal as targeting moieties. Hence, part of the work carried out in the present thesis involved the functionalization of gold nanoparticles using both luminescent metal complexes and a monoclonal antibody. The antibody conjugated nanoparticles were assessed for their potential to enhance detection sensitivity and binding affinity in biological samples, aiming to improve identification of tumor biomarkers both *in vitro* and *in vivo* imaging applications.

1.9 References:

[1] Mcguire, S. 2016. World Cancer Report 2014. Geneva, Switzerland: World Health Organization, International Agency for Research on Cancer, WHO Press, 2015. *Adv Nutr,* 7**,** 418-419.

[2] Ferlay, J., Colombet, M., Soerjomataram, I., Mathers, C., Parkin, D. M., Pineros, M., Znaor, A. & Bray, F. 2019. Estimating the global cancer incidence and mortality in 2018: GLOBOCAN sources and methods. *Int J Cancer,* 144**,** 1941-1953.

[3] Ferlay, J., Soerjomataram, I., Dikshit, R., Eser, S., Mathers, C., Rebelo, M., Parkin, D. M., Forman, D. & Bray, F. 2015. Cancer incidence and mortality worldwide: sources, methods and major patterns in GLOBOCAN 2012. *Int J Cancer,* 136**,** 359-386.

[4] Shapiro, C. L. 2016. Highlights of Recent Findings on Quality-of-Life Management for Patients With Cancer and Their Survivors. *JAMA Oncol,* 2**,** 1401-1402.

[5] Turcotte, L. M., Liu, Q., Yasui, Y., Arnold, M. A., Hammond, S., Howell, R. M., Smith, S. A., Weathers, R. E., Henderson, T. O., Gibson, T. M., Leisenring, W., Armstrong, G. T., Robison, L. L. & Neglia, J. P. 2017. Temporal Trends in Treatment and Subsequent Neoplasm Risk Among 5-Year Survivors of Childhood Cancer, 1970-2015. *JAMA,* 317**,** 814-824.

[6] Stuurman, F. E., Nuijen, B., Beijnen, J. H. & Schellens, J. H. 2013. Oral anticancer drugs: mechanisms of low bioavailability and strategies for improvement. *Clin Pharmacokinet,* 52**,** 399-414.

[7] Sawicki, E., Schellens, J. H., Beijnen, J. H. & Nuijen, B. 2016. Inventory of oral anticancer agents: Pharmaceutical formulation aspects with focus on the solid dispersion technique. *Cancer Treat Rev,* 50**,** 247-263.

[8] Ferrari, M. 2005. Cancer nanotechnology: opportunities and challenges. *Nat Rev Cancer,* 5**,** 161-171.

[9] Allen, T. M. 2002. Ligand-targeted therapeutics in anticancer therapy. *Nat Rev Cancer,* 2**,** 750-763.

[10] Jain, R. K. 1998. The next frontier of molecular medicine: delivery of therapeutics. *Nat Med,* 4**,** 655-657.

[11] Shi, J., Kantoff, P. W., Wooster, R. & Farokhzad, O. C. 2017. Cancer nanomedicine: progress, challenges and opportunities. *Nat Rev Cancer,* 17**,** 20-37.

[12] 2019. Nanomaterials definition matters. *Nat Nanotechnol,* 14**,** 193.

[13] Gao, X., Cui, Y., Levenson, R. M., Chung, L. W. & Nie, S. 2004. In vivo cancer targeting and imaging with semiconductor quantum dots. *Nat Biotechnol,* 22**,** 969-976.

[14] Bajaj, A., Miranda, O. R., Kim, I. B., Phillips, R. L., Jerry, D. J., Bunz, U. H. & Rotello, V. M. 2009. Detection and differentiation of normal, cancerous, and metastatic cells using nanoparticle-polymer sensor arrays. *Proc Natl Acad Sci U S A,* 106**,** 10912-10916.

[15] Shi, J., Votruba, A. R., Farokhzad, O. C. & Langer, R. 2010. Nanotechnology in drug delivery and tissue engineering: from discovery to applications. *Nano Lett,* 10**,** 3223-3230.

[16] Anselmo, A. C. & Mitragotri, S. 2016. Nanoparticles in the clinic. *Bioeng Transl Med,* 1**,** 10-29.

[17] Torchilin, V. P. 2014. Multifunctional, stimuli-sensitive nanoparticulate systems for drug delivery. *Nat Rev Drug Discov,* 13**,** 813-827.

[18] Min, Y., Caster, J. M., Eblan, M. J. & Wang, A. Z. 2015. Clinical Translation of Nanomedicine. *Chem Rev,* 115**,** 11147-11190.

[19] Wagner, V. , Dullaart, A. , Bock, A. K. & Zweck, A. 2006. The emerging nanomedicine landscape. *Nat Biotechnol,* 24**,** 1211-1217.

[20] Anselmo, A. C. & Mitragotri, S. 2015. A Review of Clinical Translation of Inorganic Nanoparticles. *The AAPS Journal,* 17**,** 1041-1054.
[21] Huang, H. C., Barua, S., Sharma, G., Dey, S. K. & Rege, K. 2011. Inorganic nanoparticles for cancer imaging and therapy. *J Control Release,* 155**,** 344-357.
[22] Mccarthy, J. & Weissleder, R. 2008. Multifunctional magnetic nanoparticles for targeted imaging and therapy. *Adv Drug Deliv Rev,* 60**,** 1241-1251.
[23] Yetisgin, A. A., Cetinel, S., Zuvin, M., Kosar, A. & Kutlu, O. 2020. Therapeutic Nanoparticles and Their Targeted Delivery Applications. *Molecules,* 25.
[24] Santos, A., Veiga, F. & Figueiras, A. 2019. Dendrimers as Pharmaceutical Excipients: Synthesis, Properties, Toxicity and Biomedical Applications. *Materials (Basel),* 13**,** 65.
[25] Palmerston Mendes, L., Pan, J. & Torchilin, V. P. 2017. Dendrimers as Nanocarriers for Nucleic Acid and Drug Delivery in Cancer Therapy. *Molecules,* 22**,** 1401.
[26] Begines, B., Ortiz, T., Pérez-Aranda, M., Martínez, G., Merinero, M., Argüelles-Arias, F. & Alcudia, A. 2020. Polymeric Nanoparticles for Drug Delivery: Recent Developments and Future Prospects. *Nanomaterials (Basel),* 10**,** 1403.
[27] Panyam, J. & Labhasetwar, V. 2003. Biodegradable nanoparticles for drug and gene delivery to cells and tissue. *Adv Drug Deliv Rev,* 55**,** 329-347.
[28] Li, B., Li, Q., Mo, J. & Dai, H. 2017. Drug-Loaded Polymeric Nanoparticles for Cancer Stem Cell Targeting. *Front Pharmacol,* 8**,** 51.
[29] Senapati, S., Mahanta, A. K., Kumar, S. & Maiti, P. 2018. Controlled drug delivery vehicles for cancer treatment and their performance. *Sig Transduct Target Ther,* 3.
[30] Hassan, S., Prakash, G., Bal Ozturk, A., Saghazadeh, S., Farhan Sohail, M., Seo, J., Remzi Dokmeci, M., Zhang, Y. S. & Khademhosseini, A. 2017. Evolution and clinical translation of drug delivery nanomaterials. *Nano Today,* 15**,** 91-106.
[31] Ahmad, Z., Shah, A., Siddiq, M. & Kraatz, H. B. 2014. Polymeric micelles as drug delivery vehicles. *RSC Adv,* 4**,** 17028-17038.
[32] Colone, M., Calcabrini, A. & Stringaro, A. 2020. Drug Delivery Systems of Natural Products in Oncology. *Molecules* 25**,** 4560.
[33] Akbarzadeh, A., Rezaei-Sadabady, R., Davaran, S., Joo, S. W., Zarghami, N., Hanifehpour, Y., Samiei, M., Kouhi, M. & Nejati-Koshki, K. 2013. Liposome: classification, preparation, and applications. *Nanoscale Res Lett,* 8**,** 102.
[34] Bozzuto, G. & Molinari, A. 2015. Liposomes as nanomedical devices. *Int J Nanomedicine,* 10**,** 975-999.
[35] Bulbake, U., Doppalapudi, S., Kommineni, N. & Khan, W. 2017. Liposomal Formulations in Clinical Use: An Updated Review. *Pharmaceutics,* 9**,** 12.
[36] Sercombe, L., Veerati, T., Moheimani, F., Wu, S. Y., Sood, A. K. & Hua, S. 2015. Advances and Challenges of Liposome Assisted Drug Delivery. *Front Pharmacol,* 6**,** 286-286.
[37] Baeza, A., Ruiz-Molina, D. & Vallet-Regí, M. 2017. Recent advances in porous nanoparticles for drug delivery in antitumoral applications: inorganic nanoparticles and nanoscale metal-organic frameworks. *Expert Opin Drug Deliv,* 14**,** 783-796.
[38] Soenen, S. J., Parak, W. J., Rejman, J. & Manshian, B. 2015. (Intra)cellular stability of inorganic nanoparticles: effects on cytotoxicity, particle functionality, and biomedical applications. *Chem Rev,* 115**,** 2109-2135.
[39] Maksoudian, C., Saffarzadeh, N., Hesemans, E., Dekoning, N., Buttiens, K. & Soenen, S. J. 2020. Role of inorganic nanoparticle degradation in cancer therapy. *Nanoscale Adv,* 2**,** 3734-3763.

[40] Conde, J., Dias, J. T., Grazú, V., Moros, M., Baptista, P. V. & De La Fuente, J. M. 2014. Revisiting 30 years of biofunctionalization and surface chemistry of inorganic nanoparticles for nanomedicine. *Front Chem,* 2.
[41] Mody, V. V., Siwale, R., Singh, A. & Mody, H. R. 2010. Introduction to metallic nanoparticles. *J Pharm Bioallied Scie,* 2**,** 282-289.
[42] Soetaert, F., Korangath, P., Serantes, D., Fiering, S. & Ivkov, R. 2020. Cancer therapy with iron oxide nanoparticles: Agents of thermal and immune therapies. *Adv Drug Deliv Rev,* 163-164**,** 65-83.
[43] Bae, W. K., Kwak, J., Park, J. W., Char, K., Lee, C. & Lee, S. 2009. Highly Efficient Green-Light-Emitting Diodes Based on CdSe@ZnS Quantum Dots with a Chemical-Composition Gradient. *Adv Mater,* 21**,** 1690-1694.
[44] Abdel-Salam, M., Omran, B., Whitehead, K. & Baek, K. H. 2020. Superior Properties and Biomedical Applications of Microorganism-Derived Fluorescent Quantum Dots. *Molecules,* 25**,** 4486.
[45] Michalet, X., Pinaud, F. F., Bentolila, L. A., Tsay, J. M., Doose, S., Li, J. J., Sundaresan, G., Wu, A. M., Gambhir, S. S. & Weiss, S. 2005. Quantum dots for live cells, in vivo imaging, and diagnostics. *Science* 307**,** 538-544.
[46] Ge, J., Lan, M., Zhou, B., Liu, W., Guo, L., Wang, H., Jia, Q., Niu, G., Huang, X., Zhou, H., Meng, X., Wang, P., Lee, C. S., Zhang, W. & Han, X. 2014. A graphene quantum dot photodynamic therapy agent with high singlet oxygen generation. *Nat Commun,* 5**,** 4596.
[47] Tsolekile, N., Nahle, S., Zikalala, N., Parani, S., Sakho, E. H. M., Joubert, O., Matoetoe, M. C., Songca, S. P. & Oluwafemi, O. S. 2020. Cytotoxicity, fluorescence tagging and gene-expression study of CuInS/ZnS QDS - meso (hydroxyphenyl) porphyrin conjugate against human monocytic leukemia cells. *Sci Rep,* 10**,** 4936.
[48] Gao, Y., Chen, Y., Ji, X., He, X., Yin, Q., Zhang, Z., Shi, J. & Li, Y. 2011. Controlled Intracellular Release of Doxorubicin in Multidrug-Resistant Cancer Cells by Tuning the Shell-Pore Sizes of Mesoporous Silica Nanoparticles. *ACS Nano,* 5**,** 9788-9798.
[49] Tang, L. & Cheng, J. 2013. Nonporous silica nanoparticles for nanomedicine application. *Nano Today,* 8**,** 290-312.
[50] Frasconi, M., Liu, Z., Lei, J., Wu, Y., Strekalova, E., Malin, D., Ambrogio, M. W., Chen, X., Botros, Y. Y., Cryns, V. L., Sauvage, J. P. & Stoddart, J. F. 2013. Photoexpulsion of Surface-Grafted Ruthenium Complexes and Subsequent Release of Cytotoxic Cargos to Cancer Cells from Mesoporous Silica Nanoparticles. *J Am Chem Soc,* 135**,** 11603-11613.
[51] Jafari, S., Derakhshankhah, H., Alaei, L., Fattahi, A., Varnamkhasti, B. S. & Saboury, A. A. 2019. Mesoporous silica nanoparticles for therapeutic/diagnostic applications. *Biomed Pharmacother,* 109**,** 1100-1111.
[52] Carvalho, G. C., Sábio, R. M., De Cássia Ribeiro, T., Monteiro, A. S., Pereira, D. V., Ribeiro, S. J. L. & Chorilli, M. 2020. Highlights in Mesoporous Silica Nanoparticles as a Multifunctional Controlled Drug Delivery Nanoplatform for Infectious Diseases Treatment. *Pharm Res,* 37**,** 191.
[53] Zhou, Y., Quan, G., Wu, Q., Zhang, X., Niu, B., Wu, B., Huang, Y., Pan, X. & Wu, C. 2018. Mesoporous silica nanoparticles for drug and gene delivery. *Acta Pharm Sin B,* 8**,** 165-177.
[54] Castillo, R. R., Lozano, D., González, B., Manzano, M., Izquierdo-Barba, I. & Vallet-Regí, M. 2019. Advances in mesoporous silica nanoparticles for targeted stimuli-responsive drug delivery: an update. *Expert Opin Drug Deliv,* 16**,** 415-439.
[55] Aquib, M., Farooq, M. A., Banerjee, P., Akhtar, F., Filli, M. S., Boakye-Yiadom, K. O., Kesse, S., Raza, F., Maviah, M. B. J., Mavlyanova, R. & Wang, B. 2019. Targeted and stimuli–

responsive mesoporous silica nanoparticles for drug delivery and theranostic use. *J Biomed Mater Res A,* 107**,** 2643-2666.
[56] Barui, S. & Cauda, V. 2020. Multimodal Decorations of Mesoporous Silica Nanoparticles for Improved Cancer Therapy. *Pharmaceutics,* 12**,** 527.
[57] Monopoli, M. P., Åberg, C., Salvati, A. & Dawson, K. A. 2012. Biomolecular coronas provide the biological identity of nanosized materials. *Nat Nanotechnol,* 7**,** 779-786.
[58] Nel, A. E., Madler, L., Velegol, D., Xia, T., Hoek, E. M., Somasundaran, P., Klaessig, F., Castranova, V. & Thompson, M. 2009. Understanding biophysicochemical interactions at the nano-bio interface. *Nat Mater,* 8**,** 543-557.
[59] Walkey, C. D., Olsen, J. B., Guo, H., Emili, A. & Chan, W. C. 2012. Nanoparticle Size and Surface Chemistry Determine Serum Protein Adsorption and Macrophage Uptake. *J Am Chem Soc,* 134**,** 2139-2147.
[60] Barui, A. K, Oh, J. Y, Jana, B., Kim, C. & Ryu, J. H. 2019. Cancer-Targeted Nanomedicine: Overcoming the Barrier of the Protein Corona. *Adv Therap,* 3.
[61] Salvati, A., Pitek, A. S., Monopoli, M. P., Prapainop, K., Bombelli, F. B., Hristov, D. R., Kelly, P. M., Åberg, C., Mahon, E. & Dawson, K. A. 2013. Transferrin-functionalized nanoparticles lose their targeting capabilities when a biomolecule corona adsorbs on the surface. *Nat Nanotechnol,* 8**,** 137-143.
[62] Anselmo, A. C. & Mitragotri, S. 2019. Nanoparticles in the clinic: An update. *Bioeng Transl Med,* 4**,** 1-13.
[63] Barenholz, Y. 2012. Doxil® — The first FDA-approved nano-drug: Lessons learned. *J Control Release,* 160**,** 117-134.
[64] Ning, Y. M., He, K. , Dagher, R., Sridhara, R., Farrell, A. T., Justice, R. & Pazdur, R. 2007. Liposomal doxorubicin in combination with bortezomib for relapsed or refractory multiple myeloma. *Oncology (Williston Park, NY),* 21**,** 1503-1508.
[65] Fox, J. L. 1995. FDA advisors okay NeXstar's DaunoXome. *Nat Biotechnol,* 13**,** 635-636.
[66] Dagher, R., Johnson, J., Williams, G., Keegan, P. & Pazdur, R. 2004. Accelerated Approval of Oncology Products: A Decade of Experience. *J Natl Cancer Inst,* 96**,** 1500-1509.
[67] Silverman, J. A & Deitcher, S. R. 2013. Marqibo®(vincristine sulfate liposome injection) improves the pharmacokinetics and pharmacodynamics of vincristine. *Cancer Chemother Pharmacol,* 71**,** 555-564.
[68] Carnevale, J. & Ko, A. H. 2016. MM-398 (nanoliposomal irinotecan): emergence of a novel therapy for the treatment of advanced pancreatic cancer. *Future Oncol,* 12**,** 453-464.
[69] Leonard, R., Williams, S. , Tulpule, A. , Levine, A. & Oliveros, S. 2009. Improving the therapeutic index of anthracycline chemotherapy: focus on liposomal doxorubicin (Myocet™). *The Breast,* 18**,** 218-224.
[70] Ando, K., Mori, K., Corradini, N., Redini, F. & Heymann, D. 2011. Mifamurtide for the treatment of nonmetastatic osteosarcoma. *Expert Opin Pharmacother,* 12**,** 285-292.
[71] Miele, E., Spinelli, G. P., Miele, E., Tomao, F. & Tomao, S. 2009. Albumin-bound formulation of paclitaxel (Abraxane® ABI-007) in the treatment of breast cancer. *Int J Nanomedicine,* 4**,** 99-105.
[72] Krauss, A. C., Gao, X., Li, L., Manning, M. L., Patel, P., Fu, W., Janoria, K. G., Gieser, G., Bateman, D. A., Przepiorka, D., Shen, Y. L., Shord, S. S., Sheth, C. M., Banerjee, A., Liu, J., Goldberg, K. B., Farrell, A. T., Blumenthal, G. M. & Pazdur, R. 2019. FDA Approval Summary: (Daunorubicin and Cytarabine) Liposome for Injection for the Treatment of Adults with High-Risk Acute Myeloid Leukemia. *Clin Cancer Res,* 25**,** 2685-2690.
[73] Bonvalot, S. , Rutkowski, P. L. , Thariat, J. , Carrère, S., Ducassou, A. , Sunyach, M. P. , Agoston, P., Hong, A., Mervoyer, A., Rastrelli, M., Moreno, V., Li, R. K. , Tiangco, B,

Herraez, A. C., Gronchi, A., Mangel, L., Sy-Ortin, T., Hohenberger, P., De Baère, T., Cesne, A. , Helfre, S., Saada-Bouzid, E., Borkowska, A., Anghel, R., Co, A., Gebhart, M., Kantor, G., Montero, A., Loong, H. H., Vergés, R., Lapeire, L., Dema, S., Kacso, G., Austen, L., Moureau-Zabotto, L., Servois, V., Wardelmann, E., Terrier, P., Lazar, A. J. , Bovée, J. V. M. G., Le Péchoux, C. & Zsusanna Papai, Z. 2019. NBTXR3, a first-in-class radioenhancer hafnium oxide nanoparticle, plus radiotherapy versus radiotherapy alone in patients with locally advanced soft-tissue sarcoma (Act.In.Sarc): a multicentre, phase 2–3, randomised, controlled trial. *Lancet Oncol,* 20**,** 1148-1159.

[74] Bonvalot, S., Le Pechoux, C., De Baere, T., Kantor, G., Buy, X., Stoeckle, E., Terrier, P., Sargos, P., Coindre, J. M., Lassau, N., Ait Sarkouh, R., Dimitriu, M., Borghi, E., Levy, L., Deutsch, E. & Soria, J. C. 2017. First-in-Human Study Testing a New Radioenhancer Using Nanoparticles (NBTXR3) Activated by Radiation Therapy in Patients with Locally Advanced Soft Tissue Sarcomas. *Clinical Cancer Research,* 23**,** 908-917.

[75] Xia, Y., Xiong, Y., Lim, B. & Skrabalak, S. E. 2009. Shape-Controlled Synthesis of Metal Nanocrystals: Simple Chemistry Meets Complex Physics? *Angew Chem Int Ed,* 48**,** 60-103.

[76] Langille, M. R., Personick, M. L., Zhang, J. & Mirkin, C. A. 2012. Defining Rules for the Shape Evolution of Gold Nanoparticles. *J Am Chem Soc,* 134**,** 14542-14554.

[77] Tapan, K. S & M., Catherine J. 2004. Room Temperature, High-Yield Synthesis of Multiple Shapes of Gold Nanoparticles in Aqueous Solution. *J Am Chem Soc,* 126**,** 8648-8649.

[78] Dykman, L. & Khlebtsov, N. 2012. Gold nanoparticles in biomedical applications: recent advances and perspectives. *Chem Soc Rev,* 41**,** 2256-2282.

[79] Giljohann, D. A., Seferos, D. S., Daniel, W. L., Massich, M. D., Patel, P. C. & Mirkin, C. A. 2010. Gold Nanoparticles for Biology and Medicine. *Angew Chem Int Ed,* 49**,** 3280-3294.

[80] Fen-Ying, K. Jin-Wei, Z. Rong-Fang , L. Zhong-Xia, W., Wen-Juan, W. Wei, W. 2017. Unique Roles of Gold Nanoparticles in Drug Delivery, Targeting and Imaging Applications. *Molecules,* 22**,** 1445.

[81] Khlebtsov, N. G. & Dykman, L. A. 2010. Optical properties and biomedical applications of plasmonic nanoparticles. *J Quant Spectrosc Radiat Transf,* 111**,** 1-35.

[82] Herizchi, R., Abbasi, E., Milani, M. & Akbarzadeh, A. 2016. Current methods for synthesis of gold nanoparticles. *Artif Cells Nanomed Biotechnol,* 44**,** 596-602.

[83] Turkevich, J., Stevenson, P. C. & Hillier, J. 1951. A Study of the Nucleation and Growth Processes in the Synthesis of Colloidal Gold. *Discuss Faraday Soc,* 11**,** 55-75.

[84] Zeng, Y., Hu, R., Wang, L., Gu, D., He, J., Wu, S. Y., Ho, H. P., Li, X., Qu, J., Gao, B. Z. & Shao, Y. 2017. Recent advances in surface plasmon resonance imaging: detection speed, sensitivity, and portability. *Nanophotonics,* 6**,** 1017-1030.

[85] Eustis, S. And & El-Sayed, M. A. 2006. Why gold nanoparticles are more precious than pretty gold: Noble metal surface plasmon resonance and its enhancement of the radiative and nonradiative properties of nanocrystals of different shapes. *Chem. Soc. Rev.,* 35**,** 209-2017.

[86] Singh, P., Pandit, S., Mokkapati, V. R. , Garg, A., Ravikumar, V. & Mijakovic, I. 2018. Gold Nanoparticles in Diagnostics and Therapeutics for Human Cancer. *Int J Mol Sci,* 19**,** 1979.

[87] Bansal, S. A., Kumar, V., Karimi, J., Singh, A. P. & Kumar, S. 2020. Role of gold nanoparticles in advanced biomedical applications. *Nanoscale Adv,* 2**,** 3764-3787.

[88] Graczyk, A., Pawlowska, R., Jedrzejczyk, D. & Chworos, A. 2020. Gold Nanoparticles in Conjunction with Nucleic Acids as a Modern Molecular System for Cellular Delivery. *Molecules (Basel, Switzerland),* 25**,** 204.

[89] Chuang, Y. J., Zhou, X., Pan, Z. & Turchi, C. 2009. A convenient method for synthesis of glyconanoparticles for colorimetric measuring carbohydrate–protein interactions. *Biochem Biophys Res Commun,* 389**,** 22-27.

[90] Suk, J. S., Xu, Q., Kim, N., Hanes, J. & Ensign, L. M. 2016. PEGylation as a strategy for improving nanoparticle-based drug and gene delivery. *Adv Drug Deliv Rev,* 99**,** 28-51.
[91] Catuogno, S., Esposito, C. L. & De Franciscis, V. 2016. Aptamer-Mediated Targeted Delivery of Therapeutics: An Update. *Pharmaceuticals (Basel, Switzerland),* 9**,** 69.
[92] Peng, H. S. & Chiu, D. T. 2015. Soft fluorescent nanomaterials for biological and biomedical imaging. *Chem Soc Rev,* 44**,** 4699-4722.
[93] Aggarwal, P., Hall, J. B., Mcleland, C. B., Dobrovolskaia, M. A. & Mcneil, S. E. 2009. Nanoparticle interaction with plasma proteins as it relates to particle biodistribution, biocompatibility and therapeutic efficacy. *Adv Drug Deliv Rev,* 61**,** 428-437.
[94] Zhang, J., Mou, L. & Jiang, X. 2020. Surface chemistry of gold nanoparticles for health-related applications. *Chem Sci,* 11**,** 923-936.
[95] Boisselier, E. & Astruc, D. 2009. Gold nanoparticles in nanomedicine: preparations, imaging, diagnostics, therapies and toxicity. *Chem Soc Rev,* 38**,** 1759-1782.
[96] Kim, H., Beack, S., Han, S., Shin, M. , Lee, T., Park, Y., Kim, Ki. S., Yetisen, A. K., Yun, S. H., Kwon, W. & Hahn, S. K. 2018. Multifunctional Photonic Nanomaterials for Diagnostic, Therapeutic, and Theranostic Applications. *Adv Mater,* 30.
[97] Chen, D., Ganesh, S., Wang, W. & Amiji, M. 2017. Plasma protein adsorption and biological identity of systemically administered nanoparticles. *Nanomedicine,* 12**,** 2113-2135.
[98] Chen, Y. H., Tsai, C. Y., Huang, P. Y., Chang, M. Y, P.C., Cheng, H., Chou C., Chen, D. H. , Wang, C. R., Shiau, A.L & Wu, C.L. 2007. Methotrexate Conjugated to Gold Nanoparticles Inhibits Tumor Growth in a Syngeneic Lung Tumor Model. *Mol Pharm,* 4**,** 713-722.
[99] Wang, F., Wang, Y. C., Dou, S., Xiong, M. H., Sun, T. M. & Wang, J. 2011. Doxorubicin-Tethered Responsive Gold Nanoparticles Facilitate Intracellular Drug Delivery for Overcoming Multidrug Resistance in Cancer Cells. *ACS Nano,* 5**,** 3679-3692.
[100] Park, H., Tsutsumi, H. & Mihara, H. 2014. Cell-selective intracellular drug delivery using doxorubicin and α-helical peptides conjugated to gold nanoparticles. *Biomaterials,* 35**,** 3480-3487.
[101] Ramalingam, V., Varunkumar, K., Ravikumar, V. & Rajaram, R. 2018. Target delivery of doxorubicin tethered with PVP stabilized gold nanoparticles for efective treatment of lung cancer. *Sci Rep,* 8**,** 3815.
[102] Farooq, M. U., Novosad, V. , Rozhkova, E. A., Wali, H., Ali, A., Fateh, A. A., Neogi, P. B., Neogi, A. & Wang, Z. 2018. Gold Nanoparticles-enabled Efficient Dual Delivery of Anticancer Therapeutics to HeLa Cells. *Sci Rep,* 8**,** 2907.
[103] Brown, S. D., Nativo, P. , Smith, J. A., Stirling, D. , Edwards, P. R., Venugopal, B. , Flint, D. J. , Plumb, J. A., Graham, D. & Wheate, N. J. 2010. Gold Nanoparticles for the Improved Anticancer Drug Delivery of the Active Component of Oxaliplatin. *J Am Chem Soc,* 132**,** 4678-4684.
[104] Gilad, Y., Firer, M. A., Rozovsky, A., Ragozin, E., Redko, B., Albeck, A. & Gellerman, G. 2014. "Switch off/switch on" regulation of drug cytotoxicity by conjugation to a cell targeting peptide. *European Journal of Medicinal Chemistry,* 85**,** 139-146.
[105] Kalishwaralal, K., Bat-Chen, L., Andrii, B., Gary, G., Ofer, S., Galia, L. & Michael, A.F. 2018. Gold nanoparticles stabilize peptide-drug-conjugates for sustained targeted drug delivery to cancer cells. *J Nanobiotechnology,* 16**,** 1-13.
[106] Srinivas, R. B., Kondath, S., Anantanarayanan, R. & Rajaram, R. 2015. Kaempferol mediated synthesis of gold nanoparticles and their cytotoxic effects on MCF-7 cancer cell line. *Process Biochem,* 50**,** 1966-1976.

[107] Bobo, B., Robinson, K.J., Islam, J., Thurecht, K.J. & Corrie, S.R 2016. Nanoparticle-Based Medicines: A Review of FDA-Approved Materials and Clinical Trials to Date. *Pharm Res,* 33**,** 2373-2387.
[108] Libutti, S. K., Paciotti, G. F., Byrnes, A. A., Alexander, H. R., Gannon, W. E., Walker, M., Seidel, G. D., Yuldasheva, N. & Tamarkin, L. 2010. Phase I and Pharmacokinetic Studies of CYT-6091, a Novel PEGylated Colloidal Gold-rhTNF Nanomedicine. *Clin Cancer Res,* 16**,** 6139-6149.
[109] Weissleder, R. 2001. A clearer vision for in vivo imaging. *Nat Biotechnol,* 19**,** 316-317.
[110] Seo, S. H., Kim, B. M., Joe, A., Han, H. W., Chen, X., Cheng, Z. & Jang, E. S. 2014. NIR-light-induced surface-enhanced Raman scattering for detection and photothermal/photodynamic therapy of cancer cells using methylene blue-embedded gold nanorod@SiO2 nanocomposites. *Biomaterials,* 35**,** 3309-3318.
[111] Khlebtsov, B. , Panfilova, E., Khanadeev, V. , Bibikova, O. , Terentyuk, G. , Ivanov, A. , Rumyantseva, V. , Shilov, I. , Ryabova, A., Loshchenov, V. & Khlebtsov, N. G. 2011. Nanocomposites Containing Silica Coated Gold Silver Nanocages and Yb 2,4 Dimethoxyhematoporphyrin: Multifunctional Capability of IR-Luminescence Detection, Photosensitization, and Photothermolysis. *ACS Nano,* 5**,** 7077-7089.
[112] Deng, K., Li, C., Huang, S., Xing, B., Jin, D., Zeng, Q., Hou, Z. & Lin, J. 2017. Recent Progress in Near Infrared Light Triggered Photodynamic Therapy. *Small,* 13**,** 1702299.
[113] Zhang, Y., Zhan, X., Xiong, J., Peng, S., Huang, W., Joshi, R., Cai, Y., Liu, Y., Li, R., Yuan, K., Zhou, N. & Min, W. 2018. Temperature-dependent cell death patterns induced by functionalized gold nanoparticle photothermal therapy in melanoma cells. *Sci Rep,* 8**,** 8720.
[114] Alia, M. R. K., Rahmanb, M. A., Wua, Y., Hanc, T., Peng, X., Mackeya, M. A., Wang, D., Shind, H. J., Chenb, Z. G., Xiaoa, H., Wua, R., Tangc, Y., Shinb, D. M. & El-Sayed, M. A. 2017. Efficacy, long-term toxicity, and mechanistic studies of gold nanorods photothermal therapy of cancer in xenograft mice. *Proc Natl Acad Sci U S A,* 114**,** 3110-3118.
[115] Hirsch, L. R., Stafford, R. J., Bankson, J. A., Sershen, S. R., Rivera, B., Price, R. E., Hazle, J. D., Halas, N. J. & West, J. L. 2003. Nanoshell-mediated near-infrared thermal therapy of tumors under magnetic resonance guidance. *Proc Natl Acad Sci U S A,* 100**,** 13549-13554.
[116] Schwartz, J. A., Shetty, A. M., Price, R. E., Stafford, R. J., Wang, J. C., Uthamanthil, R. K., Pham, K., Mcnichols, R. J., Coleman, C. L. & Payne, J. D. 2009. Feasibility Study of Particle-Assisted Laser Ablation of Brain Tumors in Orthotopic Canine Model. *Cancer Res,* 69**,** 1659-1667.
[117] Kumthekar, P., Rademaker, A. , Ko, C., Dixit, K. , Schwartz, M. A., Sonabend, A. M. , Sharp, L. , Lukas, R. V., Stupp, R., Horbinski, C. , Mccortney, K. & Stegh, A. H. 2019. A phase 0 first-in-human study using NU-0129: A gold base spherical nucleic acid (SNA) nanoconjugate targeting BCL2L12 in recurrent glioblastoma patients. *J Clin Oncol,* 37.
[118] Kapadia, C. H., Melamed, J. R. & Day, E. S. 2018. Spherical Nucleic Acid Nanoparticles: Therapeutic Potential. *BioDrugs,* 32**,** 297-309.
[119] Xu, Z. Q., Broza, Y. Y., Ionsecu, R., Tisch, U., Ding, L., Liu, H., Song, Q., Pan, Y. Y., Xiong, F. X., Gu, K. S., Sun, G. P. , Chen, Z. D., Leja, M. & Haick, H. 2013. A nanomaterial-based breath test for distinguishing gastric cancer from benign gastric conditions. *Br J Cancer,* 108**,** 941-950.
[120] Kharlamov, A. N., Tyurnina, A. E., Veselova, V. S., Kovtun, O. P., Shur, V. Y. & Gabinsky, J. L. 2015. Silica–gold nanoparticles for atheroprotective management of plaques: results of the NANOM-FIM trial. *Nanoscale,* 7**,** 8003-8015.

[121] Jiang, Y. , Huo, S., Mizuhara, T., Das, R. , Lee, Y. W. , Hou, S. , Moyano, D. F. , Duncan, B. , Liang, X. J. & Rotello, V. M. 2015. The Interplay of Size and Surface Functionality on the Cellular Uptake of Sub-10 nm Gold Nanoparticles. *ACS Nano,* 9**,** 9986-9993.
[122] Kapara, A., Brunton, V., Graham, D. & Faulds, K. 2020. Investigation of cellular uptake mechanism of functionalised gold nanoparticles into breast cancer using SERS. *Chem Sci,* 11**,** 5819-5829.
[123] Shang, L., Nienhaus, K. & Nienhaus, G. U. 2014. Engineered nanoparticles interacting with cells: size matters. *J Nanobiotechnology* 12**,** 1-11.
[124] Lesniak, A., Fenaroli, F. , P., Monopoli M., Åberg, C. , Dawson, K, A. & Salvati, A. 2012. Effects of the presence or absence of a protein corona on silica nanoparticle uptake and impact on cells. *ACS Nano,* 6**,** 5845-5857.
[125] Mironava, T. , Hadjiargyrou, M. , Simon, M. , Jurukovski, V. & Rafailovich, M. H. 2010. Gold nanoparticles cellular toxicity and recovery: effect of size, concentration and exposure time. *Nanotoxicology,* 4**,** 120-137.
[126] Albanese, A. , Tang, P. S. & Chan, W. C. 2012. The effect of nanoparticle size, shape, and surface chemistry on biological systems. *Annu Rev Biomed Eng,* 14**,** 1-16.
[127] Pannico, M. , Calarco, A. , Peluso, G. & Musto, P. 2018. Functionalized Gold Nanoparticles as Biosensors for Monitoring Cellular Uptake and Localization in Normal and Tumor Prostatic Cells. *Biosensors (Basel),* 8**,** 87.
[128] Escudero-Francos, M. A., Cepas, V. , González-Menédez, P. , Badía-Laíño, R. , Díaz-García, M. E. , Sainz, R. M. & Mayo, J. C. Hevia, D. 2017. Cellular Uptake and Tissue Biodistribution of Functionalized Gold Nanoparticles and Nanoclusters. *Journal of Biomedical Nanotechnology,* 13**,** 167-179.
[129] Chaudhuri, A. , Battaglia, G. & Golestanian, R. 2011. The effect of interactions on the cellular uptake of nanoparticles. *Phys Biol,* 8**,** 046002.
[130] Gao, H. , Yang, Z. , Zhang, S. , Cao, S. , Shen, S. , Pang, Z. & Jiang, X. 2013. Ligand modified nanoparticles increases cell uptake, alters endocytosis and elevates glioma distribution and internalization. *Sci Rep,* 3**,** 2534.
[131] Taylor, A., Wilson, K. M., Murray, P., Fernig, D. G. & Lévy, R. 2012. Long-term tracking of cells using inorganic nanoparticles as contrast agents: are we there yet? *Chem Soc Rev,* 41**,** 2707-2717.
[132] Yameen, B. , Choi, W. I. , Vilos, C. , Swami, A. , Shi, J. & Farokhzad, O. C. 2014. Insight into nanoparticle cellular uptake and intracellular targeting. *J Control Release,* 28**,** 485-499.
[133] Ng, C. T., Tang, F. M. A., Li, J. J., Ong, C., Yung, L. L. Y. & Bay, B. H. 2015. Clathrin-Mediated Endocytosis of Gold NanoparticlesIn Vitro. *Anat Rec,* 298**,** 418-427.
[134] Donahue, N. D., Acar, H. & Wilhelm, S. 2019. Concepts of nanoparticle cellular uptake, intracellular trafficking, and kinetics in nanomedicine. *Adv Drug Deliv Rev,* 143**,** 68-96.
[135] Tang, H. , Zhang, H. , Ye, H. & Zheng, Y. 2018. Receptor-Mediated Endocytosis of Nanoparticles: Roles of Shapes, Orientations, and Rotations of Nanoparticles. *J Phys Chem B,* 122**,** 171-180.
[136] Cho, E. C., Zhang, Q. & Xia, Y. 2011. The effect of sedimentation and diffusion on cellular uptake of gold nanoparticles. *Nat Nanotechnol,* 6**,** 385-391.
[137] Chithrani, D. B. 2010. Intracellular uptake, transport, and processing of gold nanostructures. *Mol Membr Biol,* 27**,** 299-311.
[138] Jin, H. , Heller, D. A. , Sharma, R. & Strano, M. S. 2009. Size-dependent cellular uptake and expulsion of single-walled carbon nanotubes: single particle tracking and a generic uptake model for nanoparticles. *ACS Nano,* 3**,** 149-158.

[139] Shen, Z., Ye, H. & Li, Y. 2018. Understanding receptor-mediated endocytosis of elastic nanoparticles through coarse grained molecular dynamic simulation. *Phys Chem Chem Phys,* 20**,** 16372-16385.
[140] Rejman, J. , Oberle, V. , Zuhorn, I. S. & Hoekstra, D. 2004. Size-dependent internalization of particles via the pathways of clathrin- and caveolae-mediated endocytosis. *Biochem J,* 1**,** 159-169.
[141] Behzadi, S., Serpooshan, V., Tao, W., Hamaly, M. A., Alkawareek, M. Y., Dreaden, E. C., Brown, D., Alkilany, A. M., Farokhzad, O. C. & Mahmoudi, M. 2017. Cellular uptake of nanoparticles: journey inside the cell. *Chem Soc Rev,* 46**,** 4218-4244.
[142] Canton, I. & Battaglia, G. 2012. Endocytosis at the nanoscale. *Chem Soc Rev,* 41**,** 2718-2739.
[143] Wang, T. , Bai, J. , Jiang, X. & Nienhaus, G. U. 2012. Cellular uptake of nanoparticles by membrane penetration: a study combining confocal microscopy with FTIR spectroelectrochemistry. *ACS Nano,* 6**,** 1251-1259.
[144] Leroueil, P. R. , Berry, S. A. , Duthie, K. , Han, G. , Rotello, V. M. , Mcnerny, D. Q. , Baker, J. R. Jr. , Orr, B. G. & Holl, M. M. 2008. Wide varieties of cationic nanoparticles induce defects in supported lipid bilayers. *Nano Lett,* 8**,** 420-424.
[145] Chen, J. , Hessler, J. A. , Putchakayala, K. , Panama, B. K. , Khan, D. P. , Hong, S. , Mullen, D. , Dimaggio, G. S. C. , Som, A. , Tew, G. N. , Lopatin, A. N., Baker, J. R. , Holl, M. M. B. & Orr, B. G. 2009. Cationic Nanoparticles Induce Nanoscale Disruption in Living Cell Plasma Membranes. *J Phys Chem B,* 113**,** 11179-11185.
[146] Patra, J. K., Das, G. , Fraceto, L. F. , Campos, E. , Rodriguez-Torres, M. , Acosta-Torres, L. S. , Diaz-Torres, L. A. , Grillo, R. , Swamy, M. K. , Sharma, S. , Habtemariam, S. & Shin, H. S. 2018. Nano based drug delivery systems: recent developments and future prospects. *J Nanobiotechnol,* 16**,** 71.
[147] Jung, D.H. , Hwang, S. , Song, G. W. , Ahn, C. S. , Moon, D. B. , Ha, T. Y. , Kim, K. H. , Park, G. C. , Kim, B. S. , Park, I. J. , Lim, S. B. , Kim, J. C. , Yoo, M. W. , Byeon, J. S. , Jung, H. Y. , Lee, G. H. , Myung, S. J. , Choe, J. , Choi, J. Y. , Park, H. W. & Lee, S. G. 2016. Survival Benefit of Early Cancer Detection Through Regular Endoscopic Screening for De Novo Gastric and Colorectal Cancers in Korean Liver Transplant Recipients. *Transplant Proc,* 48**,** 145-151.
[148] Lu, W. L. , Jansen, L. , Post, W. J. , Bonnema, J. , Van De Velde, J. C. & De Bock, G. H. 2009. Impact on survival of early detection of isolated breast recurrences after the primary treatment for breast cancer: a meta-analysis. *Breast Cancer Res Treat,* 14**,** 403-412.
[149] Han, X., Xu, K., Taratula, O. & Farsad, K. 2019. Applications of nanoparticles in biomedical imaging. *Nanoscale,* 11**,** 799-819.
[150] Cuccurullo, V. , Di Stasio, G. D. , Mazzarella, G. & Cascini, G. L. 2018. Microvascular Invasion in HCC: The Molecular Imaging Perspective. *Contrast Media Mol Imaging,* 4**,** 9487938.
[151] Santra, S. & Malhotra, A. 2011. Fluorescent nanoparticle probes for imaging of cancer. *Wiley Interdiscip Rev Nanomed Nanobiotechnol,* 3**,** 501-510.
[152] Foucault-Collet, A. , Gogick, K. A. , White, K. A. , Villette, S. , Pallier, A. , Collet, G. , Kieda, C. , Li, T. , Geib, S. J. , Rosi, N. L. & Petoud, S. 2013. Lanthanide near infrared imaging in living cells with Yb3+ nano metal organic frameworks. *Proc Natl Acad Sci U S A,* 110**,** 17199-17204.
[153] Hwang, E. S. , Cao, C. , Hong, S. , Jung, H. J. , Cha, C. Y. , Choi, J. B. , Kim, Y. J. & Baik, S. 2006. The DNA hybridization assay using single-walled carbon nanotubes as ultrasensitive, long-term optical labels. *Nanotechnology,* 17**,** 3442-3445.

[154] Genovese, D., Bonacchi, S., Juris, R., Montalti, M., Prodi, L., Rampazzo, E. & Zaccheroni, N. 2013. Prevention of Self-Quenching in Fluorescent Silica Nanoparticles by Efficient Energy Transfer. *Angew Chem Int Ed Engl,* 52**,** 5965-5968.
[155] Grebenik, E. A. , Nadort, A. , Generalova, A. N. , Nechaev, A. V. , Sreenivasan, V. K. , Khaydukov, E. V. , Semchishen, V. A. , Popov, A. P. , Sokolov, V. I. , Akhmanov, A. S. , Zubov, V. P. , Klinov, D. V. , Panchenko, V. Y. , Deyev, S. M. & Zvyagin, A. V. 2013. Feasibility study of the optical imaging of a breast cancer lesion labeled with upconversion nanoparticle biocomplexes. *J Biomed Opt,* 18**,** 76004.
[156] Cai, Z., Ye, Z., Yang, X., Chang, Y., Wang, H., Liu, Y. & Cao, A. 2011. Encapsulated enhanced green fluorescence protein in silica nanoparticle for cellular imaging. *Nanoscale,* 3**,** 1974.
[157] Henry, A. I., Sharma, B., Cardinal, M. F., Kurouski, D. & Van Duyne, R. P. 2016. Surface-Enhanced Raman Spectroscopy Biosensing: In Vivo Diagnostics and Multimodal Imaging. *Anal Chem,* 88**,** 6638-6647.
[158] Vats, M. , Mishra, S. K. , Baghini, M. S. , Chauhan, D. S. , Srivastava, R. & De, A. 2017. Near Infrared Fluorescence Imaging in Nano-Therapeutics and Photo-Thermal Evaluation. *Int J Mol Sci,* 18**,** 924.
[159] Hong, G. , Antaris, A. & Dai, H. 2017. Near-infrared fluorophores for biomedical imaging. *Nat Biomed Eng,* 1**,** 10.
[160] Sun, Y., Qu, C., Chen, H., He, M., Tang, C., Shou, K., Hong, S., Yang, M., Jiang, Y., Ding, B., Xiao, Y., Xing, L., Hong, X. & Cheng, Z. 2016. Novel benzo-bis(1,2,5-thiadiazole) fluorophores for in vivo NIR-II imaging of cancer. *Chem Sci,* 7**,** 6203-6207.
[161] Sun, Y., Ding, M., Zeng, X., Xiao, Y., Wu, H., Zhou, H., Ding, B., Qu, C., Hou, W., Er-Bu, A. G. A., Zhang, Y., Cheng, Z. & Hong, X. 2017. Novel bright-emission small-molecule NIR-II fluorophores for in vivo tumor imaging and image-guided surgery. *Chem Sci,* 8**,** 3489-3493.
[162] Ding, F., Zhan, Y., Lu, X. & Sun, Y. 2018. Recent advances in near-infrared II fluorophores for multifunctional biomedical imaging. *Chem Sci,* 9**,** 4370-4380.
[163] Jaiswal, J. K. , Mattoussi, H. , Mauro, J. M. & Simon, S. M. 2003. Long-term multiple color imaging of live cells using quantum dot bioconjugates. *Nat Biotechnol,* 1**,** 47-51.
[164] Chen, N. , He, Y. , Su, Y. , Li, X. , Huang, Q. , Wang, H. , Zhang, X. , Tai, R. & Fan, C. 2011. The cytotoxicity of cadmium-based quantum dots. *Biomaterials,* 33**,** 1238-1244.
[165] Schmitz, C, Gökce, B. , Jakobi, J. , Barcikowski, S. & Strehmel, B. 2016. Integration of Gold Nanoparticles into NIR-Radiation Curable Powder Resin. *ChemistrySelect,* 1**,** 5574-5578.
[166] Lee, S. J. , Lee, H. J., Kim, S. Y., Seok, J. M. , Lee, J. H. , Kim, W. D. , Kwon, I. K. , Park, S. Y. & Park, S. A. 2018. In situ gold nanoparticle growth on polydopamine-coated 3D-printed scaffolds improves osteogenic differentiation for bone tissue engineering applications: in vitro and in vivo studies. *Nanoscale,* 10**,** 15447 —15453
[167] Bhagawati, M. , You, C. & Piehler, J. 2013. Quantitative real-time imaging of protein-protein interactions by LSPR detection with micropatterned gold nanoparticles. *Anal Chem,* 85**,** 9564-9571.
[168] Kim, E. Y. , Kumar, D., Khanga, G. & Lim, D. K. 2015. Recent advances in gold nanoparticle-based bioengineering applications. *J Mater Chem B,* 3**,** 8433-8444.
[169] Dunning, C. A. S. & Bazalova-Carter, M. 2018. Sheet beam x-ray fluorescence computed tomography (XFCT) imaging of gold nanoparticles. *Med Phys,* 45**,** 2572-2582.
[170] Estrada, L. C. & Gratton, E. 2012. Spectroscopic properties of gold nanoparticles at the single-particle level in biological environments. *Chemphyschem,* 13**,** 1087-1092.

[171] Han, S., Raabe, M., Hodgson, L., Mantell, J., Verkade, P., Lasser, T., Landfester, K., Weil, T. & Lieberwirth, I. 2019. High-Contrast Imaging of Nanodiamonds in Cells by Energy Filtered and Correlative Light-Electron Microscopy: Toward a Quantitative Nanoparticle-Cell Analysis. *Nano Lett,* 19**,** 2178-2185.
[172] Huang, X. & El-Sayed, M. A. 2010. Gold nanoparticles: Optical properties and implementations in cancer diagnosis and photothermal therapy. *J Adv Res,* 1**,** 13-28.
[173] Orendorff, C. J, Sau, T. K & Murphy, C. J 2006. Shape-Dependent Plasmon-Resonant Gold Nanoparticles. *Small,* 2**,** 636-639.
[174] Ueno, H. , Nishikawa, S. , Iino, R. , Tabata, K. V. , S., Sakakihara., Yanagida, T. & Noji, H. 2010. Simple dark-field microscopy with nanometer spatial precision and microsecond temporal resolution. *Biophys J,* 98**,** 2014-2023.
[175] Lemelle, A., Veksler, B. , Kozhevnikov, I. S. , Akchurin, G. G. , Piletsky, S. A. & Meglinski, I. 2009. Application of gold nanoparticles as contrast agents in confocal laser scanning microscopy. *Laser Phys Lett,* 6**,** 71-75.
[176] Wang, T., Halaney, D. , Ho, D. , Feldman, M. D. & Milner, T. E. 2013. Two-photon luminescence properties of gold nanorods. *Biomed Opt Express,* 4**,** 584-595.
[177] De Paoli Lacerda, S. H. , Park, J. J. , Meuse, C. , Pristinski, D. , Becker, M. L. , Karim, A. & Douglas, J. F. 2010. Interaction of Gold Nanoparticles with Common Human Blood Proteins. *ACS Nano,* 4**,** 365-379.
[178] Russo, C. J. & Passmore, L. A. 2014. Ultrastable gold substrates for electron cryomicroscopy. *Science,* 346**,** 1370-1380.
[179] Cole, L. E. , Ross, R. D. , Tilley, J. M. R. , Vargo-Gogola, T. & Roeder, R. K. 2015. Gold nanoparticles as contrast agents in x-ray imaging and computed tomography. *Nanomedicine,* 10**,** 321-341.
[180] Lusic, H. & Grinstaff, M. W. 2013. X-ray-computed tomography contrast agents. *Chem Rev,* 113**,** 1641-1666.
[181] Dong, Y. C., Hajfathalian, M., Maidment, P. S. N., Hsu, J. C., Naha, P. C., Si-Mohamed, S., Breuilly, M., Kim, J., Chhour, P., Douek, P., Litt, H. I. & Cormode, D. P. 2019. Effect of Gold Nanoparticle Size on Their Properties as Contrast Agents for Computed Tomography. *Scientific Reports,* 9**,** 14912.
[182] Lohrke, J. , Frenzel, T. , Endrikat, J. , Alves, F. C. , Grist, T. M. , Law, M. , Lee, J. M. , T., Leiner., C., Li. K., Nikolaou, K. , Prince, M. R. , Schild, H. H. , Weinreb, J. C. , Yoshikawa, K. & Pietsch, H. 2016. 25 Years of Contrast-Enhanced MRI: Developments, Current Challenges and Future Perspectives. *Adv Ther,* 33**,** 1-28.
[183] Caravan, P. , Ellison, J. J. , Mcmurry, T. J. & Lauffer, R. B. 1999. Gadolinium(III) Chelates as MRI Contrast Agents: Structure, Dynamics, and Applications. *Chem Rev,* 99**,** 2293-2352.
[184] Chauhan, R. , El-Baz, N. , Keynton, R. S. , James, K. T. , Malik, D. A. , Zhu, M. , El-Baz, A. , Ng, C. K. , Bates, P. J. , Malik, M. T. & O'toole, M. G. 2019. Targeted Gold Nanoparticle-Oligonucleotide Contrast Agents in Combination with a New Local Voxel-Wise MRI Analysis Algorithm for In Vitro Imaging of Triple-Negative Breast Cancer. *Nanomaterials (Basel),* 9**,** 709.
[185] Dreaden, E. C., Alkilany, A. M., Huang, X., Murphy, C. J. & El-Sayed, M. A. 2012. The golden age: gold nanoparticles for biomedicine. *Chem Soc Rev,* 41**,** 2740-2779.
[186] Osborne, S. A. M. & Pikramenou, Z. 2015. Highly luminescent gold nanoparticles: effect of ruthenium distance for nanoprobes with enhanced lifetimes. *Faraday Discussions,* 185**,** 219-231.

[187] Rogers, N. J., Claire, S., Harris, R. M., Farabi, S., Zikeli, G., Styles, I. B., Hodges, N. J. & Pikramenou, Z. 2014. High coating of Ru(II) complexes on gold nanoparticles for single particle luminescence imaging in cells. *Chem Commun* 50**,** 617-619.
[188] King, Siobhan M., Claire, Sunil, Teixeira, Rodolfo I., Dosumu, Abiola N., Carrod, Andrew J., Dehghani, Hamid, Hannon, Michael J., Ward, Andrew D., Bicknell, Roy, Botchway, Stanley W., Hodges, Nikolas J. & Pikramenou, Zoe 2018. Iridium Nanoparticles for Multichannel Luminescence Lifetime Imaging, Mapping Localization in Live Cancer Cells. *J Am Chem Soc,* 140**,** 10242-10249.
[189] Rogers, N. J., Jeffery, H. C., Claire, S., Lewis, D. J., Zikeli, G., Hodges, N. J., Egginton, S., Nash, G. B. & Pikramenou, Z. 2017. Tailoring iridium luminescence and gold nanoparticle size for imaging of microvascular blood flow. *Nanomedicine (Lond),* 12**,** 2725-2740.
[190] Davies, A., Lewis, D. J., Watson, S. P., Thomas, S. G. & Pikramenou, Z. 2012. pH-controlled delivery of luminescent europium coated nanoparticles into platelets. *Proc Natl Acad Sci U S A,* 109**,** 1862-1867.
[191] Lewis, D. J., Day, T. M., Macpherson, J. V. & Pikramenou, Z. 2006. Luminescent nanobeads: attachment of surface reactive Eu(iii) complexes to gold nanoparticles. *Chem Commun* 1433.
[192] Lewis, D. J. & Pikramenou, Z. 2014. Lanthanide-coated gold nanoparticles for biomedical applications. *Coord Chem Rev,* 273**,** 213-225.
[193] Dosumu, A. N., Claire, S., Watson, L. S., Girio, P. M., Osborne, S. A. M., Pikramenou, Z. & Hodges, N. J. 2021. Quantification by Luminescence Tracking of Red Emissive Gold Nanoparticles in Cells. *JACS Au***,** Advance Online Publication.
[194] Moore, E. G. , Samuel, A. P. S. & Raymond, K. N. 2009. From Antenna to Assay: Lessons Learned in Lanthanide Luminescence. *Acc Chem Res,* 42**,** 542-552.
[195] Zhang, L., Zheng, X., Deng, W., Lu, Y., Lechevallier, S., Ye, Z., Goldys, E. M., Dawes, J. M., Piper, J. A., Yuan, J., Verelst, M. & Jin, D. 2014. Practical Implementation, Characterization and Applications of a Multi-Colour Time-Gated Luminescence Microscope. *Sci Rep,* 4**,** 6597.
[196] Arruebo, M., Valladares, M., & González-Fernández, A. 2009. Antibody-Conjugated Nanoparticles for Biomedical Applications. *J Nanomater,* 2009**,** 1-24.
[197] Filbrun, S. L., Filbrun, A. B., Lovato, F. L., Oh, S. H., Driskell, E. A. & Driskell, J. D. 2017. Chemical modification of antibodies enables the formation of stable antibody–gold nanoparticle conjugates for biosensing. *Analyst,* 142**,** 4456-4467.
[198] Goddard, Z. R., Marín, M. J., Russell, D. A. & Searcey, M. 2020. Active targeting of gold nanoparticles as cancer therapeutics. *Chem Soc Rev,* 49**,** 8774-8789
[199] Vidarsson, G. , Dekkers, G. & Rispens, T. 2014. IgG subclasses and allotypes: from structure to effector functions. *Front Immunol,* 5**,** 520.
[200] Porter, R. R. 1973. Structural studies of immunoglobulins. *Science,* 180**,** 713-716.
[201] Jonker, D. J., O'callaghan, C. J., Karapetis, C. S., Zalcberg, J. R., Tu, D., Au, H. J., Berry, S. R., Krahn, M., Price, T., Simes, R. J., Tebbutt, N. C., Van Hazel, G., Wierzbicki, R., Langer, C. & Moore, M. J. 2007. Cetuximab for the Treatment of Colorectal Cancer. *N Engl J Med,* 357**,** 2040-2048.
[202] Verma, S., Miles, D., Gianni, L., Krop, I. E., Welslau, M., Baselga, J., Pegram, M., Oh, D. Y., Diéras, V., Guardino, E., Fang, L., Lu, M. W., Olsen, S. & Blackwell, K. 2012. Trastuzumab Emtansine for HER2-Positive Advanced Breast Cancer. *N Engl J Med,* 367**,** 1783-1791.

[203] Chattopadhyay, N., Cai, Z., Kwon, Y. L., Lechtman, E., Pignol, J. P. & Reilly, R. M. 2013. Molecularly targeted gold nanoparticles enhance the radiation response of breast cancer cells and tumor xenografts to X-radiation. *Breast Cancer Res Treat,* 137**,** 81-91.
[204] Chattopadhyay, N., Cai, Z., Pignol, J. P., Keller, B., Lechtman, E., Bendayan, R. & Reilly, R. M. 2010. Design and Characterization of HER-2-Targeted Gold Nanoparticles for Enhanced X-radiation Treatment of Locally Advanced Breast Cancer. *Mol Pharm,* 7**,** 2194-2206.
[205] Yook, S., Cai, Z., Jeong, J. J., Lu, Y., Winnik, M. A., Pignol, J. P. & Reilly, R. M. 2020. Dual-Receptor-Targeted (DRT) Radiation Nanomedicine Labeled with 177Lu Is More Potent for Killing Human Breast Cancer Cells That Coexpress HER2 and EGFR Than Single-Receptor-Targeted (SRT) Radiation Nanomedicines. *Mol Pharmaceutics,* 17**,** 1226-1236.
[206] Qu, X. , Yao, C. , Wang, J. , Li, Z. & Zhang, Z. 2012. Anti-CD30-targeted gold nanoparticles for photothermal therapy of L-428 Hodgkin's cell. *Int J Nanomedicine,* 7**,** 6095-6103.
[207] Chen, C. H. , Wu, Y. J. & Chen, J. J. 2016. Photo-thermal therapy of bladder cancer with anti-EGFR antibody conjugated gold nanoparticles. *Front Biosci,* 21**,** 1211-1221.
[208] Patra, C. R., Bhattacharya, R., Wang, E., Katarya, A., Lau, J. S., Dutta, S., Muders, M., Wang, S., Buhrow, S. A., Safgren, S. L., Yaszemski, M. J., Reid, J. M., Ames, M. M., Mukherjee, P. & Mukhopadhyay, D. 2008. Targeted Delivery of Gemcitabine to Pancreatic Adenocarcinoma Using Cetuximab as a Targeting Agent. *Cancer Res,* 68**,** 1970-1978.
[209] Das, A., Soehnlen, E., Woods, S., Hegde, R., Henry, A., Gericke, A. & Basu, S. 2011. VEGFR-2 targeted cellular delivery of doxorubicin by gold nanoparticles for potential antiangiogenic therapy. *J Nanopart Res,* 13**,** 6283-6290.
[210] Tummala, S., Kumar, M. N. S. & Pindiprolu, S. K. 2016. Improved anti-tumor activity of oxaliplatin by encapsulating in anti-DR5 targeted gold nanoparticles. *Drug Deliv,* 23**,** 3505-3519.
[211] Spadavecchia, J., Movia, D., Moore, C., Maguire, C. M., Moustaoui, H., Casale, S., Volkov, Y. & Prina-Mello, A. 2016. Targeted polyethylene glycol gold nanoparticles for the treatment of pancreatic cancer: from synthesis to proof-of-concept in vitro studies. *Int J Nanomedicine,* 11**,** 791-822.
[212] Bhattacharyya, S., Bhattacharya, R., Curley, S., Mcniven, M. A. & Mukherjee, P. 2010. Nanoconjugation modulates the trafficking and mechanism of antibody induced receptor endocytosis. *Proc Natl Acad Sci U S A,* 107**,** 14541.
[213] Hommelgaard, A. M., Lerdrup, M. & Van Deurs, B. 2004. Association with Membrane Protrusions Makes ErbB2 an Internalization-resistant Receptor. *Mol Biol Cell,* 15**,** 1557-1567.
[214] Leyton, J. V. 2020. Improving Receptor-Mediated Intracellular Access and Accumulation of Antibody Therapeutics—The Tale of HER2. *Antibodies,* 9**,** 32.
[215] Cai, Z., Yook, S., Lu, Y., Bergstrom, D., Winnik, M. A., Pignol, J. P. & Reilly, R. M. 2017. Local Radiation Treatment of HER2-Positive Breast Cancer Using Trastuzumab-Modified Gold Nanoparticles Labeled with 177Lu. *Pharm Res,* 34**,** 579-590.
[216] Cao-Milán, R. & Liz-Marzán, L. M. 2014. Gold nanoparticle conjugates: recent advances toward clinical applications. *Expert Opin Drug Deliv,* 11**,** 741-752.
[217] Kumar, S., Aaron, J. & Sokolov, K. 2008. Directional conjugation of antibodies to nanoparticles for synthesis of multiplexed optical contrast agents with both delivery and targeting moieties. *Nat Protoc,* 3**,** 314-320.
[218] Jazayeri, M. H., Amani, H., Pourfatollah, A. A., Pazoki-Toroudi, H. & Sedighimoghaddam, B. 2016. Various methods of gold nanoparticles (GNPs) conjugation to antibodies. *Sensing and Bio-Sensing Research,* 9**,** 17-22.

[219] Oliveira, J. P., Prado, A. R., Keijok, W. J., Antunes, P. W. P., Yapuchura, E. R. & Guimarães, M. C. C. 2019. Impact of conjugation strategies for targeting of antibodies in gold nanoparticles for ultrasensitive detection of 17β-estradiol. *Sci Rep,* 9**,** 13859.
[220] Mustafaoglu, N., Kiziltepe, T. & Bilgicer, B. 2017. Site-specific conjugation of an antibody on a gold nanoparticle surface for one-step diagnosis of prostate specific antigen with dynamic light scattering. *Nanoscale,* 9**,** 8684-8694.
[221] Rayavarapu, R. G., Petersen, W., Ungureanu, C., Post, J. N., Van Leeuwen, T. G. & Manohar, S. 2007. Synthesis and Bioconjugation of Gold Nanoparticles as Potential Molecular Probes for Light-Based Imaging Techniques. *Int J Biomed Imaging,* 2007**,** 1-10.
[222] Liang, S., Li, C., Zhang, C., Chen, Y., Xu, L., Bao, C., Wang, X., Liu, G., Zhang, F. & Cui, D. 2015. CD44v6 Monoclonal Antibody-Conjugated Gold Nanostars for Targeted Photoacoustic Imaging and Plasmonic Photothermal Therapy of Gastric Cancer Stem-like Cells. *Theranostics,* 5**,** 970-984.

Chapter 2:

2. Luminescent iridium gold nanoparticles to target mitochondria in cancer cells

2.1 Introduction

The cellular metabolic pathways in cancer cells operate differently to those in healthy cells, thereby, providing opportunities for the development of targeted cancer therapies[1, 2]. After Nobel Prize winner Otto Warburg discovered that most of the energy in cancer cells is derived from aerobic glycolysis to fuel mitochondrial respiration, mitochondria have gained a lot of attention in the oncology field for their role in tumourigenesis[3, 4]. In cancer cells, both the structure and function of mitochondria differ from those in normal cells, making mitochondria a popular target for the development of tumor-selective theranostics[5]. More specifically, when compared to normal cells, cancer cells have distinctive differences in their mitochondrial metabolism, such as increased mitochondrial membrane potential (MMP) and higher oxidative stress, which promote malignant transformation. These differences provide opportunities for cancer specific mitochondrial targeting that can result to an optimal therapeutic effect through eliminating off-target toxicity[6].

Besides their critical role in generating cellular energy, mitochondria are considered as the major site of reactive oxygen species (ROS) production[7]. The basal ROS levels in cancer cells are significantly higher than the ones in normal cells due to increased metabolism and mitochondrial dysfunction[8]. As a result of their high intracellular basal ROS levels, cancer cells exhibit high antioxidant capacity, which allows them to protect cellular proliferation and maintain tumor promoting signaling[9, 1]. Even though elevated ROS levels are essential for the development and survival of cancer cells, excessive levels of ROS can promote cell death (Figure 2-1). Therefore, the use of exogenous ROS inducers to elevate intracellular ROS levels in cancer cells to toxic levels can potentiate a favorable therapeutic approach, through targeting cancer cells while sparing normal cells[10].

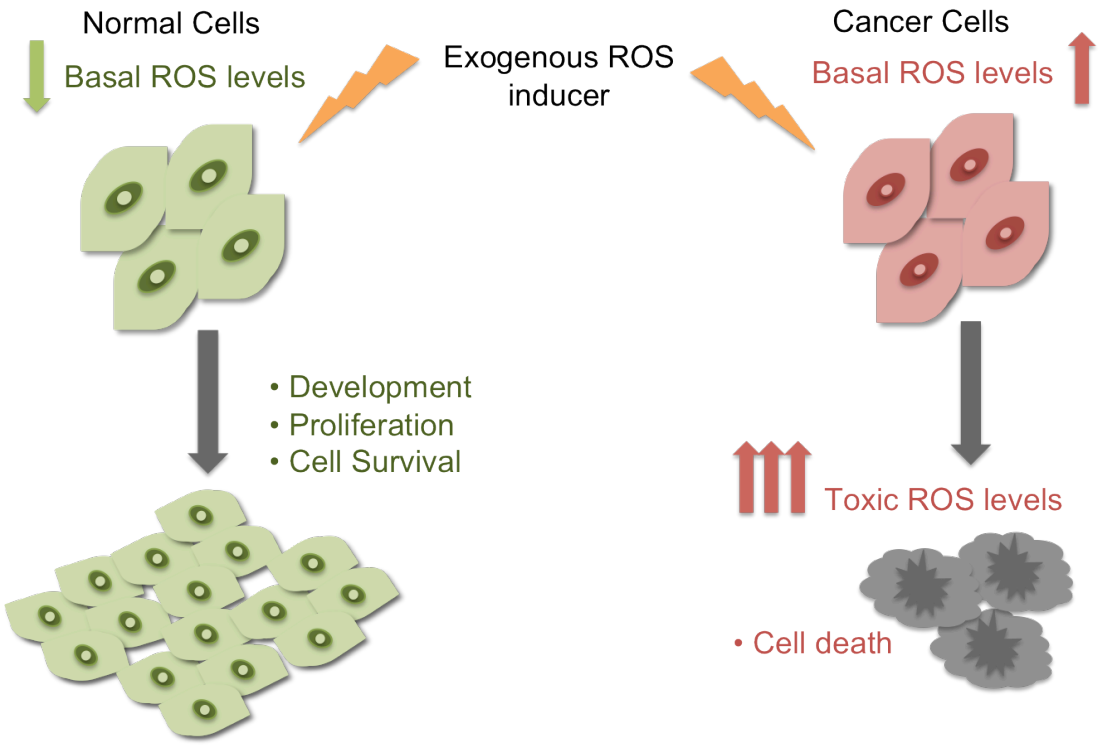


Figure 2-1. Cancer cells have higher intracellular basal ROS levels than normal cells. Increase of ROS levels via an exogenous ROS inducer promotes cellular development, proliferation and cell survival in normal cells, while in cancer cells it elevates ROS to toxic levels, leading to cell death.

There is a growing interest in the development of highly emissive multifunctional theranostic complexes to target mitochondria, which can also act as imaging agents to monitor changes in the physiological status of mitochondria upon targeting[11]. Recently, various transition metal-based complexes have gained considerable attention in the field as mitochondrial agents, both for imaging and targeting purposes[12-14]. When compared to conventional organic labels, luminescent transition metal complexes offer advantageous photophysical properties, such as high photostability, large Stokes shifts and long-lived lifetimes, which can provide enhanced detection sensitivity in imaging applications, as the short-lived auto-fluorescence signal in cancer cells can be easily gated out[15]. Besides their favorable luminescence properties, transition metal complexes can be easily modified through altering the type of ligand attached to the metal core, in order to achieve highly efficient subcellular localization in different organelles[16-19] (Figure 2-2).

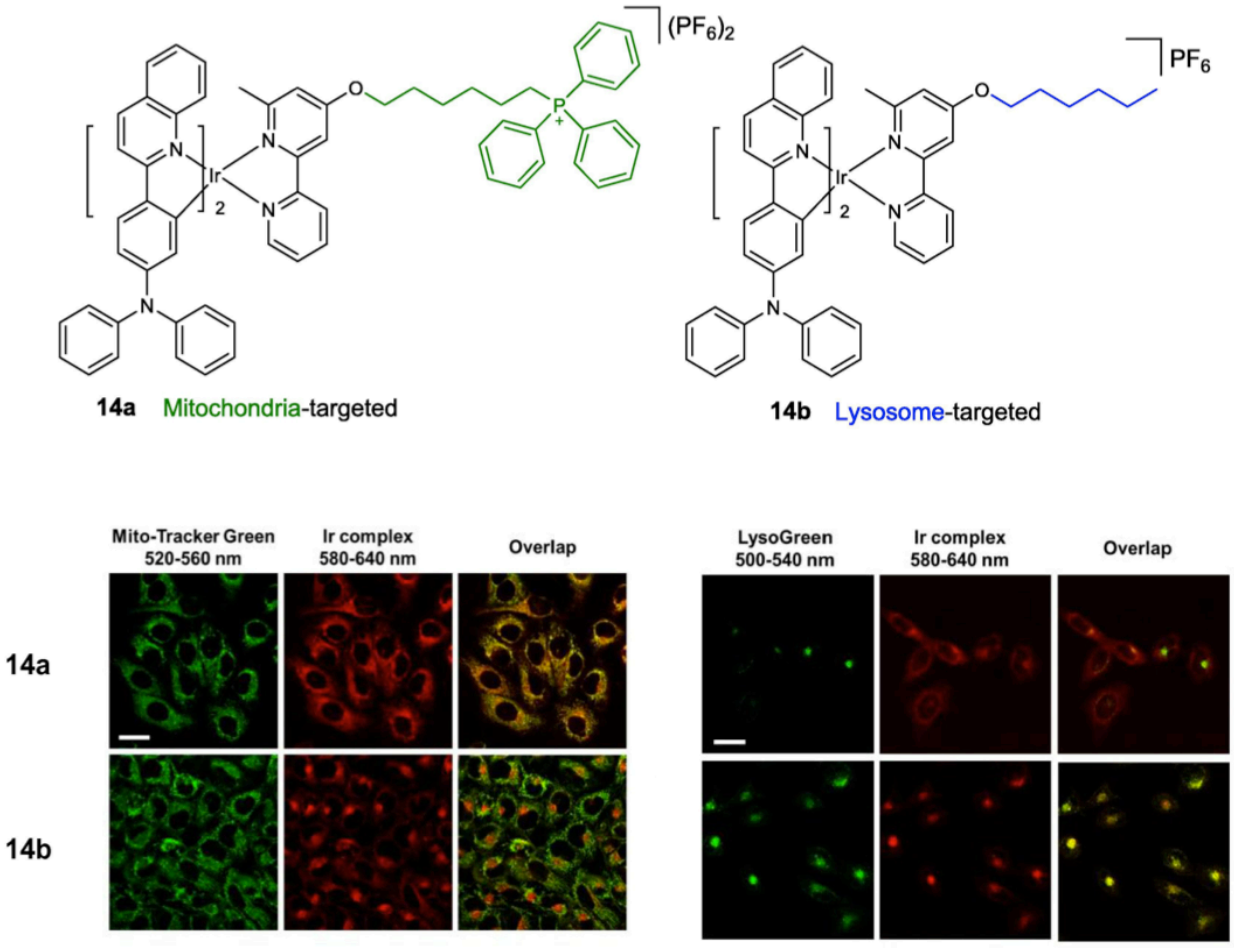


Figure 2-2. Confocal microscopy images of HeLa cells showing that subcellular localization of cyclometalated iridium(iii) complexes can be easily controlled through the introduction of different ligands. Incorporation of $(C_6H_5)_3P$ group in complex 14a using an alkyl chain promoted accumulation of the iridium complex in mitochondria, whereas complex 14b, containing only an alkyl group, was found to localize within lysosomes. (*Figure adapted from Zamora et al. 2018[19], Copyright © 2018, with permission from Elsevier*)

The characteristic photophysical properties of cyclometalated iridium complexes, along with their enhanced cell permeability, make them popular biological reagents for various applications in biomedical research[20, 21]. Iridium(III) complexes have been widely investigated as luminescent probes for cellular imaging applications, due to their distinctive luminescence signal and previous success in imaging different cell organelles including cytoplasm, nucleus, mitochondria, golgi apparatus and lysosomes[22-26].

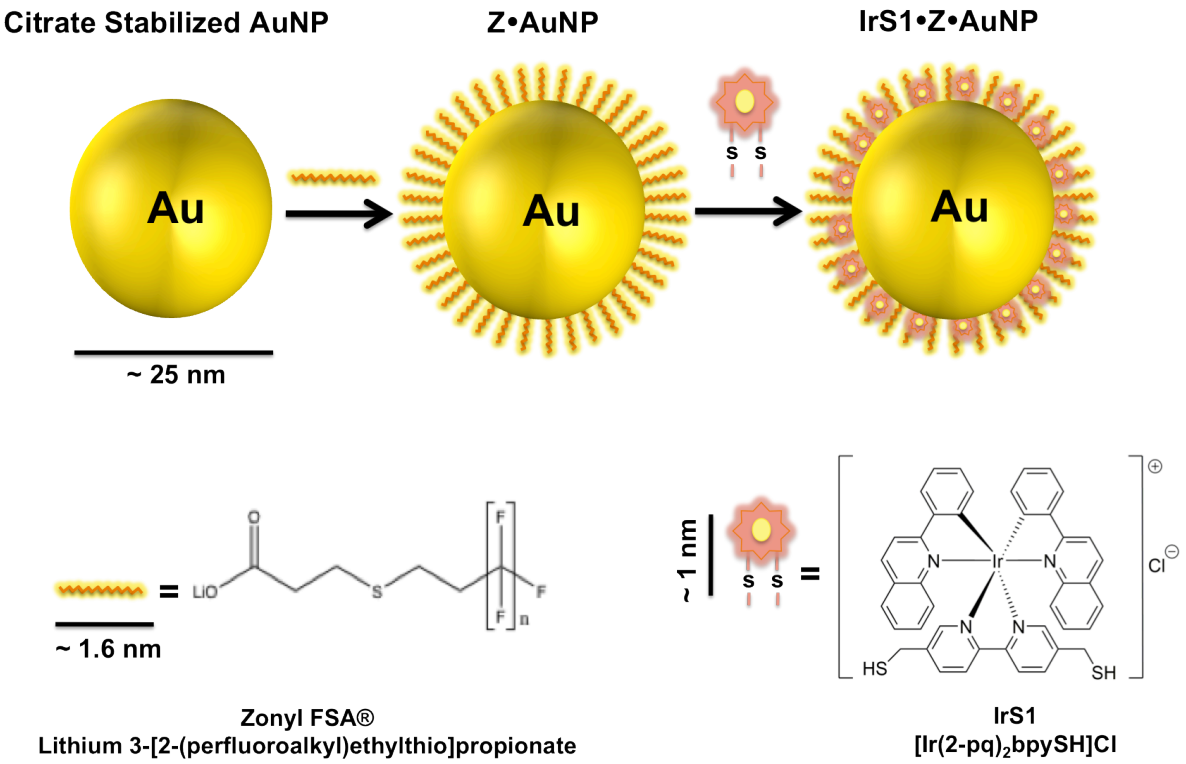
Even though luminescent metal complexes can be tuned to guide subcellular localization, their use as theranostic agents in a wide range of biomedical applications is often compromised by the high cellular toxicity they exhibit due to imprecise cellular localization[27]. However, recent advances in the nanotechnology field offer countless opportunities for the development of cancer specific nanoprobes and indicate a promising approach to overcome the aforementioned challenges[28, 29]. The use of nanocarriers to deliver targeting moieties in tumor cells enhances drastically cellular bioavailability, as it allows the agents to remain for a longer period of time at the intracellular target site. This aids in maximizing the therapeutic efficacy through the localized delivery of high administrating doses, which are highly cytotoxic when delivered alone[27, 30]. The delivery of targeting agents to mitochondria using nanovectors has been previously reported to prevent tumor recurrence, as drugs that are locally delivered to mitochondria are harder to efflux when compared to drugs randomly delivered to the cytoplasm[31]. Therefore, there is currently a growing need for developing multifunctional nanoprobes that can be used for targeted intracellular delivery, in order to improve bioavailability and overcome limitations of conventional targeting and imaging agents.

Gold nanoparticles (AuNPs) are considered as ideal nanovectors in the nanotechonolgy field, due to their unique optical properties and multifunctionality, which allows incorporation of more than one type of agents to achieve efficient localized delivery, for imaging and targeting cancer cells at the same time[32]. What is more, the large surface area offered by AuNPs allows the delivery of high concentrations of theranostic agents to the target site, which aids in enhancing detection sensitivity and therapeutic efficacy, while eliminating off-target cytoxicity[33, 34]. Also, due to their high electron density, AuNPs enable improved spatial resolution in detection and allow multimodal imaging microscopy to be used[27, 30, 33, 35]. The ease of synthesis and the size tenability of AuNPs are considered beneficial for their use as multimodal nano-sized biomaterials, as AuNPs of 25 nm or larger in size can be detected in the intracellular environment using reflectance microscopy as single, non-aggregated particles within the diffraction limit of the microscope[36-38].

Previously published studies have reported that the use of AuNPs to deliver transition metal complexes to cancer cells is highly advantageous, due to the combined favorable optical properties of the metal complex and the gold scaffold[36, 37, 39, 40]. The attachment of luminescent metal complexes to AuNPs, allows the attractive luminescent properties of the complexes to be translated onto the gold nanoprobes[36, 37, 41, 38]. Moreover, through conjugating hundreds to thousands of metal complexes to the gold surface, a strong characteristic luminescent signal can be obtained, offering high detection sensitivity both for *in vitro* and *in vivo* imaging. The luminescent signal from the metal complex can be easily detected using confocal luminescence microscopy, while scattering from the gold within an intracellular environment can be imaged using reflectance microscopy[36, 37, 39, 40]. What is more, the attachment of metal complexes to the surface of AuNPs improves radically the photostability and long half-life of the complexes in the intracellular space, as it has been formerly reported that luminescent AuNPs were able to be detected in cancer cells even three days subsequent to the chase experiment[36].

The favorable luminescent properties of iridium(III) complexes and their ability to be modified in order to achieve efficient subcellular localization, have led to the development of various complexes for targeting mitochondria in cancer cells. However, to date, the imprecise localization and high toxicity associated with the use of such complexes has hindered their successful use as theranostic agents. Hence, there is currently a growing need for the development of multifunctional nanoprobes to efficiently deliver luminescent complexes to mitochondria, both for imaging and targeting purposes.

Therefore, in this chapter, novel, iridium functionalized AuNPs are introduced, for imaging and selectively targeting mitochondria in malignant cells. More specifically, a cyclometalated iridium(iii) complex was attached to the surface of surfactant coated AuNPs, in order to promote efficient cellular uptake and high accumulation of the luminescent nanoparticles in cancer cells (Scheme 2-1).



Scheme 2-1. Schematic of coating AuNPs with zonyl fluorosurfactant and the iridium(III) complex, IrS1.

For the purposes of this study, AuNPs of 25 nm in diameter were used, as according to literature, the use of functionalized nanoparticles of sizes below 60 nm demonstrate improved cellular uptake[42, 43]. Also, nanomaterials that are smaller than 15 nm in size, have been previously reported to exocytose easily and efflux from the cells, thereby, reducing the bioavailability of the targeting agent within the intracellular environment[43-45]. Photophysical characterization of both the iridium complex and the modified AuNPs was performed, indicating that upon conjugation to the gold surface the complex retains its characteristic luminescence properties. The cellular uptake efficacy of the iridium functionalized nanoparticles in cancer cells was evaluated using fluorescence-activated cell sorting (FACS) analysis, confocal microscopy, transmission electron microscopy (TEM) and photophysical studies. The localization of the iridium complex and the luminescent AuNPs in the mitochondria in cancer cells was evaluated by inductively

coupled plasma mass spectrometry (ICP-MS), confocal microscopy and TEM. Finally, the ability of the iridium coated AuNPs developed in this chapter to selectively target mitochondria in cancer cells was evaluated via monitoring of the intracellular ROS levels in tumor and normal cells. The efficient accumulation of the iridium functionalized nanoparticles in mitochondria and their preference for targeting cancer cells over normal cells present a promising nanoparticle-based system for cancer specific theranostic applications in the nanomedicine field.

2.2 Chapter outline

In this chapter, the development of novel, luminescent gold nanoparticles is presented in the presence of a cyclometalated iridium(III) complex to selectively target mitochondria in cancer cells. The photophysical properties of both the luminescent complex and the functionalized nanoparticles are outlined. Upon conjugation of the luminescent iridium complex to the gold surface, the complex retains its characteristic luminescence properties. The iridium complex absorbs light in the visible region, between 400 and 450 nm, and displays a strong emission with a λ_{max} at 580 nm, indicating the appropriateness of the functionalized AuNPs for use in cellular uptake studies and by FACS and confocal luminescence microscopy. Subsequent to treating cancer cells with the luminescent nanoparticles, the characteristic emission and luminescence lifetime of the iridium complex were detectable within the intracellular environment. An increase in the lifetime of the iridium complex was detected in the treated cells, which was assigned to interactions between the complex and intracellular proteins. The cytotoxicity of the iridium complex and the iridium coated AuNPs, both in cancer and normal cells, was evaluated using the MTT assay, while cellular uptake was quantified by ICP-MS analysis. The cellular uptake of the luminescent nanoparticles in cancer cells was further evaluated using FACS and luminescence imaging and compared to the uptake of the iridium complex in solution. Live cell imaging performed by confocal luminescence microscopy in cancer cells after treatment with the functionalized AuNPs revealed the characteristic signal of the iridium complex in mitochondrial structures. Subcellular localization of the iridium nanoparticles in cancer cells was further investigated through TEM imaging and ICP-MS analysis, with a high number of gold nanoparticles being detected in the mitochondria. Finally, when compared to normal cells, the luminescent nanoparticles induced higher elevation of ROS levels in cancer cells, potentiating a novel therapeutic approach for cancer specific therapy.

2.3 Results and Discussion

2.3.1 Synthesis and Characterization of AuNP25

Water-soluble, monodisperse AuNPs of 25 nm in size were synthesized using an adapted protocol by the Pikramenou group, which is based on an improved method by Turkevich et al.[46, 47] and a previously published protocol by Ziegler et al.[48]. For the synthesis of AuNP25, AuNPs of 13 nm in size (AuNP13) were initially prepared through citrate reduction, and were then grown to produce 25 nm monodisperse nanoparticles, AuNP25, stabilized with citrate anions. After synthesis, the AuNP25 were fully characterized by dynamic light scattering (DLS), zeta potential (ζ), transmission electron microscopy (TEM) and surface plasmon resonance (SPR) (Figure 2-3).

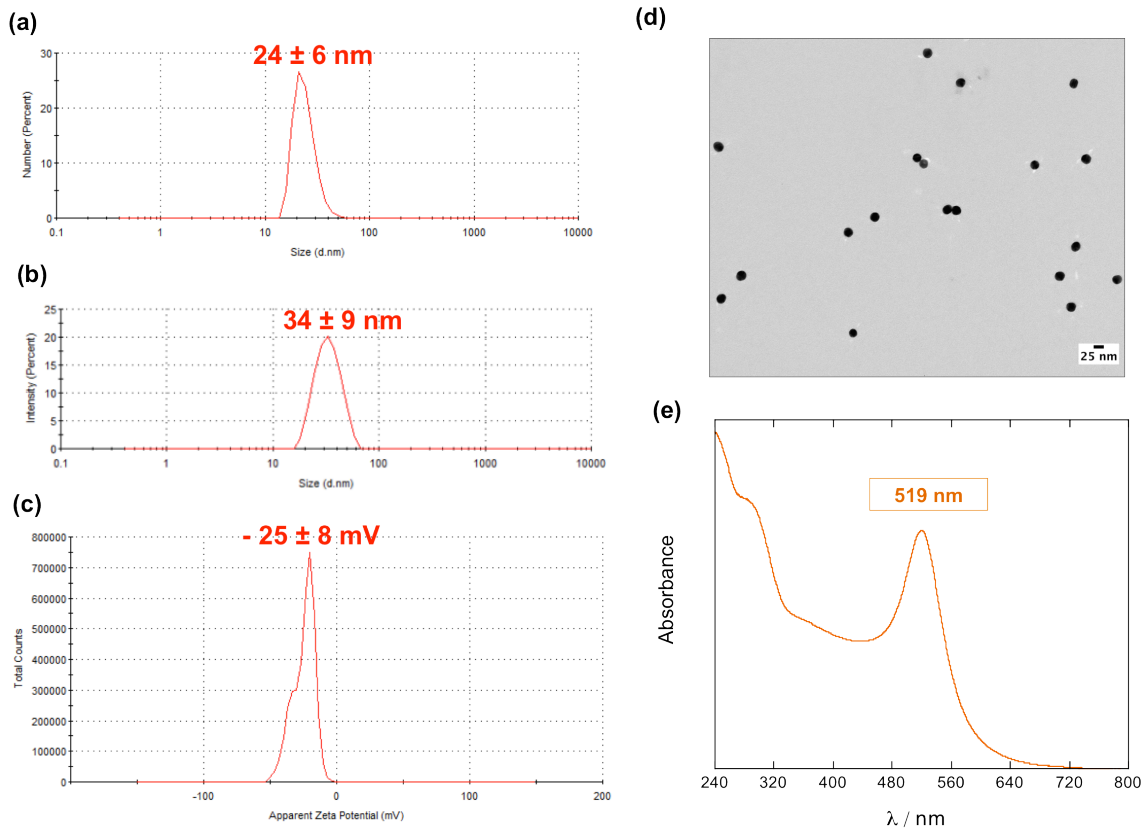


Figure 2-3. Characterization of AuNP25 by DLS, TEM and SPR. (a) DLS number distribution of AuNP25. (b) DLS intensity distribution of AuNP25. (c) Zeta potential distribution of AuNP25. (d) TEM image displaying the spherical nature of AuNP25 and a narrow size distribution (Scale bar= 25 nm). (e) UV-Vis absorption spectrum of AuNP25 in water. The λ_{max} of the SPR band is 519 nm.

The hydrodynamic diameter of AuNP25 was measured by DLS and number and intensity distribution analysis suggested sizes of 24 ± 6 and 34 ± 9 nm, respectively (PDI = 0.055) (DLS data are summarized in Table 2-1). Zeta potential measurements revealed that AuNP25 are highly stable with an average surface charge of - 25 ± 8 mV, which is attributed to the presence of the negatively charged citrate ions on the gold surface[49]. The size and high monodispersity of AuNP25 were further confirmed by TEM, as imaging analysis revealed uniformly sized nanoparticles with an average diameter of about 25 nm (n=20). AuNP25 in water demonstrated a characteristic SPR band with a λ_{max}, at 519 nm. The fact that both the size of the nanoparticles and the characteristic SPR peak obsrved agree with previously published data by the Pikramenou group, confirms the reliability and consistency of the synthesis method used for producing monodisperse AuNPs of 25 nm size[37].

2.3.2 Synthesis and Characterization of IrS1

The luminescent complex IrS1 used in this study was synthesized based on modified protocols previously published by Slinker et al.[50] and Bertoncello et al.[51] by Tasha Chauhan and Sarah Akponasa (School of Chemistry, University of Birmingham). The synthesis and characterization of the iridium complex are described in Appendix A (Appendix A, Scheme A-5 and Figure A-2).

2.3.3 Photophysical Characterization of IrS1

Photophysical characterization of the IrS1 complex in water displayed absorption within the UV-Vis region, with intense high-energy absorption bands at 250-280 nm, which are assigned to ligand-centred (LC) based transitions attributed to the spin-allowed π-π* transitions from the coordinating ligands. The luminescent complex also showed absorption bands at 300-350 nm, extending to weaker lower-energy bands between 400 and 450 nm that according to previously published assignments are attributed to singlet metal-to-ligand charge transfers, ^{1}MLCT[52-57].

The molar extinction coefficient (ε) of IrS1 was calculated both in water and in methanol. The LC molar absorptivity of the luminescent complex at 260 nm in water and in methanol is approximately 14 800 M^{-1} cm^{-1} and 18 800 M^{-1} cm^{-1}, repectvely. The MLCT molar absorptivity at 315nm and 435 nm in water is about 8 300 and 1 400 M^{-1} cm^{-1}, while in methanol is 11 000 and 1 800 M^{-1} cm^{-1}, respectively (Figure 2-4). Although the molar absorptivity of a complex is highly dependent on the solvent and the presence of the different ligands, the ε values calculated for the IrS1 complex were in agreement with literature values of similar cyclometalated iridium(III) complexes[58-61].

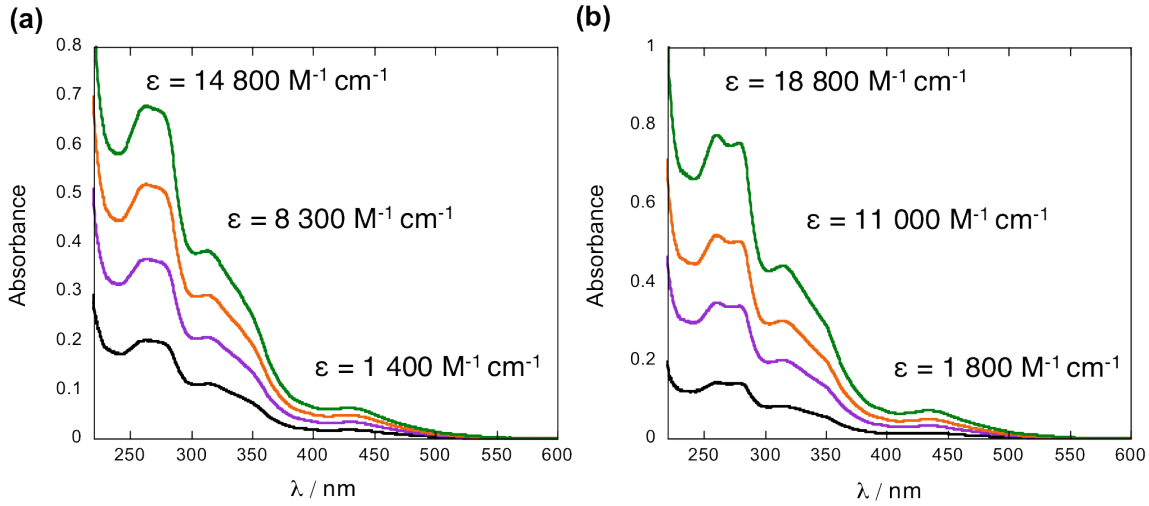


Figure 2-4. UV-Vis absorption spectra of IrS1 at concentrations between 10 to 40μM. (a) Molar extinction coefficient (ε) of the IrS1 complex in water at λ= 260 nm - ε=14 800 M^{-1} cm^{-1}, λ= 315 nm - ε= 8 300 M^{-1} cm^{-1} and at λ= 435 nm - ε= 1 400 M^{-1} cm^{-1}. (b) Molar extinction coefficient (ε) of the IrS1 complex in methanol, at λ= 260 nm - ε= 18 800 M^{-1} cm^{-1}, at λ= 315 nm - ε= 11 000 M^{-1} cm^{-1} and at λ= 435 nm - ε= 1 800 M^{-1} cm^{-1}.

The excitation profile of the IrS1 complex in water was consistent with the characteristic absorption profile observed in the UV-Vis region (Figure 2-5). Upon excitation of IrS1 at 350, 405 and 458 nm, a broad emission peak with λ_{max} at 580 nm is displayed, which is attributed to contributions from ^{3}MLCT and ^{3}LLCT transitions[50, 52, 53, 57, 62-64]. The excitation spectrum was corrected for lamp instrument response. The strong emission peak observed upon excitation at different wavelengths within the region of 400-480 nm,

suggests the appropriateness of the IrS1 complex for use in cellular uptake studies by FACS and confocal luminescence microscopy.

Luminescence lifetime measurements revealed that the lifetime of the IrS1 complex using two-component analysis is 74 ns (a_1=10%) and 471 ns (a_2=90%) in water and 74 ns (a_1=10%) and 459 ns (a_2=90%) in phosphate-buffered saline (PBS) (Appendix A – Figure A-3). These data are in agreement with previously reported luminescence lifetimes of iridium complexes with a similar chemical structure[65-67].

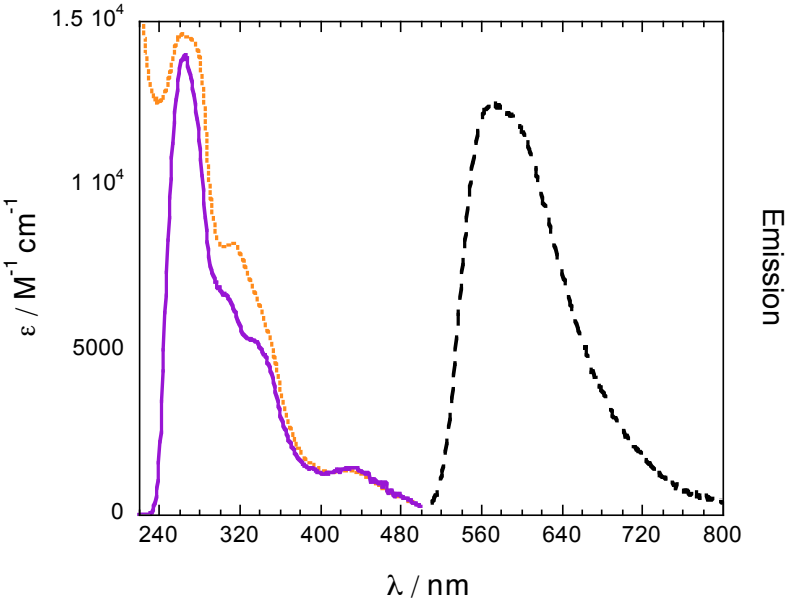


Figure 2-5. Phtophysical characterisation of IrS1 in water. UV-Vis absorption spectrum (dotted line) of 30 µM IrS1 in water. Excitation spectrum (solid line) λ_{em} = 580 nm and emission spectrum (dashed line) of 30 µM IrS1 in water λ_{exc} = 350, 405 and 458 nm.

2.3.4 Preparation of IrS1·Z·AuNP25 and characterization

Prior to conjugating the luminescent IrS1 complex on AuNPs, a fluorinated surfactant, Zonyl FSA, was used in order to stabilize the gold surface and preclude nanoparticle aggregation that can arise from directly substituting the negatively charged citrate ions found on the nanoparticle surface with positively charged metals [36, 37, 41]. The zonyl coated AuNPs were purified by centrifugation to produce Z·AuNP25. The surfactant coating on the surface of AuNP25 after purification produced a 1 nm shift in the SPR band (λ_{max}= 520 nm) and an increase in the intensity distribution of the nanoparticles as measured by DLS (DLS data are summarized in Table 2-1).

The zeta potential of the surfactant coated AuNP25 was measured to be - 49 ± 8 mV. When compared to AuNP25, the zonyl functionalized nanoparticles have a more electronegative zeta potential, which is attributed to the enhanced stability provided by the non-ionic surfactant on the surface of the negatively charged citrate AuNPs[41].

A stock solution of 1.13 mM of the IrS1 complex was prepared in methanol and added in 2 μl aliquots into an aqueous solution of Z·AuNP25. In order to confirm the attachment of the luminescent complex to the gold surface subsequent to each addition, the shift in the SPR band of the nanoparticles was monitored within the visible region (Figure 2-6). The red shift in the SPR band allowed the maximum concentration of the IrS1 complex that can be conjugated to the gold surface without causing nanoparticle aggregation to be determined. The attachment of 20 μM of IrS1 to Z·AuNP25 resulted to a further 5 nm shift in the SPR band of the nanoparticles, as λ_{max} shifted from 520 to 525 nm. The IrS1 functionalized AuNPs were then purified through size exclusion chromatography, using Sephadex G-25, in order to remove any excess, unbound molecular complex and obtain purified IrS1·Z·AuNP25. Subsequent to purification of IrS1·Z·AuNP25, the λ_{max} of the SPR band remained the same, indicating that the iridium coating on the gold surface was still present and unaltered, after exclusion of the excess molecular complex (Figure 2-7).

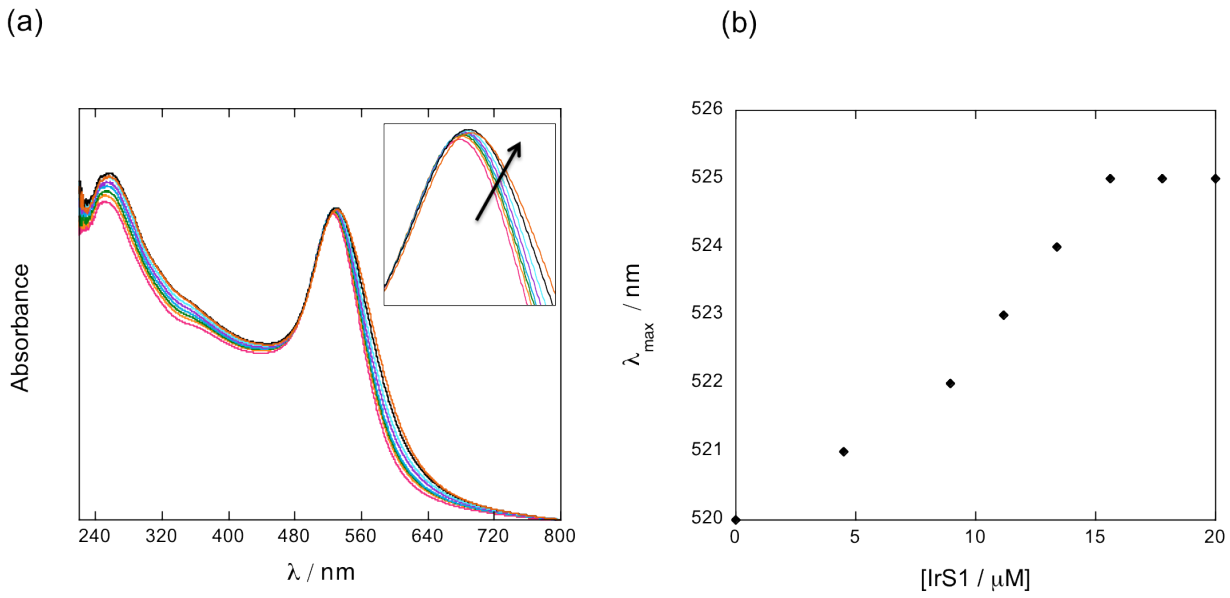


Figure 2-6. **(Left) UV-Vis titration of 1.13 mM IrS1 into 2 nM Z·AuNP25 in water. (Right) The λ_{max} of the SPR band versus the concentration of IrS1 complex added.**

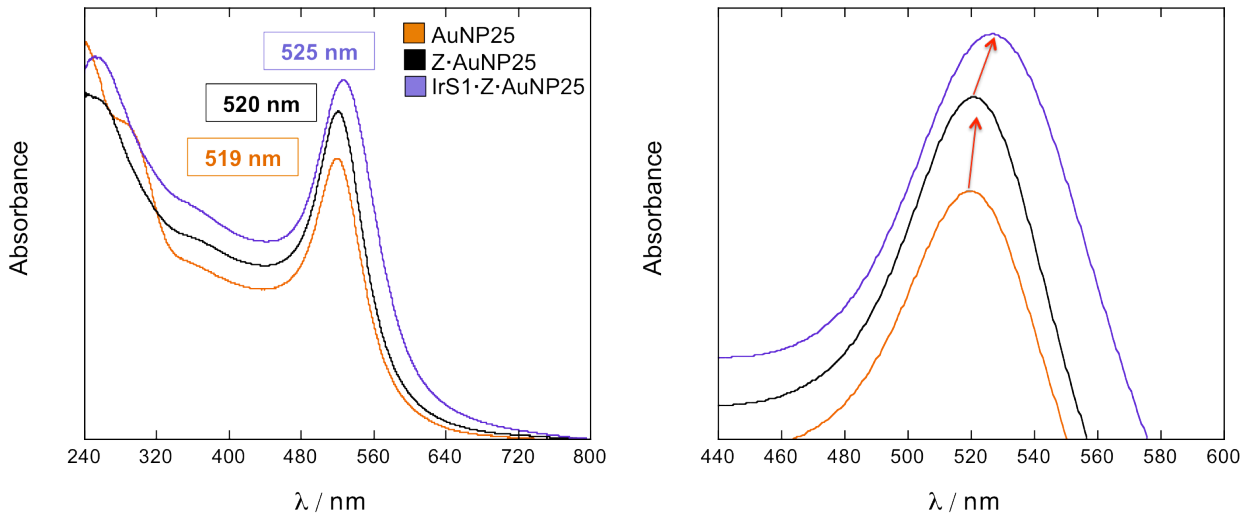


Figure 2-7. **(Left) UV-Vis absorption spectra of AuNP25, Z·AuNP25 and IrS1·Z·AuNP25 after purification. (Right) Expanded region of absorption spectra showing the shift in the SPR band upon coating with the zonyl surfactant and the IrS1 complex.**

The IrS1 functionalized AuNPs were fully characterized prior to proceeding with experimental studies in cells. DLS measurements did not indicate an increase in the number distribution of IrS1·Z·AuNP25 when compared to Z·AuNP25, which is consistent with previously published data by our group (DLS data are summarized in Table 2-1)[37, 41]. However, the conjugation of the IrS1 complex to Z·AuNP25 produced an evident increase in the DLS intensity distribution, while maintaining a low PDI, confirming the presence of the luminescent probe on the gold surface and the high monodispersity of the iridium functionalized nanoparticles (Figure 2-8).

Zeta potential measurements suggested that IrS1·Z·AuNP25 are highly stable with an average surface charge of - 42 ± 6 mV. When compared to the zeta potential of Z·AuNP25, the iridium, coated AuNPs displayed a slightly less electronegative surface charge, which is more likely attributed to the attachment of the positively charged IrS1 complex to the gold surface[41] (Figure 2-8). The size and monodispersity of both Z·AuNP25 and IrS1·Z·AuNP25 were further confirmed though analysis of TEM images, showing a uniform distribution of spherical nanoparticles with an average diameter close to 25 nm (n=20) (Figure 2-9).

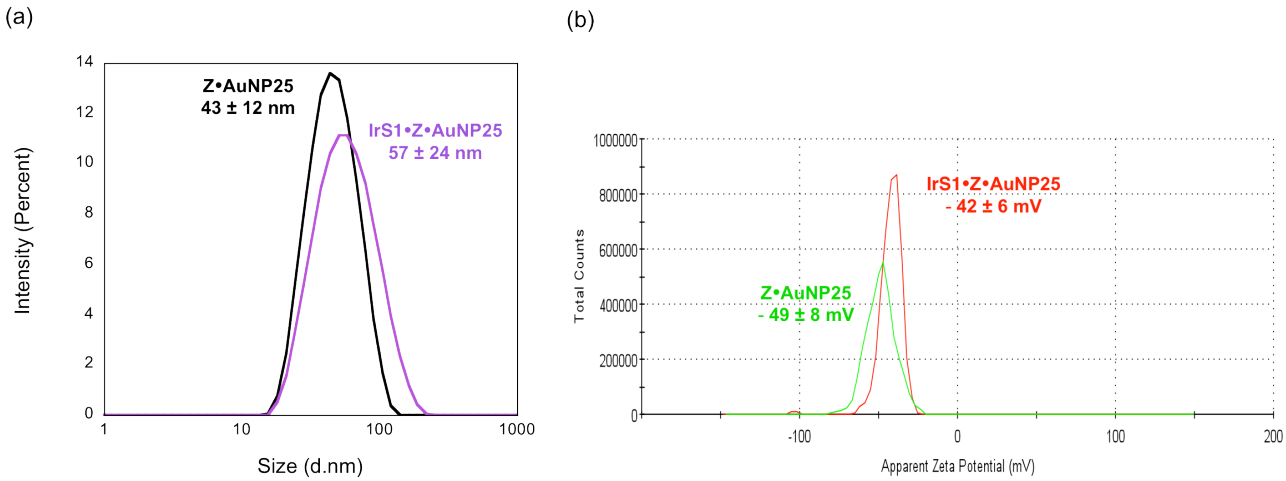


Figure 2-8. DLS size and zeta potential distributions of Z·AuNP25 and IrS1·Z·AuNP25 in water. (a) DLS intensity distributions of Z·AuNP25 and IrS1·Z·AuNP25. (b) Zeta potential distributions of Z·AuNP25 and IrS1·Z·AuNP25.

	Size by Number / nm	Size by Intensity / nm	ζ-potential (mV)	PDI
AuNP25	24 ± 6	34 ± 9	- 25 ± 8	0.055
Z•AuNP25	28 ± 7	43 ± 12	- 49 ± 8	0.085
IrS1•Z•AuNP25	28 ± 8	57 ± 24	- 42 ± 6	0.170

Table 2-1. DLS for AuNP25, Z·AuNP25 and IrS1·Z·AuNP25 in water. Results indicate polydispersity index (PDI), sizes by number and intensity (nm) and zeta potential data.

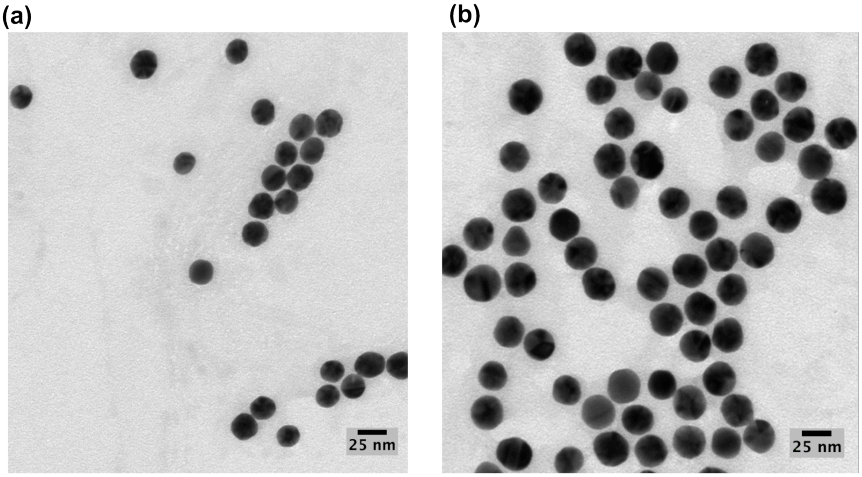


Figure 2-9. TEM images displaying the spherical nature and narrow size distribution of (a) Z·AuNP25 and (b) IrS1·Z·AuNP25 (Scale bar=25 nm).

Elemental composition analysis of the luminescent nanoparticles was carried out by ICP-MS suggested a coating of about 2 500 IrS1 complexes per AuNP25 (Appendix D-2). Similarly to IrS1, photophysical characterization of IrS1·Z·AuNP25 was performed, in order to evaluate the luminescent properties of the complex when attached to the surface of the surfactant coated AuNPs. Upon excitation at 350, 405 and 458 nm, the iridium coated nanoparticles were emissive with a λ_{max} at 585 nm, demonstrating a 5 nm red shift from the λ_{max} of the IrS1 complex in solution (Figure 2-10). The red shift observed in the emission is more likely attributed to the pressence of the fluorinated surfactant and the changes in the surrounding environment of the complex, introduced by its conjugation to the gold surface[37, 68]. The excitation spectrum of IrS1·Z·AuNP25 displayed the

characteristic SPR bands of the iridium complex in solution, which are responsible for the emission observed, confirming that the complex retains its photophysical properties when attached to the surface of the surfactant coated nanoparticles (Figure 2-10).

The effect of the surfactant on the luminescent properties of the IrS1 complex was also evident through the changes in the luminescent lifetime of the IrS1 functionalized AuNPs. The luminescence lifetime of IrS1·Z·AuNP25 using two-component analysis is 64 ns (a_1=20%) and 384 ns (a_2=80%) (Appendix A – Figure A-4) (Luminescence lifetimes are summarized in Table 2-2). The reduction observed in the luminescent lifetime of IrS1·Z·AuNP25 when compared to the free IrS1 complex in solution is assigned to the presence of the fluorinated surfactant on the surface of the nanoparticles rather than to quenching from the AuNPs. A similar effect was observed in a previously published study by the Pikramenou group, as a 160 ns decrease in the long-lived component of a luminescent iridium complex was observed upon addition of the zonyl surfactant to an aqueous solution of the complex[37].

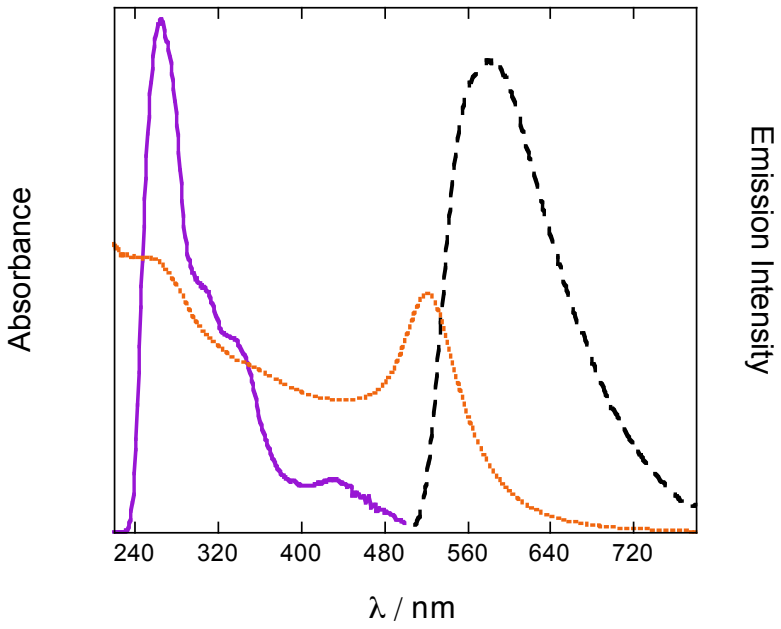


Figure 2-10. Photophysical characterisation of 2 nM IrS1·Z·AuNP25 in water. UV-Vis absorbance of IrS1·Z·AuNP25 (dotted line). Excitation spectrum, λ_{em}=585 nm (solid line) and emission spectrum of IrS1·Z·AuNP25 in water, λ_{exc}=350, 405 and 458 nm (dashed line).

2.3.5 Cytotoxicity of IrS1·Z·AuNP25 in HeLa and HEK293 cells

In order to evaluate the cytotoxicity and cellular uptake of the iridium coated AuNPs, an iridium complex without the thiol groups on the bipyridine ligand for attachment to the surface of AuNPs, Ir1, was used as the positive control (Appendix A, Scheme A-4 and Figure A-1). The Ir1 complex was synthesized and characterized by Tasha Chauhan and Sara Akponasa (School of Chemistry, University of Birmingham). The Ir1 complex was chosen over IrS1 as the positive control, as molecular probes containing thiol groups can interact with thiols present on the surface of the cells and get trapped in the phospholipid bilayer. This leads to thiol-mediated membrane trafficking, which inhibits further internalization of the complex within the intracellular space[69]. However, upon conjugation of the IrS1 complex to the gold surface the aforementioned issue is overcome, as the functionalized AuNPs enter the cells via a different uptake mechanism[44, 70, 71].

The cytotoxicity and anti-proliferative activity of the functionalized AuNP25 samples, Z·AuNP25 and IrS1·Z·AuNP25, and the molecular complexes in solution, IrS1 and Ir1, were evaluated by the MTT assay, 3-(4, 5-dimethylthiazolyl-2)-2, 5-diphenyltetrazolium-bromide. The cytotoxic effect of Z·AuNP25 and IrS1·Z·AuNP25 was evaluated at concentrations between 0.1 and 0.4 nM after treating HeLa and HEK293 cells for 24 hours (Figure 2-11). Overall, in HeLa cells, there was no significant inhibition in cell viability and proliferation activity after treatment of the cells with the AuNP5 samples. More specifically, treatment with the functionalized AuNPs at 0.1 and 0.2 nM did not produce a statistically significant reduction in cell viability, while treatment with 0.4 nM, induced a decrease in the viability of cells to about 70%. It has been previously reported that citrate nanoparticles can exhibit significantly high levels of toxicity in cells[72, 73]. However, the cytotoxic effect of nanoparticles is vastly associated with high dosing concentrations and lack of fine dispersity[74, 75]. What is more, the surface chemistry of nanoparticles, including their overall surface charge and zeta potential, can also affect critically their cytotoxicity[76, 77]. Previously published studies have reported that negatively charged gold nanoclusters and cationic spherical nanoparticles demonstrate enhanced cellular uptake and bioavailability in tumor cells, which eventually lead to high levels of toxicity[78, 79]. Therefore, the overall negative surface charge and low polydispersity of IrS1·Z·AuNP25, observed both by DLS

and TEM, along with the relatively low concentrations tested in the present study, explain the insignificant levels of toxicity observed in HeLa cells by the MTT assay.

The cytotoxic effect of the iridium complexes in solution, IrS1 and Ir1, was evaluated after treatment of the cells with concentrations between 0.5 to 3 μM for 24 hours (Figure 2-12). Treatment with the Ir1 complex induced a concentration dependant cytotoxic effect in HeLa cells, as cell viability was decreased by about 30 to 40%, with the reduction being higher with increasing concentrations of the complex.

After treating HeLa cells with 0.5 and 1 μM of the IrS1 complex, no inhibition was observed in cell viability. However, treatment of the cells with 2 and 3 μM of the IrS1 complex induced a decrease in cell viability by 20 and 35%, respectively. Cyclometalated iridium(III) complexes have been formerly reported to exhibit high cytotoxicity in cancer cells at relatively low concentrations, between 0.5 to 10 μM, with the toxicity levels being highly influenced by the structure of the complexes and their cellular uptake efficacy[25, 80-83]. The concentration dependent tocxicity of iridium complexes was further supported in the present study, as the cytotoxic effect of both Ir1 and IrS1 in HeLa cells was higher, with increasing treatment concentrations. However, the Ir1 complex displayed significantly higher cytoxicity than IrS1, which is assigned to the inefficient uptake of IrS1 by the cells, due to interactions between the thiol groups on the complex with thiols present on the cell surface membrane[69]. The difference observed in the cellular toxicity after treatment with the two iridium complexes suggests that the relatively simple structure of the Ir1 complex promotes highly efficient cellular uptake and high accumulation of the complex in the intracellular environment, inducing elevated levels of toxicity upon treatment. The optimal cellular uptake of the Ir1 complex confirms its suitability over IrS1 to be used as the positive control in the present study.

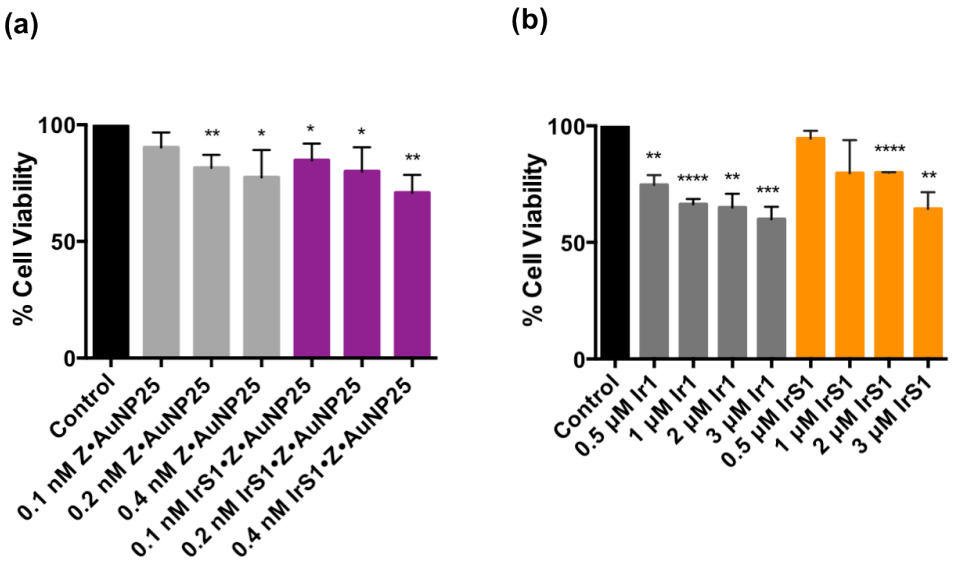


Figure 2-11. Cytotoxicity in HeLa cells determined using the MTT cell viability assay after treatment for 24 h. (a) Cytotocixity of Z·AuNP25 and IrS1·Z·AuNP25 at 0.1, 0.2 and 0.4 nM. (b) Cytotoxicity of Ir1 and IrS1 at concentrations between 0.5 to 3 µM. *P *value < 0.05, **P value < 0.01, ***P value < 0.001, ****Pvalue < 0.0001.*

It has been previously reported that several iridium complexes exhibit selective cytotoxicity for cancer over normal cells[81, 84]. The tunable properties of organometallic iridium complexes allow the attachment of ligands that can guide subcellular localization upon cellular entry in order to improve the therapeutic efficacy through eliminating off-target toxicity[24, 37, 85, 86]. Therefore, in order to determine whether the IrS1 functionalized AuNPs and the iridium complexes display selective cytotoxicity against cancer cells, the toxicity of both the nanoparticle samples and the molecular complexes was studied in normal cells under the same conditions.

After treating HEK293 cells for 24 hours, the results suggested that at the concentrations tested neither the iridium coated AuNP25 samples nor the iridium complexes in solution demonstrate any cytotoxic effects on normal cells (Figure 2-12). The selective cytotoxicity of IrS1·Z·AuNP25 and the iridium complexes observed in HeLa over HEK293 cells could be attributed to the differences in the metabolic processes and the relatively higher levels of oxidative stress in cancer cells, which can induce toxicity upon targeting[83, 87, 88]. Hence, the results provide evidence of the affinity of IrS1·Z·AuNP25 and the iridium complexes towards cancer-specific intracellular targets.

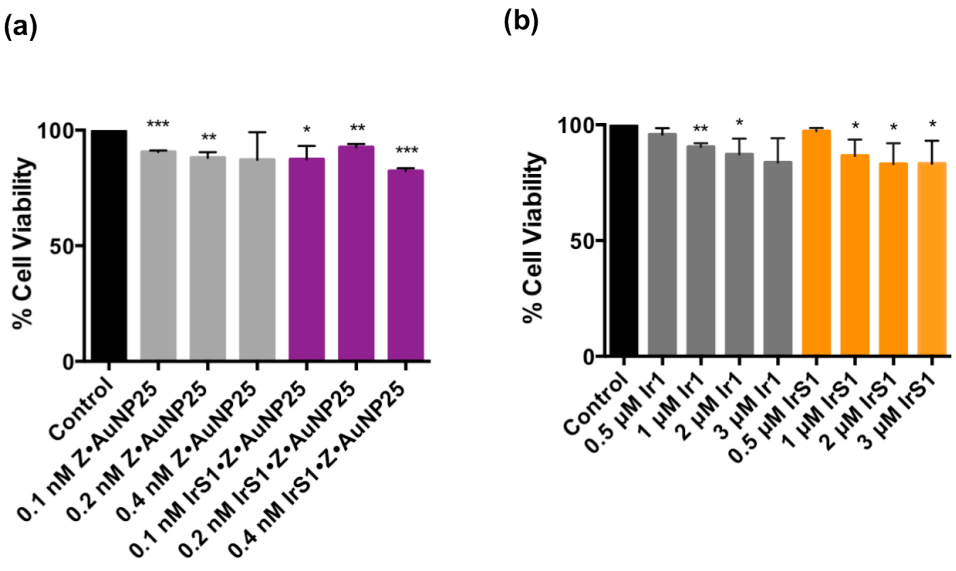


Figure 2-12. **Cytotoxicity in HEK293 cells was determined using the MTT cell viability assay after treatment for 24 h. (a) Cytotoxicity of Z·AuNP25 and IrS1·Z·AuNP25 at 0.1, 0.2 and 0.4 nM. (b) Cytotoxicity of Ir1 and IrS1 at concentrations between 0.5 to 3μM.** ***P value < 0.05, **P value < 0.01, ***P value < 0.001.***

2.3.6 Cellular uptake efficacy of IrS1·Z·AuNP25 in HeLa cells

It has been previously reported that the efficient delivery of molecular complexes in cells using nanoparticles can be challenging, due to the formation of protein corona[89-93]. Although plain AuNPs have been previously confirmed to intrude cells[94, 95], surface functionalization can alter the physicochemical properties and size of nanoparticles, having a negative impact on the endocytic mechanisms that control cellular entry[96-99]. Therefore, evaluating the cellular uptake efficacy of the IrS1 modified AuNPs is essential for determining their ability to act as a nanoparticle-based system for both imaging and targeting cancer cells. Serum proteins that are used to supplement culture media, such as Fetal Bovine Serum (FBS), can contribute vastly to the formation of protein corona. Therefore, in order to prevent alterations in the size and physiochemical properties of the IrS1 coated AuNPs upon cellular interaction, uptake studies were performed in the presence of serum-free cell culture media.

The cellular uptake efficacy of IrS1·Z·AuNP25 in HeLa cells was evaluated by FACS and histogram analysis was performed using the Qdot565 filter, violet laser with λ_{exc} at 405 nm and λ_{em} >565 nm (Figure 2-13). In order to evaluate the uptake of the iridium coated AuNPs in HeLa cells by FACS, non-luminescence citrate and surfactant coated AuNPs (AuNP25 and Z·AuNP25) were used as negative controls, while the Ir1 complex was used as the positive control, due to its optimal cellular uptake discussed earlier in this chapter. Also, the uptake of the iridium functionalized nanoparticles was compared to the uptake of the IrS1 complex in solution, aiming to interpret whether the use of AuNPs as a vehicle to deliver the luminescent complex improves its internalization within the intracellular environment.

The concentration of the iridium coated AuNPs used to evaluate uptake in HeLa cells is 0.2 nM, as no significant inhibition was observed in cell viability by MTT, hence ensuring that uptake will not be affected by toxicity induced cell lysis. The concentrations at which the IrS1 complex was tested were chosen based on elemental composition analysis of IrS1·Z·AuNP25 by ICP-MS, which determined approximately 2500 iridium complexes per AuNP25 (Concentration of IrS1 in 0.2 nM IrS1·Z·AuNP25 is 0.5 μM). The cellular uptake efficacy was evaluated through comparing the fold increase in the Mean Fluorescent Intensity (MFI) of the cells treated with the luminescent AuNPs, negative and positive controls against untreated cells (control) (Figure 2-14).

As expected, the results showed a significant increase in the fluorescence intensity of the cells treated with the Ir1 complex, indicating the highly efficient cellular uptake of the complex and further supporting the high levels of toxicity observed by the MTT assay. After treatment with the iridium coated AuNPs, a 2.5 fold increase in the MFI of the cells was observed, suggesting the successful internalization of the luminescent nanoparticles in HeLa cells.

When comparing the cellular uptake of IrS1·Z·AuNP25 to the IrS1 complex in solution, the functionalized AuNPs induced a higher increase in the MFI, suggesting the improved uptake efficacy of the complex in HeLa cells upon attachment to the gold surface. The iridium coated nanoparticles produced a higher increase in the fluorescence intensity of

the cells, even after treatment with 1 μM of the IrS1 complex in solution, which is double the concentration of the complex present on the surface of the iridium coated AuNPs.

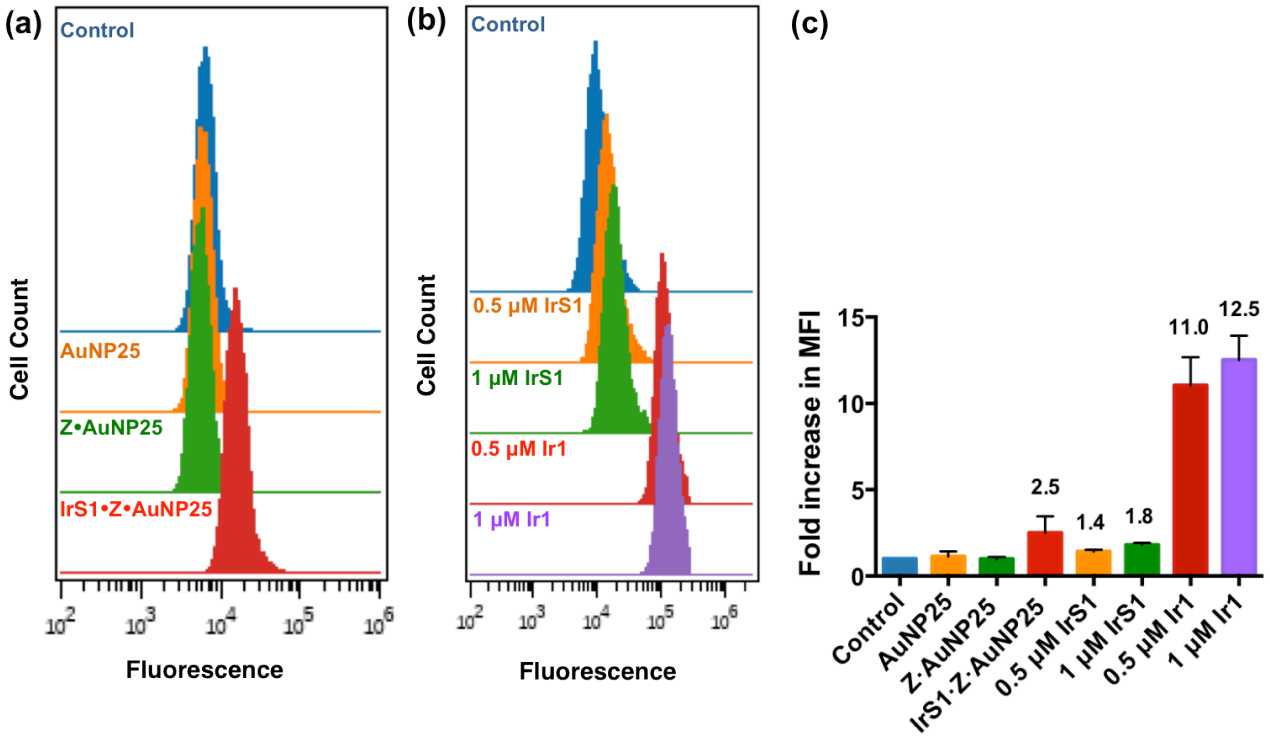


Figure 2-13. Cellular uptake efficacy in HeLa cells by FACS analysis after treatment with AuNP25 samples, IrS1 and Ir1 in serum-free cell culture media for 24 h. λ_{exc}=405 nm and λ_{em}= >565 nm. (a) Histogram analysis of cellular uptake after treatment with 0.2 nM of AuNP25, Z·AuNP25, and IrS1·Z·AuNP25 (b) Histogram analysis of the cellular uptake of IrS1 and Ir1 at 0.5 and 1 μM. (c) Fold increase in Mean Fluorescence Intensity (MFI) after treatment with 0.2 nM of AuNP25, Z·AuNP25, IrS1·Z·AuNP25, 0.5 μM and 1μM of IrS1 and Ir1. The results are mean values ± SD of three independent experiments.

Therefore, the results of the present study suggest that the use of the gold scaffold to deliver the luminescent complex in cancer cells improves drastically the cellular entry and internalization of the luminescent complex within the intracellular space. Even though the Ir1 complex, which was used as the positive control of the study, displayed significantly high cellular uptake, its high levels of toxicity imply that the complex can induce off-target toxicity upon targeting due to imprecise cellular localization[100]. Hence, the ability of the IrS1 complex to penetrate the cell membrane with high efficiency only when attached to the gold surface, provides a promising approach for improved uptake and localization in cancer cells.

2.3.7 Luminescence lifetime detection of IrS1·Z·AuNP25 in HeLa cells

The efficient cellular uptake of IrS1·Z·AuNP25 was further confirmed through detecting the luminescence properties of the iridium coated AuNPs in treated cells. Upon excitation at 405 nm, HeLa cells treated with 0.2 nM IrS1·Z·AuNP25 for 24 hours displayed the characteristic broad emission peak of the iridium coated AuNPs with a λ_{max} at 585 nm (Figure 2-14). What is more, luminescence lifetime measurements revealed that after treatment with the IrS1 functionalized AuNPs, the luminescence lifetime in the treated cells using two-component analysis is 268 ns (a_1=6%) and 1539 ns (a_2=94%) (Luminescence lifetimes are summarized in Table 2-2). The significant increase observed in the lifetime of IrS1·Z·AuNP25 in HeLa cells is more likely attributed to the interaction of the iridium complex on the gold surface with intracellular proteins. According to literature, interactions between cyclometalated iridium complexes and proteins induce enhanced luminescence and promote elongation of luminescence lifetimes[37, 68, 101].

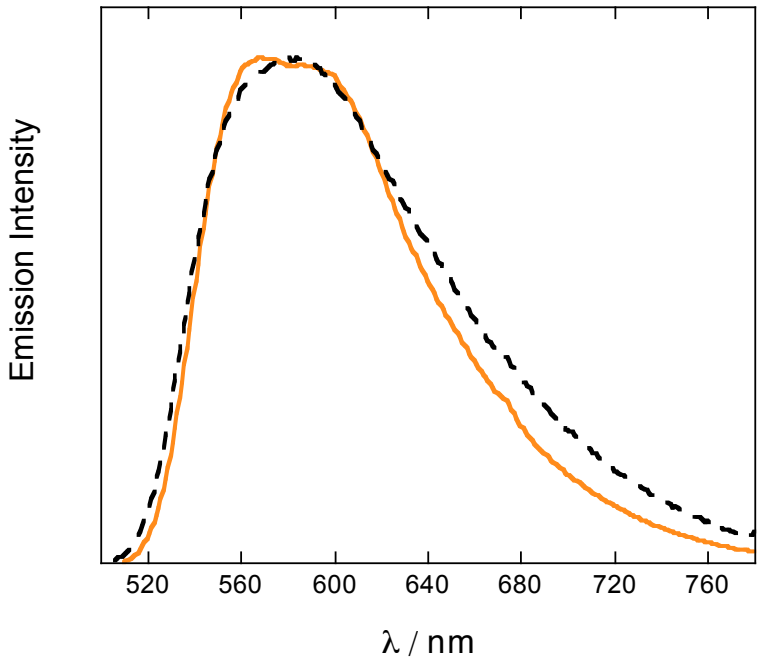


Figure 2-14. Overlay of emission spectra of IrS1·Z·AuNP25 in water (dashed line) and in HeLa cells (solid line), λ_{exc} = 350, 405 and 458 nm.

In order to further determine the efficient internalization of the iridium coated AuNPs in HeLa cells, luminescence lifetime measurements were also performed in fractionated subcellular organelles. The lifetime of the iridium coated nanoparticles in mitochondria using two-component analysis is 328 ns (a_1=11%) and 1223 ns (a_2=89%), which is consistent with the luminescence lifetime of IrS1·Z·AuNP25 in the whole cell population (Figure 2-15). The luminescence lifetime of IrS1·Z·AuNP25 in the cytosol of the treated cells is 13 ns (a_1=4%) and 1108 ns (a_2=96%), while in the nucleus is 8 ns (a_1=3%) and 982 ns (a_2=97%) (Luminescence lifetimes are summarized in Table 2-2). Even though both in the cytosol and nucleus, there is a considerable increase in the long-lived component of the IrS1 coated AuNPs, the presence of the short-lived component is not evident. The fact that the increase observed in the lifetime of IrS1·Z·AuNP25 in HeLa cells agrees with the increase observed in mitochondria, showing both an increase in the short-lived and long-lived component, could suggest the preference of the luminescent nanoparticles to localize within mitochondria and the strong interactions between the iridium complex and mitochondrial proteins. This is supported by previously published studies, which have reported a significant increase in both the emission intensity and luminescence lifetimes of cyclometalated iridium complexes that localize in mitochondria[102, 103].

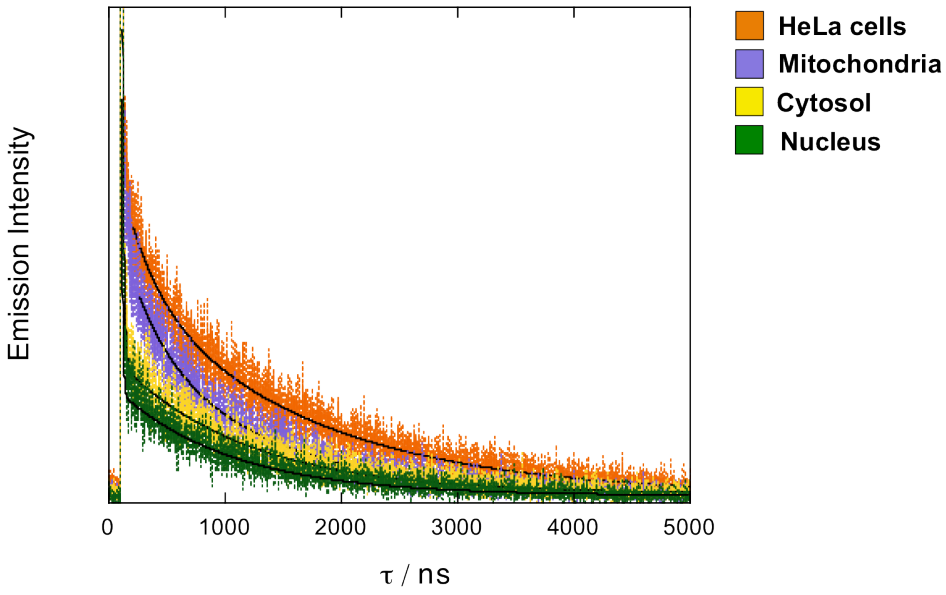


Figure 2-15. Fitted luminescence lifetime decays of IrS1·Z·AuNP25 in HeLa cells and subcellular organelles, λ_{exc}=376 nm and λ_{det}=585 nm. The luminescent lifetimes of IrS1·Z·AuNP25 in HeLa cells, mitochondria, cytosol and nucleus were fitted with a χ^2 value between 1.05 and 1.20.

As discussed earlier in this chapter, the Ir1 complex (positive control) exhibits high cytotoxicity in HeLa cells, which is more likely attributed to off-target toxicity induced by the imprecise subcellular localization of the complex in the intracellular environment. Therefore, in order to evaluate the localization of the Ir1 complex in HeLa cells, luminescence lifetime measurements were performed, both in whole cells and fractionated subcellular organelles (Figure 2-16). The luminescence lifetime of the Ir1 complex using two-component analysis is 199 ns (a_1=10%) and 646 ns (a_2=90%) in water (Appendix A – Figure A-4), while in HeLa cells is 564 ns (a_1=13%) and 1736 ns (a_2=89%) (Luminescence lifetimes summarized in Table 2-3). Similarly to the IrS1 coated AuNPs, the considerable increase in the luminescence lifetime of the Ir1 complex in HeLa cells is assigned to the high accumulation of the complex in the intracellular environment, which promotes interactions between the complex and cellular proteins. The luminescence lifetime of the Ir1 complex in mitochondria using two-component analysis is 672 ns (a_1=30%) and 1567 ns (a_2=70%), and in the cytosol is 734 ns (a_1=25%) and 1516 ns (a_2=75%). The increase in both the short-lived and long-lived component of the Ir1 complex observed in the mitochondria and cytosol is consistent with the increase observed in the whole cell population, indicating the strong interaction of the complex with mitochondrial and cytosolic proteins. In the nucleus, the long-lived component of the Ir1 complex was relatively shorter, while the short-lived component disappeared, indicating weak interaction between the complex and nuclear proteins (Luminescence lifetimes summarized in Table 2-3).

The luminescence lifetime measurements in HeLa cells indicate that neither the IrS1 coated AuNPs, nor the Ir1 complex in solution show preference for nuclear localization and interaction with nuclear proteins. The fact that IrS1·Z·AuNP25 displayed evidence for mitochondrial localization, while the Ir1 complex showed preference for localizing both in the mitochondria and cytosol, could suggest that the high toxicity of Ir1 observed in HeLa cells earlier in this chapter, is attributed to the imprecise subcellular localization of the complex, leading to off-target toxicity.

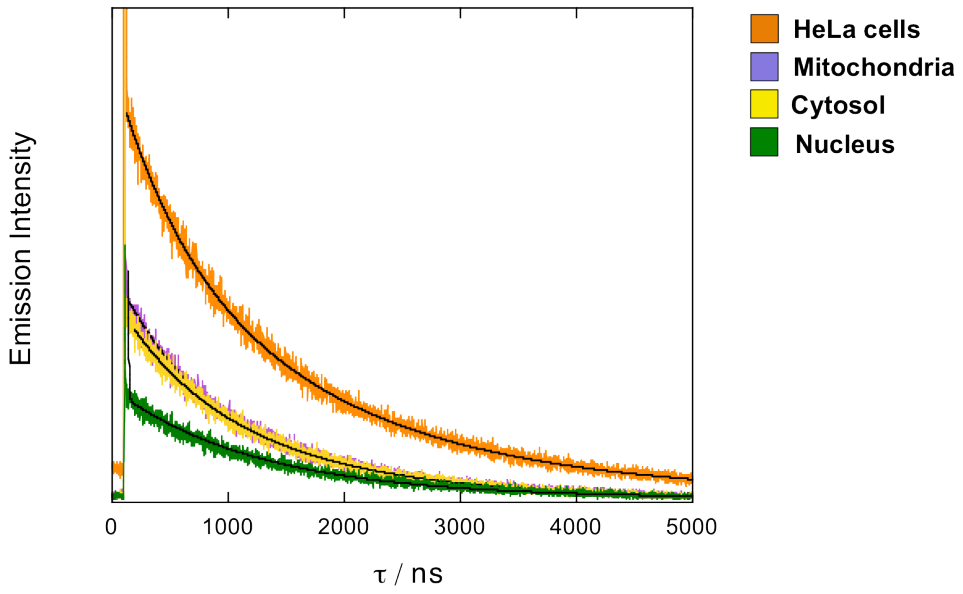


Figure 2-16. Fitted luminescence lifetime of Ir1 in HeLa cells and subcellular organelles, λ_{exc}=376 nm and λ_{det}=580 nm. The luminescent lifetimes of Ir1 in HeLa cells, mitochondria, cytosol and nucleus were fitted with a χ^2 value between 1.01 and 1.06.

IrS1•Z•AuNP25		IrS1•Z•AuNP25 + BSA		IrS1•Z•AuNP25 in HeLa cells		IrS1•Z•AuNP25 in mitochondria		IrS1•Z•AuNP25 in cytosol		IrS1•Z•AuNP25 in nucleus	
a_i (%)	τ_i (ns)	a_i (%)	τ_i (ns)	a_i (%)	τ_i (ns)	a_i (%)	τ_i (ns)	a_i (%)	τ_i (ns)	a_i (%)	τ_i (ns)
20	64	7	207	6	268	11	328	4	13	3	8
80	384	93	1503	94	1539	89	1223	96	1108	97	982

Table 2-2. Luminescence lifetimes of IrS1·Z·AuNP25 in water, HeLa cells, subcellular organelles and with BSA, along with the percentage of each component. The luminescent lifetimes were fitted with a χ^2 value between 1.05 and 1.20

Ir1		Ir1 + BSA		Ir1 in HeLa cells		Ir1 in mitochondria		Ir1 in cytosol		Ir1 in nucleus	
a_i (%)	τ_i (ns)	a_i (%)	τ_i (ns)	a_i (%)	τ_i (ns)	a_i (%)	τ_i (ns)	a_i (%)	τ_i (ns)	a_i (%)	τ_i (ns)
10	199	22	388	13	564	30	672	25	734	1	5
90	646	78	1238	87	1736	70	1567	75	1516	99	1258

Table 2-3. Luminescence lifetimes of Ir1 in water, HeLa cells, subcellular organelles and with BSA, along with the percentage of each component. The luminescent lifetimes were fitted with a χ^2 value between 1.01 and 1.06.

In order to confirm that the elongated luminescence lifetimes observed in HeLa cells are attributed to interactions with cellular proteins, lifetime measurements were carried out upon addition of the Bovine Serum Albumin (BSA) protein to the IrS1 coated AuNPs and to the Ir1 complex in solution (Luminescence lifetimes are summarized in Tables 2-2 and 2-3). The luminescence lifetime of IrS1·Z·AuNP25 after addition of BSA using two-component analysis is 207 ns (a_1=7%) and 1503 ns (a_2=93%), which agrees with the increase observed in HeLa cells after treatment with the luminescent nanoparticles. The lifetime of the Ir1 complex subsequent to addition of BSA is 388 ns (a_1=22%) and 1238 ns (a_2=78%), which is also consistent with the increase detected in HeLa cells after treatment with the complex.

The preference of the luminescence nanoaprticles for localizing in mitochondria, along with their ability to induce enhanced luminescence signal via interactions with intracellular proteins suggest that IrS1·Z·AuNP25 provide a favorable nanoparticle-based system for improved detection and selective targeting in cells.

2.3.8 Circular Dichroism (CD) of IrS1 and IrS1·Z·AuNP25

In order to further evaluate the ability of the IrS1 functionalized nanoparticles to interact with cellular proteins, circular dichroism (CD) spectroscopy was performed to monitor the conformational alterations of BSA upon addition of the IrS1 complex in solution and the IrS1 coated AuNPs. The characteristic CD spectrum of BSA exhibits one positive peak at 190 nm and two negative peaks at 209 and 222 nm, which are characteristic for proteins that have an a-helix strucutre[59, 104]. The intensity of these peaks was recorded upon the sequential addition of the IrS1 complex in solution (100 μM) and IrS1·Z·AuNP25 (2 nM) (Figure 2-18). The sequential addition of the IrS1 complex to BSA resulted to a decrease in the intensity of the positive peak and an increase in the intensity of the negative peaks, while the sequential addition of the luminescent nanoparticles resulted to an increase both in the intensity of the positive and the negative peaks. The changes detected in both the

positive and negative intensity peaks of BSA, suggest structural alterations in the features of the protein upon addition of the luminescent complex, both in solution and on the AuNPs. These changes are more likely attributed to the engagement of the IrS1 complex in strong hydrophobic and electrostatic interactions with the binding pockets of the protein[59, 105-107]. It has been previously reported that metal complexes demonstrate strong hydrophobic interactions with BSA, as the complexes are able to bind within a cavity, an active site of a sub domain of the protein, resulting to conformational changes due to unfolding of the protein[59, 108, 109].

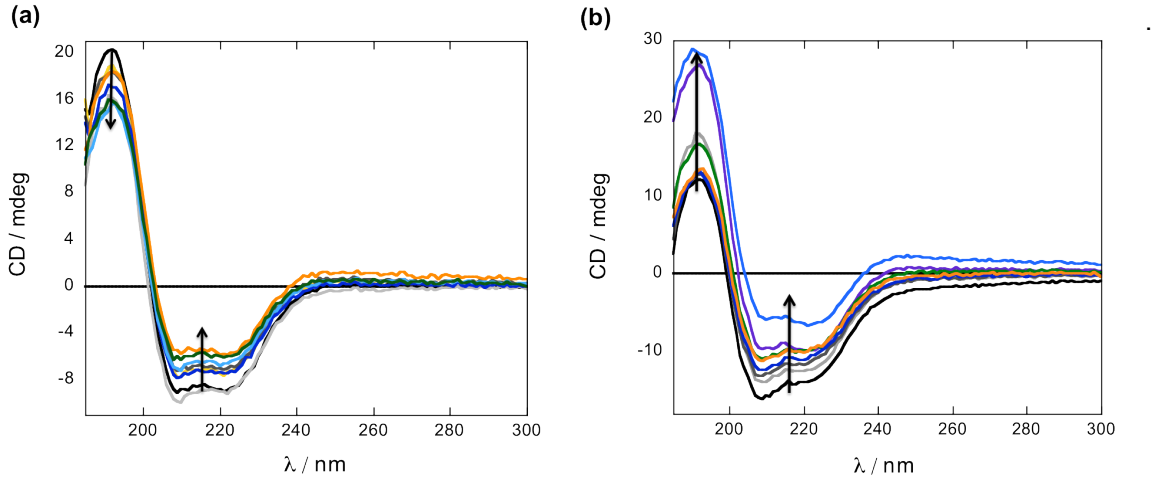


Figure 2-18. Circular dichroism spectra of BSA (0.1 μM) with sequential additions of (a) IrS1 solution (100 μM) (2.0, 4.0, 7.9, 14.6, 32.7, 53.4 and 82.6 mol equiv.) and (b) IrS1·Z·AuNP25 in water (2 nM) ($0.4x10^{-4}$, $0.8x10^{-4}$, $1.6x10^{-4}$, $2.9x10^{-4}$, $6.5x10^{-4}$, $1.1x10^{-3}$ and $1.7x10^{-3}$ mol equiv.).

The CD spectrum of BSA within the far UV region (200-260 nm) represents the secondary structural features of the protein, such as a-helix and β-pleated sheets, whereas the near UV region (250 to 320 nm) of the spectrum reflects the tertiary structure of the protein[110, 111]. Hence, the increase observed in the intensity of the negative peaks of the CD spectra, between 209 and 222 nm, suggests that upon binding of the luminescent irS1 complex to BSA conformational changes are induced in the secondary structure of the protein. In the CD spectra of BSA, no changes where observed in the near UV region, indicating that the tertiary structure of the protein is not affected upon interaction with the iridium complex. The alterations detected in the intensity of the positive peak of the CD spectra, at 190 nm, represent the loss of the a-helical structural features of the protein, due to strong interactions between the protein and the luminescent complex.

2.3.9 Cellular uptake and subcellular localization of IrS1·Z·AuNP25 in HeLa cells by Confocal Microscopy

The cellular uptake efficacy and subcellular localization of IrS1·Z·AuNP25 in HeLa cells was further evaluated in the present study using confocal microscopy. Subsequent to treating HeLa cells for 24 hours with 0.2 nM of the iridium coated AuNPs, live cell imaging revealed a strong luminescence signal in the treated cells. The strong iridium luminescence observed within the intracellular environment during live cell imaging confirms that the photostability of the IrS1 complex is not compromised upon attachment to the surface of the surfactant modified AuNPs. What is more, the intensity of the luminescence signal was not reduced over time during imaging, further confirming that the IrS1 complex does not experience photobleaching in the intracellular space when conjugated to the gold surface. In order to determine the ability of the luminescent nanoparticles to localize in mitochondria, a commercial mitochondrial fluorescent probe, MitoTracker Red (MTR), was used. Imaging analysis suggested co-localization between the luminescence signal from the iridium and MTR, suggesting the presence of the IrS1 functionalized nanoparticles within mitochondrial structures (Figure 2-19).

The cellular uptake and localization of both IrS1 and Ir1 (positive control) in HeLa cells were also evaluated using confocal luminescence imaging. After treatment of the cells for 24 hours with 0.5 μM of IrS1 and Ir1, luminescence was detected in the treated cells, indicating that both complexes can penetrate the cell membrane and internalize in the intracellular space. Even though the luminescent signal of the IrS1 complex was detectable during live cell imaging in HeLa cells, both the luminescence intensity and the co-localization signal from the iridium and MTR were considerably weaker when compared to the signal detected in the cells treated with IrS1·Z·AuNP25 (Figure 2-20). The weak co-localization signal observed between the luminescence complex and the mitochondrial probe, suggests that unlike the IrS1 coated AuNPs, the IrS1 complex in solution does not exhibit efficient mitochondrial localization. This is more likely attributed to the relatively low uptake of the complex by the cells, which was confirmed earlier in the present study through FACS analysis.

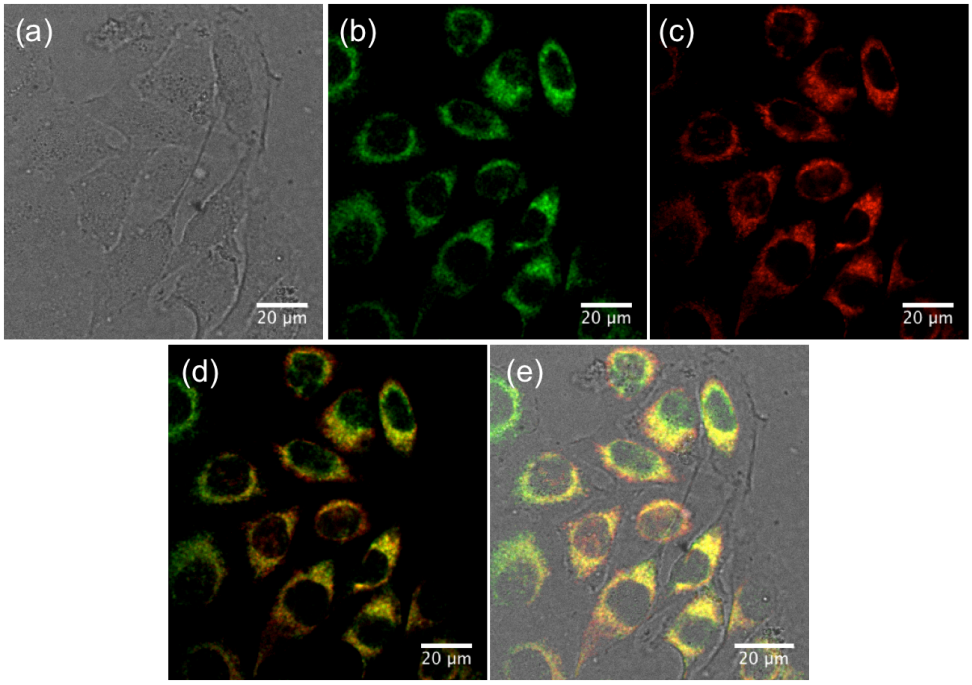


Figure 2-19. **Confocal microscopy of live HeLa cells after treatment with 0.2 nM IrS1·Z·AuNP25 in serum-free cell culture media for 24 h (Scale bar: 20 µm). (a) Bright-field, (b) Iridium luminescence (λ_{exc}=405 nm, λ_{em}=550 nm-610 nm), (c) MitoTracker Red (λ_{exc}=561 nm, λ_{em}=610 nm-640 nm), (d) Overlay of (b) and (c), and (e) Overlay of (a), (b) and (c).**

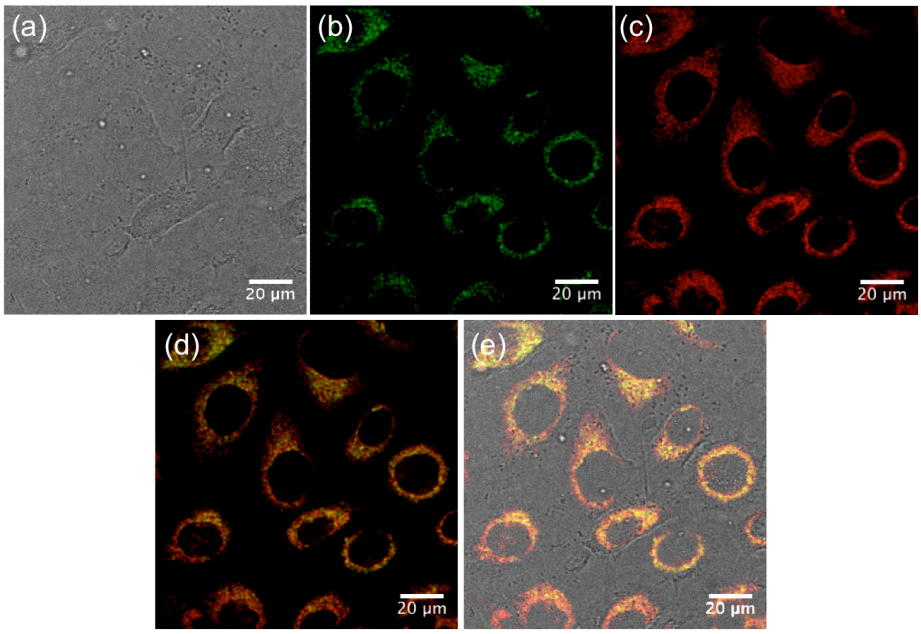


Figure 2-20. **Confocal microscopy of HeLa cells after treatment with 0.5 µM IrS1 in serum-free cell culture media for 24 h (Scale bar: 20 µm). (a) Bright-field, (b) Iridium luminescence (λ_{exc}=405 nm, λ_{em}=550 nm-610 nm), (c) MitoTracker Red (λ_{exc}=561 nm, λ_{em}=610 nm-640 nm), (d) Overlay of (b) and (c), and (e) Overlay of (a), (b) and (c).**

When compared to IrS1, treatment of the cells with the Ir1 complex produced a relatively stronger luminescence signal during imaging, which could be assigned to the higher cellular uptake of the complex, discussed earlier in this chapter. Even though imaging analysis revealed co-localization between the iridium luminescence and MTR, the signal was not as strong nor uniformly distributed within the mitochondrial structures of the cells when compared to the signal detected after treatment with IrS1·Z·AuNP25 (Figure 2-21). What is more, after treating the cells with the Ir1 complex, morphological alterations were observed in the structure of mitochondria, as they appeared to be damaged and dissociated. Similar morphological changes have been previously reported upon targeting of mitochondria using agents that induce high levels of toxicity[82, 116, 117]. Therefore, the morphological alterations detected in mitochondrial structures are more likely attributed to the enhanced cellular toxicity that the Ir1 complex exhibits in HeLa cells, which was observed earlier in this study using the MTT assay.

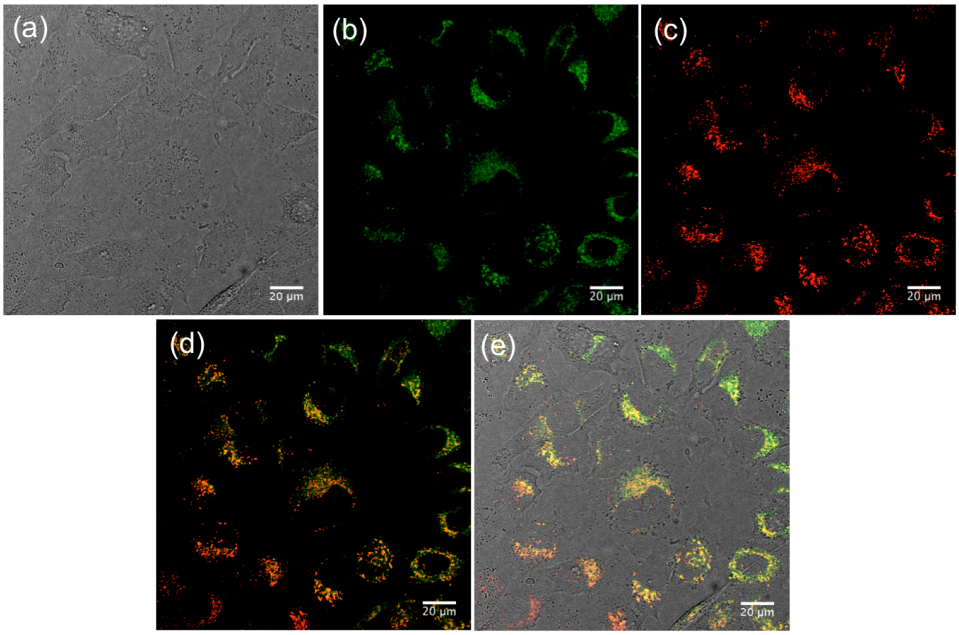


Figure 2-21. Confocal microscopy of HeLa cells after treatment with 0.5 µM IrS1 in serum-free cell culture media for 24 h (Scale bar: 20 µm). (a) Bright-field, (b) Iridium luminescence (λ_{exc}=405 nm, λ_{em}=550 nm-610 nm), (c) MitoTracker Red (λ_{exc}=561 nm, λ_{em}=610 nm-640 nm), (d) Overlay of (b) and (c), and (e) Overlay of (a), (b) and (c).

According to literature, the use of nanoparticles to deliver targeting complexes in cancer cells improves drastically the solubility and thus, bioavailability of the complexes within the intracellular environment, promoting more efficient subcellular localization[112-115]. This could explain the better co-localization signal observed between iridium luminescence and MTR in the cells treated with the IrS1 functionalized AuNPs, in comparison to the cells treated with the iridium complexes in solution.

Overall, imaging analysis performed indicates that the use of AuNPs as nanovectors promotes the improved delivery of the iridium complex within the intracellular space, as the high loading of the complex on the gold surface provides enhanced luminescence signal for imaging applications. What is more, the improved bioavailability provided through the attachment of the luminescence complex onto the gold scaffold allows precise subcellular localization of the complex and eliminates off-target toxicity. The appropriateness of the iridium coated AuNPs for live cell imaging using confocal microscopy is also confirmed through the high photostability presented by the luminescence nanoparticles within the intracellular environment. Even though the majority of organic and biological fluorophores used for imaging cells and organelles exhibit relatively high quantum yields and extinction coefficients, their use in live cell imaging is highly associated with photobleaching. Hence, the IrS1 functionalized AuNPs have the potential to overcome the limitations of conventional imaging agents due to the favourable photophysical properties of the iridium complex and at the same time improve intracellular delivery through the conjugation of the luminescent complex to the gold scaffold.

2.3.10 Cellular uptake and subcellular localization of IrS1·Z·AuNP25 in HeLa cells by TEM

Both the cellular uptake and subcellular localization of the luminescent nanoparticles and Ir1 complex in HeLa cells were further evaluated by TEM. The cells were treated with 0.2 nM of the IrS1 coated AuNPs, and 0.5 and 1 μM of the Ir1 complex for 24 hours. Treatment of the cells at two different concentrations was performed in order to further interpret the cytotoxic effect of the Ir1 complex on the mitochondrial structures observed by luminescence imaging. Relatively low concentrations were chosen, as higher concentrations of the complex induce a significant inhibition in cell viability, thus, it would be difficult to study morphological alterations in mitochondria due to the vast production of apoptotic bodies[82, 118].

After treatment with IrS1·Z·AuNP25, TEM images revealed the highly efficient cellular uptake and intracellular localization of the luminescent nanoparticles (Figure 2-22). The IrS1·Z·AuNP25 were evenly distributed within the cytoplasm, with no evidence of nuclear localization, which agrees with the imaging performed by confocal microscopy. During imaging, some iridium coated nanoparticles appeared to be trapped within endosomal vesicles, which is a characteristic of the endocytic uptake mechanism by which functionalized nanoparticles internalize within the intracellular space[37, 119] (Figure 2-23). It has been previously reported that the optimal radius size of nanoparticles for efficient uptake by endocytosis is between 25 to 30 nm[120, 121]. The cellular uptake mechanism of larger nanoparticles of sizes above 500 nm is usually phagocytsis whereas the mechanism by which cells uptake smaller nanoparticles, below 15nm, is pinocytosis[122].

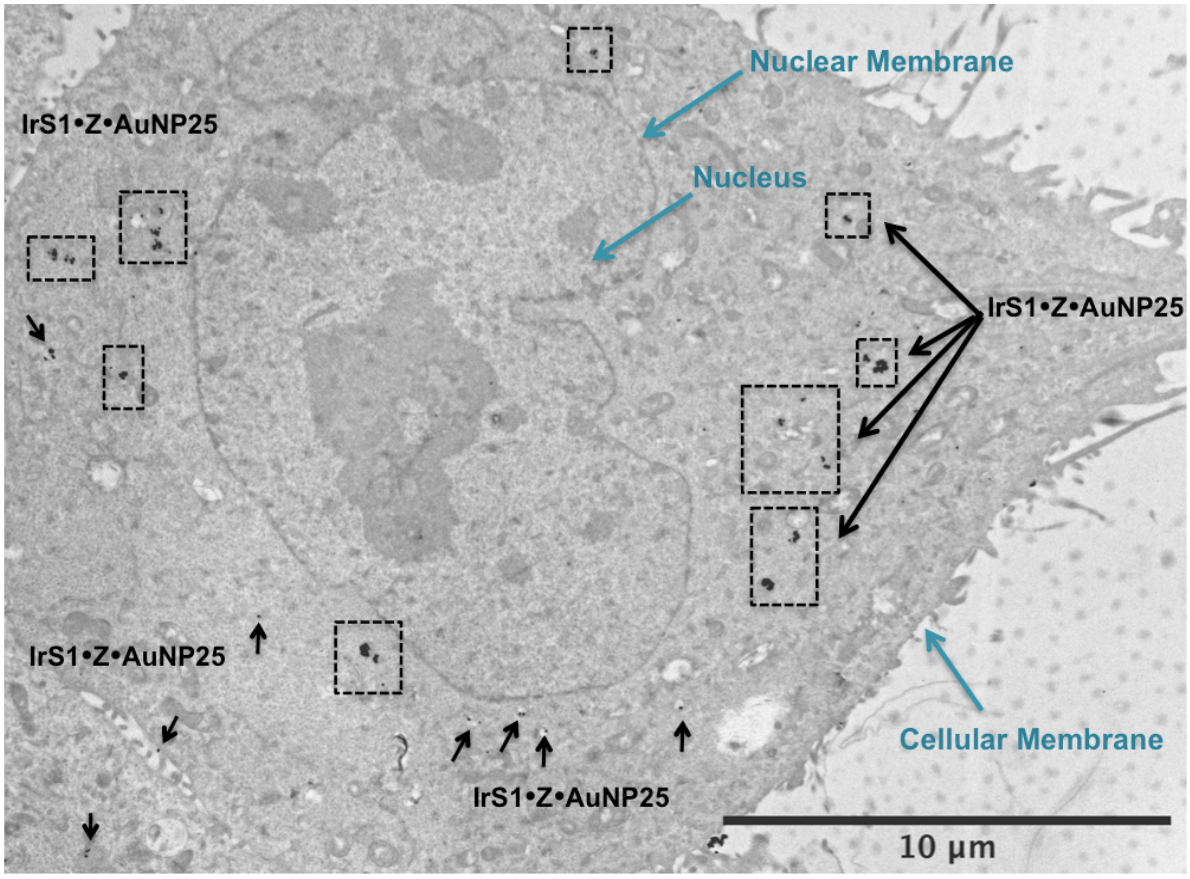


Figure 2-22. Transmission Electron Microscopy in HeLa cells after treatment with 0.2 nM IrS1·Z·AuNP25 in serum-free cell culture media for 24 h (Scale bar: 10 µm). Image acquired on Jeol 1400 Ex Bio TEM.

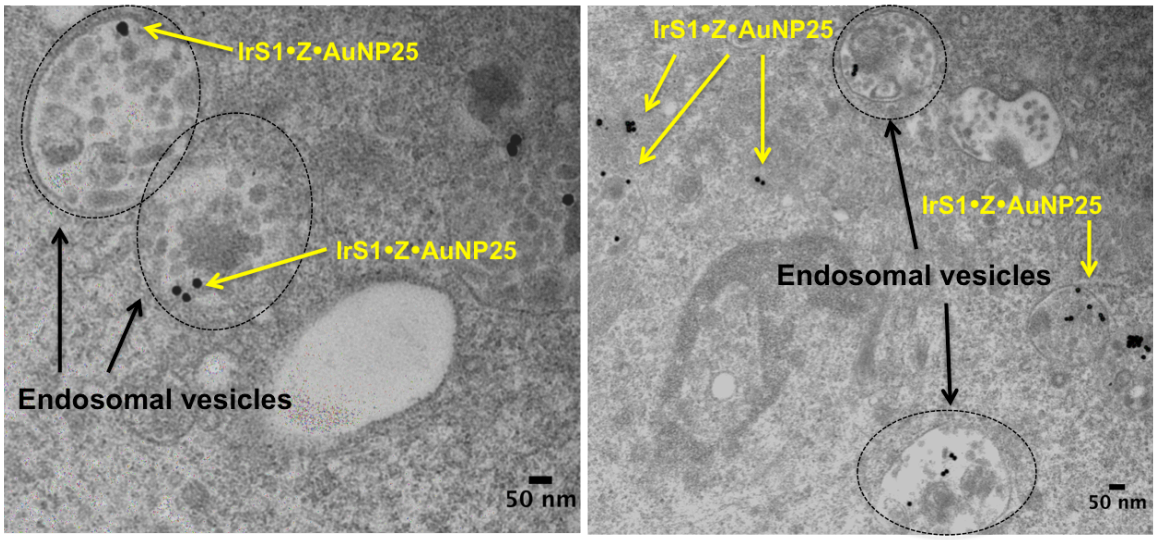


Figure 2-23. Transmission Electron Microscopy in HeLa cells after treatment with 0.2 nM IrS1·Z·AuNP25 in serum-free cell culture media for 24 h, showing nanoparticles in endosomal vesicles (Scale bar: 50 nm). Images acquired on Jeol 1400 Ex Bio TEM.

Imaging analysis by TEM revealed the preference of IrS1·Z·AuNP25 for localizing within mitochondrial structures in HeLa cells (Figure 2-24). Even tough the presence of the luminescence nanoparticles in mitochondria was evident, a number of mitochondria were presented during imaging without any nanoparticles. This can be attributed to sectioning of the cells during preparation for TEM, as ultrathin sections are used during analysis, limiting the ability to study in detail a whole organelle[123].

Subsequent to treating cells with the Ir1 complex, TEM imaging revealed disruption in the mitochondrial structures, as perinuclear clustering of abnormal, dilated and swollen mitochondria was observed, confirming the high cytotoxicity of the complex observed earlier in this chapter by the MTT assay (Figure 2-25). The morphological alterations detected in the mitochondrial structures were more evident upon increasing the treatment concentration of the Ir1 complex from 0.5 to 1 μM. The disruption of mitochondria morphology by cyclometalated iridium(III) complexes has been previously reported and similar structural alterations have been observed[82, 102, 118, 124].

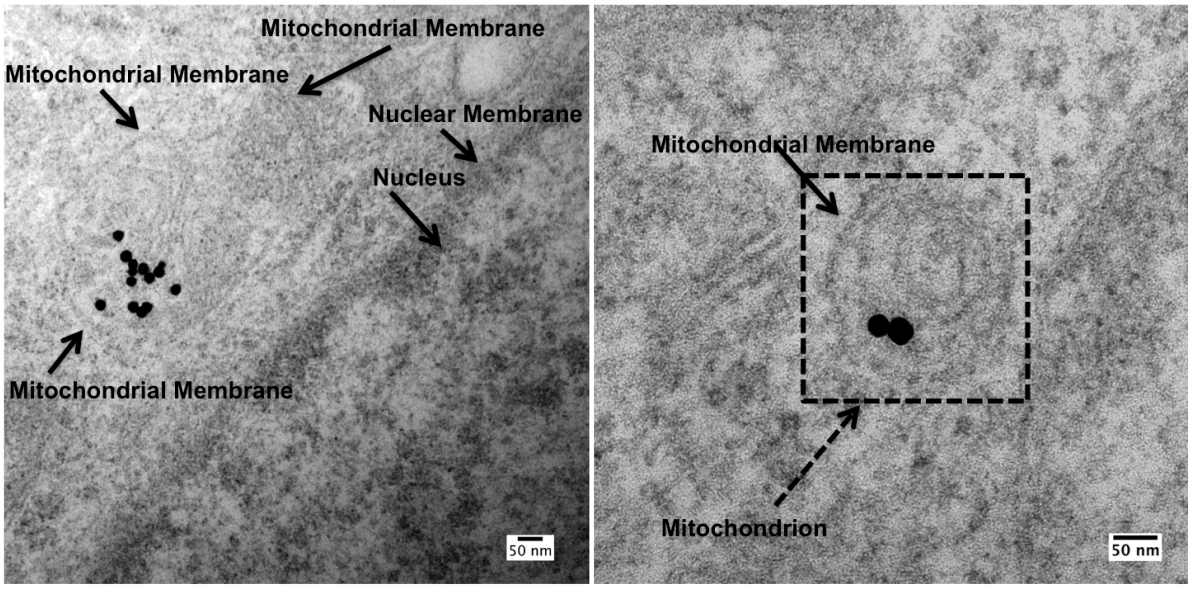


Figure 2-24. Transmission Electron Microscopy of mitochondria in HeLa cells after treatment with 0.2 nM IrS1·Z·AuNP25 in serum-free cell culture media for 24 h. (Scale bar: 50 nm). Images acquired on Jeol 1400 Ex Bio TEM.

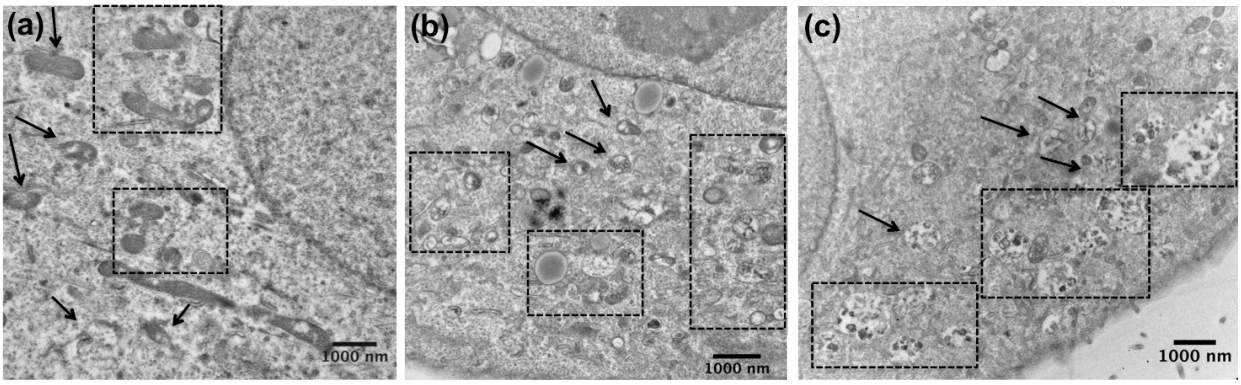


Figure 2-25. Transmission Electron Microscopy of mitochondria in HeLa cells after treatment with (a) Control (H_2O), (b) 0.5 µM Ir1 and (c) 1 µM Ir1 in serum-free cell culture media for 24 h. (Scale bar: 1000 nm). Images acquired on Jeol 1400 Ex Bio TEM.

Even though TEM is considered as a powerful tool to study the high complexity of cells and visualize organelles, it does have some limitations upon evaluating subcellular localization of nanoparticles. Due to the fact that the cells imaged by TEM are fixed and sectioned, only a thin section of each organelle is available for imaging, thereby, reducing the probability of collecting a large set of data when studying localization of nanomaterials[125, 126]. Therefore, in order to further confirm the efficient subcellular localization of the IrS1 functionalized nanoparticles in mitochondria, ICP-MS analysis was performed.

2.3.11 Cellular uptake and subcellular localization of IrS1·Z·AuNP25 in HeLa cells by ICP-MS

The cellular uptake and subcellular localization of IrS1·Z·AuNP25 were quantified using ICP-MS. ICP-MS is considered as a highly sensitive elemental analysis technique for determining the unique mass of metals or metal nanoparticles within the intracellular environment[127, 128]. Elemental analysis to quantify the uptake and localization of the luminescent nanoparticles was performed after treating HeLa and HEK293 cells with 0.2 nM IrS1·Z·AuNP25 for 24 hours. In order to quantify cellular uptake and subcellular localization, analysis was performed both in whole and fractionated cell lysates after treatment.

Through ICP-MS analysis of whole cell lysates it was determined that the number of nanoparticles per cell is approximately 16 000 in HeLa cells and 20 000 in HEK293 cells (Figure 2-26) (Appendix D-3). The high number of nanoparticles observed per cell agrees with previously published data by the Pikramenou group, reporting highly efficient cellular uptake of iridium functionalized AuNPs of about 25 nm in HeLa cells[37].

Formerly published studies however, have reported different numbers of modified AuNPs in HeLa cells, indicating that there is no definite number of nanoparticles per cell[71, 129]. Upon surface functionalization of AuNPs, the surface chemistry and charge of nanoparticles can significantly impact the cellular uptake[96, 130]. Hence, upon conjugation of different transition metal complexes to AuNPs, the cellular uptake is affected based on the chemical and physical properties of the complex[131]. The different ligands present in different transition metal complexes determine the solubility as well as the hydrophobicity and hydrophilicity of a complex in a cellular environment. This indicates that upon attachment to the surface of AuNPs, different metal complexes impact differently the interaction of the functionalized nanoparticles with the cell surface membrane, thereby affecting cellular entry[25, 132-134].

Due to the fact that all variables, including cell seeding density, cell culture conditions, concentration of IrS1·Z·AuNP25 and incubation time, were kept constant during the experiment, the difference observed in the number of nanoparticles per cell between HeLa and HEK293 cells is assigned to the different characteristics that malignant and normal cells exhibit. It has been previously reported that the cellular uptake of AuNPs is highly dependent on the cell type, as different molecules, such as proteins and lipids, present both on the cell surface membrane and in the intracellular space affect the interaction of the nanoparticles with the cell and determine the cellular fate[43, 135].

The subcellular localization of IrS1·Z·AuNP25 in HeLa and HEK293 cells was quantified through ICP-MS analysis of fractionated cell lysates, including nucleus, cytosol and mitochondria (Figure 2-26). The results indicated a higher number of nanoparticles in mitochondria in HeLa cells when compared to nucleus and cytosol, suggesting the preference of the luminescent nanoparticles to localize within mitochondrial structures. However, In HEK293 cells, the results suggested the preference of the luminescent

nanoparticles to localize mostly in the cytoplasm, as the number of AuNPs in the cytosol was considerably higher than the number of nanoparticles detected in mitochondria and nucleus.

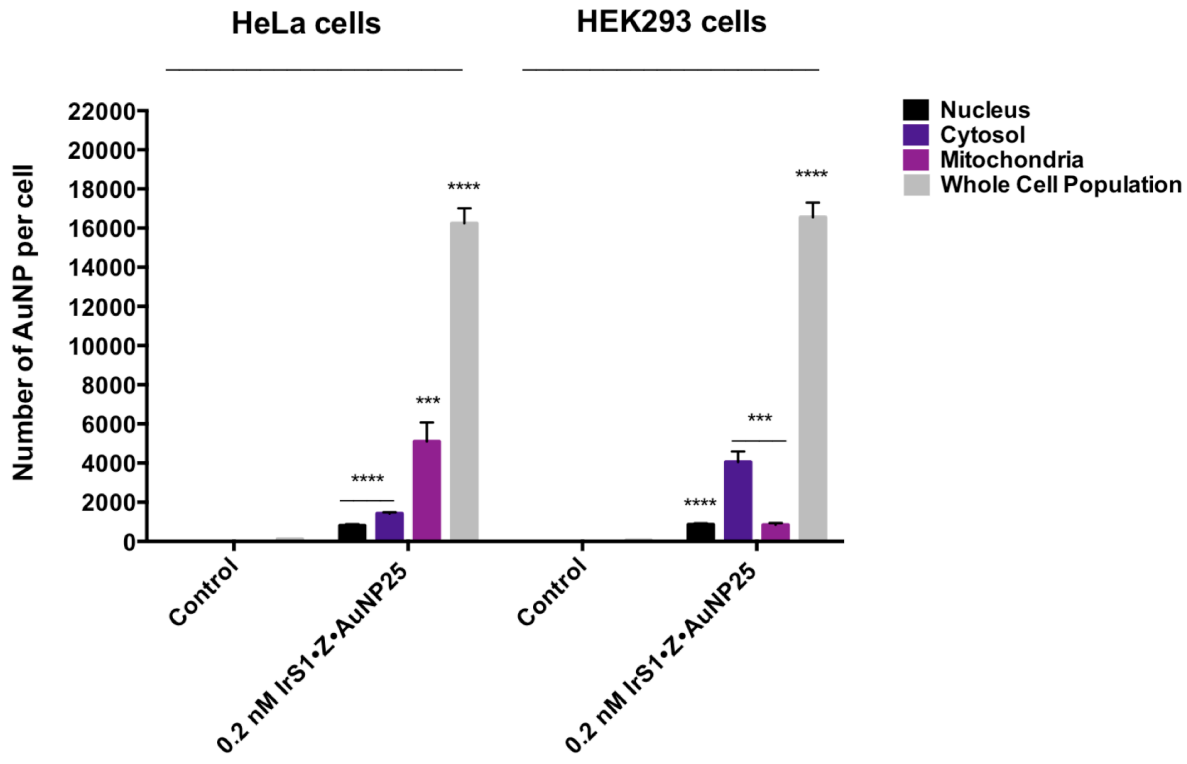


Figure 2-26. ICP-MS Analysis of the number of AuNPs per cell in HeLa and HEK293 cells in fractionated and whole cell lysates after treatment with 0.2 nM IrS1·Z·AuNP25 in serum-free cell culture media for 24 h. Statistical analysis was performed using unpaired t-test with equal SD between the samples and controls. ******P value < 0.001, ****P value < 0.0001***

The preference of IrS1·Z·AuNP25 to localize in mitochondria in HeLa cells, but not in HEK293 cells, is more likely attributed to the differences between the structure and metabolism of mitochondria in cancer and normal cells. When compared to normal cells, both the mitochondrial membrane potential (MMP) and the basicity within the mitochondrial lumen are significantly higher in cancer cells[136]. Also, the mitochondrial membrane in cancer cells is hyperpolarized, as it is -220 mV, while the membrane of mitochondria in normal cells is about -160 mV. The hyperpolarisation of the mitochondrial membrane facilitates the rapid and selective uptake and internalization of positively

charged molecules within mitochondrial structures in cancer cells[136, 137]. What is more, the hydrophobicity and associated lipophilicity of a complex also favor its interaction with the hydrophobic inner mitochondrial membrane, aiding in the efficient penetration of the mitochondrial membrane and the high accumulation of the complex in mitochondria in tumor cells[138]. This explains the preference of various cyclometalated iridium(III) complexes, previously reported in literature, to localize efficiently in mitochondria in cancer cells[14, 24, 25, 118, 139]. Therefore, the presence of the cationic IrS1 complex conjugated to the surface of AuNPs explains the preference of IrS1·Z·AuNP25 for localizing within mitochondria in HeLa cells but not in HEK293 cells.

The fact that mitochondria in normal cells do not exhibit the favorable characteristics of mitochondria in malignant cells discussed above, could explain the low number of the iridium coated AuNPs detected in the mitochondria in HEK293 cells. Upon cellular entry of IrS1·Z·AuNP25 in HEK293 cells by endocytosis[120], the nanoparticles more likely remain entrapped in endosomal vesicles within the cytosplasm in the cells[43]. The uptake mechanism by which functionalized nanoparticles enter the cells and the fact that the membrane potential of mitochondria in normal cells doesn't favor further subcellular localization, explain the higher number of IrS1·Z·AuNP25 detected within the cytosolic compartment, when compared to mitochondria and nucleus.

The cellular uptake of both the IrS1 and Ir1 complexes was also quantified by ICP-MS analysis and compared to the uptake of the luminescent nanoparticles in HeLa and HEK293 cells. Analysis was carried out after treatment of the cells for 24 hours with 0.2 nM IrS1·Z·AuNP25, 0.5 μM IrS1 and 0.5 μM Ir1. Similarly to previous cellular uptake analysis described in the present study, the concentration at which IrS1 and Ir1 were tested was chosen based on elemental composition analysis of IrS1·Z·AuNP25 by ICP-MS, indicating 2500 IrS1 complexes per AuNP25. (Concentration of IrS1 in 0.2 nM IrS1·Z·AuNP25 is 0.5 μM). The accumulation efficacy of the IrS1 complex within the intracellular space, when delivered alone and upon attachment to the gold scaffold, was evaluated through comparing the iridium content between the cells treated with the functionalized nanoparticles and the ones treated with molecular complex in solution (Figure 2-27).

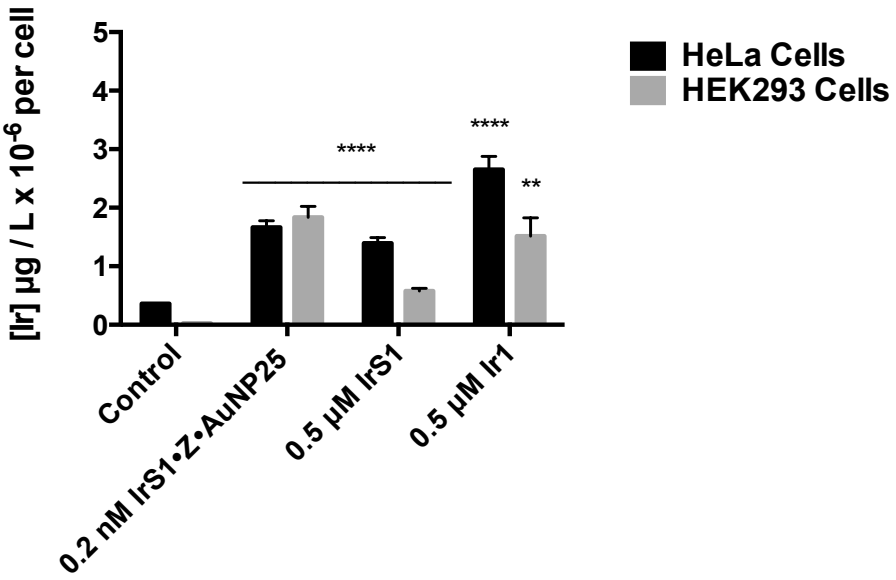


Figure 2-27. ICP-MS Analysis of iridium concentration in HeLa and HEK293 cells after treatment with 0.2 nM IrS1·Z·AuNP25, 0.5 µM IrS1 and 0.5 µM Ir1 in serum-free cell culture media for 24 h. Statistical analysis was performed using unpaired t-test with equal SD between the samples and controls. ***P value < 0.01, ****P value < 0.0001*

For both cell lines, the results indicated higher iridium content in the cells treated with the iridium modified AuNPs, when compared to the cells treated with the IrS1 complex in solution. Even though in HeLa cells the concentration of iridium was not remarkably higher after treatment with IrS1·Z·AuNP25 in comparison to the cells treated with IrS1, the difference is statistically significant (P value=0.0341). The higher iridium content quantified by ICP-MS in the cells treated with the IrS1 coated AuNPs, further supports the efficient cellular uptake of IrS1·Z·AuNP25 presented earlier in this chapter by FACS and confocal microscopy.

As expected, after treating HeLa cells with the Ir1 complex, the iridium content detected was considerably higher than the content detected in the cells treated with IrS1·Z·AuNP25 and IrS1. This is in agreement with previous analysis presented by FACS, hence, further confirming the highly efficient uptake and accumulation of the complex in cancer cells. In HEK293 cells, the concetration of iridium detected subsequent to treatment of the cells with the Ir1 complex was slightly lower than the iridium content in the cells treated with the iridium coated AuNPs. However, due to the fact that the difference was not statistically

significant (P value=0.2047), its not certain whehter the Ir1 complex exbhibits lower uptake than the luminescent nanoparticles. The lower uptake of IrS1 and Ir1 in HEK293 cells when compared to HeLa cells explains the non-cytotoxic effect observed in the HEK293 cells by the MTT assay, and supports the previously reported selectivity of cyclometalated iridium complexes against cancer over normal cells[81, 140].

2.3.12 Targeting Mitochondria in HeLa cells through inducing elevation of ROS Levels

Subsequent to studying the subcellular localization of IrS1·Z·AuNP25, the levels of reactive oxygen species (ROS) in both HeLa and HEK293 cells were evaluated by FACS. The elevation of ROS levels in the in treated cells was determined in the presence of the non-fluorescent 2′,7′-dichlorofluorescein diacetate (DCFDA) probe, which is rapidly oxidized by intracellular ROS to produce green fluorescent dichlorofluorescein (DCF). Therefore, in the present study, the elevation of intracellular ROS levels was evaluated through the increase detected in MFI after treatment and presented as a fold-increase against basal ROS levels of untreated cells. ROS levels in both cell lines were also evaluated after treatment with the Ir1 complex to determine whether the selective cytotoxic effect of the complex against HeLa cells described earlier in this chapter is related to the elevation of basal ROS levels to toxic levels.

After treatment of the cells with 0.2 nM IrS1·Z·AuNP25 for 24 hours, in HeLa cells a 6.3 fold increase was detected in the MFI of the cells (Figure 2-28 a and c), whereas in HEK293 cells the MFI was only increased by 3.7 (Figure 2-28 b and d). Intracellular ROS are produced upon targeting cells as a consequence of oxygen consumption. Due to the fact that mitochondria are responsible for the consumption of most of the oxygen in cells to generate intracellular ROS, are considered as the major site of ROS production[7, 141]. Therefore, the higher increase in generated ROS levels observed in HeLa over HEK293 cells, is more likely attributed to the preference of IrS1·Z·AuNP25 to localize in mitochondria, as observed earlier in the present study by ICP-MS analysis. The

differences in the mitochondrial metabolism, structure and function between normal and cancer cells could also explain the selectivity of IrS1·Z·AuNP25 for inducing higher ROS elevation in HeLa over HEK293 cells[142, 143].

In order to validate that the generation of intracellular ROS levels is attributed to the presence of the targeting iridium complex on the gold surface, surfactant coated AuNPs without the iridium complex were used as the negative control. Treatment of both HeLa and HEK293 cells with 0.2 nM Z·AuNP25 for 24 hours did not induce an increase in the MFI of the cells, confirming that in the absence of the iridium complex, neither the fluorinated surfactant nor the AuNPs promote mitochondrial dysfunction.

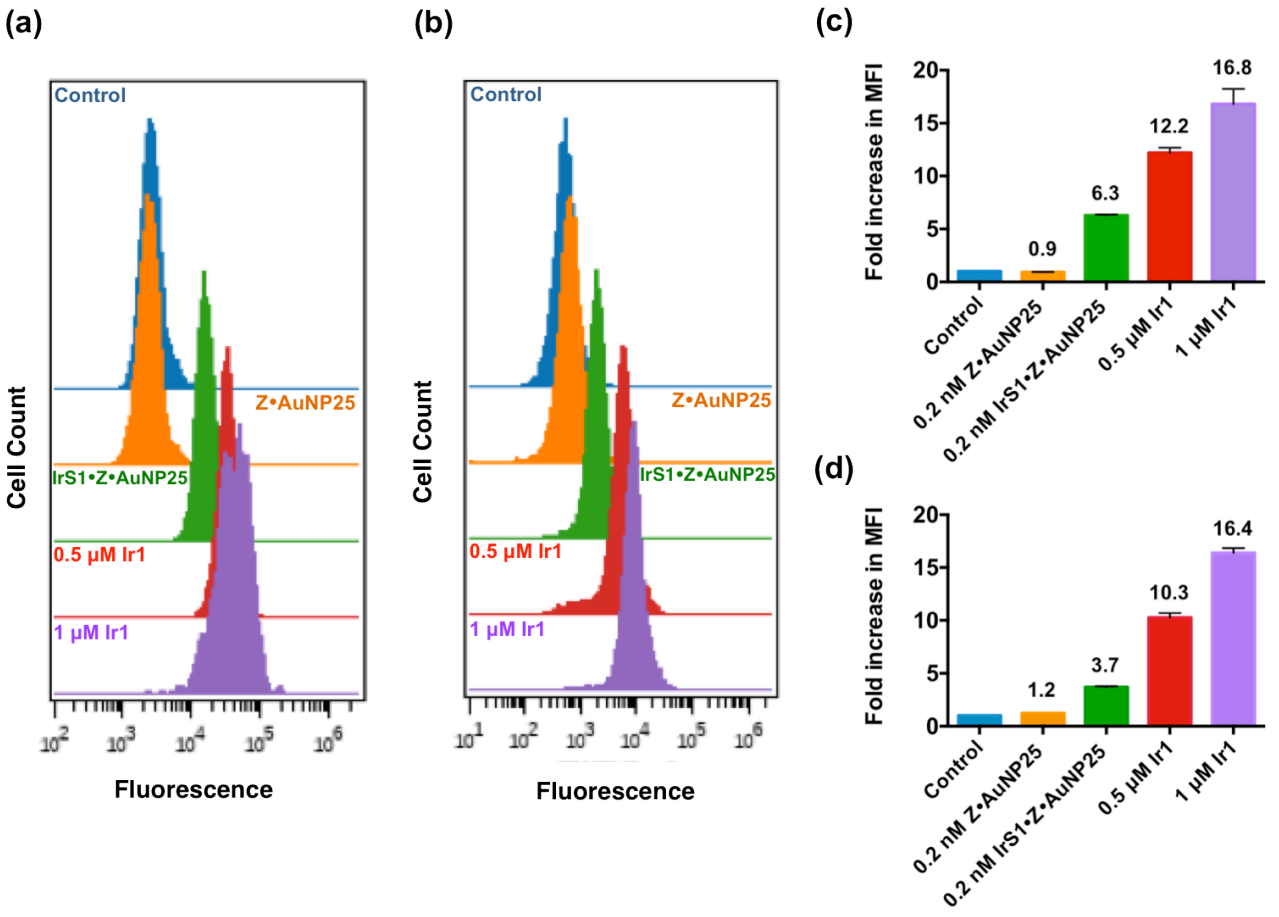


Figure 2-28. **Intracellular ROS levels as evaluated by FACS in the presence of the H_2DCFDA probe after treatment for 24 h with 0.2 nM Z·AuNP25, 0.2 nM IrS1·Z·AuNP25, 0.5 µM Ir1 and 1 µM Ir1. (a) Histogram analysis of ROS levels in HeLa cells (b) Histogram analysis of ROS levels in HEK293 cells (c) Fold increase in Mean Fluorescence Intensity (MFI) in HeLa cells. The results are mean values ± SD of two independent experiments and (d) Fold increase in Mean Fluorescence Intensity (MFI) in HEK293 cells. The results are mean values ± SD of two independent experiments.**

In both cell lines, ROS levels were significantly elevated subsequent to treatment with 0.5 and 1 μM of the Ir1 complex, with the increase being concentration dependent (Figure 2-28). Normal intracellular ROS levels are essential in promoting cell proliferation and migration, however highly elevated ROS levels, such as the ones observed after treatment with Ir1, can induce excess oxidative stress that eventually leads to cellular damage and apoptotic cell death[9, 144]. The fact that upon treatment with Ir1 intracellular ROS levels were significantly elevated both in the cancer and normal cell line, suggests that the complex is not selectively targeting cancer cells. Even though Ir1 doesn't induce any cytotoxicity in HEK293 cells, as observed by MTT assay at the concentrations tested earlier in this study, it still significantly impacts ROS production.

In normal cells, ROS levels are tightly controlled, as there is a constant balance between ROS production and elimination of antioxidant agents. This favorable for the cells redox balance prevents ROS accumulation and induced cell death[145, 146]. Therefore, besides its low cytotoxicity in HEK293 cells, the high levels of ROS detected suggest that the Ir1 complex is a ROS inducer, disrupting the redox homeostasis of ROS production in normal cells that can eventually result to inhibition of cell growth, proliferation and variable levels of cell death.

Developing an approach that can lead to a specific redox-dependent effect in cancer cells, while avoiding redox alterations in normal cells, could be the foundation for improved efficacy in clinical research and cancer therapy. This can be accomplished through inducing oxidative stress to increase intracellular ROS in cancer cells above the levels of toxicity threshold, while not affecting the lower basal ROS levels present in normal cells to the same extent[10, 145, 147].

Therefore, the ability of IrS1·Z·AuNP25 to induce higher generation of ROS levels in HeLa over HEK293 cells indicates the ability of the nanoparticles to promote selective mitochondrial dysfunction in cancer cells. The site-specific delivery of the IrS1 functionalized nanopaticles to mitochondria, along with their selectivity for cancer over normal cells, potentiate a favorable therapeutic approach for treating cancer, as off-target toxicity and adverse side effects can be significantly reduced.

2.4 Conclusion

Luminescent gold nanoparticles were developed in the presence of a fluorinated surfactant and a cyclometalated iridium(III) complex, IrS1. Subsequent to conjugation of the iridium complex to the surface of the nanoparticles, the complex retains its characteristic photophysical properties, demonstrating long luminescence lifetimes and emission within the visible range. Upon excitation at 350, 405 and 458 nm, the IrS1 functionalized nanoparticles displayed the characteristic broad emission peak of the iridium complex. At the concentrations tested, the iridium coated nanoparticles did not demonstrate a significant cytotoxic effect in HeLa and HEK293 cells, suggesting their appropriateness to be used for further cellular uptake, live cell imaging and subcellular localization studies. Cytotoxicity was only detected after treatment of the cells with the Ir1 complex, the positive control of the study, which is attributed to the highly efficient uptake of the complex by HeLa cells. The fact that no cytotoxicity was detected in HEK293 cells after treatment with the Ir1 complex, suggests the selectivity of the complex for cancer over normal cells. This is more likely attributed to differences in the cellular metabolic processes and higher oxidative stress levels present in cancer cells, which induce cellular toxicity upon targeting.

Through FACS analysis, the cellular uptake of the iridium modified AuNPs in HeLa cells was evaluated and compared to the uptake of the IrS1 complex in solution. The results indicated the improved cellular uptake and internalization of the complex in the intracellular space upon attachment to the gold surface. Live cell imaging in live HeLa cells further confirmed the efficient cellular uptake of functionalized AuNPs, as a strong luminescence signal from the iridium complex was detected within the cytoplasm of the cells. In order to further evaluate the localization of the luminescent nanoparticles in the cells, a mitochondrial fluorescent probe, MTR, was used. Imaging analysis revealed co-localization between the signal from the luminescent nanoparticles and the MTR, suggesting subcellular localization of the IrS1 modified nanoparticles within mitochondrial structures in HeLa cells.

The cellular uptake and subcellular localization of the iridium coated nanoparticles were further studied through detecting the luminescence properties of the modified AuNPs in treated cells and subcellular organelles. Upon excitation at 405 nm, HeLa cells treated with the IrS1 modified AuNPs, displayed the characteristic broad emission peak of the luminescent nanoparticles. Luminescence lifetime measurements in the treated cells revealed an increase in the lifetime of the iridium coated AuNPs, which was attributed to interactions between cellular proteins and the IrS1 complex. This was confirmed through the similar increase detected in the lifetime of the luminescent nanoparticles upon addition of BSA. Lifetime measurements in subcellular organelles revealed the preference of the luminescence nanoparticles for localizing in mitochondria and interacting with mitochondrial proteins.

The biomolecular interaction of the IrS1 complex with BSA was further examined by CD spectroscopy, showing that binding of the complex induces structural alterations in the features of the protein, both when in solution and attached to the surface of AuNPs. The conformational changes observed in the structure of BSA were assigned to the engagement of the IrS1 complex in strong hydrophobic and electrostatic interactions with the protein.

The highly efficient cellular uptake and subcellular localization of the IrS1 functionalized nanoparticles in HeLa cells was further confirmed by TEM imaging and quantified by ICP-MS analysis. TEM imaging revealed clusters of nanoparticles within the cytoplasm of the cells, and provided evidence of mitochondrial localization. The cytotoxic effect of the Ir1 complex in HeLa cells was also assessed by TEM, showing significant disruption of the mitochondrial structures. ICP-MS analysis confirmed the highly efficient uptake of the IrS1 coated nanoparticles in HeLa cells, as about 16 000 AuNP25 were detected per cell. Furthermore, elemental analysis in fractionated subcellular organelles, suggested the preference of the iridium modified AuNPs to accumulate within mitochondria in HeLa cells. The preference of the luminescent nanoparticles for localizing in mitochondria was only evident in cancer cells, as in normal cells the number of nanoparticles in the cytosol was considerably higher than the nanoparticles detected in mitochondria.

The selectivity of the IrS1 coated AuNPs for targeting cancer cells was evident through the higher generation of intracellular ROS levels observed in HeLa over HEK293 cells. The site-specific delivery of the iridium coated AuNPs along with their ability to induce selective mitochondrial dysfunction in tumor cells, present a promising approach for eliminating off-target toxicity and adverse side effects, associated with conventional therapeutic approaches.

In conclusion, in this chapter, novel iridium coated nanoparticles were introduced, with optimal cellular uptake and efficient localization in mitochondria in cancer cells. The use of AuNPs as a vehicle to deliver the luminescent complex in the intracellular space improves drastically the bioavailability of the complex and allows efficient subcellular localization. Finally, the selectivity of the luminescent nanoparticles for cancer over normal cells presents a favourable therapeutic approach for cancer treatment.

2.5 Acknowledgments

I wish to pay my special regards to both Tasha Chauhan and Sara Akponasa (School of Chemistry, University of Birmingham) for providing the IrS1 and Ir1 complexes used in this chapter. Also, I would like to thank Mr. Paul Stanley (School of Metallurgy and Materials, University of Birmingham) for the preparation of the cell sections used for TEM and his assistance in obtaining the images presented in this study. Finally, I would like to thank Dr. Lijiang Song (Department of Chemistry, University of Warwick) for performing the elemental analysis by ICP-MS.

2.6 Experimental

2.6.1 Synthesis of IrS1 and Ir1

The synthesis and chatacterization of the IrS1 and Ir1 complexes were performed by Tasha Chauhan and Sarah Akponasa, (School of Chemistry, University of Birmingham) (Synthesis is described in Appendix A).

2.6.2 Preparation of IrS1·Z·AuNP25

Initially, 4 ml of AuNP25 of 0.65 nM were centrifuged twice at 10, 000 g for 20 minutes. The supernatant after each centrifugation was discarded and the pellet was re-suspended in 1 ml of fresh filtered miliQ H_2O. Then, the centrifuged nanoparticles were coated with a 2.5% Zonyl FSA (Sigma-Aldrich) stock solution (0.2 mM), which was prepared in miliQ H_2O and filtered. In 1 ml of AuNP25, 10 µl (2 µM) of the fluorinated surfactant were added and stirred for about 10 minutes. The zonyl coated nanoparticles were centrifuged twice at 10, 000 g for 20 minutes to remove excess, unbound zonyl. The centrifuged nanoparticles were re-suspended in 1ml of fresh filtered miliQ H_2O to produce Z·AuNP25 (Final concentration ~ 2.5 nM). UV-Vis (H_2O) λ_{max} = 520 nm (SPR). Diameter = 28 ± 7 nm (DLS number distribution). Diameter = 43 ± 12 nm (DLS intensity distribution). Zeta potential = -49 ± 8 mV (1 nM in miliQ H_2O).

The IrS1 complex (Stock solution in methanol: 1.13 mM) was titrated in 2 µl aliquots into a solution of Z·AuNP25 with stirring in between each addition. The attachment of the complex to the gold surface was confirmed through monitoring the shift in the SPR band of the nanoparticles subsequent to each addition using UV-Vis spectroscopy (Cary 5000 Spectrometer). The red shift in the SPR band allowed the maximum concentration of the IrS1 complex that is required to fully coat the gold surface without inducing nanoparticle aggregation to be determined. The maximum concentration of the IrS1 complex required to reach saturation on the surface of Z·AuNP25 is 20 µM.

Hence, 20 μM of the IrS1 complex were added in 2 μl aliquots into 1 ml of Z·AuNP25 (2 nM) with stirring in between each addition. After the last addition, the nanoparticles were stirred for an additional 20 minutes. Finally, size exclusion chromatography was performed using Sephadex G-25 (Sigma-Aldrich) to remove any excess, unbound iridium complex and produce purified IrS1·Z·AuNP25 (Final concentration ~ 2 nM). UV-Vis (H_2O) λ_{max} = 525 nm (SPR). Diameter = 28 ± 8 nm (DLS number distribution). Diameter = 57 ± 24 nm (DLS intensity distribution). Zeta potential = - 42 ± 6 mV (1 nM in miliQ water).

2.6.3 MTT Cell Viability Assay

Cell viability in HeLa and HEK293 cells after treatment with nanoparticle samples and the iridium complexes was assessed using the MTT cell viability assay. For the purposes of the assay, a fresh solution of the MTT reagent, [3-(4,5-dimethylthiazol-2-yl)-2,5-diphenyl tetrazolium bromide] (Thermo Fisher Scientific, Catalogue number: M6494), was prepared in PBS (5 mg/ml). $1x10^4$ cells per well were seeded in a 96-well plate and were incubated overnight to allow the cells to adhere. For each experimental group the cells were seeded in triplicate. The cells were then washed twice with sterile PBS and fresh culture media was added, followed by the addition of Z·AuNP25, IrS1·Z·AuNP25, IrS1 and Ir1 for 24 hours. Samples were added in the cells at a ratio of 1:10 (sample:culture media). Cytotocixity was evaluated at increasing concentrations of Z·AuNP25 and IrS1·Z·AuNP25, between 0.1 to 0.4 nM and at concentrations between 0.5 to 3 μM for both IrS1 and Ir1. After 24 hours, the cells were washed three times with sterile PBS and fresh cell culture media was added followed, by the addition of 20 μl of the MTT solution. The 96-well plate was covered in foil and the treated cells were incubated with the MTT reagent for 4 hours. Finally, the culture media containing the MTT reagent was discarded and 150 μl of Dimethyl Sulfoxide (DMSO) (Sigma-Aldrich) were added to the cells in each well. The 96-well plate was placed on a plate shaker for 20 minutes and it was then read using the iMark™ Microplate Absorbance Reader (Bio Rad). The absorbance was measured at OD = 590 nm.

2.6.4 Cellular uptake by FACS

HeLa cells were seeded in 60 mm dishes, $1x10^6$ cells per dish, and incubated overnight in order to allow the cells to adhere. The cells were washed twice with sterile PBS and fresh serum-free DMEM culture media was added, followed by the addition of the samples. Samples were added at a ratio of 1:10 (sample:culture media) and incubated with the cells for 24 hours. The cellular uptake efficacy of the IrS1 coated nanoparticles and the IrS1 complex in solution was evaluated after treatment of the cells with 0.2 nM of the AuNP25 samples, AuNP25, Z·AuNP25, IrS1·Z·AuNP25 and 0.5 and 1 μM of the iridium complexes, IrS1 and Ir1. AuNP25 and Z·AuNP were used as negative controls and Ir1 was used as the positive control. After treatment for 24 hours, the cells were washed three times with sterile PBS to ensure removal of excess samples and were then trypsinized, using Trypsin-EDTA (0.25%) (Gibco®-Thermo Fisher Scientific) for approximately 5 minutes. Fresh culture media was added to quench tryspinization and the cells were collected and centrifuged at 1 000 rpm for 5 minutes. The supernatant was then discarded and the cells were re-suspended in 1 ml of PBS supplemented with 1% FBS and transferred into FACS tubes for analysis. Samples were run on the LSRII Flow Cytometer (BD Biosciences, Oxford, UK) using the BD FACSDiva Software. Analysis was performed using FlowJo and Cytobank.

2.6.5 Live cell imaging by Confocal microscopy

HeLa cells were seeded in 35 mm dishes, $1x10^5$ cells per dish, and incubated overnight for cells to adhere. The cells were then washed twice with sterile PBS and fresh serum-free DMEM culture media was added. The IrS1 coated nanoparticles and the iridium complexes in solution were added to the cells at a ratio of 1:10 (sample:culture media). The cells were incubated with the samples for 24 hours. The cells were treated with 0.2 nM IrS1·Z·AuNP25 and 0.5 μM of the iridium complexes, IrS1 and Ir1. The culture media was then discarded and the cells were washed three times with sterile PBS to remove any excess samples. The treated cells were then stained with MitoTracker Red (MTR). MTR (Invitrogen, Catalogue number: M22425) of 1 mM, as provided by the manufacturer, was diluted to a final concentration of 50 nM in DMEM media (Gibco®-Thermo Fisher

Scientific) and incubated with the cells for 20 minutes. The cell media containing the MTR was then removed and the cells were washed twice with sterile PBS. Fresh cell culture media, DMEM phenol red free media (Gibco®-Thermo Fisher Scientific) was added and the cells were imaged immediately using the Leica TCS SP8 upright confocal scanning system with a 40x water immersion objective lens.

2.6.6 Cellular uptake and subcellular localization by ICP-MS

HeLa and HEK293 cells were seeded in 150 mm dishes at a $1x10^7$ density, and incubated overnight to allow cells to adhere. The cells were then washed twice with sterile PBS and fresh serum-free DMEM culture media was added, followed by the addition of the iridium-coated nanoparticles and iridium samples for 24 hours. Samples were added at a ratio of 1:10 (sample:culture media). The cells were treated with 0.2 nM IrS1·Z·AuNP25 and 0.5 µM of the iridium complexes, IrS1 and Ir1. After 24 hours, the cells were washed three times with sterile PBS and trypsinized using Trypsin-EDTA (0.25%) (Gibco®-Thermo Fisher Scientific) for about 5 minutes. Fresh culture media was then added and the cells were collected and centrifuged at 1 000 rpm for 5 minutes. The supernatant was then discarded, and the cells were re-suspended in 10 ml of fresh media. The treated cells were counted using Trypan Blue dye (Gibco®-Thermo Fisher Scientific) and a haemocytometer.

The cells were then divided in two equal aliquots, one was used as a “whole cell” population and the other one was fractionated. For the fractionation of subcellular organelles, the Mitochondria isolation kit by Qiagen (Catalogue number: 37612) was used and the isolation was performed according to the protocol provided by the manufacturer. Digestion of the treated cells and subcellular organelles was performed in glass vials (V-Vials by Sigma-Aldrich, Catalogue number: Z115118). The cell samples were transferred in the vials, followed by the addition of 300 µl of ultra-pure HNO_3 (Traceselect Ultra, Aldrich – 68%) and left overnight at 80 °C. The digested samples were then transferred into polypropylene tubes for ICP-MS (Agilent) and the volume was adjusted using ultra-pure H_2O to obtain a 4% final dilution of HNO_3. (Final volume for each sample was 5 ml). The samples were kept at 4 °C until analysis.

2.6.7 Cellular uptake and subcellular localization by TEM

HeLa cells were cultured on square quartz cover slips (19 mm x 19 mm x 0.5 mm). Before seeding, the cover slips were placed in a 6-well plate, 1 cover slip per well, and sterilized using 100% ethanol for 1 hour. The cover slips were then washed twice with sterile PBS and $1x10^6$ cells were seeded on each cover slip. The cells were incubated overnight in order to adhere. The cell media was then removed and the cells were washed twice with sterile PBS. Fresh serum-free DMEM culture media was then added, followed by the addition of the samples. The IrS1 coated nanoparticles and the iridium complexes in solution were added to the cells at a ratio of 1:10 (sample:culture media). The cells were then incubated with the samples for 24 hours. In order to study cellular uptake and localization of the iridium coated nanoparticles the cells were treated with 0.2 nM IrS1·Z·AuNP25. Morphological alterations in mitochondrial structures upon targeting were evaluated by incubating the cells with 0.5 and 1 μM of the Ir1 complex. After treatment for 24 hours, the cells were washed three times with sterile PBS and were then fixed on the cover slips using freshly made 2.5% glutaraldehyde fixative in 100 nM phosphate buffer. The cells were covered in foil and kept at 4 °C overnight. The treated cells were sectioned into ultrathin slices of about 70 nm thick and placed on 200-mesh formvar-coated copper TEM grids for imaging. Processing of the cells for TEM was performed by Mr. Paul Stanley (School of Metallurgy and Materials, University of Birmingham). TEM analysis was carried out using the Jeol 1400 Ex Bio TEM at the Department of Materials and Metallurgy.

2.6.8 DCFDA/H_2DCFDA Assay for detection of ROS

HeLa cells were seeded in 60 mm dishes, $1x10^6$ cells per dish, and incubated overnight to allow the cells to adhere. The cells were then washed twice with sterile PBS and fresh serum-free DMEM culture media was added. ROS levels were evaluated after treatment of the cells with 0.2 nM of the AuNP25 samples, Z·AuNP25 and IrS1·Z·AuNP25, and 0.5 and 1 μM of the Ir1 complex. The samples were added at a ratio of 1:10 (sample:culture media) and incubated with the cells for 24 hours. The cell media was then removed and the cells were washed three times with sterile PBS to ensure removal of any excess

samples. Cells were stained with 10 μM of 2,7-dichlorodihydrofluorescein diacetate (DCFDA) (Sigma Aldrich, Catalogue number: D6883) in sterile PBS, for 30 minutes in the dark. Then, the cells were washed twice with sterile PBS and trypsinized, using Trypsin-EDTA (0.25%) (Gibco®-Thermo Fisher Scientific) for about 5 minutes. Fresh culture media was added to quench tryspsinization and the cells were collected and centrifuged at 1000 rpm for 5 minutes. The supernatant was discarded and the cells were re-suspended in 1 ml PBS supplemented with 1% FBS and transferred to FACS tubes for analysis. Samples were run on the LSRII Flow Cytometer (BD Biosciences, Oxford, UK) using the BD FACSDiva Software. Analysis was performed using FlowJo and Cytobank.

2.7 References

[1] Cairns, R. A., Harris, I. S. & Mak, T. W. 2011. Regulation of cancer cell metabolism. *Nat Rev Cancer,* 11**,** 85-95.

[2] Koppenol, W. H., Bounds, P. L. & Dang, C. V. 2011. Otto Warburg's contributions to current concepts of cancer metabolism. *Nat Rev Cancer,* 11**,** 325-337.

[3] Warburg, O. 1956. On the origin of cancer cells. *Science,* 123**,** 309-314.

[4] Hanahan, D. & Weinberg, R. A. 2011. Hallmarks of cancer: the next generation. *Cell,* 144**,** 646-674.

[5] Kroemer, G. & Pouyssegur, J. 2008. Tumor cell metabolism: cancer's Achilles' heel. *Cancer Cell,* 13**,** 472-482.

[6] Fulda, S., Galluzzi, L. & Kroemer, G. 2010. Targeting mitochondria for cancer therapy. *Nat Rev Drug Discov,* 9**,** 447-464.

[7] Vyas, S., Zaganjor, E. & Haigis, M. C. 2016. Mitochondria and Cancer. *Cell,* 166**,** 555-566.

[8] Sabharwal, S. S. & Schumacker, P. T. 2014. Mitochondrial ROS in cancer: initiators, amplifiers or an Achilles' heel? *Nat Rev Cancer,* 14**,** 709-721.

[9] Gorrini, C., Harris, I. S. & Mak, T. W. 2013. Modulation of oxidative stress as an anticancer strategy. *Nat Rev Drug Discov,* 12**,** 931-947.

[10] Trachootham, D., Alexandre, J. & Huang, P. 2009. Targeting cancer cells by ROS-mediated mechanisms: a radical therapeutic approach? *Nat Rev Drug Discov,* 8**,** 579-591.

[11] Kumar, R., Shin, W. S., Sunwoo, K., Kim, W. Y., Koo, S., Bhuniya, S. & Kim, J. S. 2015. Small conjugate-based theranostic agents: an encouraging approach for cancer therapy. *Chem Soc Rev,* 44**,** 6670-6683.

[12] Liu, J., Chen, Y., Li, G., Zhang, P., Jin, C., Zeng, L., Ji, L. & Chao, H. 2015. Ruthenium(II) polypyridyl complexes as mitochondria-targeted two-photon photodynamic anticancer agents. *Biomaterials,* 56**,** 140-153.

[13] Ma, D. L., He, H. Z., Leung, K. H., Chan, D. S. & Leung, C. H. 2013. Bioactive luminescent transition-metal complexes for biomedical applications. *Angew Chem Int Ed Engl,* 52**,** 7666-7682.

[14] Li, S. P., Lau, C. T., Louie, M. W., Lam, Y. W., Cheng, S. H. & Lo, K. K. 2013. Mitochondria-targeting cyclometalated iridium(III)-PEG complexes with tunable photodynamic activity. *Biomaterials,* 34**,** 7519-7532.

[15] Byrne, A., Burke, C. S. & Keyes, T. E. 2016. Precision targeted ruthenium(ii) luminophores; highly effective probes for cell imaging by stimulated emission depletion (STED) microscopy. *Chem Sci,* 7**,** 6551-6562.

[16] Poynton, F. E., Bright, S. A., Blasco, S., Williams, D. C., Kelly, J. M. & Gunnlaugsson, T. 2017. The development of ruthenium(ii) polypyridyl complexes and conjugates for in vitro cellular and in vivo applications. *Chem Soc Rev,* 46**,** 7706-7756.

[17] Pierroz, V., Joshi, T., Leonidova, A., Mari, C., Schur, J., Ott, I., Spiccia, L., Ferrari, S. & Gasser, G. 2012. Molecular and cellular characterization of the biological effects of ruthenium(II) complexes incorporating 2-pyridyl-2-pyrimidine-4-carboxylic acid. *J Am Chem Soc,* 134**,** 20376-20387.

[18] Zhou, Z., Liu, J., Rees, T. W., Wang, H., Li, X., Chao, H. & Stang, P. J. 2018. Heterometallic Ru-Pt metallacycle for two-photon photodynamic therapy. *Proc Natl Acad Sci U S A,* 115**,** 5664-5669.

[19] Zamora, A., Vigueras, G., Rodríguez, V., Santana, M. D. & Ruiz, J. 2018. Cyclometalated iridium(III) luminescent complexes in therapy and phototherapy. *Coord Chem Rev,* 360**,** 34-76.

[20] Fernandez-Moreira, V., Thorp-Greenwood, F. L. & Coogan, M. P. 2010. Application of d6 transition metal complexes in fluorescence cell imaging. *Chem Commun (Camb),* 46**,** 186-202.
[21] Liu, Z., Habtemariam, A., Pizarro, A. M., Fletcher, S. A., Kisova, A., Vrana, O., Salassa, L., Bruijnincx, P. C., Clarkson, G. J., Brabec, V. & Sadler, P. J. 2011. Organometallic half-sandwich iridium anticancer complexes. *J Med Chem,* 54**,** 3011-3026.
[22] Lo, K. K. 2015. Luminescent Rhenium(I) and Iridium(III) Polypyridine Complexes as Biological Probes, Imaging Reagents, and Photocytotoxic Agents. *Acc Chem Res,* 48**,** 2985-2995.
[23] Henwood, A. F. & Zysman-Colman, E. 2017. Lessons learned in tuning the optoelectronic properties of phosphorescent iridium(iii) complexes. *Chem Commun (Camb),* 53**,** 807-826.
[24] Venkatesh, V., Berrocal-Martin, R., Wedge, C. J., Romero-Canelon, I., Sanchez-Cano, C., Song, J. I., Coverdale, J. P. C., Zhang, P., Clarkson, G. J., Habtemariam, A., Magennis, S. W., Deeth, R. J. & Sadler, P. J. 2017. Mitochondria-targeted spin-labelled luminescent iridium anticancer complexes. *Chem Sci,* 8**,** 8271-8278.
[25] Wang, F. X., Chen, M. H., Hu, X. Y., Ye, R. R., Tan, C. P., Ji, L. N. & Mao, Z. W. 2016. Ester-Modified Cyclometalated Iridium(III) Complexes as Mitochondria-Targeting Anticancer Agents. *Sci Rep,* 6**,** 38954.
[26] Abbas, S., Din, I-D., Raheel, A. & Tameez Ud Din, A. 2020. Cyclometalated Iridium (III) complexes: Recent advances in phosphorescence bioimaging and sensing applications. *Appl Organometal Chem,* 34**,** e5413.
[27] Yao, S. Q., Liew, S. S., Qin, X., Zhou, J., Li, L. & Huang, W. 2020. Smart Design of Nanomaterials for Mitochondria-Targeted Nanotherapeutics. *Angew Chem Int Ed Engl*.
[28] Kwon, H. J., Kim, D., Seo, K., Kim, Y. G., Han, S. I., Kang, T., Soh, M. & Hyeon, T. 2018. Ceria Nanoparticle Systems for Selective Scavenging of Mitochondrial, Intracellular, and Extracellular Reactive Oxygen Species in Parkinson's Disease. *Angew Chem Int Ed Engl,* 57**,** 9408-9412.
[29] Haddad, S., Abanades Lazaro, I., Fantham, M., Mishra, A., Silvestre-Albero, J., Osterrieth, J. W. M., Kaminski Schierle, G. S., Kaminski, C. F., Forgan, R. S. & Fairen-Jimenez, D. 2020. Design of a Functionalized Metal-Organic Framework System for Enhanced Targeted Delivery to Mitochondria. *J Am Chem Soc,* 142**,** 6661-6674.
[30] Jhaveri, A. & Torchilin, V. 2016. Intracellular delivery of nanocarriers and targeting to subcellular organelles. *Expert Opin Drug Deliv,* 13**,** 49-70.
[31] Hong, W., Chen, D., Zhang, X., Zeng, J., Hu, H., Zhao, X. & Qiao, M. 2013. Reversing multidrug resistance by intracellular delivery of Pluronic(R) P85 unimers. *Biomaterials,* 34**,** 9602-9614.
[32] Boisselier, E. & Astruc, D. 2009. Gold nanoparticles in nanomedicine: preparations, imaging, diagnostics, therapies and toxicity. *Chem Soc Rev,* 38**,** 1759-1782.
[33] Sperling, R. A., Rivera Gil, P., Zhang, F., Zanella, M. & Parak, W. J. 2008. Biological applications of gold nanoparticles. *Chem Soc Rev,* 37**,** 1896-1908.
[34] Dreaden, E. C., Austin, L. A., Mackey, M. A. & El-Sayed, M. A. 2012. Size matters: gold nanoparticles in targeted cancer drug delivery. *Ther Deliv,* 3**,** 457-478.
[35] Dreaden, E. C., Alkilany, A. M., Huang, X., Murphy, C. J. & El-Sayed, M. A. 2012. The golden age: gold nanoparticles for biomedicine. *Chem Soc Rev,* 41**,** 2740-2779.
[36] Rogers, N. J., Claire, S., Harris, R. M., Farabi, S., Zikeli, G., Styles, I. B., Hodges, N. J. & Pikramenou, Z. 2014. High coating of Ru(II) complexes on gold nanoparticles for single particle luminescence imaging in cells. *Chem Commun* 50**,** 617-619.

[37] King, Siobhan M., Claire, Sunil, Teixeira, Rodolfo I., Dosumu, Abiola N., Carrod, Andrew J., Dehghani, Hamid, Hannon, Michael J., Ward, Andrew D., Bicknell, Roy, Botchway, Stanley W., Hodges, Nikolas J. & Pikramenou, Zoe 2018. Iridium Nanoparticles for Multichannel Luminescence Lifetime Imaging, Mapping Localization in Live Cancer Cells. *J Am Chem Soc,* 140**,** 10242-10249.

[38] Davies, A., Lewis, D. J., Watson, S. P., Thomas, S. G. & Pikramenou, Z. 2012. pH-controlled delivery of luminescent europium coated nanoparticles into platelets. *Proc Natl Acad Sci U S A,* 109**,** 1862-1867.

[39] Rogers, N. J., Jeffery, H. C., Claire, S., Lewis, D. J., Zikeli, G., Hodges, N. J., Egginton, S., Nash, G. B. & Pikramenou, Z. 2017. Tailoring iridium luminescence and gold nanoparticle size for imaging of microvascular blood flow. *Nanomedicine (Lond),* 12**,** 2725-2740.

[40] Dosumu, A. N., Claire, S., Watson, L. S., Girio, P. M., Osborne, S. A. M., Pikramenou, Z. & Hodges, N. J. 2021. Quantification by Luminescence Tracking of Red Emissive Gold Nanoparticles in Cells. *JACS Au***,** Advance Online Publication.

[41] Osborne, S. A. M. & Pikramenou, Z. 2015. Highly luminescent gold nanoparticles: effect of ruthenium distance for nanoprobes with enhanced lifetimes. *Faraday Discussions,* 185**,** 219-231.

[42] Hoshyar, N., Gray, S., Han, H. & Bao, G. 2016. The effect of nanoparticle size on in vivo pharmacokinetics and cellular interaction. *Nanomedicine (Lond),* 11**,** 673-692.

[43] Behzadi, S., Serpooshan, V., Tao, W., Hamaly, M. A., Alkawareek, M. Y., Dreaden, E. C., Brown, D., Alkilany, A. M., Farokhzad, O. C. & Mahmoudi, M. 2017. Cellular uptake of nanoparticles: journey inside the cell. *Chem Soc Rev,* 46**,** 4218-4244.

[44] Chithrani, B. D. & Chan, W. C. 2007. Elucidating the mechanism of cellular uptake and removal of protein-coated gold nanoparticles of different sizes and shapes. *Nano Lett,* 7**,** 1542-1550.

[45] Serda, R. E., Mack, A., Van De Ven, A. L., Ferrati, S., Dunner, K., Jr., Godin, B., Chiappini, C., Landry, M., Brousseau, L., Liu, X., Bean, A. J. & Ferrari, M. 2010. Logic-embedded vectors for intracellular partitioning, endosomal escape, and exocytosis of nanoparticles. *Small,* 6**,** 2691-2700.

[46] Turkevich, J., Stevenson, P. C. & Hillier, J. 1951. A Study of the Nucleation and Growth Processes in the Synthesis of Colloidal Gold. *Discuss Faraday Soc,* 11**,** 55-75.

[47] Schulz, F., Homolka, T., Bastus, N. G., Puntes, V., Weller, H. & Vossmeyer, T. 2014. Little adjustments significantly improve the Turkevich synthesis of gold nanoparticles. *Langmuir,* 30**,** 10779-10784.

[48] Ziegler, C. & Eychmuller, A. 2011. Seeded Growth Synthesis of Uniform Gold Nanoparticles with Diameters of 15-300 nm. *J Phys Chem C,* 115**,** 4502-4506.

[49] Park, J. W. & Shumaker-Parry, J. S. 2014. Structural study of citrate layers on gold nanoparticles: role of intermolecular interactions in stabilizing nanoparticles. *J Am Chem Soc,* 136**,** 1907-1921.

[50] Slinker, J. D., Gorodetsky, A. A., Lowry, M. S., Wang, J., Parker, S., Rohl, R., Bernhard, S. & Malliaras, G. G. 2004. Efficient yellow electroluminescence from a single layer of a cyclometalated iridium complex. *J Am Chem Soc,* 126**,** 2763-2767.

[51] Bertoncello, P., Kefalas, E. T., Pikramenou, Z., Unwin, P. R. & Forster, R. J. 2006. Adsorption dynamics and electrochemical and photophysical properties of thiolated ruthenium 2,2'-bipyridine monolayers. *J Phys Chem B,* 110**,** 10063-10069.

[52] Lamansky, S., Djurovich, P., Murphy, D., Abdel-Razzaq, F., Kwong, R., Tsyba, I., Bortz, M., Mui, B., Bau, R. & Thompson, M. E. 2001. Synthesis and characterization of phosphorescent cyclometalated iridium complexes. *Inorg Chem,* 40**,** 1704-1711.

[53] Lamansky, S., Djurovich, P., Murphy, D., Abdel-Razzaq, F., Lee, H. E., Adachi, C., Burrows, P. E., Forrest, S. R. & Thompson, M. E. 2001. Highly phosphorescent bis-cyclometalated iridium complexes: synthesis, photophysical characterization, and use in organic light emitting diodes. *J Am Chem Soc,* 123**,** 4304-4312.
[54] Ding, Yong, Liu, Di, Li, Jiuyan, Li, Huiting, Ma, Haiyang, Li, Deli & Niu, Rui 2020. Saturated red phosphorescent Iridium(III) complexes containing phenylquinoline ligands for efficient organic light-emitting diodes. *Dyes and Pigments,* 179**,** 108405.
[55] Wong, W. Y., Zhou, G. J., Yu, X. M., Kwok, H. S. & Tang, B. Z. 2006. Amorphous Diphenylaminofluorene-Functionalized Iridium Complexes for High-Efficiency Electrophosphorescent Light-Emitting Diodes. *Advanced Functional Materials,* 16**,** 838-846.
[56] Chen, Hsiao-Fan, Wu, Chao, Kuo, Ming-Cheng, Thompson, Mark E. & Wong, Ken-Tsung 2012. Anionic iridium complexes for solid state light-emitting electrochemical cells. *Journal of Materials Chemistry,* 22**,** 9556.
[57] Hasan, K., Bansal, A. K., Samuel, I. D., Roldan-Carmona, C., Bolink, H. J. & Zysman-Colman, E. 2015. Tuning the Emission of Cationic Iridium (III) Complexes Towards the Red Through Methoxy Substitution of the Cyclometalating Ligand. *Sci Rep,* 5**,** 12325.
[58] Scarpelli, F., Ionescu, A., Ricciardi, L., Plastina, P., Aiello, I., La Deda, M., Crispini, A., Ghedini, M. & Godbert, N. 2016. A novel route towards water-soluble luminescent iridium(iii) complexes via a hydroxy-bridged dinuclear precursor. *Dalton Trans,* 45**,** 17264-17273.
[59] Adams, S. J., Lewis, D. J., Preece, J. A. & Pikramenou, Z. 2014. Luminescent gold surfaces for sensing and imaging: patterning of transition metal probes. *ACS Appl Mater Interfaces,* 6**,** 11598-11608.
[60] Zhou, Y., Ding, Y., Huang, Y., Cai, L., Xu, J. & Ma, X. 2020. Synthesis and Structural Optimization of Iridium(III) Solvent Complex for Electrochemiluminescence Labeling of Histidine-Rich Protein and Immunoassay Applications for CRP Detection. *ACS Omega,* 5**,** 3638-3645.
[61] Bezzubov, Stanislav I., Doljenko, Vladimir D., Troyanov, Sergey I. & Kiselev, Yuri M. 2014. Tuning the photophysical and electrochemical properties of iridium(III) 2-aryl-1-phenylbenzimidazole complexes. *Inorganica Chimica Acta,* 415**,** 22-30.
[62] Colombo, M. G. & Güdel, H. U. 1993. Synthesis and High-Resolution Optical Spectroscopy of bis(2-(2-thienyl)pyridinato-C9,Ar/)(2,2,-bipyridine)iridium(III). *Inorg Chem,* 32**,** 3081-3087.
[63] Xiong, L., Zhao, Q., Chen, H., Wu, Y., Dong, Z., Zhou, Z. & Li, F. 2010. Phosphorescence imaging of homocysteine and cysteine in living cells based on a cationic iridium(III) complex. *Inorg Chem,* 49**,** 6402-6408.
[64] Colombo, M. G. , Hauser, A. & Giidel, H. U. 1993. Evidence for Strong Mixing between the LC and MLCT Excited States in Bis(2-phenylpyridinato-C2,Ar0(2,2'-bipyridine)iridium(III). *Inorg Chem,* 32**,** 3088-3092.
[65] Tao, Peng, Li, Wei-Ling, Zhang, Jing, Guo, Song, Zhao, Qiang, Wang, Hua, Wei, Bin, Liu, Shu-Juan, Zhou, Xin-Hui, Yu, Qi, Xu, Bing-She & Huang, Wei 2016. Facile Synthesis of Highly Efficient Lepidine-Based Phosphorescent Iridium(III) Complexes for Yellow and White Organic Light-Emitting Diodes. *Advanced Functional Materials,* 26**,** 881-894.
[66] Qin, W. W., Pan, Z. Y., Cai, D. H., Li, Y. & He, L. 2020. Cyclometalated iridium(iii) complexes for mitochondria-targeted combined chemo-photodynamic therapy. *Dalton Trans,* 49**,** 3562-3569.

[67] Lo, K. K., Chung, C. K., Lee, T. K., Lui, L. H., Tsang, K. H. & Zhu, N. 2003. New luminescent cyclometalated iridium(III) diimine complexes as biological labeling reagents. *Inorg Chem,* 42**,** 6886-6897.
[68] Adams, S. J., Carrod, A. J., Rochford, L. A., Walker, M. & Pikramenou, Z. 2018. Surfactant-Enhanced Luminescence Lifetime for Biomolecular Detection on Luminescent Gold Surfaces Decorated with Transition Metal Complexes. *Chemistryselect,* 3**,** 3251-3257.
[69] Li, T. & Takeoka, S. 2014. Enhanced cellular uptake of maleimide-modified liposomes via thiol-mediated transport. *Int J Nanomedicine,* 9**,** 2849-2861.
[70] Nel, A. E., Madler, L., Velegol, D., Xia, T., Hoek, E. M., Somasundaran, P., Klaessig, F., Castranova, V. & Thompson, M. 2009. Understanding biophysicochemical interactions at the nano-bio interface. *Nat Mater,* 8**,** 543-557.
[71] Chithrani, B. D., Ghazani, A. A. & Chan, W. C. 2006. Determining the size and shape dependence of gold nanoparticle uptake into mammalian cells. *Nano Lett,* 6**,** 662-668.
[72] Pernodet, N., Fang, X., Sun, Y., Bakhtina, A., Ramakrishnan, A., Sokolov, J., Ulman, A. & Rafailovich, M. 2006. Adverse effects of citrate/gold nanoparticles on human dermal fibroblasts. *Small,* 2**,** 766-773.
[73] Uboldi, C., Bonacchi, D., Lorenzi, G., Hermanns, M. I., Pohl, C., Baldi, G., Unger, R. E. & Kirkpatrick, C. J. 2009. Gold nanoparticles induce cytotoxicity in the alveolar type-II cell lines A549 and NCIH441. *Part Fibre Toxicol,* 6**,** 18.
[74] Zook, J. M., Maccuspie, R. I., Locascio, L. E., Halter, M. D. & Elliott, J. T. 2011. Stable nanoparticle aggregates/agglomerates of different sizes and the effect of their size on hemolytic cytotoxicity. *Nanotoxicology,* 5**,** 517-530.
[75] Sharma, G., Kodali, V., Gaffrey, M., Wang, W., Minard, K. R., Karin, N. J., Teeguarden, J. G. & Thrall, B. D. 2014. Iron oxide nanoparticle agglomeration influences dose rates and modulates oxidative stress-mediated dose-response profiles in vitro. *Nanotoxicology,* 8**,** 663-675.
[76] He, C., Hu, Y., Yin, L., Tang, C. & Yin, C. 2010. Effects of particle size and surface charge on cellular uptake and biodistribution of polymeric nanoparticles. *Biomaterials,* 31**,** 3657-3666.
[77] Surapaneni, S. K., Bashir, S. & Tikoo, K. 2018. Gold nanoparticles-induced cytotoxicity in triple negative breast cancer involves different epigenetic alterations depending upon the surface charge. *Sci Rep,* 8**,** 12295.
[78] Wang, J. Y., Chen, J., Yang, J., Wang, H., Shen, X., Sun, Y. M., Guo, M. & Zhang, X. D. 2016. Effects of surface charges of gold nanoclusters on long-term in vivo biodistribution, toxicity, and cancer radiation therapy. *Int J Nanomedicine,* 11**,** 3475-3485.
[79] Goodman, C. M., Mccusker, C. D., Yilmaz, T. & Rotello, V. M. 2004. Toxicity of gold nanoparticles functionalized with cationic and anionic side chains. *Bioconjug Chem,* 15**,** 897-900.
[80] Zhang, K. Y., Liu, H. W., Fong, T. T., Chen, X. G. & Lo, K. K. 2010. Luminescent dendritic cyclometalated iridium(III) polypyridine complexes: synthesis, emission behavior, and biological properties. *Inorg Chem,* 49**,** 5432-5443.
[81] Zhang, L. X., Gu, Y. Y., Wang, Y. J., Bai, L., Du, F., Zhang, W. Y., He, M., Liu, Y. J. & Chen, Y. Z. 2019. Design, Synthesis, and Anticancer Effect Studies of Iridium(III) Polypyridyl Complexes against SGC-7901 Cells. *Molecules,* 24.
[82] Cao, J. J., Tan, C. P., Chen, M. H., Wu, N., Yao, D. Y., Liu, X. G., Ji, L. N. & Mao, Z. W. 2017. Targeting cancer cell metabolism with mitochondria-immobilized phosphorescent cyclometalated iridium(iii) complexes. *Chem Sci,* 8**,** 631-640.

[83] Zhang, W. Y., Wang, Y. J., Du, F., He, M., Gu, Y. Y., Bai, L., Yang, L. L. & Liu, Y. J. 2019. Evaluation of anticancer effect in vitro and in vivo of iridium(III) complexes on gastric carcinoma SGC-7901cells. *Eur J Med Chem,* 178**,** 401-416.
[84] Lord, R. M., Zegke, M., Henderson, I. R., Pask, C. M., Shepherd, H. J. & Mcgowan, P. C. 2019. beta-Ketoiminato Iridium(III) Organometallic Complexes: Selective Cytotoxicity towards Colorectal Cancer Cells HCT116 p53. *Chemistry,* 25**,** 495-500.
[85] Tian, X., Zhu, Y., Zhang, M., Luo, L., Wu, J., Zhou, H., Guan, L., Battaglia, G. & Tian, Y. 2017. Localization matters: a nuclear targeting two-photon absorption iridium complex in photodynamic therapy. *Chem Commun (Camb),* 53**,** 3303-3306.
[86] Nam, J. S., Kang, M. G., Kang, J., Park, S. Y., Lee, S. J., Kim, H. T., Seo, J. K., Kwon, O. H., Lim, M. H., Rhee, H. W. & Kwon, T. H. 2016. Endoplasmic Reticulum-Localized Iridium(III) Complexes as Efficient Photodynamic Therapy Agents via Protein Modifications. *J Am Chem Soc,* 138**,** 10968-10977.
[87] Liu, Z., Romero-Canelon, I., Qamar, B., Hearn, J. M., Habtemariam, A., Barry, N. P., Pizarro, A. M., Clarkson, G. J. & Sadler, P. J. 2014. The potent oxidant anticancer activity of organoiridium catalysts. *Angew Chem Int Ed Engl,* 53**,** 3941-3946.
[88] Parveen, S., Hanif, M., Leung, E., Tong, K. K. H., Yang, A., Astin, J., De Zoysa, G. H., Steel, T. R., Goodman, D., Movassaghi, S., Sohnel, T., Sarojini, V., Jamieson, S. M. F. & Hartinger, C. G. 2019. Anticancer organorhodium and -iridium complexes with low toxicity in vivo but high potency in vitro: DNA damage, reactive oxygen species formation, and haemolytic activity. *Chem Commun (Camb),* 55**,** 12016-12019.
[89] Lundqvist, M., Stigler, J., Cedervall, T., Berggard, T., Flanagan, M. B., Lynch, I., Elia, G. & Dawson, K. 2011. The evolution of the protein corona around nanoparticles: a test study. *ACS Nano,* 5**,** 7503-7509.
[90] Tenzer, S., Docter, D., Kuharev, J., Musyanovych, A., Fetz, V., Hecht, R., Schlenk, F., Fischer, D., Kiouptsi, K., Reinhardt, C., Landfester, K., Schild, H., Maskos, M., Knauer, S. K. & Stauber, R. H. 2013. Rapid formation of plasma protein corona critically affects nanoparticle pathophysiology. *Nat Nanotechnol,* 8**,** 772-781.
[91] Carril, M., Padro, D., Del Pino, P., Carrillo-Carrion, C., Gallego, M. & Parak, W. J. 2017. In situ detection of the protein corona in complex environments. *Nat Commun,* 8**,** 1542.
[92] Lu, X., Xu, P., Ding, H. M., Yu, Y. S., Huo, D. & Ma, Y. Q. 2019. Tailoring the component of protein corona via simple chemistry. *Nat Commun,* 10**,** 4520.
[93] Li, Y. & Monteiro-Riviere, N. A. 2016. Mechanisms of cell uptake, inflammatory potential and protein corona effects with gold nanoparticles. *Nanomedicine (Lond),* 11**,** 3185-3203.
[94] Cho, E. C., Zhang, Q. & Xia, Y. 2011. The effect of sedimentation and diffusion on cellular uptake of gold nanoparticles. *Nat Nanotechnol,* 6**,** 385-391.
[95] Ghosh, P., Han, G., De, M., Kim, C. K. & Rotello, V. M. 2008. Gold nanoparticles in delivery applications. *Adv Drug Deliv Rev,* 60**,** 1307-1315.
[96] Nativo, P., Prior, I. A. & Brust, M. 2008. Uptake and intracellular fate of surface-modified gold nanoparticles. *ACS Nano,* 2**,** 1639-1644.
[97] Saha, K., Kim, S. T., Yan, B., Miranda, O. R., Alfonso, F. S., Shlosman, D. & Rotello, V. M. 2013. Surface functionality of nanoparticles determines cellular uptake mechanisms in mammalian cells. *Small,* 9**,** 300-305.
[98] Dausend, J., Musyanovych, A., Dass, M., Walther, P., Schrezenmeier, H., Landfester, K. & Mailander, V. 2008. Uptake mechanism of oppositely charged fluorescent nanoparticles in HeLa cells. *Macromol Biosci,* 8**,** 1135-1143.
[99] Jiang, W., Kim, B. Y., Rutka, J. T. & Chan, W. C. 2008. Nanoparticle-mediated cellular response is size-dependent. *Nat Nanotechnol,* 3**,** 145-150.

[100] Ndagi, U., Mhlongo, N. & Soliman, M. E. 2017. Metal complexes in cancer therapy - an update from drug design perspective. *Drug Des Devel Ther,* 11**,** 599-616.
[101] Zhang, K. Y., Li, S. P., Zhu, N., Or, I. W., Cheung, M. S., Lam, Y. W. & Lo, K. K. 2010. Structure, photophysical and electrochemical properties, biomolecular interactions, and intracellular uptake of luminescent cyclometalated iridium(III) dipyridoquinoxaline complexes. *Inorg Chem,* 49**,** 2530-2540.
[102] Hao, L., Li, Z. W., Zhang, D. Y., He, L., Liu, W., Yang, J., Tan, C. P., Ji, L. N. & Mao, Z. W. 2019. Monitoring mitochondrial viscosity with anticancer phosphorescent Ir(iii) complexes via two-photon lifetime imaging. *Chem Sci,* 10**,** 1285-1293.
[103] Guan, R., Xie, L., Ji, L. & Chao, H. 2020. Phosphorescent Iridium(III) Complexes for Anticancer Applications. *Eur J Inorg Chem,* 2020**,** 3978-3986.
[104] Rogozea, A., Matei, I., Turcu, I. M., Ionita, G., Sahini, V. E. & Salifoglou, A. 2012. EPR and circular dichroism solution studies on the interactions of bovine serum albumin with ionic surfactants and beta-cyclodextrin. *J Phys Chem B,* 116**,** 14245-14253.
[105] Huang, C., Ran, G., Zhao, Y., Wang, C. & Song, Q. 2018. Synthesis and application of a water-soluble phosphorescent iridium complex as turn-on sensing material for human serum albumin. *Dalton Trans,* 47**,** 2330-2336.
[106] Gu, W., Zhang, T., Gao, J., Wang, Y., Li, D., Zhao, Z., Jiang, B., Dong, Z. & Liu, H. 2019. Albumin-bioinspired iridium oxide nanoplatform with high photothermal conversion efficiency for synergistic chemo-photothermal of osteosarcoma. *Drug Deliv,* 26**,** 918-927.
[107] Kratz, F. 2008. Albumin as a drug carrier: design of prodrugs, drug conjugates and nanoparticles. *J Control Release,* 132**,** 171-183.
[108] Ambika, S., Manojkumar, Y., Arunachalam, S., Gowdhami, B., Meenakshi Sundaram, K. K., Solomon, R. V., Venuvanalingam, P., Akbarsha, M. A. & Sundararaman, M. 2019. Biomolecular Interaction, Anti-Cancer and Anti-Angiogenic Properties of Cobalt(III) Schiff Base Complexes. *Sci Rep,* 9**,** 2721.
[109] Lu, Lihua, He, Hong-Zhang, Zhong, Hai-Jing, Liu, Li-Juan, Chan, Daniel Shiu-Hin, Leung, Chung-Hang & Ma, Dik-Lung 2014. Luminescent detection of human serum albumin in aqueous solution using a cyclometallated iridium(III) complex. *Sensors and Actuators B: Chemical,* 201**,** 177-184.
[110] Sun, C., Yang, J., Wu, X., Huang, X., Wang, F. & Liu, S. 2005. Unfolding and refolding of bovine serum albumin induced by cetylpyridinium bromide. *Biophys J,* 88**,** 3518-3524.
[111] Yu, J., Chen, Y., Xiong, L., Zhang, X. & Zheng, Y. 2019. Conductance Changes in Bovine Serum Albumin Caused by Drug-Binding Triggered Structural Transitions. *Materials,* 12**,** 1022.
[112] Spadavecchia, J., Movia, D., Moore, C., Maguire, C. M., Moustaoui, H., Casale, S., Volkov, Y. & Prina-Mello, A. 2016. Targeted polyethylene glycol gold nanoparticles for the treatment of pancreatic cancer: from synthesis to proof-of-concept in vitro studies. *Int J Nanomedicine,* 11**,** 791-822.
[113] Farooq, M. U., Novosad, V., Rozhkova, E. A., Wali, H., Ali, A., Fateh, A. A., Neogi, P. B., Neogi, A. & Wang, Z. 2018. Gold Nanoparticles-enabled Efficient Dual Delivery of Anticancer Therapeutics to HeLa Cells. *Sci Rep,* 8**,** 2907.
[114] Cho, E. C., Xie, J., Wurm, P. A. & Xia, Y. 2009. Understanding the role of surface charges in cellular adsorption versus internalization by selectively removing gold nanoparticles on the cell surface with a I2/KI etchant. *Nano Lett,* 9**,** 1080-1084.
[115] Kodiha, M., Wang, Y. M., Hutter, E., Maysinger, D. & Stochaj, U. 2015. Off to the organelles - killing cancer cells with targeted gold nanoparticles. *Theranostics,* 5**,** 357-370.

[116] Kamogashira, T., Hayashi, K., Fujimoto, C., Iwasaki, S. & Yamasoba, T. 2017. Functionally and morphologically damaged mitochondria observed in auditory cells under senescence-inducing stress. *NPJ Aging Mech Dis,* 3**,** 2.
[117] Sorvina, A., Bader, C. A., Darby, J. R. T., Lock, M. C., Soo, J. Y., Johnson, I. R. D., Caporale, C., Voelcker, N. H., Stagni, S., Massi, M., Morrison, J. L., Plush, S. E. & Brooks, D. A. 2018. Mitochondrial imaging in live or fixed tissues using a luminescent iridium complex. *Sci Rep,* 8**,** 8191.
[118] He, L., Wang, K. N., Zheng, Y., Cao, J. J., Zhang, M. F., Tan, C. P., Ji, L. N. & Mao, Z. W. 2018. Cyclometalated iridium(iii) complexes induce mitochondria-derived paraptotic cell death and inhibit tumor growth in vivo. *Dalton Trans,* 47**,** 6942-6953.
[119] Salatin, S. & Yari Khosroushahi, A. 2017. Overviews on the cellular uptake mechanism of polysaccharide colloidal nanoparticles. *J Cell Mol Med,* 21**,** 1668-1686.
[120] Gao, H., Shi, W. & Freund, L. B. 2005. Mechanics of receptor-mediated endocytosis. *Proc Natl Acad Sci U S A,* 102**,** 9469-9474.
[121] Zhang, S., Li, J., Lykotrafitis, G., Bao, G. & Suresh, S. 2009. Size-Dependent Endocytosis of Nanoparticles. *Adv Mater,* 21**,** 419-424.
[122] Donahue, N. D., Acar, H. & Wilhelm, S. 2019. Concepts of nanoparticle cellular uptake, intracellular trafficking, and kinetics in nanomedicine. *Adv Drug Deliv Rev,* 143**,** 68-96.
[123] Winey, M., Meehl, J. B., O'toole, E. T. & Giddings, T. H., Jr. 2014. Conventional transmission electron microscopy. *Mol Biol Cell,* 25**,** 319-323.
[124] Guan, R., Chen, Y., Zeng, L., Rees, T. W., Jin, C., Huang, J., Chen, Z. S., Ji, L. & Chao, H. 2018. Oncosis-inducing cyclometalated iridium(iii) complexes. *Chem Sci,* 9**,** 5183-5190.
[125] Frankl, A., Mari, M. & Reggiori, F. 2015. Electron microscopy for ultrastructural analysis and protein localization in Saccharomyces cerevisiae. *Microb Cell,* 2**,** 412-428.
[126] Mcintosh, J. R. 2001. Electron microscopy of cells: a new beginning for a new century. *J Cell Biol,* 153**,** F25-32.
[127] Wang, P., Wu, Q., Wang, F., Zhang, Y., Tong, L., Jiang, T., Gu, C., Huang, S., Wang, H., Bu, S. & Zhou, J. 2018. Evaluating cellular uptake of gold nanoparticles in HL-7702 and HepG2 cells for plasmonic photothermal therapy. *Nanomedicine (Lond),* 13**,** 2245-2259.
[128] Hsiao, I. L., Bierkandt, F. S., Reichardt, P., Luch, A., Huang, Y. J., Jakubowski, N., Tentschert, J. & Haase, A. 2016. Quantification and visualization of cellular uptake of TiO2 and Ag nanoparticles: comparison of different ICP-MS techniques. *J Nanobiotechnology,* 14**,** 50.
[129] Albanese, A. & Chan, W. C. 2011. Effect of gold nanoparticle aggregation on cell uptake and toxicity. *ACS Nano,* 5**,** 5478-5489.
[130] Abdelkhaliq, A., Van Der Zande, M., Punt, A., Helsdingen, R., Boeren, S., Vervoort, J. J. M., Rietjens, Imcm & Bouwmeester, H. 2018. Impact of nanoparticle surface functionalization on the protein corona and cellular adhesion, uptake and transport. *J Nanobiotechnology,* 16**,** 70.
[131] Zhu, M., Nie, G., Meng, H., Xia, T., Nel, A. & Zhao, Y. 2013. Physicochemical properties determine nanomaterial cellular uptake, transport, and fate. *Acc Chem Res,* 46**,** 622-631.
[132] Puckett, C. A. & Barton, J. K. 2007. Methods to explore cellular uptake of ruthenium complexes. *J Am Chem Soc,* 129**,** 46-47.
[133] Sun, S., Huang, Y., Zhou, C., Chen, S., Yu, M., Liu, J. & Zheng, J. 2018. Effect of Hydrophobicity on Nano-Bio Interactions of Zwitterionic Luminescent Gold Nanoparticles at the Cellular Level. *Bioconjug Chem,* 29**,** 1841-1846.
[134] Foroozandeh, P. & Aziz, A. A. 2018. Insight into Cellular Uptake and Intracellular Trafficking of Nanoparticles. *Nanoscale Res Lett,* 13**,** 339.

[135] Kumar, D., Mutreja, I., Chitcholtan, K. & Sykes, P. 2017. Cytotoxicity and cellular uptake of different sized gold nanoparticles in ovarian cancer cells. *Nanotechnology,* 28**,** 475101.
[136] Jeena, M. T., Kim, S., Jin, S. & Ryu, J. H. 2019. Recent Progress in Mitochondria-Targeted Drug and Drug-Free Agents for Cancer Therapy. *Cancers (Basel),* 12.
[137] Zorova, L. D., Popkov, V. A., Plotnikov, E. Y., Silachev, D. N., Pevzner, I. B., Jankauskas, S. S., Babenko, V. A., Zorov, S. D., Balakireva, A. V., Juhaszova, M., Sollott, S. J. & Zorov, D. B. 2018. Mitochondrial membrane potential. *Anal Biochem,* 552**,** 50-59.
[138] Zielonka, J., Joseph, J., Sikora, A., Hardy, M., Ouari, O., Vasquez-Vivar, J., Cheng, G., Lopez, M. & Kalyanaraman, B. 2017. Mitochondria-Targeted Triphenylphosphonium-Based Compounds: Syntheses, Mechanisms of Action, and Therapeutic and Diagnostic Applications. *Chem Rev,* 117**,** 10043-10120.
[139] Li, Y., Liu, B., Xu, C. X., He, L., Wan, Y. C., Ji, L. N. & Mao, Z. W. 2020. Mitochondria-targeted phosphorescent cyclometalated iridium(III) complexes: synthesis, characterization, and anticancer properties. *J Biol Inorg Chem,* 25**,** 597-607.
[140] Li, Y., Liu, B., Xu, C. X., He, L., Wan, Y. C., Ji, L. N. & Mao, Z. W. 2020. Mitochondria-targeted phosphorescent cyclometalated iridium(III) complexes: synthesis, characterization, and anticancer properties. *J Biol Inorg Chem*.
[141] Zhang, W. J., Hu, X. L., Shen, Q. & Xing, D. 2019. Mitochondria-specific drug release and reactive oxygen species burst induced by polyprodrug nanoreactors can enhance chemotherapy (vol 10, 1704, 2019). *Nature Communications,* 10.
[142] Porporato, P. E., Filigheddu, N., Pedro, J. M. B., Kroemer, G. & Galluzzi, L. 2018. Mitochondrial metabolism and cancer. *Cell Res,* 28**,** 265-280.
[143] Wallace, D. C. 2012. Mitochondria and cancer. *Nat Rev Cancer,* 12**,** 685-698.
[144] Kumari, S., Badana, A. K., Mohan, G. M., Shailender, G. & Malla, R. 2018. Reactive Oxygen Species: A Key Constituent in Cancer Survival. *Biomarker Insights,* 13.
[145] Panieri, E. & Santoro, M. M. 2016. ROS homeostasis and metabolism: a dangerous liason in cancer cells. *Cell Death Dis,* 7**,** e2253.
[146] Panieri, E. & Santoro, M. M. 2015. ROS signaling and redox biology in endothelial cells. *Cell Mol Life Sci,* 72**,** 3281-3303.
[147] Harris, I. S. & Brugge, J. S. 2015. Cancer: The enemy of my enemy is my friend. *Nature,* 527**,** 170-171.
[148] Chen, Y., Qiao, L., Ji, L. & Chao, H. 2014. Phosphorescent iridium(III) complexes as multicolor probes for specific mitochondrial imaging and tracking. *Biomaterials,* 35**,** 2-13.

Chapter 3:

3. Development of luminescent iridium gold nanoparticles with optimal cellular uptake to study subcellular localization in cancer cells

3.1 Introduction

Current approaches for treating cancer include the targeting of tumor-specific oncogenic mediators that control essential biological processes for the survival of cancer cells[1, 2]. One of the major challenges in developing effective treatments for cancer is the astounding level of heterogeneity displayed by tumors, which is mainly determined by the genetic variability and epigenetic plasticity of cancer cells[3, 4]. What is more, recent advances in the oncology field that focus on the decoding of the genomic content of tumors have led to the conclusion that no "perfect" cancer-specific targets exist, as there are no universally abnormal molecules or cellular processes in cancer cells that are fully unessential for normal cells[5, 6]. Therefore, one of the most commonly and successfully used therapeutic approaches for treating cancer is the use of conventional chemotherapy to target DNA[7-9]. However, the effectiveness of DNA-targeted chemotherapeutics is often compromised by the inability of the delivery methods currently used in the clinic to deliver doses high enough to induce DNA damage and kill all cancer cells while sparing normal cells, which leads to long-lasting and severe side effects[10, 11].

Moreover, recent advances in the oncology field have recognised that besides DNA, nuclear proteins found in eukaryotic cells are also actively involved in the development of carcinogenesis, as they control many cellular processes that are essential for proliferation and survival of cancer cells, with many of these processes taking place in specialized compartments within the nucleus[12, 13]. Therefore, nuclear proteins such as histones and chromatin have become popular targets of cancer-targeted therapies[12, 14]. But similarly to DNA-targeting drugs, therapeutic approaches to target nuclear proteins lack specificity and are highly associated with adverse side effects[15].

There is a growing interest in the development of luminescent multifunctional theranostic complexes that can efficiently penetrate the nuclear membrane and target DNA and/or nuclear proteins, which can also be used as imaging agents to monitor morphological changes in the nucleus upon targeting[16-18]. Recently, many transition metal complexes have gained a lot of attention in the nanotechnology field for their ability to be easily modified through changing the type of ligands attached to the metal core in order to enhance cellular uptake and achieve efficient nuclear localization[16, 18, 19].

The ability of metal complexes to penetrate the cell membrane and internalize successfully into cells is highly dependent on the different types of ligands present in different complexes, as they determine the solubility and the hydrophobicity/hydrophilicity of a complex[20]. For instance, incorporation of long alkyl chains has been previously reported to improve significantly the hydrophobicity of metal complexes and thus, their cellular uptake in malignant cells, with the uptake efficacy being enhanced with increasing length of the alkyl chain[21].

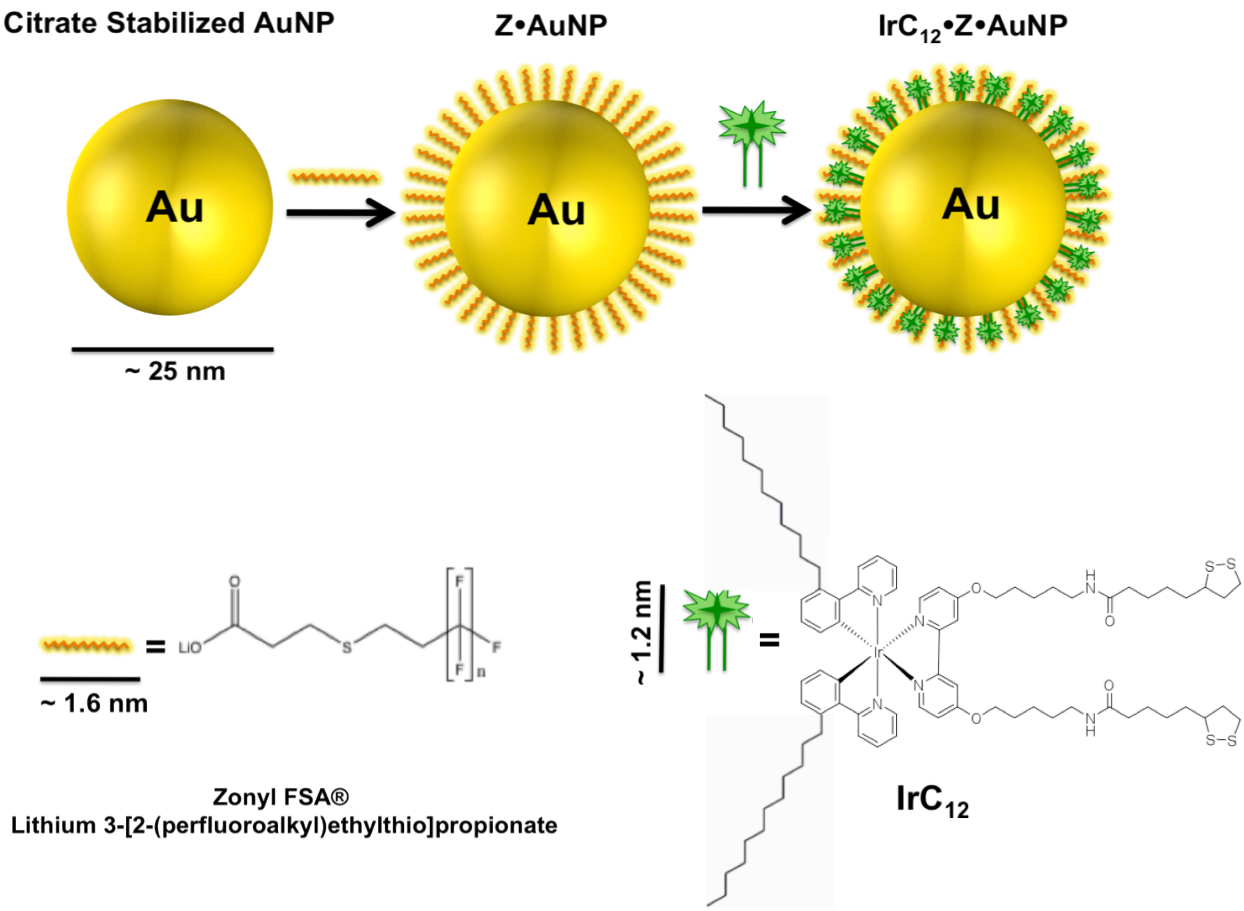
Cyclometalated iridium(III) complexes are popular luminescent complexes for biomedical imaging applications as they exhibit a distinctive luminescent signal for detection in biological samples and their ability to be easily modified allows efficient localization into different organelles[22, 23]. Previously published studies have reported the ability of organometallic iridium complexes to penetrate the nuclear membrane and interact with DNA and cellular proteins in cancer cells[24-27]. What is more, when compared to conventional organic labels, iridium(III) complexes have advantageous photophysical properties, including high photostability, large Stoke shifts and long-lived lifetimes[28, 29], which provide enhanced signal detection sensitivity as the short-lived signal from auto-fluorescence in cells can be easily gated out[30]. Therefore, the advantageous photophysical properties of the iridium(III) complexes, along with their enhanced cell permeability, make them ideal as biological reagents for use in biomedical applications, including cancer theranostics and live cell imaging[31].

Even though metal complexes can be easily tuned to guide subcellular localization, their use as theranostic agents can still be rather challenging due to the inability of all complexes to reach successfully the target site[32]. It has been previously reported that subsequent to internalization of metal complexes by endocytosis into cells, the complexes fail to escape from the internalized endosomes and thus, accumulate within the cytoplasm, which inhibits their further localization into different organelles[33]. This results to the complexes not always being used to their full potential, which can often lead to off-target toxicity due to imprecise subcellular localization[34].

Recent advances in the nanomedicine field have led to the development of multifunctional nanometarials, aiming to overcome the aforementioned challenges and successfully deliver a complex to the target site[35, 36]. The use of nanocarriers as a vehicle to deliver targeting complexes provides enhanced bioavailability, as accumulation and retention of the complexes within the intracellular environment are significantly improved[37]. Furthermore, the use of nanocarriers can aid in maximizing the therapeutic efficacy of targeting complexes, as high administration doses can be delivered while minimizing off-target toxicity due to localized delivery[38]. Therefore, there is currently a growing interest in the development of novel, multifunctional theranostic nanomaterials with highly efficient cellular uptake and improved subcellular localization in malignant cells.

In order to achieve optimal cellular uptake and nuclear localization in cancer cells, luminescent iridium gold nanoparticles (AuNPs) were developed in the presence of an iridium complex incorporating a dodecyl chain, IrC_{12} (Scheme 3-1). The dodecyl chain incorporated on the phenylpyridine ligand increases the hydrophobicity of the complex and improves stabilization upon attachment to the gold surface[39], which can enhance permeability across the cell membrane and provide a strong luminescent signal during live cell imaging[20]. Also, the IrC_{12} complex has a bipyridine ligand with long legs for conjugation to the gold surface, as it has been previously reported that a long distance between the metal centre and the nanoparticle enhances the photophysical properties of the complex[40, 39]. Photophysical characterization of both the IrC_{12} complex and the IrC_{12} coated nanoparticles was performed, indicating the suitability of the luminescent AuNPs for luminescence imaging and cellular uptake studies by flow cytometry. The cellular

uptake efficacy of the iridium functionalized AuNPs was evaluated by fluorescence-activated cell sorting (FACS), while their efficient nuclear localization in HeLa cells was supported both by live cell imaging using confocal microscopy and inductively coupled plasma mass spectrometry (ICP-MS) in fractionated cell lysates.



Scheme 3-1. **Schematic of coating AuNPs with the zonyl fluorosurfactant and the luminescent iridium(III) complex, IrC_{12}.**

3.2 Chapter outline

In this chapter, novel, luminescent gold nanoparticles are introduced for the improved delivery and subcellular localization of a cyclometalated iridium complex in cancer cells. Photophysical characterization of both the iridium complex and the luminescent nanoparticles is presented, confirming that the complex retains its luminescent properties upon conjugation to the gold surface. The iridium coated nanoparticles absorb light within the visible region, between 400 and 450 nm, and emit at λ_{max}=595 nm, which makes them ideal for cellular uptake studies by FACS and confocal luminescence microscopy. The ability of the iridium complex to interact with cellular proteins, both in solution and upon conjugation to the gold surface, was shown using CD spectroscopy. The stability of the IrC_{12} complex and the iridium functionalized nanoparticles within the intracellular environment was evident through the enhanced luminescence detected in cancer cells after treatment. Treatment of cancer cells with the IrC_{12} complex resulted to an increase in the lifetime of the complex, further confirming its interaction with intracellular proteins. The increase observed in the luminescence lifetime of the IrC_{12} complex in fractionated lysates of treated cells was higher in the nucleus when compared to other organelles, suggesting the strong interaction of the IrC_{12} complex with nuclear proteins. The cytotoxicity of the iridium complex and the luminescent nanoparticles in cancer cells was evaluated using the MTT assay. Cellular uptake studies performed by FACS and confocal microscopy indicated that the use of gold nanoparticles as a scaffold to deliver the iridium complex in cancer cells improves significantly its cellular entry and internalization within the intracellular space. Live cell imaging revealed the strong luminescent signal of the iridium complex in the nucleus and cytoplasm of cancer cells treated with the IrC_{12} coated nanoparticles. The nuclear localization of the luminescent nanoparticles was further confirmed by ICP-MS, as elemental analysis suggested higher accumulation of the IrC_{12} modified nanoparticles in the nucleus of the treated cells when compared to cytosol and mitochondria. The penetration of the nuclear membrane observed by the iridium coated nanoparticles as well as their ability to interact with proteins within an intracellular environment offer opportunities for the development of novel nanoprobes for site-specific delivery of theranostic complexes in cancer cells.

3.3 Results and Discussion

3.3.1 Synthesis and Characterization of IrC_{12}

The cyclometalated iridium complex, IrC_{12}, was synthesised and characterized by Andrew Carrod, School of Chemistry, University of Birmingham (Appendix B – Scheme B-1 and Figure B-1). The synthesis of the iridium complex was performed following previously published methods by the Pikramenou group[39, 41, 42].

3.3.2 Photophysical characterization of IrC_{12}

Photophysical characterization of the IrC_{12} complex in water displayed absorption bands within the UV-Vis region, with intense high-energy absorption bands at 230 and 260 nm, which are assigned to LC based transitions that arise from the spin-allowed π-π* transitions from the coordinating ligands. The iridium complex also displayed absorption bands at 300 and 350 nm that extend to lower-energy bands between 400 and 450 nm, which based on previously reported assignments are attributed to ^{1}MLCT transitions[39, 43]. The excitation profile of IrC_{12} displayed the characteristic absorption profile of the complex within the UV-Vis region. Excitation of the complex at 350 and 405 nm produces a broad emission peak with a λ_{max} at 585 nm, arising from contributions of both ^{3}MLCT and ^{3}LMCT transitions[39, 43-46] (Figure 3-1). The strong emission peak observed upon excitation of the IrC_{12} complex in water at 405 nm, suggests the suitability of the complex for use in cellular uptake studies by FACS and confocal luminescence microscopy.

The luminescence lifetime of the IrC_{12} complex in water using two-component analysis is 104 ns (a_1=26%) and 260 ns (a_3=74%), which agrees with previously published analysis of phenyl-pyridine iridium complexes[47, 48] (Appendix B – Figure B-3).

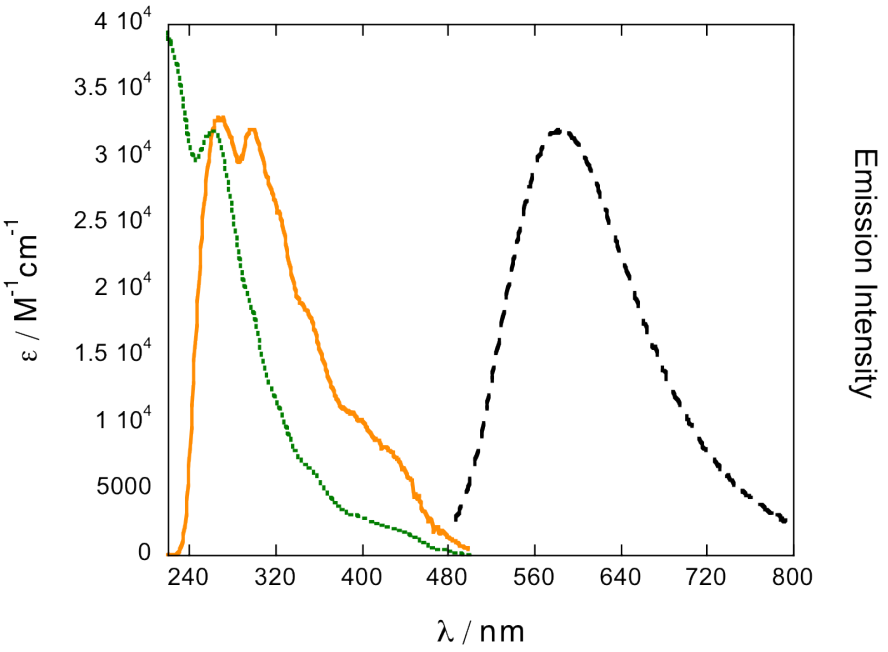


Figure 3-1. Phtophysical characterisation of IrC_{12} in water. UV-Vis absorption spectrum (dotted line) of 30 μM IrC_{12} in water. Excitation spectrum (solid line) λ_{em} = 585 nm and emission spectrum (dashed line) of 30 μM IrC_{12} in water λ_{exc} = 350 and 405 nm.

3.3.3 Synthesis and characterization of AuNPs

For the purposes of the present study, water-soluble, monodisperse 25 nm AuNPs (AuNP25) were synthesised according to an adapted protocol by the Pikramenou group, which is based on an improved method by Turkevich et.[49] and a protocol published by Ziegler et al.[50]. The synthesis of AuNP25 is described in Chapter 2. In brief, 13 nm AuNPs were initially synthesized through reduction of gold by citrate and were then grown into citrate-stabilized AuNP25. The characterization of AuNP25 by DLS, ζ-potential, TEM and SPR is presented in Chapter 2.

3.3.4 Preparation and characterization of IrC_{12}·Z·AuNP25

Prior to attaching the luminescent IrC_{12} complex on AuNP25, the fluorinated surfactant Zonyl FSA was used to further stabilize the gold surface. The use of the fluorinated surfactant aids in preventing nanoparticle aggregation that can arise from the direct replacement of the negatively charged citrate ions present on the surface of AuNPs by the positively charged luminescent complex[39, 51, 40]. The zonyl FSA coated AuNP25 were isolated by centrifugation to remove excess surfactant and produce purified Z·AuNP25. The coating of AuNP25 with zonyl FSA resulted to a 1 nm shift in the SPR band and an increase in the intensity distribution of the nanoparticles as measured by DLS, confirming the presence of the fluorinated surfactant on the gold surface. The characterization of the surfactant modified AuNP25 by DLS, ζ-potential, TEM and SPR is presented in Chapter 2.

A stock solution of 1 mM of the IrC_{12} complex was prepared in methanol and added in 2 µl aliquots in an aqueous solution of Z·AuNP25. The conjugation of the iridium complex to the gold surface subsequent to each addition was confirmed via monitoring the shift in the SPR band of the nanoparticles within the visible region (Figure 3-2). The red shift produced in the SPR allowed the maximum concentration of IrC_{12} that can be used to coat the gold surface without causing nanoparticle aggregation to be determined. Upon coating of Z·AuNP25 with 40 µM of IrC_{12} a 5 nm shift in the SPR band was observed, as λ_{max} shifted from 520 nm to 525 nm.

The iridium coated nanoparticles were then isolated by size exclusion chromatography using Sephadex G-10 to remove excess molecular complex and produce purified IrC_{12}·Z·AuNP25. After isolation of IrC_{12}·Z·AuNP25, the λ_{max} of the SPR band remained the same, confirming that the iridium coating on the gold surface was not altered during the purification process (Figure 3-3).

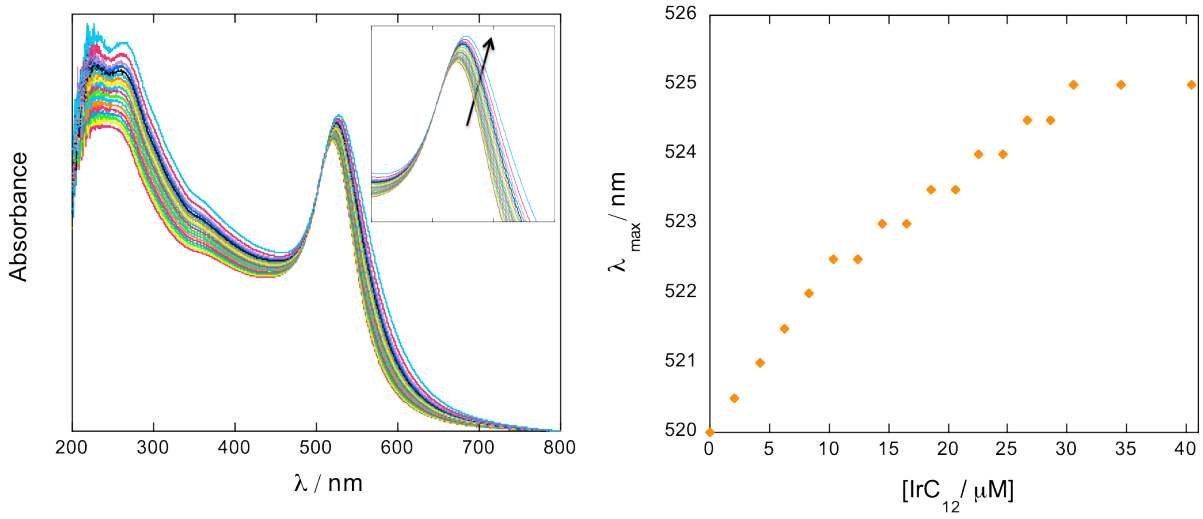


Figure 3-2. **(Left) UV-Vis titration of 1 mM IrC_{12} into 2 nM Z·AuNP25 in water. (Right) The λ_{max} of the SPR band versus the concentration of the IrC_{12} complex added.**

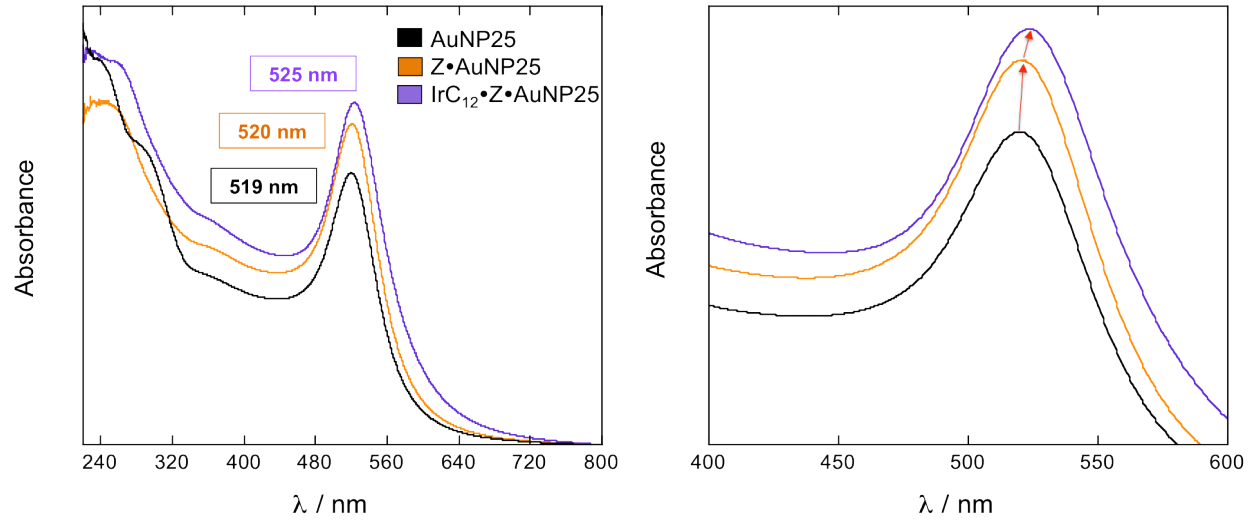


Figure 3-3. **(Left) UV-Vis absorption spectra of AuNP25 and purified Z·AuNP25 and IrC_{12}·Z·AuNP25 in water. (Right) Expanded region of absorption spectra showing the shift in the SPR band upon coating with the IrC_{12} complex.**

The attachment of the IrC_{12} complex to the surface of AuNPs was further confirmed by DLS, as an increase was observed in the intensity distribution of IrC_{12}·Z·AuNP25 when compared to Z·AuNP25 (DLS data are summarized in Table 3-1).

In order to evaluate whether the incorporation of the dodecyl chain on the phenylpyridine ligand of the IrC_{12} complex can aid in improving the uptake of IrC_{12}·Z·AuNP25 in cancer cells, iridium coated AuNPs were also developed, under the same conditions, using the cyclometalated iridium(III) complex, IrbpySS (Figure 3-4). The IrbpySS complex has the same chemical structure as IrC_{12} but without the dodecyl chain on the phenylpyridine ligand. Both the synthesis and characterization of the IrbpySS complex were performed by Dr. Samuel Adams, School of Chemistry, University of Birmingham, and the work has been published by the Pikramenou group[42] .

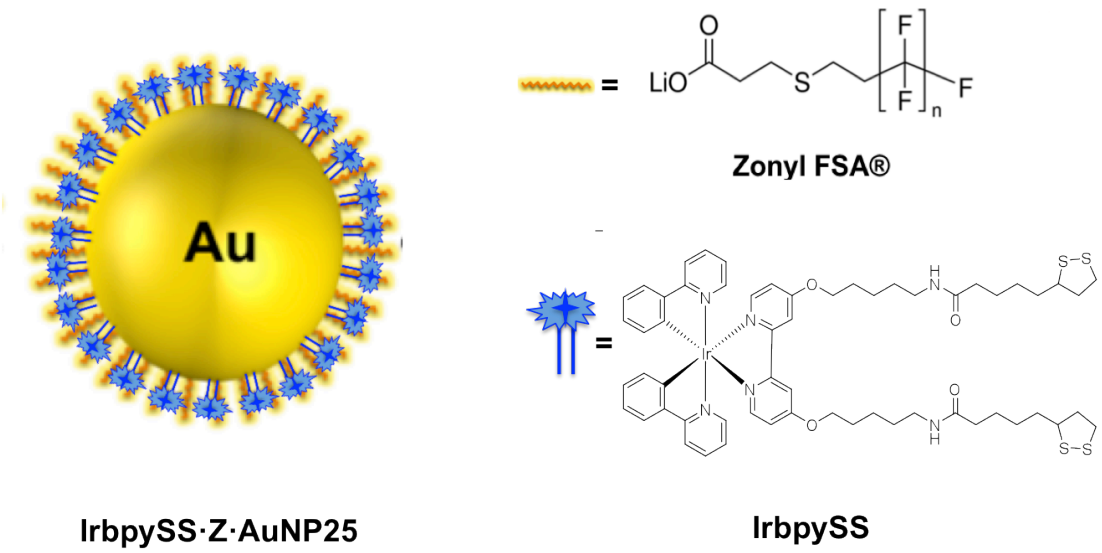


Figure 3-4. Functionalized AuNP25 with the zonyl fluorosurfactant and the IrbpySS complex.

The luminescent nanoparticles coated with the IrbpySS complex were prepared in the same manner as IrC_{12}·Z·AuNP25. In brief, AuNP25 were initially coated with the fluorinated surfactant zonyl FSA to produce Z·AuNP25. Subsequently, a stock solution of the IrbpySS complex of 1 mM was prepared in methanol, and added in 2 μl aliquots in an aqueous solution of Z·AuNP25. The attachment of IrbpySS to the gold surface after each addition was confirmed through monitoring and recording the shift in the SPR band of the nanoparticles within the visible region (Figure 3-5). Similarly to IrC_{12}, the maximum

concentration of IrbpySS that can be attached to the gold surface without causing aggregation of nanoparticles was determined to be 40 μM. Upon addition of 40 μM of IrbpySS to Z·AuNP25, a 5 nm shift was observed in the SPR band, with λ_{max} shifting from 520 nm to 525 nm.

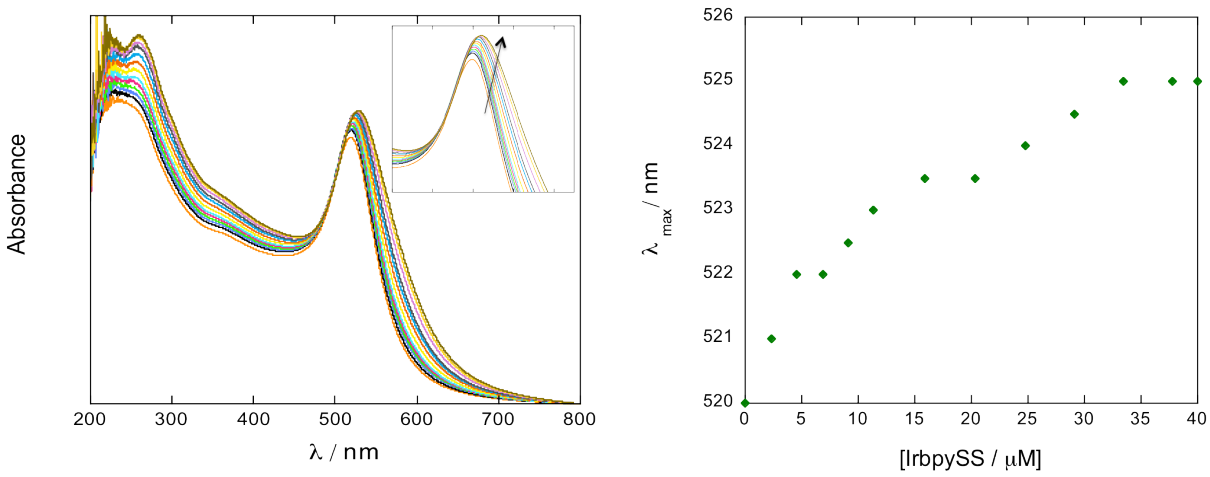


Figure 3-5. (Left) UV-Vis titration of 1 mM IrbpySS on 2 nM Z·AuNP25 in water. (Right) The λ_{max} of the SPR band versus the concentration of the IrbpySS complex added.

The presence of the IrbpySS complex on the surface of the surfactant modified AuNPs was further confirmed by DLS, as an evident increase was observed in the intensity distribution of IrbpySS·Z·AuNP25 when compared to Z·AuNP25 (DLS data are summarized in Table 3-1). Overlay of the intensity distributions of IrbpySS·Z·AuNP25 and IrC_{12}·Z·AuNP25 suggests a slightly larger increase in the hydrodynamic diameter of the IrC_{12} coated nanoparticles, which could be attributed to the presence of the dodecyl chain on the phenylpyridine ligand of the complex (Figure 4-6). The increase in the intensity distribution of both the IrC_{12} and IrbpySS functionalized AuNPs along with the relatively low PDI observed indicate the successful conjugation of the iridium complexes to the gold surface and the monodispersity of the functionalized nanoparticles. Prior to proceeding with experimental studies in cells, the high monodispersity of both IrC_{12}·Z·AuNP25 and IrbpySS·Z·AuNP25 was further validated by TEM, as imaging analysis of IrC_{12}·Z·AuNP25 and IrbpySS·Z·AuNP25 revealed spherical AuNPs of about 25 nm in diameter (n=15) (Figure 3-7).

	Size by Number / nm	Size by Intensity / nm	Z-average / nm	PDI
AuNP25	24 ± 6	34 ± 9	31	0.055
Z•AuNP25	28 ± 7	43 ± 12	39	0.085
IrC_{12}•Z•AuNP25	29 ± 9	80 ± 24	63	0.247
IrbpySS•Z•AuNP25	28 ± 8	74 ± 22	56	0.235

Table 3-1. DLS for AuNP25, Z·AuNP25, IrC_{12}·Z·AuNP25 and IrbpySS·Z·AuNP25 in water. Results display sizes by number and intensity (nm), z-average (nm) and PDI.

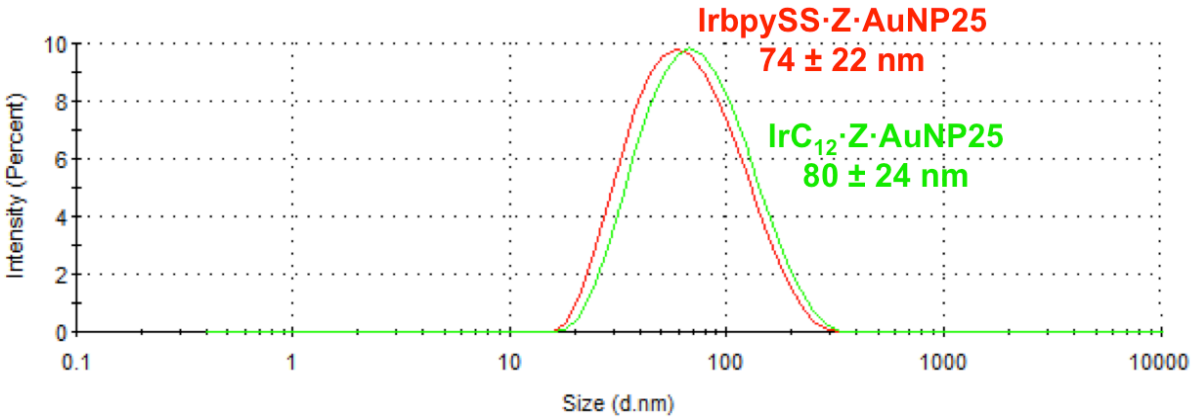


Figure 3-6. DLS intensity distributions of IrC_{12}·Z·AuNP25 and IrbpySS·Z·AuNP25.

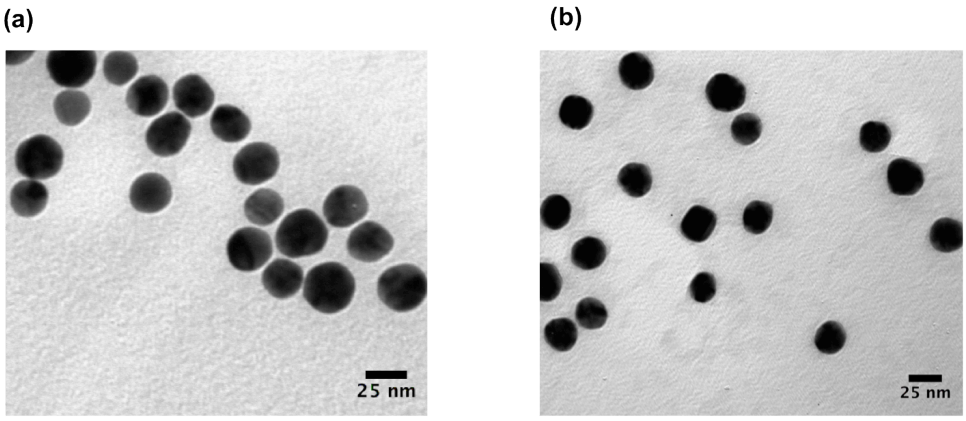


Figure 3-7. TEM images displaying the monodispersity and spherical nature of the iridium coated AuNP25. (a) IrC_{12}·Z·AuNP25 and (b) IrbpySS·Z·AuNP25 (Scale bar=25 nm).

3.3.5 Photophysical characterization of IrC_{12}·Z·AuNP25

The photophysical properties of IrC_{12}·Z·AuNP25 were investigated in order to determine whether the iridium complex retains its characteristic luminescent properties when conjugated to the gold surface. Upon excitation of IrC_{12}·Z·AuNP25 at 350 and 405 nm, a broad emission peak is produced with a λ_{max} at 595 nm. The emission maximum of IrC_{12}·Z·AuNP25 was red-shifted by 10 nm when compared to the IrC_{12} complex in solution, which could be attributed to changes in the surrounding environment of the complex due to the presence of the fluorinated surfactant[41, 39]. The excitation spectrum of IrC_{12}·Z·AuNP25 displayed the characteristic absorption bands of the IrC_{12} complex that are responsible for the broad emission peak observed, suggesting that the complex translates its luminescent properties onto the functionalized AuNPs (Figure 3-8).

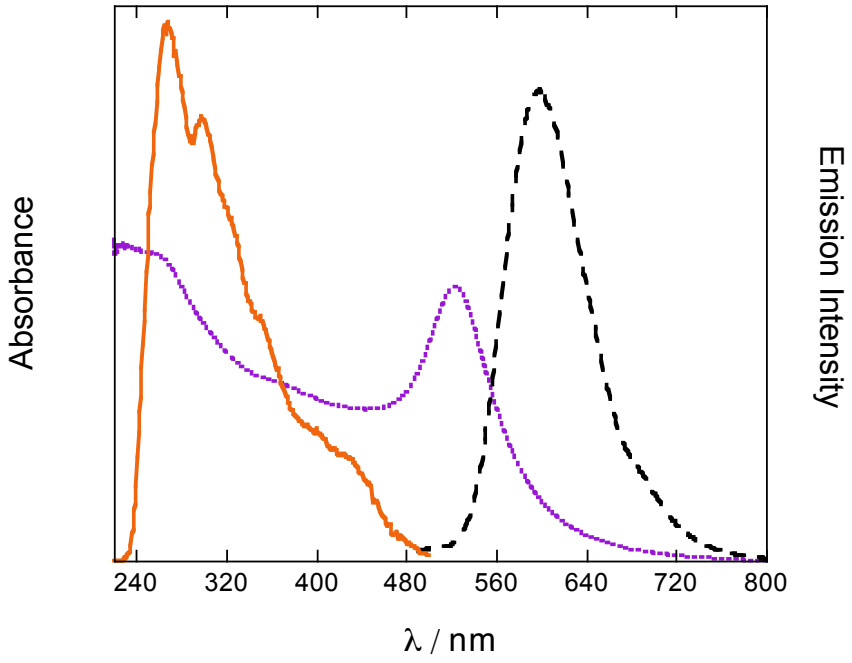


Figure 3-8. Photophysical characterisation of 2 nM IrC_{12}·Z·AuNP25 in water. UV-Vis absorbance of purified IrC_{12}·Z·AuNP25 (dotted line). Excitation spectrum, λ_{em}=595 nm (solid line) and emission spectrum of IrC_{12}·Z·AuNP25 in water, λ_{exc} = 350 and 405 nm (dashed line).

In order to validate that the bathochromic red shift observed in the emission of IrC_{12}·Z·AuNP25 is attributed to the presence of the fluorinated surfactant, the emission of 30 µM IrC_{12} subsequent to the addition of 10 µl of 2.5 % zonyl FSA in water (2 µM) was recorded (Figure 3-9). The emission maximum of the IrC_{12} complex in water was red-shifted by 5 nm in the presence of the fluorinated surfactant, indicating that the interaction between IrC_{12} and the surfactant alters the surrounding environment of the complex and possibly changes the charge transfer transition[39].

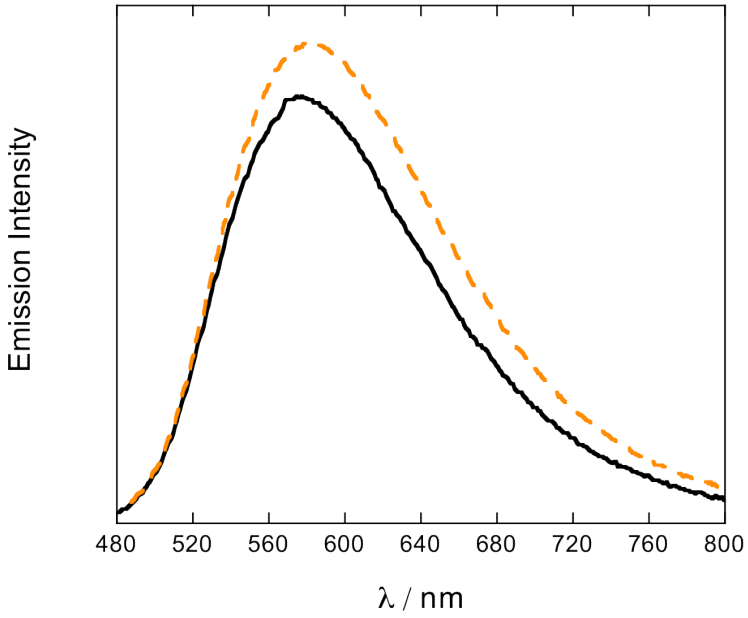


Figure 3-9. Emission spectra of 30 µM IrC_{12} in water (solid line) and 30 µM IrC_{12} with 2 µM of 2.5 % zonyl FSA in water (dashed line). λ_{exc} = 350 and 405 nm, λ_{max} = 585 nm for IrC_{12} and λ_{max} = 590 nm for IrC_{12} with zonyl.

The luminescence lifetime of IrC_{12}·Z·AuNP25 using two-component analysis is 103 ns (a_1=21%) and 303 ns (a_2=79%) (Appendix B, Figure B-3). The increase observed in the long-lived component of IrC_{12}·Z·AuNP25 in comparison to the IrC_{12} complex in solution could be attributed to the presence of the fluorinated surfactant on the surface of AuNPs. The addition of fluorinated surfactants to transition metal complexes on gold surfaces has been previously reported to enhance the luminescence properties of the complexes and lead to longer luminescence lifetimes[41].

3.3.6 Cytotoxicity of IrC_{12}·Z·AuNP25 in HeLa cells

The cytotoxic effect and anti-proliferative activity of both the IrC_{12} complex and IrC_{12}·Z·AuNP25 in HeLa cells were investigated using the MTT assay (Figure 3-10). The cells were treated with Z·AuNP25 and IrC_{12}·Z·AuNP25 at 0.2, 0.4 and 0.6 nM for 24 hours. The results indicated that at 0.2 nM, neither Z·AuNP25 nor IrC_{12}·Z·AuNP25 induce any cytotoxic effects in HeLa cells, as there was no inhibition in cell viability. Treatment of the cells with 0.4 and 0.6 nM of Z·AuNP25 resulted to an inhibition in cell viability of about 30%, while treating the cells with IrC_{12}·Z·AuNP25 at the same concentrations induced an inhibition in cell viability of about 20%.

The cytotoxicity observed is more likely attributed to the fluorinated surfactant and the AuNPs rather than the IrC_{12} complex, as treatment of the cells with the iridium functionalized nanoparticles resulted to fairly lower levels of toxicity. Previously published studies have reported that the cytotoxicity of AuNPs is greatly dependent on the dosing concentration[52, 53]. Therefore, the fact that both Z·AuNP25 and IrC_{12}·Z·AuNP25 induced cellular toxicity at 0.4 and 0.6 nM, with no signs of cytotoxicity at 0.2 nM, is attributed to the concentration-dependant cytotoxic effects of AuNPs. Besides the dosing concentration, the surface chemistry and charge of nanoparticles can also impact greatly their levels of toxicity in cells[54, 55]. More specifically, it has been formerly reported that negatively charged gold nanoclusters display improved cellular uptake and bioavailability in cancer cells, and therefore, enhanced cytotoxicity[56]. The presence of the fluorinated surfactant on the gold surface provides AuNPs with a highly electronegative surface charge, which becomes less negative upon conjugation of the positively charged metal complex[40, 57]. Thus, the slightly lower inhibition in cell viability observed after treatment with IrC_{12}·Z·AuNP25 when compared to Z·AuNP25 could be attributed to the less electronegative surface charge of the iridium functionalized AuNPs, induced by the presence of the positively charged IrC_{12} complex on the gold surface.

The cytotoxicity of the IrC_{12} complex in HeLa cells was evaluated after treatment of the cells at concentrations between 0.5 to 3 µM for 24 hours. The results indicated that at relatively low concentrations the molecular complex does not exhibit any cytotoxic effects in HeLa cells, as there was no evident reduction in cell viability after treating the cells with 0.5 and 1 µM of IrC_{12}. However, upon treatment of the cells with 2 and 3 µM of the iridium complex, a decrease in cell viability of about 20% was observed.

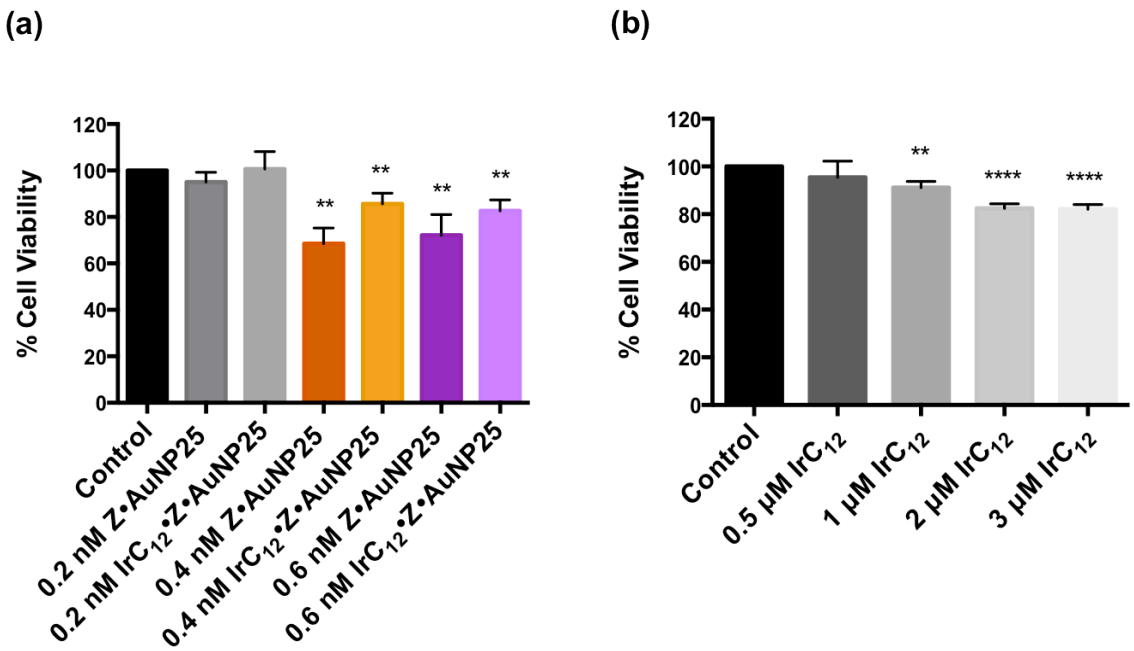


Figure 3-10. Cytotoxicity in HeLa cell determined using the MTT cell viability assay after treatment for 24 h. (a) Cytotocixity of Z·AuNP25 and IrC_{12}·Z·AuNP25 at 0.2, 0.4 and 0.6 nM. (b) Cytotoxicity of IrC_{12} at concentrations between 0.5 to 3 µM. **P value < 0.01, ****Pvalue < 0.0001.*

Many cyclometalated iridium(III) complexes have been previously reported to display high cytotoxicity in cancer cells at relatively low dosing concentrations, with the levels of toxicity being highly dependent on the cellular uptake efficacy, which is influenced by the design and chemical structure of the complexes[58-60]. Therefore, the low cytotoxicity of the IrC_{12} complex in HeLa cells could be attributed to the inefficient uptake of the complex by the cells, possibly due to the presence of the long spacer chains on the metal complex that contain the disulfide attachments for conjugation to the gold surface. Molecular complexes

containing disulfide attachments and thiol groups can cross-react with thiols present on the surface of the cell, leading to disulfide/thiol exchange reactions[61]. The cross-linking of molecular complexes by thiol containing proteins on the cell surface can lead to thiol-mediated membrane trafficking, as the complexes get trapped in the lipid bilayer and thereby, prevent further cellular internalization[61, 62]. However, upon conjugation of the complex to a nanocarrier such as AuNPs, this issue is overcome, as nanoparticles enter the cells via a different uptake mechanism[63-65].

3.3.7 Cellular uptake efficacy of IrC_{12}·Z·AuNP25 in HeLa cells

The cellular uptake efficacy of IrC_{12}·Z·AuNP25 and the appropriateness of the IrC_{12} complex for the development of luminescent nanoprobes with optimal cellular uptake in HeLa cells were evaluated by FACS. Histogram analysis was performed using the Qdot565 filter, violet laser with λ_{exc} at 405 nm and λ_{em} >565 nm. In order to evaluate the uptake efficacy of the IrC_{12} coated AuNPs, luminescent AuNPs functionalized with the IrbpySS complex were also prepared to establish whether the presence of the dodecyl chain on the luminescent complex aids in improving the cellular uptake efficacy of the nanoparticles. Previously published studies have reported that the efficient delivery of molecular complexes in cells using nanoparticles as a delivery scaffold can be challenging due to the formation of a protein corona[66, 67]. Even though plain citrate AuNPs have been formerly confirmed to internalize efficiently into cells, functionalization of the gold surface can alter interactions at the nano-bio interface in a physiological environment and impact negatively the endocytic pathways by which nanoparticles enter the intracellular space[63, 68-70]. Serum proteins, such as Fetal Bovine Serum (FBS), which are used to supplement cell culture media can contribute greatly to the formation of protein corona on the surface of AuNPs. Therefore, similarly to Chapter 2, the cellular uptake of both the IrC_{12} and IrbpySS coated AuNPs was evaluated in the presence of serum-free cell culture media to preclude the formation of protein corona and prevent changes in the physiochemical properties and size of nanoparticles upon cellular interaction.

Prior to treating the cells, the absorbance of both IrC_{12}·Z·AuNP25 and IrbpySS·Z·AuNP25 was monitored by UV-Vis to confirm that both nanoparticle samples are at the same concentration (Figure 3-11). However, when evaluating cellular uptake by FACS, a highly emissive complex or luminescent nanoprobe might show high increase in the fluorescence intensity of the treated cells, suggesting high cellular uptake even if the uptake is relative low. Therefore, even though the concentration of the two iridium complexes used to functionalize the AuNPs was the same, the emission intensity of IrC_{12}·Z·AuNP25 and IrbpySS·Z·AuNP25 was recorded and the area under the curve (AUC) was taken into consideration prior to interpreting the results from FACS analysis (Figure 3-9).

After treating HeLa cells with IrC_{12}·Z·AuNP25 and IrbpySS·Z·AuNP25 at the same concentration (0.4 nM) for 24 hours, the increase observed in the fluorescence intensity was significantly higher in the cells treated with IrC_{12}·Z·AuNP25 when compared to the ones treated with IrbpySS·Z·AuNP25 (Figure 3-12). However, the AUC of the emission intensity of IrC_{12}·Z·AuNP25 was also significantly higher than the one of IrbpySS·Z·AuNP25, suggesting that when conjugated to the gold surface, the IrC_{12} complex exhibits a stronger luminescence signal than the IrpbySS complex. In fact, the fold increase in the MFI of the treated cells and the fold difference in the AUC were higher by 1.9 and 1.8, respectively, for IrC_{12}·Z·AuNP25 when compared to IrbpySS·Z·AuNP25. Therefore, when taking into account the strength of the luminescence signal of the two iridium complexes, IrC_{12} and IrbpySS, when attached to the surface of AuNPs, both IrC_{12}·Z·AuNP25 and IrbpySS·Z·AuNP25 exhibit the same cellular uptake efficacy in HeLa cells.

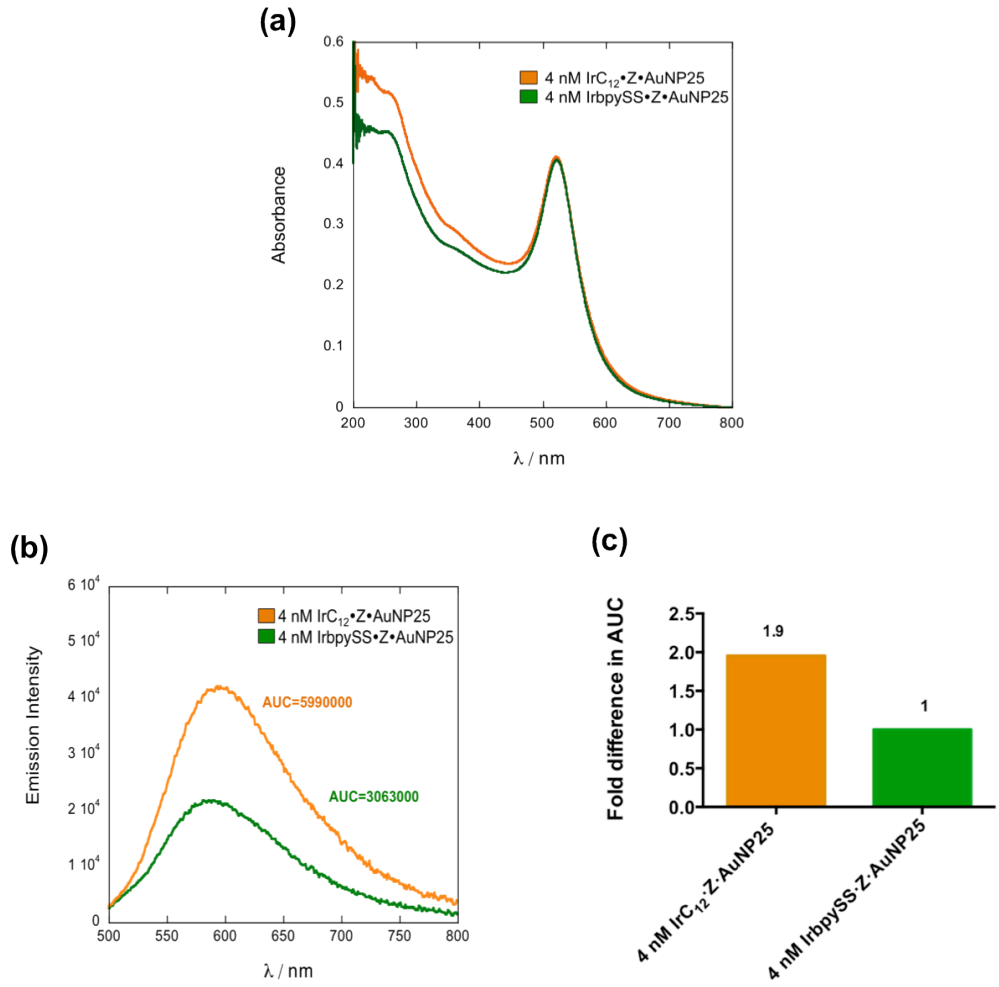


Figure 3-11. **(a) UV-Vis absorption spectra of 4 nM IrC_{12}·Z·AuNP25 and IrbpySS·Z·AuNP25 in water. (b) Emission spectra of 4 nM IrC_{12}·Z·AuNP25 and IrbpySS·Z·AuNP25 in water. λ_{exc} = 405 nm, λ_{max} = 595 nm (IrC_{12}·Z·AuNP25) and 585 nm (IrbpySS·Z·AuNP25) (c) Fold difference in the area under the curve (AUC) of the emission intensity of 4 nM IrC_{12}·Z·AuNP25 and IrbpySS·Z·AuNP25 in water.**

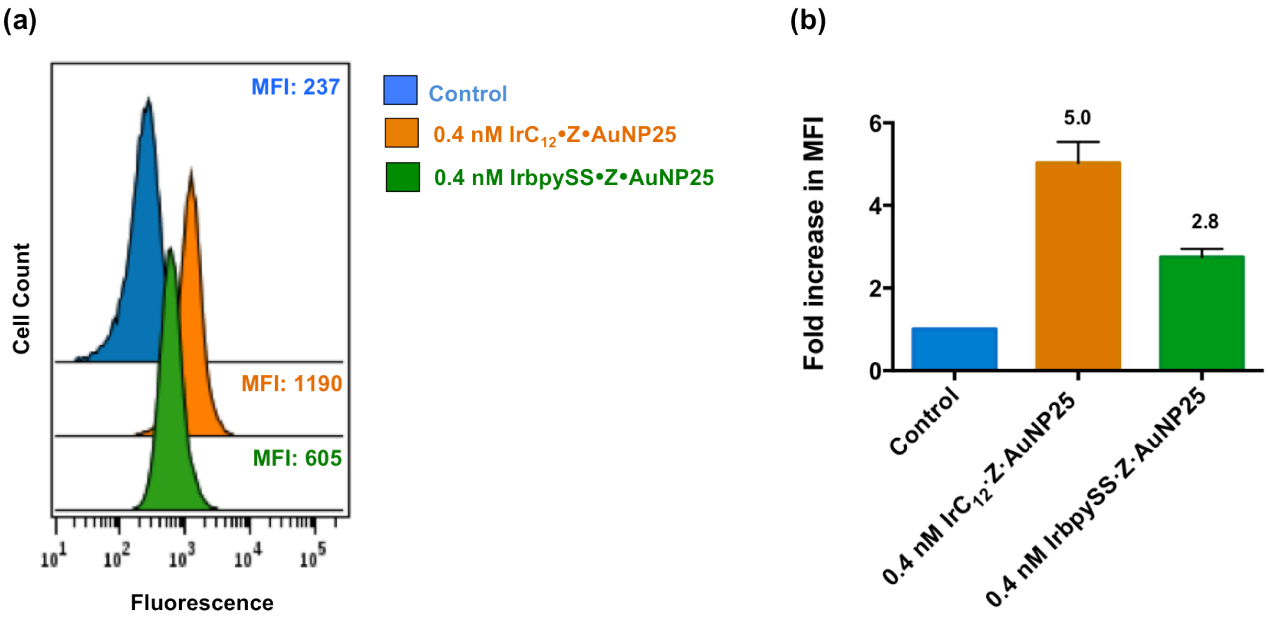


Figure 3-12. **Cellular uptake efficacy in HeLa cells by FACS analysis after treatment with IrC_{12}·Z·AuNP25 and IrbpySS·Z·AuNP25 in serum-free cell culture media for 24 h. λ_{exc}=405 nm and λ_{em}= >565 nm. (a) Histogram analysis of cellular uptake after treatment with 0.4 nM IrC_{12}·Z·AuNP25 and IrbpySS·Z·AuNP25. (b) Fold increase in Mean Fluorescence Intensity (MFI) after treatment with 0.4 nM IrC_{12}·Z·AuNP25 and IrbpySS·Z·AuNP25. The results are mean values ± SD of three independent experiments.**

In order to assess whether the use of AuNPs improves the delivery of IrC_{12} and IrbpySS in HeLa cells, the cellular uptake efficacy of the two molecular complexes in solution was also evaluated by FACS and compared to the uptake of IrC_{12}·Z·AuNP25 and IrbpySS·Z·AuNP25. As discussed previously in this chapter, IrC_{12} displays relatively low cytotoxicity in HeLa cells, which was attributed to the low uptake of the complex by the cells as result of the long spacer chains present on the bipyridine ligand of the complex that contain disulfide attachments for conjugation to the surface of AuNPs. More specifically, cross-linking between disulfide attachments on molecular complexes and thiol containing proteins present on the surface of cells can inhibit cellular uptake and thereby, internalization of the complexes within the intracellular environment[61, 62]. Therefore, the cellular uptake of IrC_{12} and IrbpySS was evaluated in the presence of two iridium complexes without the long spacer chains with disulfide attachments for attachment to the gold surface. The IrC_{12}bpy and Irbpy complexes were used as the positive control for IrC_{12} and IrbpySS, respectively (The chemical structures of the iridium complexes are outlined in

Figure 3-13). The $IrC_{12}bpy$ complex was synthesised and characterized by Andrew Carrod, School of Chemistry, University of Birmingham (Appendix B – Scheme B-1 and Figure B-2). The Irbpy complex was synthesised and characterized by Dr. Samuel Adams, School of Chemistry, University of Birmingham.

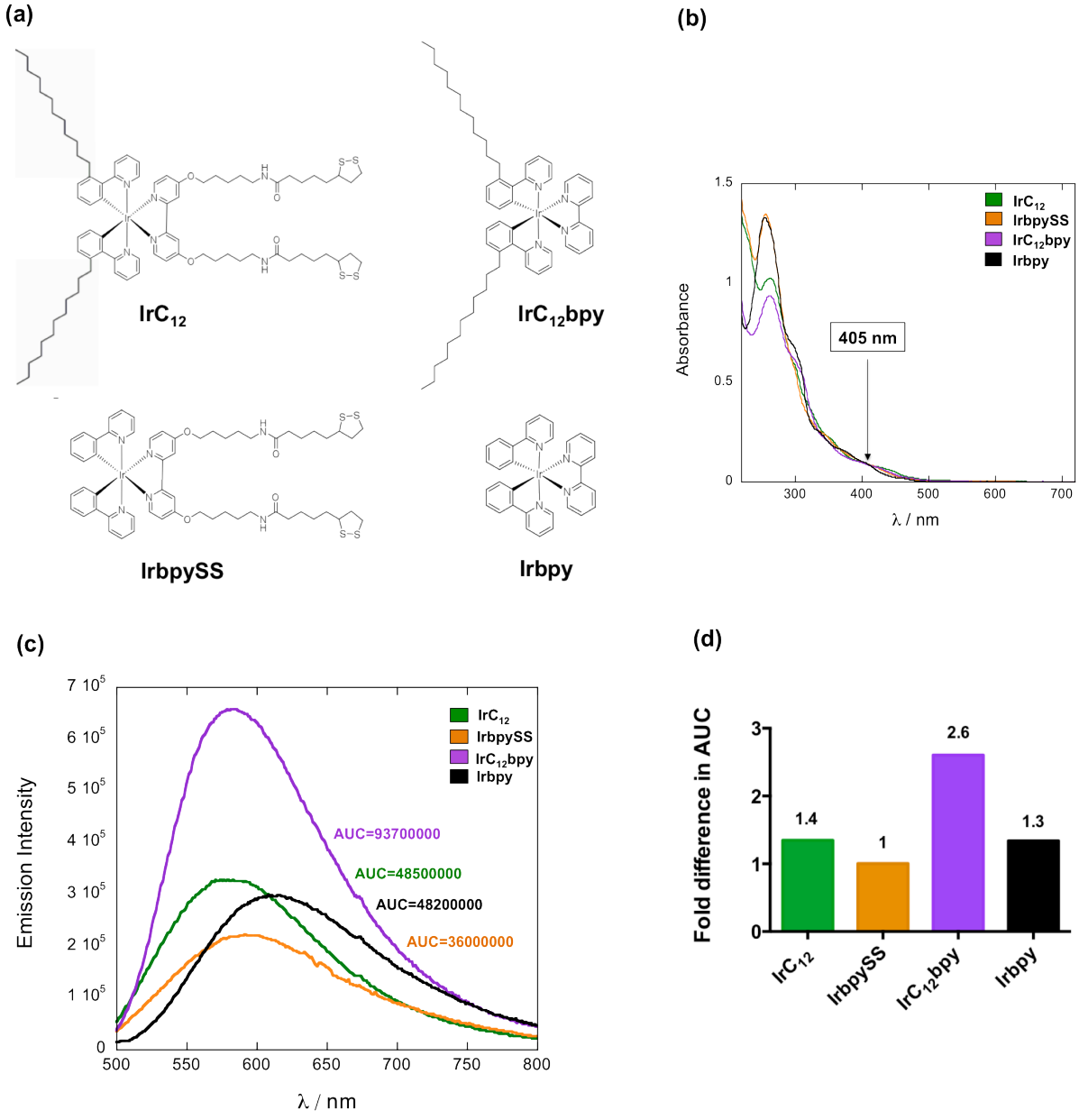


Figure 3-13. **(a) Chemical structures of IrC_{12}, IrbpySS, $IrC_{12}bpy$ and Irbpy. (b) UV-Vis absorption spectra of IrC_{12}, IrbpySS, $IrC_{12}bpy$ and Irbpy in water. (c) Emission spectra of IrC_{12}, IrbpySS, $IrC_{12}bpy$ and Irbpy in water. λ_{exc} = 405 nm, λ_{max} = 585 nm (IrC_{12}), 590 nm (IrbpySS), 580 nm ($IrC_{12}bpy$) and 610 nm (Irbpy). (d) Fold difference in the area under the curve (AUC) of the emission intensity of IrC_{12}, IrbpySS, $IrC_{12}bpy$ and Irbpy.**

Before treating the cells, the dosing concentration of each complex was determined through monitoring the absorbance of the luminescent iridium complexes by UV-Vis spectroscopy. For the purposes of assessing the cellular uptake of the luminescent complexes in the present study by FACS, a laser with an excitation wavelength at 405 nm was used. Therefore, the treatment concentration chosen for each iridium complex was the one at which all complexes displayed the same absorption at 405 nm (Figure 3-13). However, as discussed earlier in this chapter, the increase in the MFI of the treated cells during FACS analysis is highly influenced by how emissive a luminescent complex is. For that reason, in order to evaluate the cellular uptake efficacy of the iridium complexes in HeLa cells, the emission intensity of the complexes in solution was also recorded and the AUC was taken into account prior to interpreting the results (Figure 3-13).

Subsequent to treating HeLa cells with the iridium complexes for 24 hours, the increase observed in the MFI of the cells treated with the Irbpy complex was considerably higher than the increase observed in the cells treated with the other three complexes (Figure 3-14). The fold difference in the AUC of the emission intensity of Irbpy suggests that the complex does not exhibit stronger luminescence than the other iridium complexes. Therefore, the higher increase detected in the MFI of the cells treated with the Irbpy complex is attributed to the highly efficient uptake of the complex by the cells. The fact that the Irbpy complex displayed higher uptake than IrC_{12} and IrC_{12}bpy in HeLa cells was not expected, as according to literature, the presence of the dodecyl chain on the phenylpyridine ligand of the complexes provides greater hydrophobicity, which could have improved the permeability of IrC_{12} and IrC_{12}bpy across the cell membrane[20, 71]. However, previously published studies have suggested that due to the fact that molecular complexes enter the cells by passive diffusion, complexes that are smaller in size and have a simple chemical structure usually demonstrate better cellular uptake and internalization[33, 72].

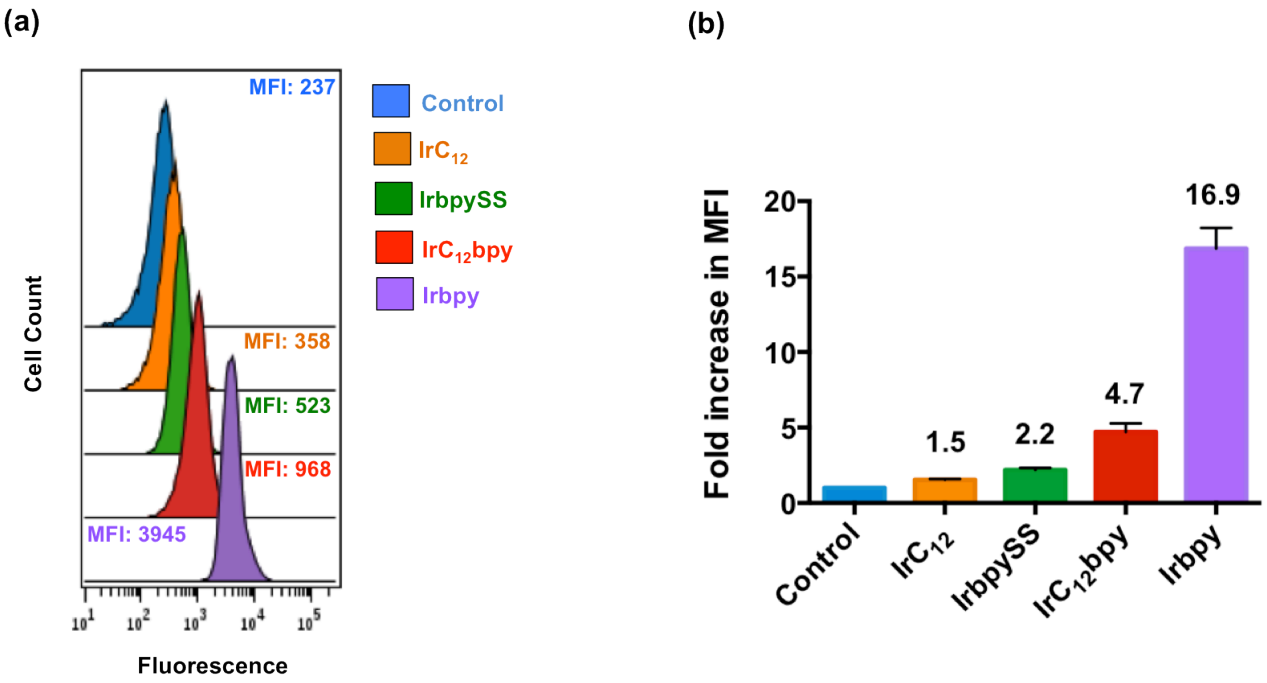


Figure 3-14. Cellular uptake efficacy in HeLa cells by FACS analysis after treatment with IrC_{12}, IrbpySS, IrC_{12}bpy and Irbpy in serum-free cell culture media for 24 h. λ_{exc}=405 nm and λ_{em}= >565 nm. (a) Histogram analysis of cellular uptake after treatment with IrC_{12}, IrbpySS, IrC_{12}bpy and Irbpy. (b) Fold increase in Mean Fluorescence Intensity (MFI) after treatment with IrC_{12}, IrbpySS, IrC_{12}bpy and Irbpy. The results are mean values ± SD of three independent experiments.

Besides the smaller size and simple structure of Irbpy, interactions between the dodecyl chain and membrane proteins might have also contributed to the lower uptake efficacy observed in the cells treated with IrC_{12} and IrC_{12}bpy. It has been previously reported that modification of the substituent groups attached to the bipyridine ligand of a metal complex can induce interaction of the complex with the plasma membrane through binding to proteoglycans present on the surface of the cell[73]. What is more, carbon chains have also been reported to inhibit the internalization of iridium complexes into cells due to interactions between the lipophilic complexes and the lipophilic bilayer membrane, with longer carbon chains exhibiting a stronger affinity towards the cell membrane[74]. The interaction of metal complexes with the plasma membrane can result to retention of the complexes in the phospholipid bilayer during their internalization[74]. This property of metal complexes has led to the development of several metal-based probes that can be used for labelling of the cell plasma membrane to examine membrane dynamics[73, 75, 76].

Treatment with the IrC_{12}bpy complex induced a higher increase in the fluorescence intensity of the cells when compared to the increase observed in the cells treated with the IrC_{12} complex. Even though the IrC_{12}bpy complex exhibits stronger luminescence than IrC_{12}, the fold increase in the emission intensity of IrC_{12}bpy is higher than the one of IrC_{12} by 1.9, whereas the increase in the MFI of the cells treated with IrC_{12}bpy is higher than the increase in the MFI of the cells treated with IrC_{12} by 3.1. Hence, the higher fold increase observed in the fluorescence intensity of the cells treated with the IrC_{12}bpy complex is due the higher cellular cellular uptake rather than the stronger emission of the complex. Again, the improved uptake of the IrC_{12}bpy complex in HeLa cells in comparison to IrC_{12} could be attributed to the relatively smaller structure of the complex. The use of IrC_{12}bpy and Irbpy as positive controls confirms that in the absence of the long spacer chains with the disulfide attachments for conjugation to the surface of AuNPs, the molecular complexes exhibit significantly higher cellular uptake.

Even though the cellular uptake of IrC_{12} and IrC_{12}bpy in HeLa cells was not highly efficient, the results of the present study indicate that upon conjugation of the IrC_{12} complex to the gold surface the aforementioned issues discussed are overcome. This is attributed to the fact that the luminescent nanoparticles enter the cells via a different mechanism[77], as the molecular complexes usually internalize into cells by passive diffusion[33, 78, 79] whereas functionalized nanoparticles by endocytosis[80-82]. When comparing the cellular uptake of IrC_{12}·Z·AuNP25 to IrC_{12} and IrC_{12}bpy (positive control), the cells treated with the IrC_{12} coated AuNPs displayed higher increase in the MFI, even though both IrC_{12} and IrC_{12}bpy in solution exhibit a stronger luminescent signal than IrC_{12}·Z·AuNP25 (FACS data are summarized in Figure 3-15).

The fact that the IrC_{12} coated nanoparticles demonstrate higher uptake efficacy than the positive control suggests that the use of AuNPs as a scaffold to deliver the IrC_{12} complex in HeLa cells enhances drastically the internalization of the complex within the intracellular environment. This was not evident upon attachment of the IrbpySS complex to the surface of AuNPs, as even though IrbpySS·Z·AuNP25 displayed higher cellular uptake than the IrbpySS complex in solution, the Irbpy complex (positive control) showed significantly higher penetration of the cell membrane in HeLa cells.

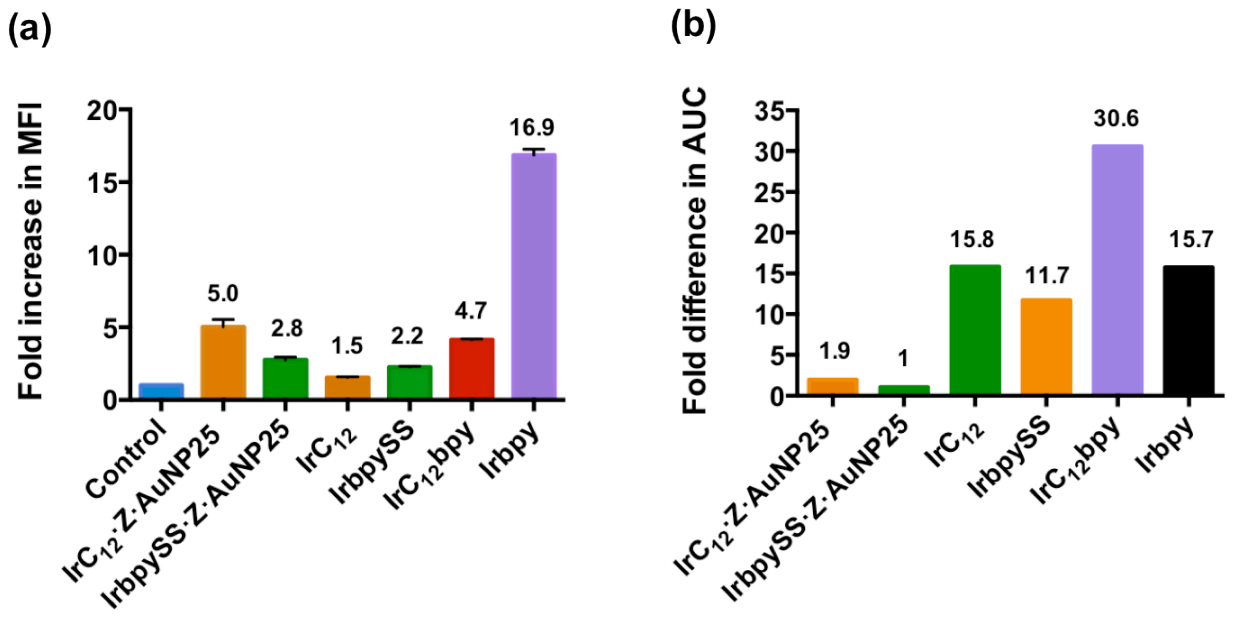


Figure 3-15. **(a) Cellular uptake efficacy in HeLa cells by FACS analysis after treatment with IrC_{12}·Z·AuNP25, IrbpySS·Z·AuNP25, IrC_{12}, IrbpySS, IrC_{12}bpy and Irbpy in serum-free cell culture media for 24 h. λ_{exc}=405 nm and λ_{em}= >565 nm. Fold increase in Mean Fluorescence Intensity (MFI) after treatment with IrC_{12}·Z·AuNP25, IrbpySS·Z·AuNP25, IrC_{12}, IrbpySS, IrC_{12}bpy and Irbpy. The results are mean values ± SD of three independent experiments. (b) Fold difference in the area under the curve (AUC) of the emission intensity of IrC_{12}·Z·AuNP25, IrbpySS·Z·AuNP25, IrC_{12}, IrbpySS, IrC_{12}bpy and Irbpy.**

Even though the efficient uptake of the Irbpy complex suggests that the molecular complex can successfully internalize into HeLa cells without the use of AuNPs, the delivery of metal-based complexes in cancer cells can be challenging, as it is highly associated with imprecise subcellular localization that eventually leads to off target toxicity[83]. Therefore, the ability of IrC_{12} to internalize into cells with high efficiency only when conjugated to the surface of AuNPs provides opportunities for the development of luminescent nanoprobes with improved localization in tumor cells.

What is more, although both the IrC_{12} and IrbpySS coated AuNPs exhibit efficient uptake in HeLa cells, the suitability of IrC_{12}·Z·AuNP25 over IrbpySS·Z·AuNP25 for use in cellular uptake studies and luminescence imaging was evident through the stronger emission displayed by IrC_{12}·Z·AuNP25 upon excitation at 405 nm. The fact that the same concentration of IrC_{12} and IrbpySS was used for the preparation of IrC_{12}·Z·AuNP25 and IrbpySS·Z·AuNP25, suggests that the stronger luminescence signal of the IrC_{12} coated AuNPs is attributed to the presence of the dodecyl chain and the improved luminescence properties of the complex[84, 85]. The enhanced emission of IrC_{12}·Z·AuNP25 allows the development of highly luminescent AuNPs for studying cellular internalization and subcellular localization using confocal luminescence microscopy.

3.3.8 Luminescence lifetime detection of IrC_{12}·Z·AuNP25 in HeLa cells

The efficient cellular uptake of IrC_{12}·Z·AuNP25 in HeLa cells was further confirmed through detecting the luminescence properties of the iridium functionalized AuNPs in treated cells. Luminescence lifetime measurements revealed that after treatment with 0.4 nM of the IrC_{12} coated AuNPs for 24 hours the luminescence lifetime in the treated cells using two-component analysis is 94 ns (a_1=27%) and 367 ns (a_2=73%) (Appendix B – Figure B-4). The increase in the luminescence lifetime of IrC_{12}·Z·AuNP25 observed in HeLa cells from 303 to 367 ns is most likely attributed to the interaction of the iridium complex on the gold surface with cellular proteins. It has been previously reported that interaction of cyclometalated iridium complexes with intracellular proteins results to enhanced luminescence and elongation of luminescence lifetimes[39, 41].

In order to further establish whether the increase detected in the luminescence lifetime of IrC_{12}·Z·AuNP25 in cells is the result of interactions between the iridium complex present on the surface of AuNPs and cellular proteins, lifetime measurements were also performed in HeLa cells treated with the IrC_{12} in solution. After treatment of the cells with 0.3 μM of the IrC_{12} complex for 24 hours, the luminescence lifetime in the treated cells using two-component analysis is 56 ns (a_1=8%) and 403 ns (a_2=92%) (Appendix B – Figure B-4) (Luminescence lifetimes are summarized in Table 3-2). The lifetime of IrC_{12} increased from 260 to 403 ns in the treated cells, further confirming that the enhanced luminescence observed in HeLa cells subsequent to treatment with the IrC_{12} coated nanoparticles is attributed to interactions between the iridium complex and intracellular proteins. The improved luminescence properties of transition metal complexes in cells have been previously linked to hydrophobic attractions between the complex and the binding pockets of a protein, with highly lipophillic complexes exhibiting stronger affinity towards a protein[86].

The increase induced in the luminescence lifetime of the IrC_{12} complex upon interaction with proteins was further confirmed through the addition of the Bovine Serum Albumin (BSA) protein into a solution of the iridium complex. The lifetime of IrC_{12} after addition of BSA using two-component analysis is 130 ns (a_1=29%) and 377 ns (a_2=71%), showing an increase in the lifetime of the complex of about 120 ns, which is similar to the increase observed in the cells after treatment with IrC_{12} (Luminescence lifetimes are summarized in Table 3-2).

Luminescence lifetime measurements were also performed in fractionated subcellular organelles after treating HeLa cells with 0.3 μM of the IrC_{12} complex. The lifetime of the IrC_{12} complex both in the cytosol and mitochondria was increased by about 90 ns, suggesting that the interaction of the complex with cytosolic and mitochondrial proteins is similar. However, the increase observed in the lifetime of the IrC_{12} complex in the nucleus was significantly higher, as the lifetime of the iridium complex displayed an increase of about 230 ns from the complex in solution (Luminescence lifetimes are summarized in Table 3-2). The considerably elongated lifetime of the iridium complex detected in the nucleus is indicative of the strong affinity of the complex towards nuclear proteins.

IrC_{12}		IrC_{12} + BSA		IrC_{12} In HeLa cells		IrC_{12} in cytosol		IrC_{12} in mitochondria		IrC_{12} in nucleus	
a_i (%)	τ_i (ns)	a_i (%)	τ_i (ns)	a_i (%)	τ_i (ns)	a_i (%)	τ_i (ns)	a_i (%)	τ_i (ns)	a_i (%)	τ_i (ns)
26	104	21	130	8	56	18	85	29	88	20	109
74	260	79	377	92	403	82	348	71	351	80	494

Table 3-2. Luminescence lifetimes of IrC_{12} in water, IrC_{12} with BSA, and IrC_{12} in HeLa cells and subcellular organelles. Lifetimes were recorded using a 376 nm laser and fitted using two-component analysis with a χ^2 value between 1.02 and 1.21.

3.3.9 Circular Dichroism (CD) of IrC_{12} and IrC_{12}·Z·AuNP25

The ability of transition metal complexes to be purposely designed to interact with biomolecules within an intracellular environment makes them ideal candidates as targeting moieties, which can be used to alter biological processes that are essential for the survival of tumor cells[87, 88]. Therefore, the study of the different interactions between biological molecules, such as proteins, and metal complexes potentiates an improved therapeutic outcome through targeting specific biological functions in diseases like cancer[89, 90]. In fact, many studies have reported that inorganic chemistry offers both versatility and diversity in the design and synthesis of metal complexes, which can act as highly effective protein modulators[91-93].

In order to study the ability of both the IrC_{12} complex in solution and the IrC_{12} functionalized nanoparticles to interact with biological proteins, CD spectroscopy was performed to monitor the conformational changes of BSA upon addition of IrC_{12} and IrC_{12}·Z·AuNP25. CD spectroscopy is considered as an excellent method for rapidly evaluating the binding properties of biological proteins. In brief, CD refers to the unequal absorption of right and left-handed circular polarized light by a molecule that contains at least one chiral molecule[94]. This method is widely used to study conformational alterations of several biomolecules like proteins and DNA, as their structures are sensitive to interactions with other molecules and changes in environmental conditions, such as temperature and pH[95].

The characteristic CD spectrum of BSA shows two negative peaks at 209 and 222 nm, and one positive peak at 190 nm, which are characteristic for proteins that exhibit an a-helix structure[42, 96]. The intensity of the positive and negative peaks of BSA was recorded upon the sequential addition of the IrC_{12} complex in solution (100 μM) and IrC_{12}·Z·AuNP25 (4 nM) (Figure 3-16). The addition of both the IrC_{12} complex in solution and the IrC_{12} coated AuNPs to BSA resulted to a decrease in the intensity of the positive peak and an increase in the intensity of the negative peaks in the CD spectra. The changes observed indicate structural alterations in the characteristic features of the protein both upon addition of the IrC_{12} complex in solution and on the surface of AuNPs. The conformational changes in the structure of BSA are more likely attributed to the engagement of the IrC_{12} complex in strong electrostatic and hydrophobic interactions with the binding pockets of the protein[42, 97, 98]. Such interactions allow binding of the luminescent complex within an active site of a sub domain of BSA, resulting to loss of structural conformation due to protein unfolding[42, 99, 100].

The CD spectrum of BSA within the far UV region (200-260 nm) reflects the secondary structural features of the protein, such as a-helix and β-pleated sheets, while the near UV region (250 to 320 nm) of the spectrum provides information about the tertiary structure of the protein[101, 102]. Therefore, the increase observed in the intensity of the CD spectra between 209 and 222 nm indicates that upon interaction of the IrC_{12} complex with BSA conformational alterations are induced in the secondary structure of the protein. The CD spectra revealed no changes within the near UV region, suggesting that the tertiary structure of the protein does not change upon binding of the iridium complex. The decrease detected in the intensity of the CD spectra at 190 nm reflects the loss of the a-helical structural features of the protein due to strong interactions with the IrC_{12} complex.

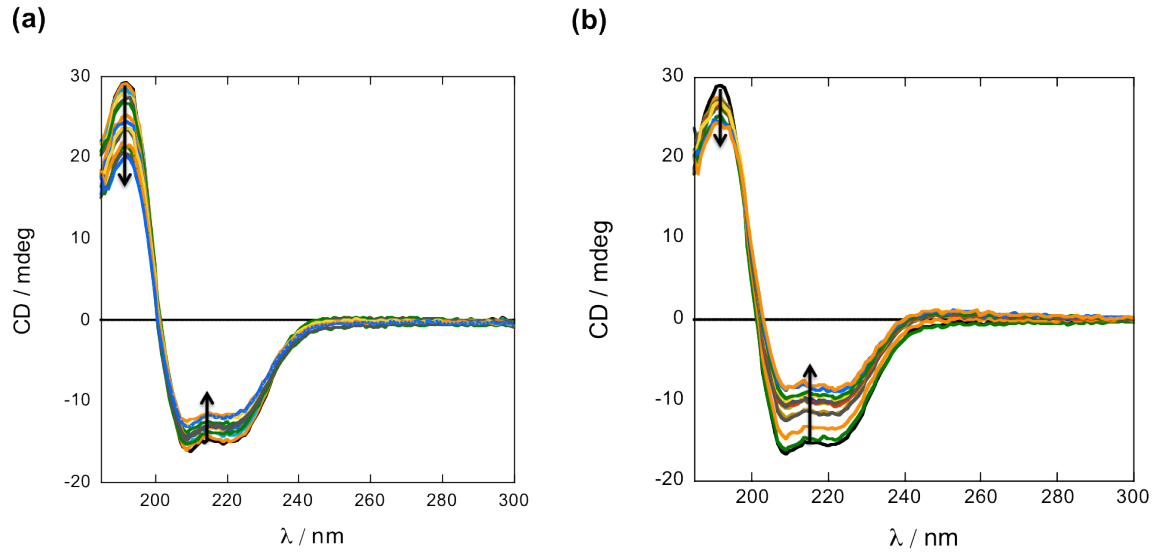


Figure 3-16. Circular dichroism spectra of BSA (0.1 μM) with sequential additions of (a) IrC_{12} solution (100 μM) (0.5, 1.0, 1.5, 2.0, 2.5, 5.0, 7.4, 9.8, 14.6, 28.3, 41.2, 49.4 and 61.1 mol equiv.) and (b) IrC_{12}·Z·AuNP25 in water (4 nM) ($0.2x10^{-4}$, $0.4x10^{-4}$, $0.6x10^{-4}$, $0.8x10^{-4}$, $1.0x10^{-4}$, $2.0x10^{-4}$, $3.9x10^{-4}$, $5.8x10^{-4}$, $1.1x10^{-3}$, $1.8x10^{-3}$, $2.7x10^{-3}$, and $3.3x10^{-3}$ mol equiv.).

3.3.10 Cellular uptake and subcellular localization of IrC_{12}·Z·AuNP25 in HeLa cells by Confocal Microscopy

The cellular uptake efficacy of IrC_{12}·Z·AuNP25 in HeLa cells was further examined by confocal microscopy. Live cell imaging was performed after treating the cells with 0.4 nM of the IrC_{12} coated AuNPs for 4 and 24 hours (Figures 3-17). Similarly to FACS analysis, luminescence imaging revealed the successful internalization of IrC_{12}·Z·AuNP25 in HeLa cells. Even though the luminescence of the iridium functionalized nanoparticles was detectable in live HeLa cells both after 4 and 24 hours of treatment, the luminescence signal was considerably stronger during imaging of the cells treated for 24 hours, suggesting that cellular uptake is time-dependant. The time-dependant cellular uptake of IrC_{12}·Z·AuNP25 observed agrees with previously published studies that have reported enhanced cellular uptake of nanoparticles by endocytosis upon treatment of cells for 24 hours in comparison to shorter periods of incubation[103, 104].

The strong luminescence signal from the iridium complex detected within the intracellular space during live cell imaging subsequent to treating the cells for 24 hours confirms that the IrC_{12} complex retains its high photostability upon attachment to the surface of the surfactant modified nanoparticles. Furthermore, the intensity of the iridium luminescence was not decreased after imaging of the cells both after 4 and 24 hours of treatment, suggesting that the IrC_{12} complex does not experience photobleaching in a biological environemnt when conjugated to the surface of AuNPs.

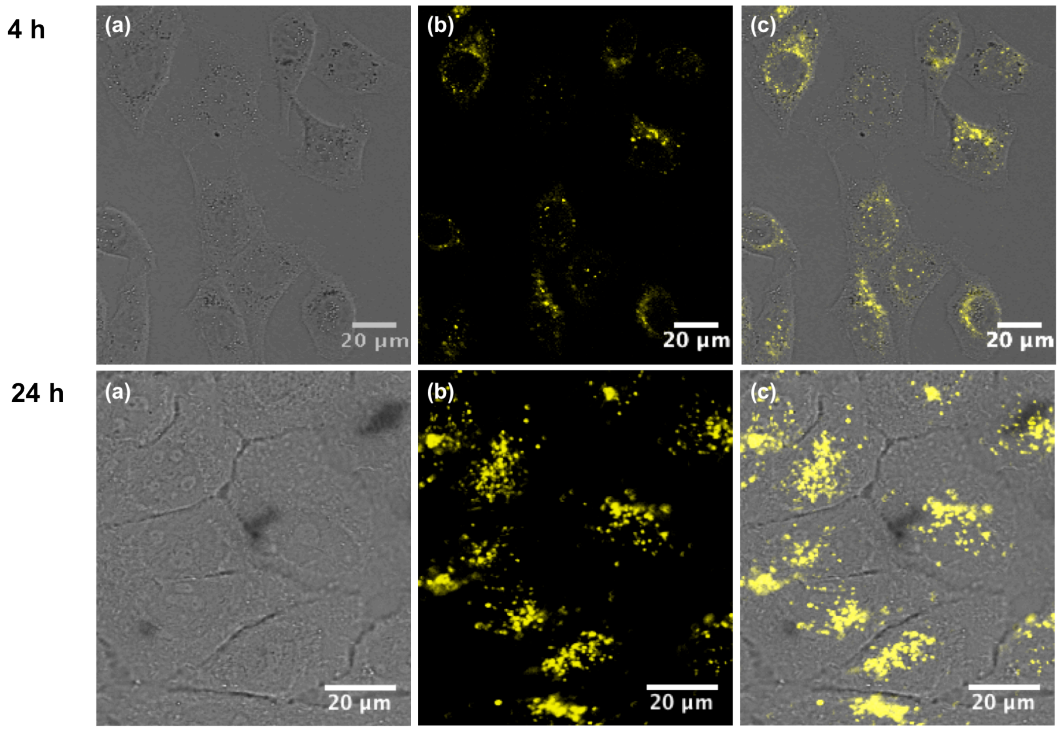


Figure 3-17. Confocal microscopy of live HeLa cells after treatment with 0.4 nM IrC_{12}·Z·AuNP25 in serum-free cell culture media for 4 h (Top) and 24 h (Bottom) (Scale bar: 20 µm). (a) Bright-field, (b) Iridium luminescence (λ_{exc}=405 nm, λ_{em}=550 nm-750 nm) and (c) Overlay of (a) and (b).

The cellular uptake and localization of the IrC_{12} complex in HeLa cells was also evaluated by confocal microscopy. After treatment of the cells with the iridium complex in solution for 4 and 24 hours, luminescence imaging revealed the presence of IrC_{12} within the intracellular environment (Figure 3-18). During imaging, there was no evident enhancement in the luminescence signal of the cells treated with the iridium complex for 24 hours when compared to the ones treated for 4 hours. This is most likely attributed to

the fact that metal complexes internalize in cells by passive diffusion, which allows the rapid translocation of the complexes within the intracellular space[105]. Even though the signal from the IrC_{12} complex was detectable in live HeLa cells, the luminescence intensity was noticeably weaker when compared to the iridium signal detected in the cells treated with IrC_{12}·Z·AuNP25. The stronger iridium signal detected in HeLa cells after treatment with IrC_{12}·Z·AuNP25 is the result of the improved uptake of the IrC_{12} complex upon attachment to the surface of AuNPs, which was confirmed earlier in the present study through FACS analysis.

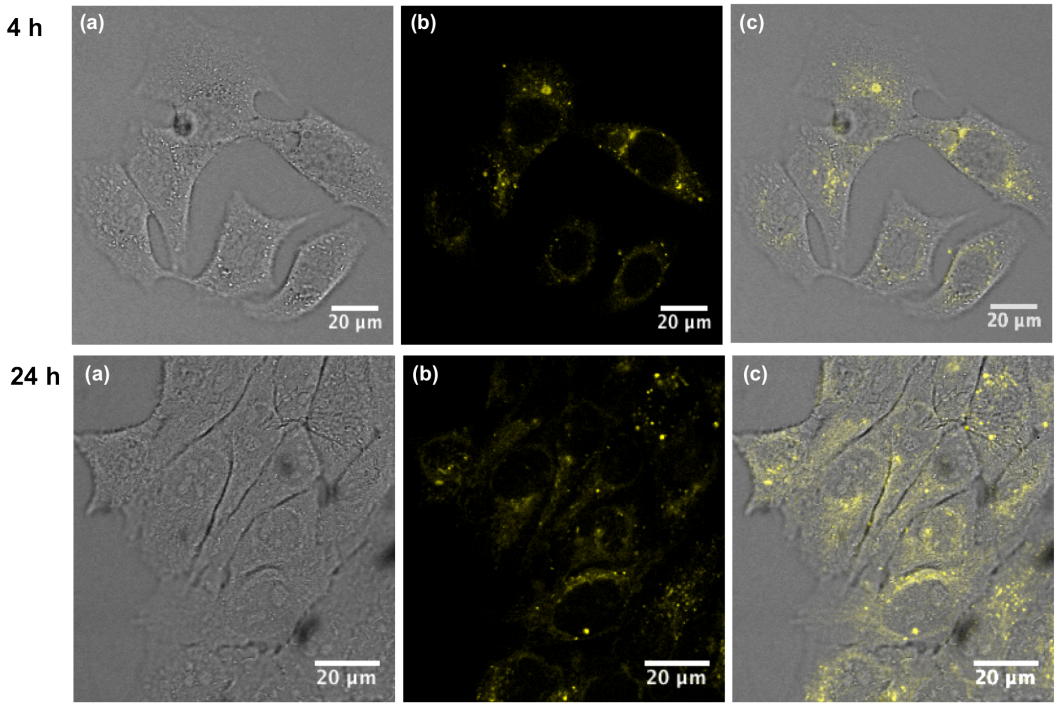


Figure 3-18. Confocal microscopy of live HeLa cells after treatment with 0.3 µM of the IrC_{12} complex in serum-free cell culture media for 4 h (Top) and 24 h (Bottom) (Scale bar: 20 µm). (a) Bright-field), (b) Iridium luminescence (λ_{exc}=405 nm, λ_{em}=550 nm-750 nm) and (c) Overlay of (a) and (b).

The use of AuNPs as a vehicle to deliver targeting complexes in cancer cells has been previously reported to improve drastically the solubility and bioavailability of the complexes in the intracellular environment[106, 107], thereby providing opportunities for more efficient subcellular localization[108, 109]. This could explain the efficient localization of IrC_{12}·Z·AuNP25 in the nucleus, which was not evident in the cells treated with the IrC_{12} complex in solution (Figure 3-19). When comparing the localization of the IrC_{12} coated

AuNPs to the molecular complex, it was observed that after 24 hours of treatment the luminescent nanoparticles show preference for both cytoplasmic and nuclear localization whereas luminescence signal in the cells treated with the IrC_{12} complex was only detected in the cytoplasm. Localization of IrC_{12}·Z·AuNP25 in the nucleus was not evident after treatment of the cells for 4 hours, suggesting that a longer incubation period is required for the nanoparticles to penetrate the nuclear membrane.

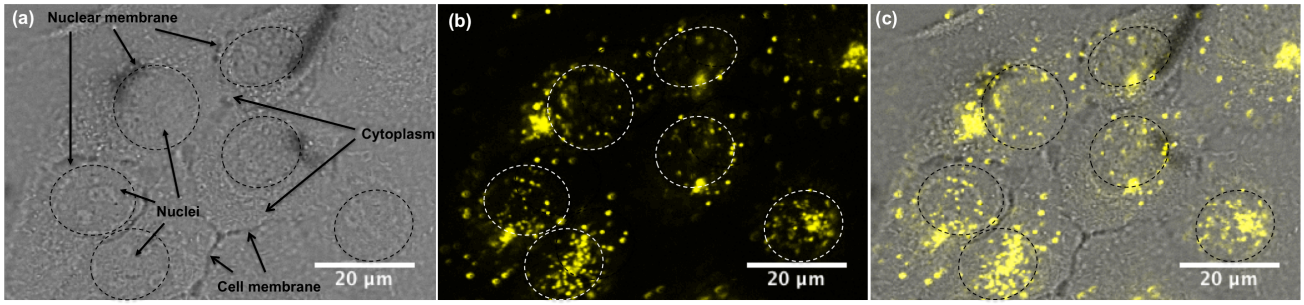


Figure 3-19. Confocal microscopy of live HeLa cells after treatment with 0.4 nM IrC_{12}·Z·AuNP25 in serum-free cell culture media for 24 h (Scale bar: 20 µm). (a) Bright-field, (b) Iridium luminescence (λ_{exc}=405 nm, λ_{em}=550 nm-750 nm) and (c) Overlay of (a) and (b).

The results of the present study indicate that the use of AuNPs provides an improved method for the delivery of the IrC_{12} complex in HeLa cells, as the attachment of the complex to the gold surface resulted to an enhanced luminescence signal during imaging and promoted nuclear localization. The high photostability of the IrC_{12} complex when conjugated to AuNPs suggests the ability of the luminescent nanoparticles to overcome the limitations associated with the use of organic fluorophores in imaging applications such as photobleaching. The relatively low cytotoxicity and high stability of IrC_{12}·Z·AuNP25 in cells, along with their strong luminescence signal, offer opportunities for the development of novel luminescent nanoprobes with favourable photophysical properties encoded by the metal complex. Such nanoprobes present great potential for detection and monitoring of biomolecular interactions in live cells using conventional confocal microscopes.

3.3.11 Cellular uptake and subcellular localization of IrC_{12}·Z·AuNP25 in HeLa cells by ICP-MS

The cellular uptake and subcellular localization of IrC_{12}·Z·AuNP25 in HeLa cells were further evaluated by inductively coupled plasma mass spectrometry (ICP-MS). The highly sensitive elemental analysis provided by ICP-MS allows both detection and quantification of the unique mass of metals and metal nanoparticles within a cellular environment[110-112]. The cellular uptake and subcellular localization of the luminescent nanoparticles were quantified both in whole and fractionated cell lysates subsequent to treating HeLa cells with 0.4 nM IrC_{12}·Z·AuNP25 for 24 hours (Figure 3-20). Analysis of whole cell lysates by ICP-MS revealed approximately 11 000 IrC_{12} coated AuNPs per cell, confirming the highly efficient cellular uptake of the luminescent nanoparticles observed earlier in this chapter both by FACS and confocal luminescence microscopy.

The subcellular localization of IrC_{12}·Z·AuNP25 in HeLa cells after treatment for 24 hours was also evaluated through analysis of fractionated cell lysates, including nucleus, cytosol and mitochondria (Figure 3-20). The results suggested a higher number of nanoparticles in the nucleus, when compared to cytosol and mitochondria, indicating the preference of the IrC_{12} coated AuNPs for nuclear localization. ICP-MS analysis revealed that besides their preference for nuclear localization, the luminescent IrC_{12} coated nanoparticles also exhibit cytosolic localization, while only a small number of IrC_{12}·Z·AuNP25 was detected in mitochondria. These results are in agreement with the images acquired during live cell imaging by confocal microscopy, as both nuclear and cytoplasmic localization of IrC_{12}·Z·AuNP25 in HeLa cells was observed.

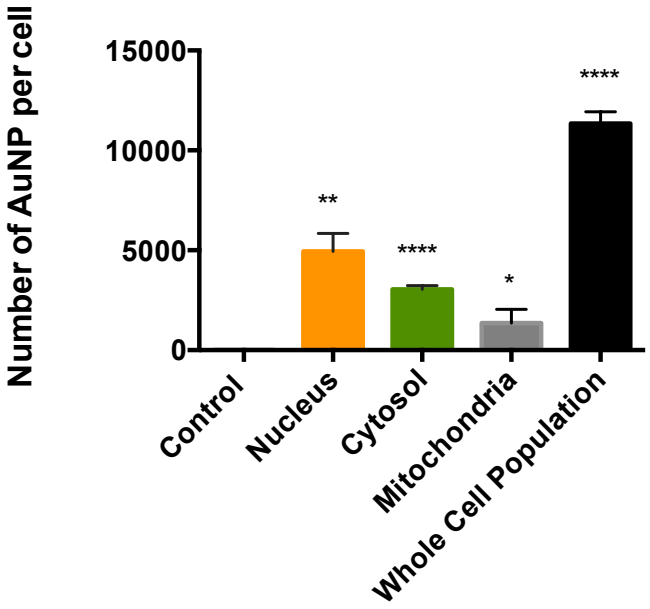


Figure 3-20. ICP-MS analysis of the number of AuNPs per cell in HeLa cells in fractionated and whole cell lysates after treatment with 0.4 nM IrC_{12}·Z·AuNP25 in serum-free cell culture media for 24 h. Statistical analysis was performed using unpaired t-test with equal SD between the samples and control. ***P value < 0.1, **P value < 0.01, ****Pvalue < 0.0001***

The cellular uptake and subcellular localization of the IrC_{12} complex in solution was also studied by ICP-MS and compared to the uptake and localization of IrC_{12}·Z·AuNP25. Similarly to IrC_{12}·Z·AuNP25, analysis was performed both in whole and fractionated cell lysates after treating HeLa cells with the iridium complex for 24 hours (Figure 3-21). In the cells treated with the IrC_{12} coated AuNPs a higher content of iridium was detected in the nucleus when compared to cytosol and mitochondria, which agrees with the number of AuNPs observed in the different fractions. Both in cytosol and mitochondria, the concentration of iridium observed is also consistent with the number of AuNPs detected. For the cells treated with the IrC_{12} complex in solution, the results indicated higher concentration of iridium in the cytosol when compared to nucleus and mitochondria, suggesting that the luminescent complex in solution shows preference for cytoplasmic localization. When compared to IrC_{12}·Z·AuNP25, the IrC_{12} complex in solution displays significantly lower iridium content in the nucleus, indicating poor penetration of the nuclear membrane. These results are consistent with the luminescence imaging performed in HeLa cells, as the luminescence signal of the iridium complex was mostly visible within the cytoplasm upon treatment of the cells with the IrC_{12} complex in solution.

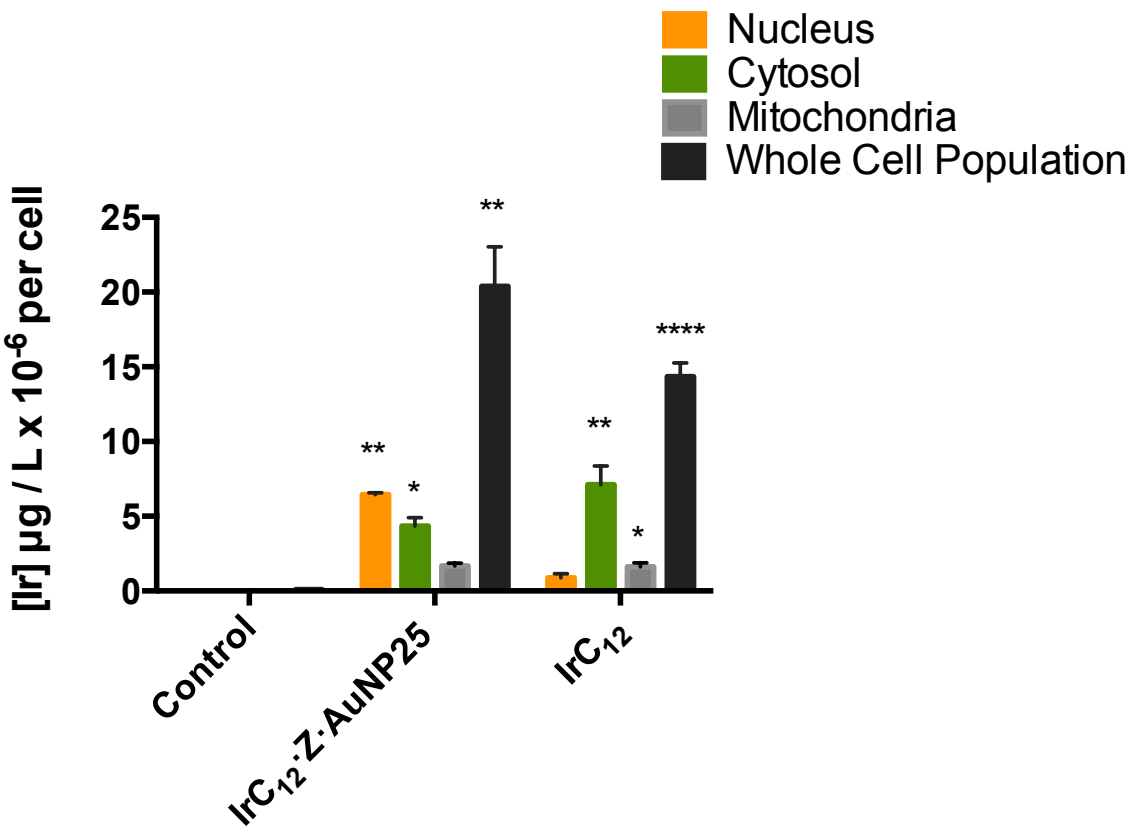


Figure 3-21. **ICP-MS Analysis of iridium concentration per cell in HeLa cells in fractionated and whole cell lysates after treatment with 0.4 nM IrC_{12}·Z·AuNP25 and 0.3 µM of the IrC_{12} complex in serum-free cell culture media for 24 h. Statistical analysis was performed using unpaired t-test with equal SD between the samples and controls.** ***P value < 0.1, **P value < 0.01 and ***P value < 0.001***

Luminescence lifetime measurements in HeLa cells, discussed earlier in this chapter, provide evidence that the IrC_{12} complex in solution exhibits strong interactions with nuclear proteins, which could potentiate a favourable therapeutic outcome upon targeting of cancer cells. However, the data obtained from ICP-MS analysis suggests that the delivery of the iridium complex in solution hinders its successful accumulation within the nucleus, preventing the complex from targeting effectively biomolecules enclosed within the nuclear membrane. According to literature, the delivery of highly lipophilic complexes to cells can be challenging due to their poor aqueous solubility, which reduces bioavailability within the intracellular environment and thereby, preventing their efficient localization to the target site[113-115].

However, upon attachment to the surface of AuNPs, the aforementioned issues are overcome, as the use of the gold scaffold as a vehicle to deliver metal complexes in the intracellular space has been previously reported to provide improved solubility and at the same time allow high concentrations to be delivered[38, 116, 117]. This was further supported in the present study, as elemental analysis carried out in different organelles confirms that the conjugation of the IrC_{12} complex to the gold surface promotes efficient cellular localization due to the improved bioavailability of the complex in the intracellular environment, which enables the successful penetration of the nuclear envelope.

3.4 Conclusion

In this chapter, luminescent nanoparticles were developed through the attachment of a cyclometalated iridium(III) complex, IrC_{12}, to the surface of surfactant coated AuNPs. The successful functionalization of AuNPs with the iridium complex was confirmed by DLS size measurements and through monitoring the characteristic SPR band of the nanoparticles. Photophysical characterization of the luminescent AuNPs revealed that upon conjugation to the gold surface, the complex translates its favourable luminescence properties to the modified nanoparticles, displaying the characteristic broad emission peak of the IrC_{12} complex and long luminescence lifetimes. Upon excitation at 405 nm, the IrC_{12} coated AuNPs exhibit strong emission within the visible region, which makes them ideal for detection in cells using FACS and luminescence imaging.

The IrC_{12} functionalized nanoparticles did not display significant cytotoxicity in HeLa cells at the concentrations tested, indicating their suitability to be used for cellular uptake and subcellular localization studies. The uptake of the IrC_{12} coated AuNPs in HeLa cells was evaluated and compared to the uptake of AuNPs modified with the IrbpySS complex, to determine whether the presence of the dodecyl chain on the IrC_{12} complex improves internalization of nanoparticles. The results indicate no differences in the uptake efficacy between the IrC_{12} and IrbpySS coated AuNPs, with both luminescent nanoprobes exhibiting efficient cellular entry in HeLa cells. However, upon excitation at 405 nm, the IrC_{12} coated AuNPs display significantly stronger emission than the IrbpySS modified AuNPs, indicating the enhanced luminescence properties of the IrC_{12} complex induced by the presence of the long alkyl chain. The advantageous photophysical properties of the IrC_{12} complex upon attachment to the gold surface suggest the appropriateness of the luminescent nanoparticles for improved detection sensitivity in cancer cells.

The efficient uptake of the functionalized nanoparticles in HeLa cells was also supported by luminescence lifetime measurements, as luminescence from the iridium complex was detectable in treated cells. Analysis revealed an increase in the luminescence lifetime of the IrC_{12} coated AuNPs in HeLa cells, which was attributed to interactions between the iridium complex and intracellular proteins. The ability of the

luminescent nanoparticles to interact with proteins was further examined by CD spectroscopy, indicating that binding of the iridium complex to BSA induces conformational changes in the secondary structure of the protein. The alterations observed in the structure of BSA suggest that the iridium complex can engage in strong electrostatic and hydrophobic biomolecular interactions with cellular proteins and alter biological processes that are essential for cell proliferation and survival.

The efficient cellular uptake of the IrC_{12} coated nanoparticles in HeLa cells was further confirmed by confocal luminescence microscopy, as live cell imaging revealed a strong luminescence signal from the iridium complex within the nucleus and cytoplasm of the cells. The nuclear localization observed in the cells treated with the luminescent nanoparticles was not evident upon treatment of the cells with the IrC_{12} complex in solution, indicating that the conjugation of the complex to the surface of AuNPs improves drastically its bioavailability within the intracellular environment, promoting efficient subcellular localization.The uptake and subcellular localization of the luminescent AuNPs in HeLa cells were quantified by ICP-MS, both in whole and fractionated cell lysates. ICP-MS analysis performed in whole cell lysates revealed approximately 11 000 IrC_{12} coated AuNPs per cell, confirming the efficient cellular uptake of the luminescent nanoparticles observed by FACS and confocal luminescence microscopy. The nuclear localization of the iridium modified AuNPs observed by luminescence imaging was further validated by ICP-MS, as analysis in fractionated lysates suggested the ability of the IrC_{12} coated nanoparticles to penetrate the nuclear membrane and accumulate within the nucleus.

In conclusion, in this chapter, novel luminescent nanoparticles were presented with efficient cellular uptake and nuclear localization in cancer cells. The results support that the use of AuNPs as a scaffold to deliver luminescent metal complexes in cancer cells provides significantly improved bioavailability within an intracellular environment and promotes subcellular localization. The favourable luminescence properties of the IrC_{12} coated nanoparticles, along with their ability to penetrate the nuclear membrane, present a promising approach for monitoring biomolecular interactions with nuclear proteins in *in vivo* models.

3.5 Acknowledgments

I would like to thank both Andrew Carrod and Dr. Samuel Adams (School of Chemistry, University of Birmingham), for providing the luminescent iridium complexes used in this chapter. Also, I wish to acknowledge Mr. Paul Stanley (School of Metallurgy and Materials, University of Birmingham) for performing the TEM imaging of the iridium coated nanoparticle samples. Finally, I wish to thank Dr. Lijiang Song (Department of Chemistry, University of Warwick) for carrying out the elemental analysis in HeLa cells by ICP-MS.

3.6 Experimental

3.6.1 Synthesis of Iridium complexes

The synthesis and characterization of the IrC_{12} and IrC_{12}bpy complexes was carried out by Andrew Carrod (School of Chemistry, University of Birmingham) (Appendix B – Scheme B-1, Figures B-1 and B-2). The synthesis and characterization of the IrbpySS[42] and Irbpy complexes was performed by Dr. Samuel Adams, (School of Chemistry, University of Birmingham).

3.6.2 Preparation of IrC_{12}·Z·AuNP25 and IrbpySS·Z·AuNP25

Firstly, 8 ml of AuNP25 of 0.65 nM were centrifuged twice at 10, 000 g for 20 minutes. After each centrifugation the supernatant was discarded and the AuNP25 pellet was re-suspended in 1 ml of fresh filtered miliQ H_2O. The centrifuged nanoparticles were then coated with a 2.5% Zonyl FSA (Sigma-Aldrich) stock solution (0.2 mM) that was prepared in miliQ H_2O and filtered. In 1 ml of centrifuged AuNP25, 20 µl (4 µM) of Zonyl FSA were added and stirred for about 10 minutes. The zonyl coated nanoparticles were centrifuged twice at 10, 000 g for 20 minutes, in order to remove excess zonyl. The centrifuged zonyl coated AuNP25 were re-suspended in 1 ml of fresh filtered miliQ H_2O to produce Z·AuNP25 (Final concentration ~ 5 nM). UV-Vis (H_2O) λ_{max}= 520 nm (SPR). Diameter = 28 ± 7 nm (DLS number distribution). Diameter = 43 ± 12 nm (DLS intensity distribution) (1 nM in miliQ H_2O).

The preparation of the IrC_{12} coated AuNP25 and the IrbpySS coated AuNP25 was performed under the same conditions. The IrC_{12} and IrpbySS complexes (Stock solution in methanol: 1 mM) were titrated in 2 µl aliquots to an aqueous solution of Z·AuNP25 (2 nM), while stirring in between each addition. The successful attachment of the complexes to the gold surface subsequent to each addition was confirmed through monitoring the SPR band of the nanoparticles using UV-Vis spectroscopy (Cary 5000 Spectrometer). The red shift in the SPR allowed the maximum concentration of IrC_{12} and IrbpySS that can be used to coat

the gold surface without inducing nanoparticle aggregation to be determined. The maximum concentration, for both the IrC_{12} and the IrbpySS complex, that is required to reach saturation on the surface of the zonyl coated AuNP25 is 40 μM. Therefore, 40 μM of IrC_{12} and IrbpySS were added in 2 μl aliquots into 1 ml of Z·AuNP25 (2 nM) with stirring in between each addition. After the last addition, the functionalized nanoparticles were stirred for a further 20 minutes.

Finally, size exclusion chromatography was performed using Sephadex G-10 (Sigma-Aldrich) to remove excess, unbound iridium complex and obtain purified IrC_{12}·Z·AuNP25 and IrbpySS·Z·AuNP25 (Final concentration ~ 1.8 nM). UV-Vis (H_2O) λ_{max} = 525 nm (SPR). IrC_{12}·Z·AuNP25: Diameter = 29 ± 9 nm (DLS number distribution). Diameter = 80 ± 24 nm (DLS intensity distribution) (1 nM in miliQ H_2O). IrbpySS·Z·AuNP25: Diameter = 28 ± 8 nm (DLS number distribution). Diameter = 74 ± 22 nm (DLS intensity distribution) (1 nM in miliQ H_2O).

3.6.3 MTT Cell Viability Assay

Cell viability in HeLa cells after treatment with both the functionalized AuNP25 samples and the IrC_{12} complex in solution was assessed using the MTT cell viability assay. For the purposes of the assay, a fresh stock solution of the MTT reagent (Thermo Fisher Scientific, Catalogue number: M6494) was prepared in PBS (5 mg/ml). $1x10^4$ cells per well were seeded in a 96-well plate and were incubated overnight to allow the cells to adhere. Seeding of the cells for each experimental group was performed in triplicate. The cells were then washed twice with sterile PBS and fresh culture media was added, followed by the addition of Z·AuNP25, IrC_{12}·Z·AuNP25 and the IrC_{12} complex in solution for 24 hours. Both the nanoparticle samples and the molecular complex were added in the cells at a ratio of 1:10 (sample:culture media). Cytotocixity in HeLa cells was evaluated at 0.2, 0.4 and 0.6 nM of Z·AuNP25 and IrC_{12}·Z·AuNP25 and at concentrations between 0.5 to 3 μM for the IrC_{12} complex. After 24 hours, the cells were washed three times with sterile PBS and fresh cell culture media was added, followed by the addition of 20 μl of the MTT solution. The 96-well plate was covered in foil and the cells were incubated with the MTT

reagent for 4 hours. Finally, the cell media containing the MTT reagent was discarded and 150 µl of DMSO (Sigma-Aldrich) were added to the cells in each well. The 96-well plate was placed on a plate shaker for 20 minutes and it was then read using the iMarkTM Microplate Absorbance Reader (Bio Rad). The absorbance was measured at OD = 590 nm.

3.6.4 Cellular uptake by FACS

Initially, HeLa cells were cultured in 60 mm dishes, $1x10^6$ cells per dish, and incubated overnight in order for the cells to adhere. The cells were washed twice with sterile PBS and then fresh serum-free DMEM culture media was added, followed by the addition of the samples. The cells were incubated with the samples for 24 hours. All samples were added at a ratio of 1:10 (sample:culture media). The cellular uptake efficacy of the iridium coated nanoparticles was evaluated subsequent to treatment of the cells with 0.4 nM IrC_{12}·Z·AuNP25 and IrbpySS·Z·AuNP25. The concentration of each of the iridium complexes used to evaluate cellular uptake in HeLa cells was chosen through photophysical characterization. The treatment concentration used for IrC_{12}, IrbpySS and IrC_{12}bpy is 0.3 µM and for Irbpy is 0.2 µM. IrC_{12}bpy and Irbpy were used as the positive controls of the experiment. After treatment of the cells for 24 hours, the cells were washed three times with sterile PBS and were then trypsinized, using Trypsin-EDTA (0.25%) (Gibco®-Thermo Fisher Scientific) for about 5 minutes. Fresh culture media was added to quench tryspinization and the cells were collected and centrifuged at 1 000 rpm for 5 minutes. The supernatant was discarded and the cells were re-suspended in 1 ml of PBS supplemented with 1% FBS and transferred to FACS tubes for analysis. Samples were run on the LSRII Flow Cytometer (BD Biosciences, Oxford, UK) using the BD FACSDiva Software. Analysis was performed using FlowJo and Cytobank.

3.6.5 Live cell imaging by Confocal microscopy

The cells were seeded in 35 mm dishes, $1x10^5$ cells per dish, and incubated overnight for cells to adhere. The cells were then washed twice with sterile PBS and fresh serum-free DMEM culture media was added. The IrC_{12} coated nanoparticles and the iridium complex in solution were added to the cells at a ratio of 1:10 (sample:culture media) and incubated with the samples for both 4 and 24 hours. The cells were treated with 0.4 nM IrC_{12}·Z·AuNP25 and 0.3 µM of IrC_{12}. The culture media was then discarded and the cells were washed three times with sterile PBS. Fresh cell culture media, DMEM phenol red free media (Gibco®-Thermo Fisher Scientific) was added and the cells were imaged immediately using the Leica TCS SP8 upright confocal scanning system with a 40x water immersion objective lens. Imaging analysis was performed using ImageJ 2.0.0 software.

3.6.6 Cellular uptake and subcellular localization by ICP-MS

HeLa cells were cultured in 150 mm dishes at a $1x10^7$ density, and incubated overnight for cells to adhere. The cells were then washed twice with sterile PBS and fresh serum-free DMEM culture media was added to the cells, followed by the addition of the IrC_{12} coated nanoparticles and the molecular IrC_{12} complex for 24 hours. Samples were added to the cells at a ratio of 1:10 (sample:culture media). The cellular uptake and subcellular localization in HeLa cells were evaluated after treatment of the cells with 0.4 nM IrC_{12}·Z·AuNP25 and 0.3 µM of the IrC_{12} complex in solution. After treatment for 24 hours, the cells were washed three times with sterile PBS and were then trypsinized using Trypsin-EDTA (0.25%) (Gibco®-Thermo Fisher Scientific) for 5 minutes. Fresh culture media was added and the cells were collected and centrifuged at 1 000 rpm for 5 minutes. The supernatant was then discarded, the cell pellets were re-suspended in 10 ml of fresh media and the cells were counted using Trypan Blue dye (Gibco®-Thermo Fisher Scientific) and a haemocytometer.

The treated cells were then divided in two equal aliquots, one was used as a “whole cell” population and the other one was fractionated into nucleus, cytosol and mitochondria. For the isolation of the different organelles the Mitochondria isolation kit by Qiagen (Catalogue number: 37612) was used and the fractionation was performed according to the protocol provided by the manufacturer. Digestion of cells was carried out in glass vials (V-Vials by Sigma-Aldrich, Catalogue number: Z115118). The cell samples were transferred into the vials, followed by the addition of 300 µl of ultra-pure HNO_3 (Traceselect Ultra, Aldrich – 68%) and left overnight at 80 °C. Finally, the digested samples were filtered and transferred to polypropylene tubes for ICP-MS (Agilent). The volume was adjusted using ultra-pure H_2O to obtain a 4% final dilution of HNO_3. (Final volume for each sample was 5 ml). The samples were kept at 4 °C until analysis.

3.7 References

[1] Colaprico, A., Olsen, C., Bailey, M. H., Odom, G. J., Terkelsen, T., Silva, T. C., Olsen, A. V., Cantini, L., Zinovyev, A., Barillot, E., Noushmehr, H., Bertoli, G., Castiglioni, I., Cava, C., Bontempi, G., Chen, X. S. & Papaleo, E. 2020. Interpreting pathways to discover cancer driver genes with Moonlight. *Nat Commun,* 11**,** 69.

[2] Willis, R. E. 2016. Targeted Cancer Therapy: Vital Oncogenes and a New Molecular Genetic Paradigm for Cancer Initiation Progression and Treatment. *Int J Mol Sci,* 17**,** 1552.

[3] Hanahan, D. & Weinberg, R. A. 2011. Hallmarks of cancer: the next generation. *Cell,* 144**,** 646-674.

[4] Meacham, C. E. & Morrison, S. J. 2013. Tumour heterogeneity and cancer cell plasticity. *Nature,* 501**,** 328-337.

[5] Iranzo, J., Martincorena, I. & Koonin, E. V. 2018. Cancer-mutation network and the number and specificity of driver mutations. *Proc Natl Acad Sci U S A,* 115**,** E6010.

[6] Mcgranahan, N. & Swanton, C. 2017. Clonal Heterogeneity and Tumor Evolution: Past, Present, and the Future. *Cell,* 168**,** 613-628.

[7] Cheung-Ong, K., Giaever, G. & Nislow, C. 2013. DNA-Damaging Agents in Cancer Chemotherapy: Serendipity and Chemical Biology. *Chem Biol* 20**,** 648-659.

[8] Helleday, T., Petermann, E., Lundin, C., Hodgson, B. & Sharma, R. A. 2008. DNA repair pathways as targets for cancer therapy. *Nat Rev Cancer,* 8**,** 193-204.

[9] Pfitzer, L., Moser, C., Gegenfurtner, F., Arner, A., Foerster, F., Atzberger, C., Zisis, T., Kubisch-Dohmen, R., Busse, J., Smith, R., Timinszky, G., Kalinina, O. V., Müller, R., Wagner, E., Vollmar, A. M. & Zahler, S. 2019. Targeting actin inhibits repair of doxorubicin-induced DNA damage: a novel therapeutic approach for combination therapy. *Cell Death Dis,* 10**,** 302.

[10] Nurgali, K., Jagoe, R. T. & Abalo, R. 2018. Editorial: Adverse Effects of Cancer Chemotherapy: Anything New to Improve Tolerance and Reduce Sequelae? *Front Pharmacol,* 9**,** 245-245.

[11] Senapati, S., Mahanta, A. K., Kumar, S. & Maiti, P. 2018. Controlled drug delivery vehicles for cancer treatment and their performance. *Sig Transduct Target Ther,* 3.

[12] Yao, Y. L. & Yang, W. M. 2005. Nuclear proteins: promising targets for cancer drugs. *Curr Cancer Drug Targets,* 5**,** 595-610.

[13] Esteves, P., Dard, L., Brillac, A., Hubert, C., Sarlak, S., Rousseau, B., Dumon, E., Izotte, J., Bonneu, M., Lacombe, D., Dupuy, J. W., Amoedo, N. & Rossignol, R. 2020. Nuclear control of lung cancer cells migration, invasion and bioenergetics by eukaryotic translation initiation factor 3F. *Oncogene,* 39**,** 617-636.

[14] Morgan, M. A. & Shilatifard, A. 2015. Chromatin signatures of cancer. *Genes Dev,* 29**,** 238-249.

[15] Gurova, K. V. Chromatin Stability as a Target for Cancer Treatment. *Bioassays,* 41**,** 1800141.

[16] Baggaley, E., Weinstein, J. A. & Williams, J. A. G. 2012. Lighting the way to see inside the live cell with luminescent transition metal complexes. *Coord Chem Rev,* 256**,** 1762-1785.

[17] Puckett, C. A. & Barton, J. K. 2010. Targeting a ruthenium complex to the nucleus with short peptides. *Bioorg Med Chem,* 18**,** 3564-3569.

[18] Huang, R., Zhu, J. Q., Tang, M., Huang, C. H., Zhang, Z. H., Sheng, Z. G., Liu, S. & Zhu, B. Z. 2020. Unexpected reversible and controllable nuclear uptake and efflux of the DNA "light-switching" Ru(ii)-polypyridyl complex in living cells via ion-pairing with chlorophenolate counter-anions. *J Mater Chem B,* 8**,** 10327-10336.

[19] Tian, X., Zhu, Y., Zhang, M., Luo, L., Wu, J., Zhou, H., Guan, L., Battaglia, G. & Tian, Y. 2017. Localization matters: a nuclear targeting two-photon absorption iridium complex in photodynamic therapy. *Chem Commun (Camb),* 53**,** 3303-3306.
[20] Komatsu, H., Yoshihara, K., Yamada, H., Kimura, Y., Son, A., Nishimoto, S. & Tanabe, K. 2013. Ruthenium Complexes with Hydrophobic Ligands That Are Key Factors for the Optical Imaging of Physiological Hypoxia. *Chem – Eur J,* 19**,** 1971-1977.
[21] Schattschneider, C., Doniz Kettenmann, S., Hinojosa, S., Heinrich, J. & Kulak, N. 2019. Biological activity of amphiphilic metal complexes. *Coord Chem Rev,* 385**,** 191-207.
[22] Zamora, A., Vigueras, G., Rodríguez, V., Santana, M. D. & Ruiz, J. 2018. Cyclometalated iridium(III) luminescent complexes in therapy and phototherapy. *Coord Chem Rev,* 360**,** 34-76.
[23] Abbas, S., Din, I-D., Raheel, A. & Tameez Ud Din, A. 2020. Cyclometalated Iridium (III) complexes: Recent advances in phosphorescence bioimaging and sensing applications. *Appl Organometal Chem,* 34**,** e5413.
[24] Ruiz, J., Vicente, C., De Haro, C. & Bautista, D. 2013. Novel Bis-C,N-Cyclometalated Iridium(III) Thiosemicarbazide Antitumor Complexes: Interactions with Human Serum Albumin and DNA, and Inhibition of Cathepsin B. *Inorg Chem,* 52**,** 974-982.
[25] Kar, B., Roy, N., Pete, S., Moharana, P. & Paira, P. 2020. Ruthenium and iridium based mononuclear and multinuclear complexes: A Breakthrough of Next-Generation anticancer metallopharmaceuticals. *Inorg Chim Acta,* 512**,** 119858.
[26] Zhang, W. Y., Banerjee, S., Hughes, G. M., Bridgewater, H. E., Song, J. I., Breeze, B. G., Clarkson, G. J., Coverdale, J. P. C., Sanchez-Cano, C., Ponte, F., Sicilia, E. & Sadler, P. J. 2020. Ligand-centred redox activation of inert organoiridium anticancer catalysts. *Chemical Science,* 11**,** 5466-5480.
[27] Novohradsky, V., Zerzankova, L. , Stepankova, J., Kisova, A., Kostrhunova, H., Liu, Z., Sadler, P. J., Kasparkova, J. & Brabec, V. 2014. A dual-targeting, apoptosis-inducing organometallic half-sandwich iridium anticancer complex. *Metallomics,* 6**,** 1491-1501.
[28] Liu, J. B., Vellaisamy, K. , Guodong, L., Chao, Y., Wong, S. Y., Leung, C. H., Pu, S. Z. & Ma, D. L. 2018. A long-lifetime iridium(iii) complex for lysosome tracking with high specificity and a large Stokes shift. *J Mater Chem B,* 6**,** 3855-3858.
[29] Jin, C., Liu, J., Chen, Y., Guan, R., Ouyang, C., Zhu, Y., Ji, L. & Chao, H. 2016. Cyclometalated Iridium(III) Complexes as AIE Phosphorescent Probes for Real-Time Monitoring of Mitophagy in Living Cells. *Sci Rep,* 6**,** 22039.
[30] Byrne, A., Burke, C. S. & Keyes, T. E. 2016. Precision targeted ruthenium(ii) luminophores; highly effective probes for cell imaging by stimulated emission depletion (STED) microscopy. *Chem Sci,* 7**,** 6551-6562.
[31] Ma, D. L., Wu, C., Tang, W., Gupta, A. R., Lee, F. W., Li, G. & Leung, C. H. 2018. Recent advances in iridium(iii) complex-assisted nanomaterials for biological applications. *J Mater Chem B,* 6**,** 537-544.
[32] Mjos, K. D. & Orvig, C. 2014. Metallodrugs in Medicinal Inorganic Chemistry. *Chem Rev,* 114**,** 4540-4563.
[33] Puckett, C. A., Ernst, R. J. & Barton, J. K. 2010. Exploring the cellular accumulation of metal complexes. *Dalton Trans,* 39**,** 1159-1170.
[34] Komor, A. C. & Barton, J. K. 2013. The path for metal complexes to a DNA target. *Chem Commun (Camb),* 49**,** 3617-3630.
[35] Patra, J. K., Das, G. , Fraceto, L. F. , Campos, E. , Rodriguez-Torres, M. , Acosta-Torres, L. S. , Diaz-Torres, L. A. , Grillo, R. , Swamy, M. K. , Sharma, S. , Habtemariam, S. & Shin, H.

S. 2018. Nano based drug delivery systems: recent developments and future prospects. *J Nanobiotechnol,* 16**,** 71.
[36] Rosenblum, D., Joshi, N., Tao, W., Karp, J. M. & Peer, D. 2018. Progress and challenges towards targeted delivery of cancer therapeutics. *Nat Commun,* 9**,** 1410.
[37] Din, F. U., Aman, W., Ullah, I., Qureshi, O. S., Mustapha, O., Shafique, S. & Zeb, A. 2017. Effective use of nanocarriers as drug delivery systems for the treatment of selected tumors. *Int J Nanomedicine,* 12**,** 7291-7309.
[38] Mitchell, M. J., Billingsley, M. M., Haley, R. M., Wechsler, M. E., Peppas, N. A. & Langer, R. 2020. Engineering precision nanoparticles for drug delivery. *Nat Rev Drug Discov*.
[39] King, Siobhan M., Claire, Sunil, Teixeira, Rodolfo I., Dosumu, Abiola N., Carrod, Andrew J., Dehghani, Hamid, Hannon, Michael J., Ward, Andrew D., Bicknell, Roy, Botchway, Stanley W., Hodges, Nikolas J. & Pikramenou, Zoe 2018. Iridium Nanoparticles for Multichannel Luminescence Lifetime Imaging, Mapping Localization in Live Cancer Cells. *J Am Chem Soc,* 140**,** 10242-10249.
[40] Osborne, S. A. M. & Pikramenou, Z. 2015. Highly luminescent gold nanoparticles: effect of ruthenium distance for nanoprobes with enhanced lifetimes. *Faraday Discussions,* 185**,** 219-231.
[41] Adams, S. J., Carrod, A. J., Rochford, L. A., Walker, M. & Pikramenou, Z. 2018. Surfactant-Enhanced Luminescence Lifetime for Biomolecular Detection on Luminescent Gold Surfaces Decorated with Transition Metal Complexes. *Chemistryselect,* 3**,** 3251-3257.
[42] Adams, S. J., Lewis, D. J., Preece, J. A. & Pikramenou, Z. 2014. Luminescent gold surfaces for sensing and imaging: patterning of transition metal probes. *ACS Appl Mater Interfaces,* 6**,** 11598-11608.
[43] Lamansky, S., Djurovich, P., Murphy, D., Abdel-Razzaq, F., Kwong, R., Tsyba, I., Bortz, M., Mui, B., Bau, R. & Thompson, M. E. 2001. Synthesis and characterization of phosphorescent cyclometalated iridium complexes. *Inorg Chem,* 40**,** 1704-1711.
[44] Lamansky, S., Djurovich, P., Murphy, D., Abdel-Razzaq, F., Lee, H. E., Adachi, C., Burrows, P. E., Forrest, S. R. & Thompson, M. E. 2001. Highly phosphorescent bis-cyclometalated iridium complexes: synthesis, photophysical characterization, and use in organic light emitting diodes. *J Am Chem Soc,* 123**,** 4304-4312.
[45] Slinker, J. D., Gorodetsky, A. A., Lowry, M. S., Wang, J., Parker, S., Rohl, R., Bernhard, S. & Malliaras, G. G. 2004. Efficient yellow electroluminescence from a single layer of a cyclometalated iridium complex. *J Am Chem Soc,* 126**,** 2763-2767.
[46] Colombo, M. G. , Hauser, A. & Giidel, H. U. 1993. Evidence for Strong Mixing between the LC and MLCT Excited States in Bis(2-phenylpyridinato-C2,Ar0(2,2'-bipyridine)iridium(III). *Inorg Chem,* 32**,** 3088-3092.
[47] Constable, E. C., Ertl, C. F. , Housecroft, C. E. & Zampese, J. A. 2014. Green-emitting iridium(III) complexes containing sulfanyl- or sulfone-functionalized cyclometallating 2-phenylpyridine ligands. *Dalton Trans,* 43**,** 5343-5356.
[48] Kawamorita, S., Ahadito, B. R. & Naota, T. 2020. Proximity effects on the phosphorescent properties of dinuclear salicylaldiminato cyclometalated iridium(III) complexes linked with polymethylene spacers. *Transit Met Chem,* 45**,** 173-186.
[49] Turkevich, J., Stevenson, P. C. & Hillier, J. 1951. A Study of the Nucleation and Growth Processes in the Synthesis of Colloidal Gold. *Discuss Faraday Soc,* 11**,** 55-75.
[50] Ziegler, C. & Eychmuller, A. 2011. Seeded Growth Synthesis of Uniform Gold Nanoparticles with Diameters of 15-300 nm. *J Phys Chem C,* 115**,** 4502-4506.

[51] Rogers, N. J., Claire, S., Harris, R. M., Farabi, S., Zikeli, G., Styles, I. B., Hodges, N. J. & Pikramenou, Z. 2014. High coating of Ru(II) complexes on gold nanoparticles for single particle luminescence imaging in cells. *Chem Commun* 50**,** 617-619.
[52] Adewale, O. B., Davids, H., Cairncross, L. & Roux, S. 2019. Toxicological Behavior of Gold Nanoparticles on Various Models: Influence of Physicochemical Properties and Other Factors. *Int J Toxicol,* 38**,** 357-384.
[53] Sukhanova, A., Bozrova, S., Sokolov, P., Berestovoy, M., Karaulov, A. & Nabiev, I. 2018. Dependence of Nanoparticle Toxicity on Their Physical and Chemical Properties. *Nanoscale Res Lett,* 13**,** 44-44.
[54] Sun, H., Jiang, C. , Wu, L., Bai, X. & Zhai, S. 2019. Cytotoxicity-Related Bioeffects Induced by Nanoparticles: The Role of Surface Chemistry. *Front Bioeng Biotechnol,* 7**,** 414.
[55] Chandran, P., Riviere, J. E. & Monteiro-Riviere, N. A. 2017. Surface chemistry of gold nanoparticles determines the biocorona composition impacting cellular uptake, toxicity and gene expression profiles in human endothelial cells. *Nanotoxicology,* 11**,** 507-519.
[56] Wang, J. Y., Chen, J., Yang, J., Wang, H., Shen, X., Sun, Y. M., Guo, M. & Zhang, X. D. 2016. Effects of surface charges of gold nanoclusters on long-term in vivo biodistribution, toxicity, and cancer radiation therapy. *Int J Nanomedicine,* 11**,** 3475-3485.
[57] Rogers, N. J., Jeffery, H. C., Claire, S., Lewis, D. J., Zikeli, G., Hodges, N. J., Egginton, S., Nash, G. B. & Pikramenou, Z. 2017. Tailoring iridium luminescence and gold nanoparticle size for imaging of microvascular blood flow. *Nanomedicine (Lond),* 12**,** 2725-2740.
[58] Zhang, W. Y., Wang, Y. J., Du, F., He, M., Gu, Y. Y., Bai, L., Yang, L. L. & Liu, Y. J. 2019. Evaluation of anticancer effect in vitro and in vivo of iridium(III) complexes on gastric carcinoma SGC-7901cells. *Eur J Med Chem,* 178**,** 401-416.
[59] Ma, D. L., Wu, C., Wu, K. J. & Leung, C. H. 2019. Iridium(III) Complexes Targeting Apoptotic Cell Death in Cancer Cells. *Molecules,* 24**,** 2739.
[60] Cao, J. J., Tan, C. P., Chen, M. H., Wu, N., Yao, D. Y., Liu, X. G., Ji, L. N. & Mao, Z. W. 2017. Targeting cancer cell metabolism with mitochondria-immobilized phosphorescent cyclometalated iridium(iii) complexes. *Chem Sci,* 8**,** 631-640.
[61] Aubry, S., Burlina, F., Dupont, E., Delaroche, D., Joliot, A., Lavielle, S., Chassaing, G. & Sagan, S. 2009. Cell-surface thiols affect cell entry of disulfide-conjugated peptides. *FASEB J,* 23**,** 2956-2967.
[62] Saito, G., Swanson, J. A. & Lee, K. D. 2003. Drug delivery strategy utilizing conjugation via reversible disulfide linkages: role and site of cellular reducing activities. *Adv Drug Deliv Rev,* 55**,** 199-215.
[63] Foroozandeh, P. & Aziz, A. A. 2018. Insight into Cellular Uptake and Intracellular Trafficking of Nanoparticles. *Nanoscale Res Lett,* 13**,** 339.
[64] Chou, L. Y. T., Ming, K. & Chan, W. C. W. 2011. Strategies for the intracellular delivery of nanoparticles. *Chem Soc Rev,* 40**,** 233-245.
[65] Mahmoudi, M., Meng, J., Xue, X., Liang, X. J., Rahman, M., Pfeiffer, C., Hartmann, R., Gil, P. R., Pelaz, B., Parak, W. J., Del Pino, P., Carregal-Romero, S., Kanaras, A. G. & Tamil Selvan, S. 2014. Interaction of stable colloidal nanoparticles with cellular membranes. *Biotechnol Adv,* 32**,** 679-692.
[66] Docter, D., Westmeier, D., Markiewicz, M., Stolte, S., Knauer, S. K. & Stauber, R. H. 2015. The nanoparticle biomolecule corona: lessons learned – challenge accepted? *Chem Soc Rev,* 44**,** 6094-6121.
[67] Dennis, A. M., Delehanty, J. B. & Medintz, I. L. 2016. Emerging Physicochemical Phenomena along with New Opportunities at the Biomolecular–Nanoparticle Interface. *J Phys Chem Lett,* 7**,** 2139-2150.

[68] Petros, R. A. & Desimone, J. M. Strategies in the design of nanoparticles for therapeutic applications. *Nat Rev Drug Discov*.
[69] Yameen, B. , Choi, W. I. , Vilos, C. , Swami, A. , Shi, J. & Farokhzad, O. C. 2014. Insight into nanoparticle cellular uptake and intracellular targeting. *J Control Release,* 28**,** 485-499.
[70] Rees, P., Wills, J. W., Brown, M. R., Barnes, C. M. & Summers, H. D. 2019. The origin of heterogeneous nanoparticle uptake by cells. *Nat Commun,* 10**,** 2341.
[71] Jiang, W., Gao, Y., Sun, Y., Ding, F., Xu, Y., Bian, Z., Li, F., Bian, J. & Huang, C. 2010. Zwitterionic iridium complexes: synthesis, luminescent properties, and their application in cell imaging. *Inorg Chem,* 49**,** 3252-3260.
[72] Puckett, C. A. & Barton, J. K. 2007. Methods to explore cellular uptake of ruthenium complexes. *J Am Chem Soc,* 129**,** 46-47.
[73] Zava, O., Zakeeruddin, S. M., Danelon, C., Vogel, H., Grätzel, M. & Dyson, P. J. 2009. A Cytotoxic Ruthenium Tris(Bipyridyl) Complex that Accumulates at Plasma Membranes. *ChemBioChem,* 10**,** 1796-1800.
[74] Zhang, K. Y., Zhang, T., Wei, H., Wu, Q., Liu, S., Zhao, Q. & Huang, W. 2018. Phosphorescent iridium(iii) complexes capable of imaging and distinguishing between exogenous and endogenous analytes in living cells. *Chem Sci,* 9**,** 7236-7240.
[75] Zhang, K. Y., Song, L., Gu, T., Wang, H., Yang, C., Zhou, H., Gao, P., Liu, S. & Zhao, Q. 2020. Cell-Membrane Staining Properties and Photocytotoxicity of a Ruthenium(II) Photosensitizer. *Eur J Inorg Chem,* 2020**,** 3996-4001.
[76] Otero, C., Carreño, A., Polanco, R., Llancalahuen, F. M., Arratia-Pérez, R., Gacitúa, M. & Fuentes, J. A. 2019. Rhenium (I) Complexes as Probes for Prokaryotic and Fungal Cells by Fluorescence Microscopy: Do Ligands Matter? *Front Chem,* 7**,** 454.
[77] Conner, S. D. & Schmid, S. L. 2003. Regulated portals of entry into the cell. *Nature,* 422**,** 37-44.
[78] Martinho, N., Santos, T. C. B., Florindo, H. F. & Silva, L. C. 2019. Cisplatin-Membrane Interactions and Their Influence on Platinum Complexes Activity and Toxicity. *Front Physiol,* 9**,** 1898.
[79] Mathieu, E., Sipos, A., Demeyere, E., Phipps, D., Sakaveli, D. & Borbas, K. E. 2018. Lanthanide-based tools for the investigation of cellular environments. *Chem Commun* 54**,** 10021-10035.
[80] Kapara, A., Brunton, V., Graham, D. & Faulds, K. 2020. Investigation of cellular uptake mechanism of functionalised gold nanoparticles into breast cancer using SERS. *Chem Sci,* 11**,** 5819-5829.
[81] Salatin, S. & Yari Khosroushahi, A. 2017. Overviews on the cellular uptake mechanism of polysaccharide colloidal nanoparticles. *J Cell Mol Med,* 21**,** 1668-1686.
[82] Zhao, F., Zhao, Y., Liu, Y., Chang, X., Chen, C. & Zhao, Y. 2011. Cellular Uptake, Intracellular Trafficking, and Cytotoxicity of Nanomaterials. *Small,* 7**,** 1322-1337.
[83] Ndagi, U., Mhlongo, N. & Soliman, M. E. 2017. Metal complexes in cancer therapy - an update from drug design perspective. *Drug Des Devel Ther,* 11**,** 599-616.
[84] Han, Y., Cao, H. T., Sun, H. Z., Shan, G. G., Wu, Y., Su, Z. M. & Liao, Y. 2015. Simultaneous modification of N-alkyl chains on cyclometalated and ancillary ligands of cationic iridium(iii) complexes towards efficient piezochromic luminescence properties. *J Mater Chem C,* 3**,** 2341-2349.
[85] Dong, Y. B., Chen, Z., Yang, L., Hu, Y. X., Wang, X. Y., Yin, J. & Liu, S. H. 2018. Effect of alkyl chain length on the luminescence on-off mechanochromic behavior of solid-state Gold(I) isocyanide complexes. *Dyes Pigm,* 150**,** 315-322.

[86] Mazuryk, O., Magiera, K., Rys, B., Suzenet, F., Kieda, C. & Brindell, M. 2014. Multifaceted interplay between lipophilicity, protein interaction and luminescence parameters of non-intercalative ruthenium(II) polypyridyl complexes controlling cellular imaging and cytotoxic properties. *J Biol Inorg Chem,* 19**,** 1305-1316.
[87] Haas, K. L. & Franz, K. J. 2009. Application of metal coordination chemistry to explore and manipulate cell biology. *Chem Rev,* 109**,** 4921-4960.
[88] Anthony, E. J., Bolitho, E. M., Bridgewater, H. E., Carter, O. W. L., Donnelly, J. M., Imberti, C., Lant, E. C., Lermyte, F., Needham, R. J., Palau, M., Sadler, P. J., Shi, H., Wang, F. X., Zhang, W. Y. & Zhang, Z. 2020. Metallodrugs are unique: opportunities and challenges of discovery and development. *Chem Sci,* 11**,** 12888-12917.
[89] Ambika, S., Manojkumar, Y., Arunachalam, S., Gowdhami, B., Meenakshi Sundaram, K. K., Solomon, R. V., Venuvanalingam, P., Akbarsha, M. A. & Sundararaman, M. 2019. Biomolecular Interaction, Anti-Cancer and Anti-Angiogenic Properties of Cobalt(III) Schiff Base Complexes. *Sci Rep,* 9**,** 2721.
[90] Orvig, C. & Abrams, M. J. 1999. Medicinal Inorganic Chemistry: Introduction. *Chem Rev,* 99**,** 2201-2204.
[91] Thamilarasan, V., Sengottuvelan, N., Sudha, A., Srinivasan, P. & Chakkaravarthi, G. 2016. Cobalt(III) complexes as potential anticancer agents: Physicochemical, structural, cytotoxic activity and DNA/protein interactions. *J Photochem Photobiol B, Biol,* 162**,** 558-569.
[92] Hussain, A., Alajmi, M. F., Rehman, M. T., Amir, S., Husain, F. M., Alsalme, A., Siddiqui, M. A., Alkhedhairy, A. A. & Khan, R. A. 2019. Copper(II) complexes as potential anticancer and Nonsteroidal anti-inflammatory agents: In vitro and in vivo studies. *Sci Rep,* 9**,** 5237.
[93] Palermo, G., Magistrato, A., Riedel, T., Von Erlach, T., Davey, C. A., Dyson, P. J. & Rothlisberger, U. 2016. Fighting Cancer with Transition Metal Complexes: From Naked DNA to Protein and Chromatin Targeting Strategies. *ChemMedChem,* 11**,** 1199-1210.
[94] Greenfield, N. J. 2006. Using circular dichroism spectra to estimate protein secondary structure. *Nat Protoc,* 1**,** 2876-2890.
[95] Martin, S. R. & Schilstra, M. J. 2008. Circular Dichroism and Its Application to the Study of Biomolecules. *Methods Cell Biol.* Academic Press.
[96] Rogozea, A., Matei, I., Turcu, I. M., Ionita, G., Sahini, V. E. & Salifoglou, A. 2012. EPR and circular dichroism solution studies on the interactions of bovine serum albumin with ionic surfactants and beta-cyclodextrin. *J Phys Chem B,* 116**,** 14245-14253.
[97] Roy, A. S., Dinda, A. K., Pandey, N. K. & Dasgupta, S. 2016. Effects of urea, metal ions and surfactants on the binding of baicalein with bovine serum albumin. *J Pharm Anal,* 6**,** 256-267.
[98] Samari, F., Hemmateenejad, B., Shamsipur, M., Rashidi, M. & Samouei, H. 2012. Affinity of Two Novel Five-Coordinated Anticancer Pt(II) Complexes to Human and Bovine Serum Albumins: A Spectroscopic Approach. *Inorg Chem,* 51**,** 3454-3464.
[99] Wani, T. A., Bakheit, A. H., Ansari, M. N., Al-Majed, A. R. A., Al-Qahtani, B. M. & Zargar, S. 2018. Spectroscopic and molecular modeling studies of binding interaction between bovine serum albumin and roflumilast. *Drug Des Devel Ther,* 12**,** 2627-2634.
[100] Zhang, Q., Ni, Y. & Kokot, S. 2010. Molecular spectroscopic studies on the interaction between Ractopamine and bovine serum albumin. *J Pharm Biomed,* 52**,** 280-288.
[101] Sun, C., Yang, J., Wu, X., Huang, X., Wang, F. & Liu, S. 2005. Unfolding and refolding of bovine serum albumin induced by cetylpyridinium bromide. *Biophys J,* 88**,** 3518-3524.
[102] Yu, J., Chen, Y., Xiong, L., Zhang, X. & Zheng, Y. 2019. Conductance Changes in Bovine Serum Albumin Caused by Drug-Binding Triggered Structural Transitions. *Materials,* 12**,** 1022.

[103] Xie, X., Liao, J., Shao, X., Li, Q. & Lin, Y. 2017. The Effect of shape on Cellular Uptake of Gold Nanoparticles in the forms of Stars, Rods, and Triangles. *Sci Rep,* 7**,** 3827.
[104] Cho, E. C., Zhang, Q. & Xia, Y. 2011. The effect of sedimentation and diffusion on cellular uptake of gold nanoparticles. *Nat Nanotechnol,* 6**,** 385-391.
[105] Novohradsky, V., Liu, Z., Vojtiskova, M., Sadler, P. J., Brabec, V. & Kasparkova, J. 2014. Mechanism of cellular accumulation of an iridium(iii) pentamethylcyclopentadienyl anticancer complex containing a C,N-chelating ligand. *Metallomics,* 6**,** 682-690.
[106] Ouellette, M., Masse, F., Lefebvre-Demers, M., Maestracci, Q., Grenier, P., Millar, R., Bertrand, N., Prieto, M. & Boisselier, É. 2018. Insights into gold nanoparticles as a mucoadhesive system. *Sci Rep,* 8**,** 14357.
[107] Fratoddi, I., Venditti, I., Battocchio, C., Carlini, L., Amatori, S., Porchia, M., Tisato, F., Bondino, F., Magnano, E., Pellei, M. & Santini, C. 2019. Highly Hydrophilic Gold Nanoparticles as Carrier for Anticancer Copper(I) Complexes: Loading and Release Studies for Biomedical Applications. *Nanomaterials (Basel),* 9**,** 772.
[108] Ghosh, P., Han, G., De, M., Kim, C. K. & Rotello, V. M. 2008. Gold nanoparticles in delivery applications. *Adv Drug Deliv Rev,* 60**,** 1307-1315.
[109] Fen-Ying, K. Jin-Wei, Z. Rong-Fang , L. Zhong-Xia, W., Wen-Juan, W. Wei, W. 2017. Unique Roles of Gold Nanoparticles in Drug Delivery, Targeting and Imaging Applications. *Molecules,* 22**,** 1445.
[110] Hu, J., Deng, D., Liu, R. & Lv, Y. 2018. Single nanoparticle analysis by ICPMS: a potential tool for bioassay. *J Anal At Spectrom,* 33**,** 57-67.
[111] Kruszewska, J., Kur, A., Kulpińska, D., Grabowska-Jadach, I., Matczuk, M., Keppler, B. K., Timerbaev, A. R. & Jarosz, M. 2019. An improved protocol for ICP-MS-based assessment of the cellular uptake of metal-based nanoparticles. *J Pharmaceut Biomed,* 174**,** 300-304.
[112] Allabashi, R., Stach, W., De La Escosura-Muñiz, A., Liste Calleja, L. & Merkoçi, A. 2008. ICP-MS: A powerful technique for quantitative determination of gold nanoparticles without previous dissolving. *J Nanopart Res,* 11**,** 2003-2011.
[113] Barry, N. P. E. & Sadler, P. J. 2013. Challenges for Metals in Medicine: How Nanotechnology May Help To Shape the Future. *ACS Nano,* 7**,** 5654-5659.
[114] Sato, M. R. , Da Silva, P. B. , De Souza, R. A. , Dos Santos, K. C. & Chorilli, M. 2015. Recent advances in nanoparticle carriers for coordination complexes. *Curr Top Med Chem,* 15**,** 287-297.
[115] Zeng, L., Gupta, P., Chen, Y., Wang, E., Ji, L., Chao, H. & Chen, Z. S. 2017. The development of anticancer ruthenium(ii) complexes: from single molecule compounds to nanomaterials. *Chem Soc Rev,* 46**,** 5771-5804.
[116] Wang, W., Wang, J. & Ding, Y. 2020. Gold nanoparticle-conjugated nanomedicine: design, construction, and structure–efficacy relationship studies. *J Mater Chem B,* 8**,** 4813-4830.
[117] Hu, X., Zhang, Y., Ding, T., Liu, J. & Zhao, H. 2020. Multifunctional Gold Nanoparticles: A Novel Nanomaterial for Various Medical Applications and Biological Activities. *Front Bioeng Biotechnol,* 8**,** 990.

Chapter 4:

4. Antibody conjugated luminescent gold nanoparticles for enhanced detection of tumor biomarkers

4.1 Introduction

Precision medicine focuses on the development of patient-specific therapeutics in order to overcome the limitations associated with conventional treatment approaches and thus, improve the therapeutic outcome in the clinic[1, 2]. In the oncology field, the stratification of patients through the detection of tumor biomarkers is considered as the current standard for the design of novel theranostics, as the majority of cancer medicines fail to show positive results in unstratified clinical studies[3]. For successful stratification of patients, current developments involve the use of both biomarkers and companion diagnostics, which aid in addressing the high complexity and heterogeneity of tumors. The use of companion diagnostics has led to the successful development of many targeted therapies in the clinic, including tyrosine kinase inhibitors and antibodies for blocking growth factor receptors[3-5]. For instance, in the clinical trials that the monoclonal antibodies Trastuzumab (Herceptin)[6] and Pertuzumab (Perjeta)[7] received approval, patients with high expression of epidermal growth factor receptor 2 (HER2) were recruited using immunostaining and fluorescence in situ hybridization (FISH) to ensure high response to treatment[8, 9].

Within the last few decades, the use of nanotechnology-based materials has gained a lot of attention in the medical field for improving the specificity of diagnostic tools and conventional treatments currently used in the clinic[10]. What is more, the use of engineered nanomaterials in cancer research provides opportunities to overcome current limitations associated with the efficient delivery of targeting moieties, intracellular trafficking, bioavailability and biodistribution[11-13].

Interestingly, neither companion diagnostics nor tumor biomarkers are currently well established in the nanomedicine field for predicting treatment response in cancer patients. Although stratification of patients has been critical for the development of cancer precision medicines in the clinic, there are currently nanoparticle-based clinical trials conducted in the presence of unstratified patient populations[14]. However, as the importance of patient stratification becomes more evident, this is likely to change in the near future. The nanotechnology field is constantly emerging, and thus provides opportunities for the design and development of nanoparticles for targeting specific patient populations. The fact that nanoparticles are able to overcome current limitations related to drug delivery suggests that their use in the clinic can potentially enhance the treatment efficacy of precision medicines and thereby, allow a larger number of patients to qualify in clinical studies and benefit from personalized treatments[2, 15, 16].

Several antibody-modified nanoparticle formulations have been recently developed in the nanomedicine field for improving both *in vitro* and *in vivo* diagnostic applications including cell sorting, sensing and immunoassays. For instance, in a previously published study, the anti-EGFR antibody was used to modify silica core/gold shell nanoparticles in order to enhance the sensitivity of the enzyme-linked immunosorbent assay (ELISA). The anti-EGFR modified nanoparticles were used to treat three different cell lines, a normal cell line with no EGFR expression, a cell line with moderate expression of EGFR and a cell line with high expression of EGFR. The results indicated that when compared to the anti-EGFR alone, the antibody-modified nanoparticles induce a 13-fold increase in the sensitivity of the ELISA assay for the cells with high EGFR expression and a considerable decrease in the detection limit of the conventional assay[17]. In a different study, the anti-PSMA antibody was used to functionalize superparamagnetic iron oxide nanoparticles (SPION) for tracking prostate cancer cells, using Magnetic Resonance Imaging (MRI). The antibody-modified nanoparticles induced a significant increase in MRI contrast, indicating their ability to act as highly specific contrast agents[18]. The same antibody was used in another study to develop antibody modified Quantum Dots (QDs) for *in vivo* fluorescent cancer imaging. The anti-PSMA antibody was attached to the carboxyl group of QDs through the formation of amidic bonds, and the antibody-functionalized nanoparticles were

injected into prostate cancer-bearing mice. When compared against QDs without the antibody, the anti-PSMA modified QDs produced significantly stronger fluorescence signals upon *in vivo* imaging[19].

Inorganic nanoparticles, including gold, mesoporous silica, QDs and iron oxide nanoparticles, have been widely used in the nanotechnology field to combine both the treatment and imaging modalities of cancer diagnosis[20, 21]. The ability of inorganic nanoparticles to be formulated accurately into a wide range of structures, shapes and sizes provides countless possibilities for the development of theranostic nanoprobes. Gold nanoparticles (AuNPs) are currently considered as the most widely investigated nanoparticles in the medical field due to their ease of synthesis, multi-functionality and unique physico-chemical and optical properties[22-24]. What is more, AuNPs exhibit minimal toxicity and high biocompatibility, which makes them ideal nanocarriers for theranostic applications in biological environments[25].

The attachment of highly specific targeting moieties to AuNPs allows the development of tumor selective nanocarriers with improved therapeutic efficacy due to the favourable properties of AuNPs and the specificity provided by the targeting structures on the gold surface[26]. The high specificity and affinity of monoclonal antibodies towards a receptor and their approval in the clinic for therapeutic purposes have encouraged considerably the development of antibody-modified AuNPs for biomedical applications[27, 28]. Antibody-modified AuNPs were first introduced in 2008 in the presence of the monoclonal antibody Cetuximab for the targeted delivery of the anticancer agent Gemcitabine to pancreatic adenocarcinoma[29]. The presence of Cetuximab on Gemcitabine functionalized AuNPs induced significantly higher cytotoxicity in cancer cells when compared to AuNPs modified with Gemcitabine only, suggesting that the antibody improves drastically the delivery of the anticancer agent to the target site. Since then, AuNPs have been widely used for the improved delivery of many chemotherapeutic drugs including oxaliplatin[30] and doxorubicin[31, 32]. Antibodies are usually attached to the surface of AuNPs through adsorption to the gold surface via hydrophobic interactions (random antibody orientation), or directional conjugation via PEG ligands (controlled antibody orientation)[30-32] (Figure 4-1).

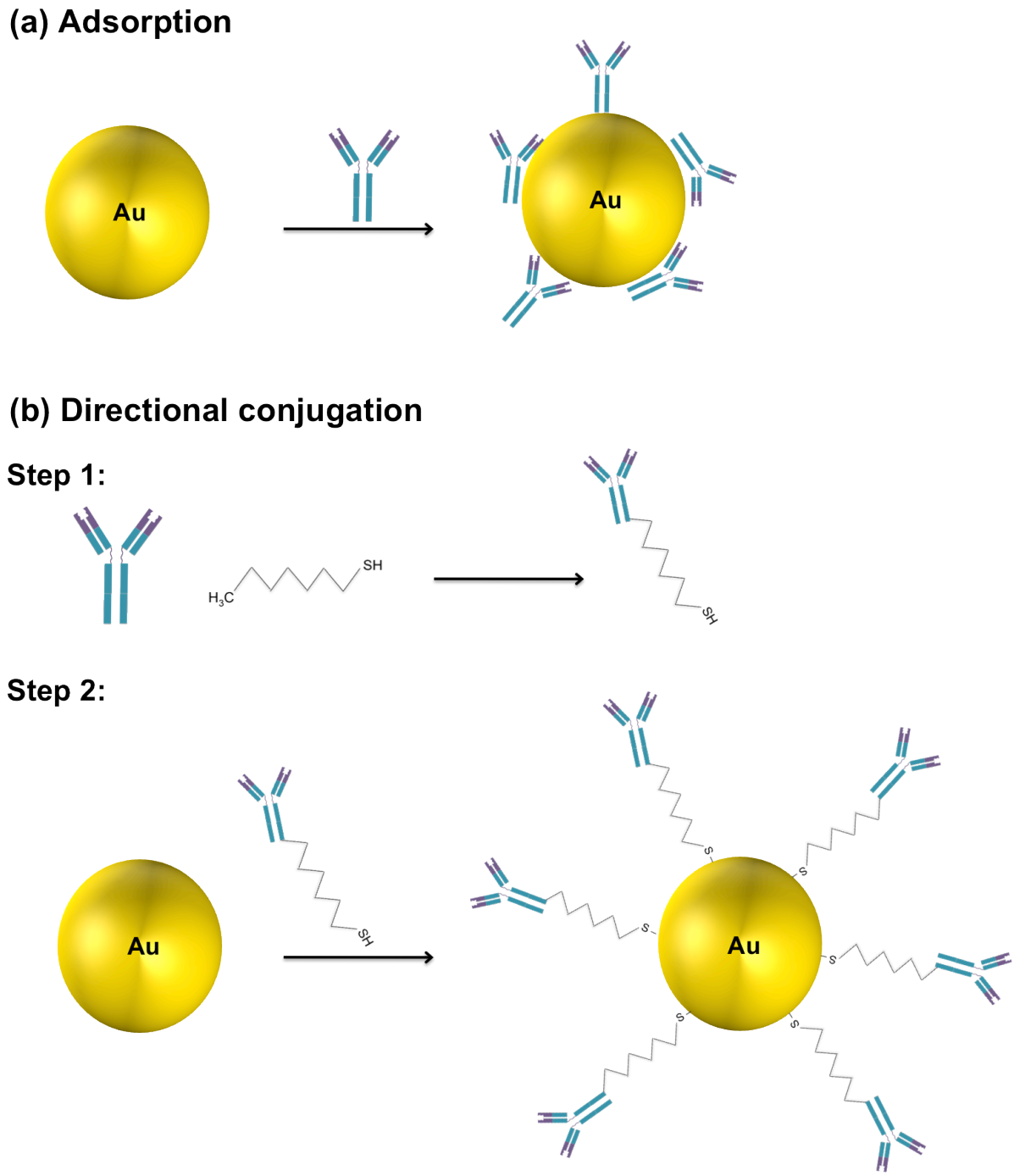


Figure 4-1. **Schematic representation of the two different functionalization methods used to attach antibodies to the surface of AuNPs. (a) Adsorption and (b) Directional conjugation using intermediary PEG linker.**

The targeting efficacy of antibody functionalized AuNPs depends vastly on the number of binding sites available and the affinity of the antibody towards cell surface antigen receptors. The attachment of an antibody to AuNPs through hydrophobic interactions induces the direct adsorption of the antibody to the gold surface, resulting to random antibody orientation[33]. The random orientation of antibodies on AuNPs compromises the accessibility of binding sites and thereby, limits the efficient targeting of antigen receptors[34, 35].

Therefore, many studies have focused on improving the efficacy of targeting AuNPs through controlling the orientation of antibodies on the gold surface. Directional conjugation of antibodies to AuNPs allows antibody orientation in a manner that improves biological labelling, as fewer antibodies per nanoparticle are required to achieve highly efficient targeting, thus, reducing significantly the cost per assay. Several methods have been employed for the directional conjugation of antibodies to AuNPs using intermediary PEG linkers, as they are highly water soluble and approved for safe use in the clinic[33, 36-38]. What is more, the hydrophilic nature of PEG linkers enhances radically the biocompatibility of the antibody-conjugated nanoparticles in biological systems[39, 40].

Within the past few years, several studies have shown that the directional conjugation of clinically approved antibodies to the surface of nanoparticles can enhance drastically their delivery efficacy to target cells and thereby, improve the therapeutic outcome. For instance, even though the monoclonal antibody Trastuzumab is widely used in the clinic for treating HER2 overexpressing breast and gastric cancers, it has been previously associated with off-target toxicity and resistance upon treatment[41]. The directional conjugation of Trastuzumab to AuNPs, using an intermediary short PEG chain, was reported to overcome resistance and induce significantly higher toxicity in HER2 positive gastric cell lines and *in vivo* mouse models when compared to the antibody alone[42]. In a different study, a nanoparticle-based combination therapy was developed through the directional conjugation of anti-PD-L1 and doxorubicin to AuNPs for targeting overexpressing PD-L1 colorectal cancer. Both the antibody and the chemotherapeutic agent were conjugated to AuNPs in a controlled orientation using a PEG linker. The results demonstrated that the directional conjugation of anti-PD-L1 and doxorubicin to AuNPs

enhances the binding affinity of the antibody against PD-L1 overexpressing colon carcinoma cells and improves the therapeutic efficacy of doxorubicin[43].

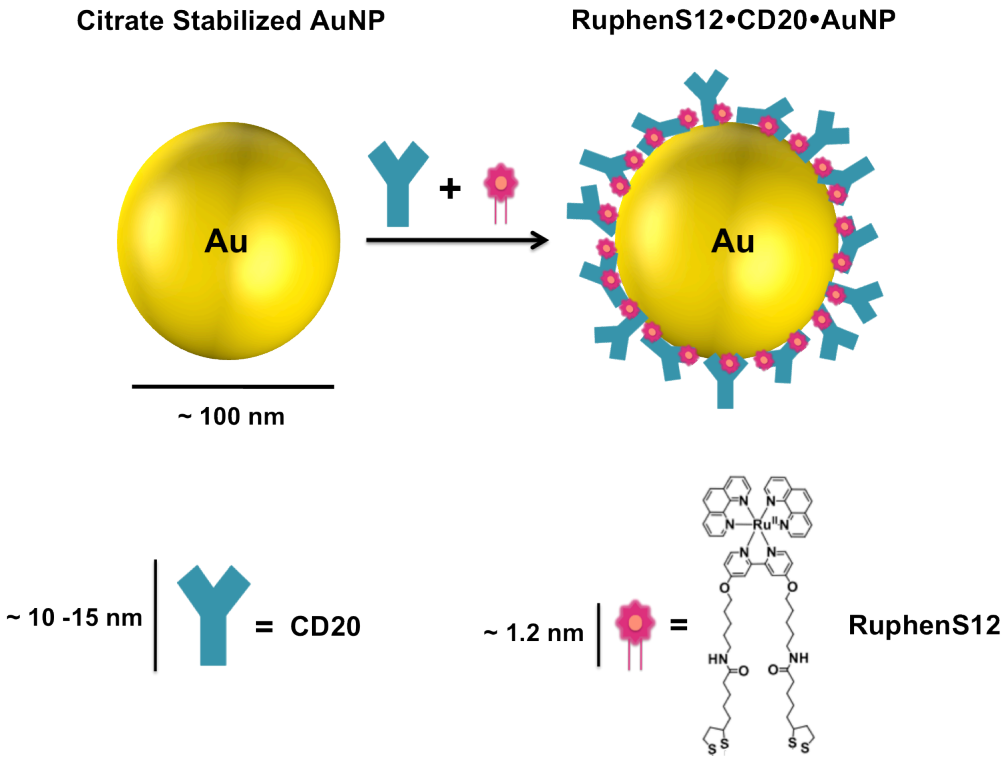
The efficient binding of antibody-coated AuNPs to cell surface receptors can be evaluated by various optical techniques, as the high electron density and light scattering properties of gold offer opportunities for transmission and reflectance microscopy[44, 45]. However, the use of luminescent transition metal complexes has recently gained a lot of attention in the nanotechnology field for the development of luminescent AuNPs with improved detection in cells[46-48]. More specifically, the attachment of luminescence complexes to AuNPs allows a high coating with hundreds to thousands complexes per nanoparticle, which provides a strong luminescence signal for nanoparticle detection in biological samples using flow cytometry and confocal luminescence microscopy[46-49].

In this chapter, novel luminescent AuNPs were developed in the presence of the monoclonal antibody CD20, to evaluate the binding affinity of the antibody modified nanoparticles for CD20 antigen receptors in cancer cells and tonsil tissue specimens. Due to the significant success of monoclonal CD20 antibodies in the clinic, there is a growing interest in the oncology field for further interpreting their exact mechanism of action and developing novel nanoprobes for theranostic purposes[50, 51]. Therapeutic monoclonal antibodies that bind to the CD20 antigen expressed on the surface of B-cells have been widely used in the medical field for the targeting of malignant B-cells in different types of cancer[52]. Targeting with CD20 antibodies induces depletion of CD20 expressing cancer cells via several mechanisms including antibody-dependent cell-mediated cytotoxicity (ADCC), antibody-dependent cell-mediated phagocytosis (ADCP), complement-dependent lysis (CDC) or programmed cell death (PCD)[53-55].

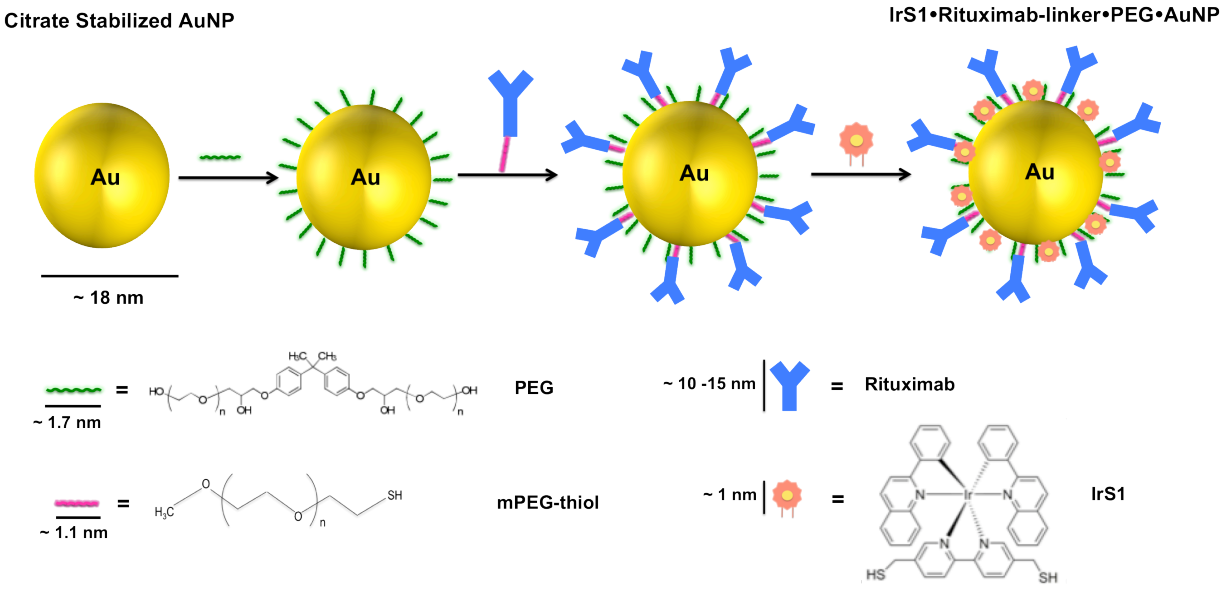
Preliminary studies were performed to evaluate the cellular uptake of AuNPs functionalized with CD20 and a luminescent ruthenium complex, RuphenS12, in malignant human B-cells expressing CD20. The ruthenium complex was first added to the CD20 antibody and the produced mixture was then attached to the surface of AuNPs. The attachment of the ruthenium and CD20 mixture to AuNPs was achieved through direct adsorption of the antibody to the gold surface, via ionic interactions between the negatively

charged citrate ions present on the gold surface and the positively charged residues in the sequences of the antibody[33, 56] (Scheme 4-1).

In order to further elaborate the binding affinity of the CD20 antibody against CD20 antigen receptors upon attachment to AuNPs, a directional conjugation method described by Kumar et al. was employed[37]. The monoclonal CD20 antibody Rituximab was directly conjugated to AuNPs using an intermediary PEG linker to attain controlled antibody orientation on the gold surface, and thereby, achieve strong binding affinity of the antibody against CD20 expressing biological specimens. The high targeting efficacy of Rituximab for CD20 expressing malignant B-cells is well-established in the medical field as it was the first CD20 monoclonal antibody that received approval by the FDA for the treatment of B-cell haematological malignancies, including Chronic Lymphocytic Leukaemia (CLL) and different types of Non-Hodgkin Lymphoma (NHL)[57, 58]. The Rituximab conjugated AuNPs were further modified with a luminescent iridium complex, IrS1, to enable detection in sectioned tonsil tissue samples using confocal luminescence microscopy (Scheme 4-2).



Scheme 4-1. Schematic of coating AuNPs with CD20 antibody and the ruthenium(II) complex, RuphenS12.



Scheme 4-2. Schematic of coating AuNPs with Rituximab and the iridium(III) complex, IrS1.

4.2 Chapter outline

In this chapter, novel luminescent antibody functionalized AuNPs were developed, in order to enhance the antigen-binding affinity of the antibody towards antigen receptors expressed on the surface of B-cell malignant cells. Preliminary studies involved the attachment of a ruthenium complex and the direct adsorption of the monoclonal CD20 antibody to AuNPs to evaluate whether the presence of the antibody on the gold surface improves the cellular uptake of nanoparticles in CD20 expressing malignant cells. The characterization of the modified nanoparticles by SPR and DLS measurements confirms the successful attachment of both the antibody and the luminescent complex to the surface of AuNPs. The improved cellular uptake of the luminescent nanoparticles in the presence of the CD20 antibody is presented by FACS analysis. The efficient internalization of the ruthenium and antibody coated nanoparticles in malignant B-cells that express CD20 was further confirmed by confocal microscopy. The ability of the functionalized nanoparticles to penetrate the nuclear membrane and accumulate within the nucleus of CD20 expressing cells is also presented. Further studies were performed to investigate the binding affinity of the CD20 antibody towards CD20 antigen receptors upon attachment to the surface of AuNPs. The monoclonal CD20 antibody Rituximab, which is currently used in the clinic for treating B-cell malignancies, was attached to the gold surface using a directional conjugation method in the presence of an intermediary PEG linker. The antibody modified AuNPs were further functionalized with a luminescent iridium complex. The attachment of the iridium complex and Rituximab to the gold surface is presented by SPR, DLS size and zeta potential measurements and gel electrohoresis. What is more, photophysical characterization of the functionalized nanoparticles was performed, indicating that the iridium complex retains its luminescence properties upon attachment to AuNPs. The strong binding affinity of the novel, antibody conjugated nanoparticles developed against CD20 expressing malignant cells is described using confocal luminescence imaging in tonsil tissue samples through detecting the luminescent signal of the iridium complex. The results described in this chapter represent a promising approach for the development of highly selective theranostic nanoprobes. The use of AuNPs as a scaffold to simultaneously deliver luminescent complexes and targeting antibodies in

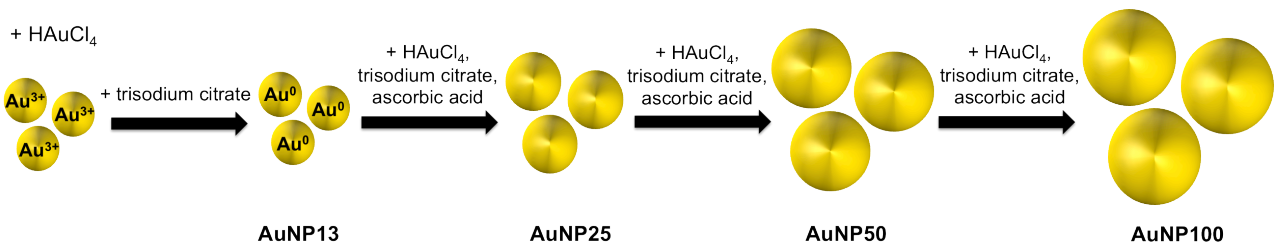
cancer cells can provide improved characterization of the tumor microenvironment through overcoming limitations of conventional diagnostic methods, such as non-specific binding observed with pathological stains.

4.3 Results and Discussion

4.3.1 Synthesis and characterization of AuNP100

For the preliminary studies of this chapter, 100 nm AuNPs were chosen due to their favourable light scattering properties, as scattering increases drastically with larger in size nanoparticles, thus, offering improved detection with reflectance microscopy[59, 60]. Upon binding to antigen receptors expressed on the cell surface membrane, different antibodies display different mechanisms of action. More specifically, various targeting antibodies act through blocking cell surface receptors to induce inhibition of downstream cell signalling, while other antibodies exhibit cellular entry and act on intracellular targets[61, 62]. Hence, detection of gold with reflectance microscopy can aid in interpreting whether antibody modified AuNPs remain attached to extracellular receptors or undergo cellular internalization after binding.

The water-soluble, monodisperse AuNPs of 100 nm in size, AuNP100, were synthesised according to an adapted protocol by the Pikramenou group, which is based on an improved method previously reported by Turkevich et al.[63, 64] and a published protocol by Ziegler et al.[65]. In brief, the synthesis of AuNP100 is based on a growth procedure through the addition of Au^{3+} salt and trisodium citrate to AuNP13 seeds (Scheme 4-3). Initially, AuNPs of 13 nm size (AuNP13) were synthesized through citrate reduction and were then grown to produce 25 nm AuNPs (AuNP25) as previously described in Chapters 2 and 3. The 25 nm monodisperse AuNPs were then grown into 50 nm AuNPs (AuNP50), which were finally grown to produce 100 nm AuNPs stabilized with citrate ions.



Scheme 3-3. Schematic representation of the AuNP synthesis and the growth procedure to form 100 nm AuNPs.

The hydrodynamic diameter and monodispersity of AuNP13, AuNP25, AuNP50 and AuNP100 during the seeding procedure were monitored by DLS (Figure 4-2) (DLS data are summarized in Table 4-1). After synthesis, the AuNP100 were further characterized by SPR and ζ-potential (Figure 4-3). The number and intensity distribution analysis of AuNP100 as measured by DLS revealed sizes of 76 ± 19 nm and 101 ± 26 nm (PDI=0.041), respectively. Zeta potential measurements suggested an average surface charge of -27 ± 9 mV, indicating the high stability of AuNP100, which is attributed to the presence of the negatively charged citrate ions on the gold surface[66, 67]. AuNP100 in water after synthesis (AuNP100 stock) displayed a characteristic SPR band with a maximum, λ_{max}, at 552 nm. The UV-Vis spectrum of AuNP100 shows an absorption band at around 294 nm, which is attributed to remaining ascorbic acid from the nanoparticle synthesis. Prior to functionalization of AuNP100, the excess ascorbic acid is removed by centrifugation (Figure 4-2).

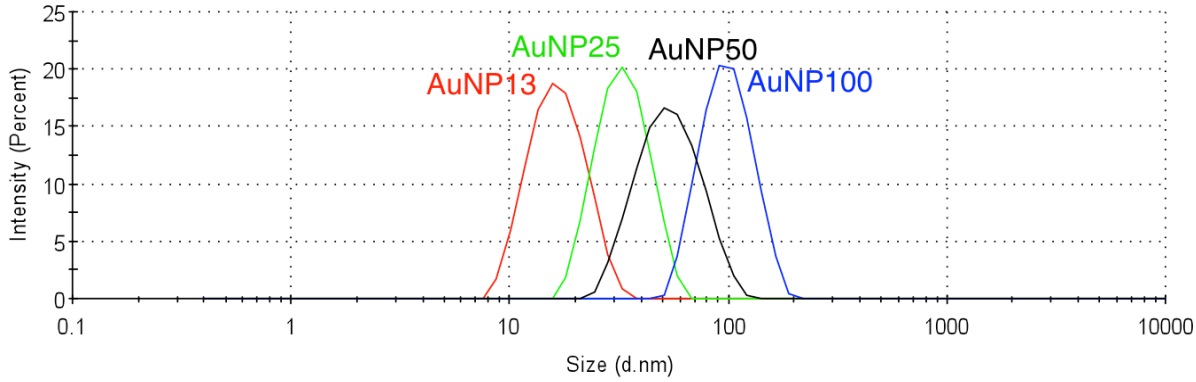


Figure 4-2. DLS intensity distributions of AuNP13, AuNP25, AuNP50 and AuNP100.

	Size by Number / nm	Size by Intensity / nm	Z-average / nm	PDI
AuNP13	12 ± 3	17 ± 5	16	0.067
AuNP25	24 ± 6	34 ± 9	32	0.055
AuNP50	35 ± 10	56 ± 18	50	0.101
AuNP100	76 ± 19	101 ± 26	95	0.041

Table 4-1. DLS for AuNP13, AuNP25, AuNP50 and AuNP100 in water. Results display sizes by number and intensity (nm), z-average (nm) and PDI.

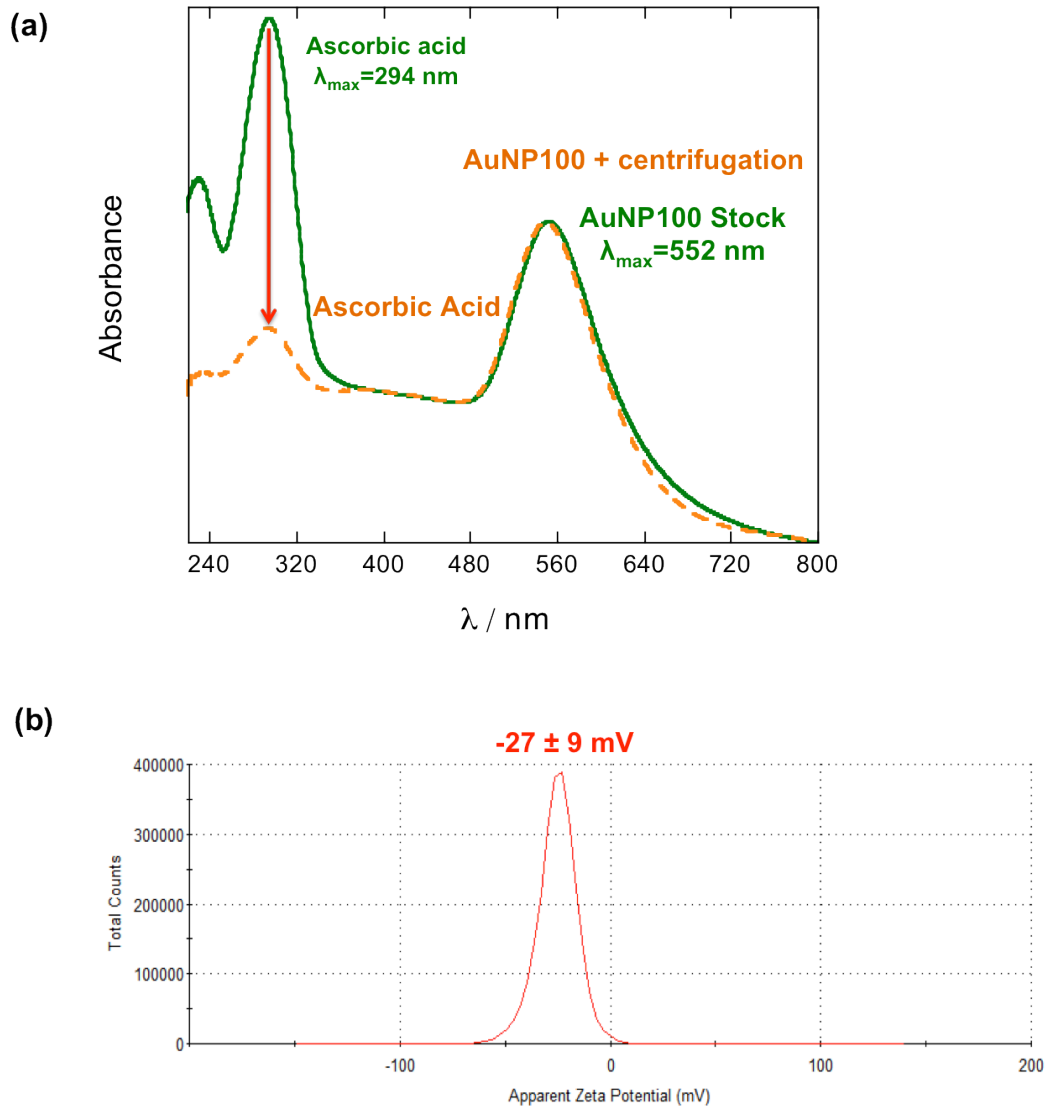


Figure 4-3. **(a) UV-Vis absorption spectra of AuNP100 stock and AuNP100 in water after centrifugation to remove excess ascorbic acid from nanoparticle synthesis. The λ_{max} of the SPR band is 552 nm. (b) Zeta potential distribution of AuNP100.**

The size analysis, zeta potential and SPR band of AuNP100 agree with previously published data by the Pikramenou group, suggesting the consistency and reproducibility of the nanoparticle synthesis method used to produce monodisperese 100 nm AuNPs[47, 48, 46].

4.3.2 Preparation and characterization of RuphenS12·CD20·AuNP100

The direct adsorption of the monoclonal CD20 antibody and the attachment of the luminescent ruthenium complex, RuphenS12, to the surface of AuNPs were performed following a protocol optimized in collaboration with Dr. Sunil Claire, School of Chemistry, University of Birmingham. The synthesis and full characterization of the RuphenS12 complex were performed by Dr. Shani Osborne (School of Chemistry, University of Birmingham) (Appendix C – Scheme C-1 and Figure C-1).

Adsorption of the CD20 antibody to the gold surface was achieved via ionic interactions between the positively charged residues in the sequences of the antibody and the negatively charged citrate ions on the surface of AuNPs[68-70]. The CD20 antibody was added in excess to AuNP100 to ensure full coverage of the gold surface and unbound antibody was then removed by centrifugation to isolate purified CD20 coated AuNP100 (CD20·AuNP100). The presence of the antibody on the gold surface provides high stability and thus, prevents nanopaticle aggregation upon attachment of the luminescent complex.

For the preparation of the ruthenium and CD20 modified AuNPs, the antibody and the luminescent complex were first mixed to form an antibody-ruthenium complex, which was then used to coat the gold surface. It has been previously reported that upon attachment of molecular complexes to antibody-coated nanopartices, the antibody can easily be replaced as it is held onto the gold surface via physical interactions[33, 37]. Therefore, through attaching the ruthenium complex to CD20 rather than directly attaching it to CD20 coated AuNPs, a larger area was provided on the gold surface for coating with the CD20 antibody. A high antibody loading on the surface of AuNPs can improve significantly receptor-mediated cellular uptake in CD20 positive cells, due to the greater number of binding sites available[71, 72]. The concentration of the RuphenS12 complex used for the preparation of the luminescent antibody modified AuNPs was chosen based on preliminary experiments performed in collaboration with Dr Sunil Claire, School of Chemistry, University of Birmingham, and it was the maximum amount that could be used to functionalize the CD20 coated AuNP100 without inducing nanoparticle aggregation.

Subsequent to adding the ruthenium and CD20 mixture to AuNP100, the nanoparticles were isolated by centrifugation to remove excess antibody and thus, produce purified RuphenS12·CD20·AuNP100. The attachment of CD20 to AuNP100 produced a 4 nm shift in the SPR band of the nanoparticles (λ_{max}=556 nm), while the attachment of the antibody with the ruthenium complex induced a 5 nm shift (λ_{max}=557 nm) (Figure 4-4). The SPR of AuNPs is defined as the collective oscillation of conduction electrons on the gold surface and is highly sensitive to changes in the surroundings of the nanoparticles[73]. Therefore, the red shift observed in the SPR band of AuNP100 is a well known-effect of the adsorption of molecules to the gold surface and confirms the successful functionalization of AuNP100 with the antibody and the luminescent complex[74, 34].

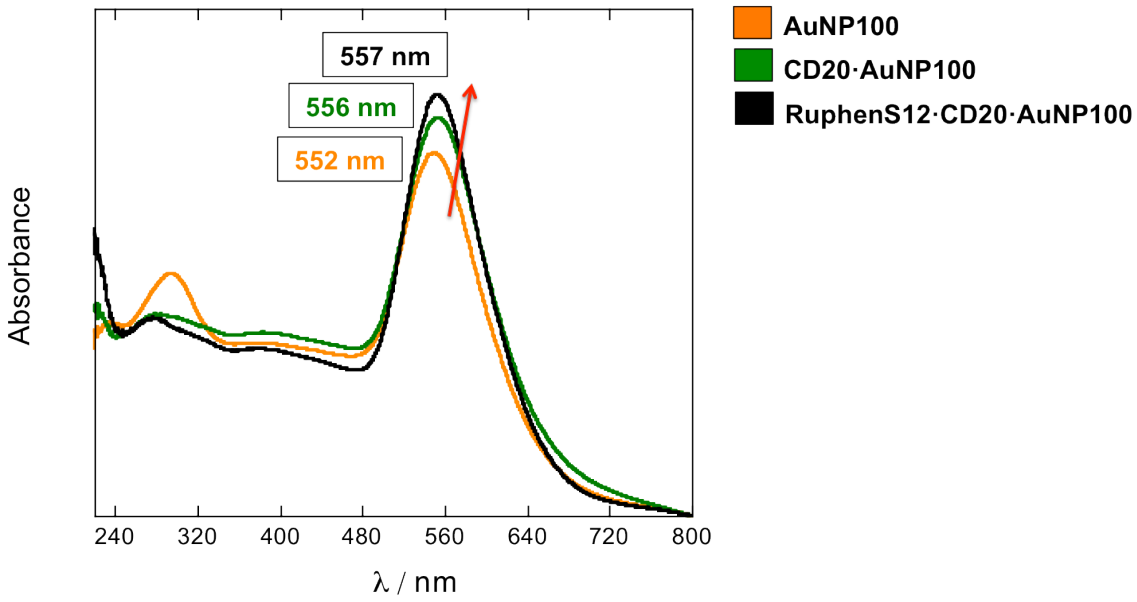


Figure 4-4. UV-Vis absorption spectra of purified AuNP100, CD20·AuNP100 and RuphenS12·CD20·AuNP100 in water, showing the shift in the SPR band upon coating with the CD20 antibody and the RuphenS12 complex.

The adsorption of the CD20 antibody to the surface of AuNPs was further confirmed by DLS through the increase observed in the intensity distribution of CD20·AuNP100 when compared to AuNP100 (DLS data are summarized in Table 4-2). The presence of the RuphenS12 on the antibody modified AuNPs was also evident by DLS, as the luminescent

complex induced a further increase in the intensity distribution. Even though the increase observed for both CD20·AuNP100 and RuphenS12·CD20·AuNP100 was within the error range, overlay of the intensity distributions of the different nanoparticle samples does indicate an increase in the hydrodynamic diameter of the functionalized AuNPs (Figure 4-5). The increase in the DLS intensity distribution along with the low PDI observed suggest the successful functionalization of the gold surface with the CD20 antibody and the ruthenium complex as well as the high monodispersity of the coated AuNPs. This was further confirmed through TEM, as imaging analysis of RuphenS12·CD20·AuNP100 revealed spherical AuNPs of about 90 nm in diameter (n=15) (Figure 4-6).

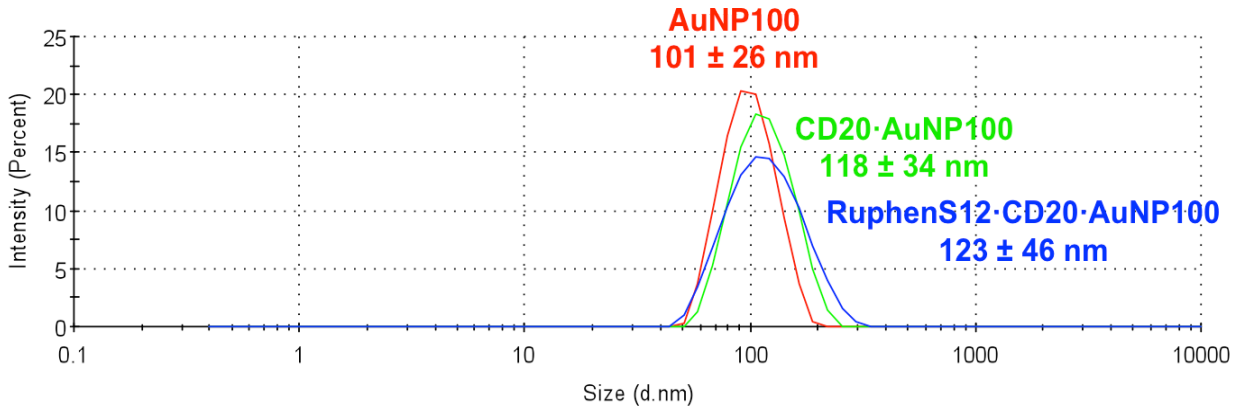


Figure 4-5. DLS intensity distributions of AuNP100, CD20·AuNP100 and RuphenS12·CD20·AuNP100.

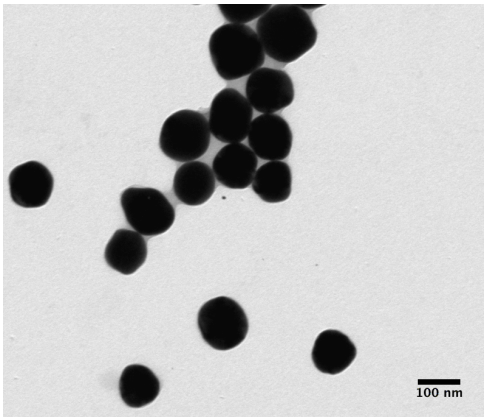


Figure 4-6. TEM image displaying the spherical nature of RuphenS12·CD20·AuNP100 and a narrow size distribution (Scale bar= 20 nm).

In order to determine whether the presence of the CD20 antibody improves the cellular uptake and internalization of nanoparticles in CD20 expressing cells, luminescent ruthenium AuNPs were prepared in the absence of the antibody and their uptake efficacy was compared to RuphenS12·CD20·AuNP100. The RuphenS12 complex was attached to AuNP100 coated with the fluorinated surfactant, zonyl FSA. The surfactant was used to stabilize the gold surface and prevent aggregation that can occur from directly substituting the negatively charged citrate ions on the nanoparticles surface with the positively charged metal complex[47, 48, 46]. For the preparation of the ruthenium and surfactant coated AuNPs, the concentration of the RuphenS12 complex used was the same as the concentration used for the ruthenium and CD20 coated nanoparticles. This ensures that the strength of the luminescent signal won't affect the fluorescence intensity during FACS analysis. Purification of the RuphenS12 and surfactant coated AuNPs was performed by size exclusion chromatography using Sephadex G-10 to produce RuphenS12·Z·AuNP100. Similarly to RuphenS12·CD20·AuNP100, the size of RuphenS12·Z·AuNP100 was measured by DLS to confirm the stability and monodispersity of the functionalized nanopaticles prior to proceeding with cellular uptake studies (DLS data are summarized in Table 4-2). DLS measurements revealed that attachment of the ruthenium complex to the surfactant coated AuNP100 results to a relatively smaller increase in the intensity distribution of the AuNPs when compared to the increase produced after coating with the ruthenium complex and the CD20 antibody (Appendix C – Figure C-2). This is attributed to the longer length of the CD20 antibody present on the gold surface, as a monoclonal antibody like CD20 is approximately 10 to 15 nm long[75, 76], whereas the fluorinated surfactant is only about 1.6 nm.

	Size by Number / nm	Size by Intensity / nm	ζ-potential / mV	PDI
AuNP100	76 ± 19	101 ± 26	- 27 ± 9	0.041
CD20·AuNP100	78 ± 21	118 ± 34	- 31 ± 9	0.064
RuphenS12·CD20·AuNP100	79 ± 23	123 ± 46	- 35 ± 6	0.113
RuphenS12·Z·AuNP100	77 ± 19	113 ± 38	- 37 ± 8	0.111

Table 4-2. DLS for AuNP100, CD20·AuNP100, RuphenS12·CD20·AuNP100 and RuphenS12·Z·AuNP100 in water. Results indicate PDI, sizes by number and intensity (nm) and zeta potential data.

Zeta potential represents the charge on the surface of AuNPs and is a crucial measurement to study the stability of nanoparticles in suspension[77]. A positive zeta potential can result to strong electrostatic repulsive interactions between nanoparticles, which compromise drastically their stability[78]. According to literature, an inherent increase in the zeta potential of nanoparticles is expected after the attachment of antibodies or antibody fragments to the gold surface due to their less overall negative charge[79-81]. The presence of an antibody on the surface of AuNPs can induce an increase in the zeta potential by about 10 to 20 mV, depending on the size of the antibody and the method used for attachment to the gold surface[82]. This however, was not evident upon attachment of the CD20 antibody and the CD20-ruthenium conjugate to AuNP100. DLS zeta potential measurements revealed that the zeta potential of CD20·AuNP100 and RuphenS12·CD20·AuNP100 in water are -31 ± 9 and -35 ± 6 mV, respectively, indicating that the antibody modified nanoparticles are slightly more electronegative than the citrate AuNP100 (Figure 4-7). This could be attributed to the negatively charged groups, such as carboxyl, aldehyde and phosphate groups, that are present throughout the structure of antibodies[83, 84] or the high stability of the functionalized nanoparticles, induced by the presence of the antibody on the gold surface. The electronegative zeta potential and thus, high stability of RuphenS12·CD20·AuNP100 in suspension makes them ideal nanoprobes for cancer theranostic applications, as positively charged nanoparticles have been previously associated with high cytotoxicity in normal cells[85-87].

The zeta potential of RuphenS12·Z·AuNP100 in water as measured by DLS is - 37 ± 8 mV, suggesting that similarly to RuphenS12·CD20·AuNP100, RuphenS12·Z·AuNP100 exhibit high stability in suspension (Appendix C – Figure C-3). According to literature, the surface charge of nanoparticles impacts greatly their uptake in cells, as cationic nanopartcles have been previously reported to penetrate more efficiently the anionic phospholipid bilayer[88-90]. Therefore, the fact that both RuphenS12·CD20·AuNP100 and RuphenS12·Z·AuNP100 possess the same surface charge suggests that their cellular uptake efficacy in CD20 positive cells is only affected by the presence of the antibody on the gold surface and not their overall surface charge.

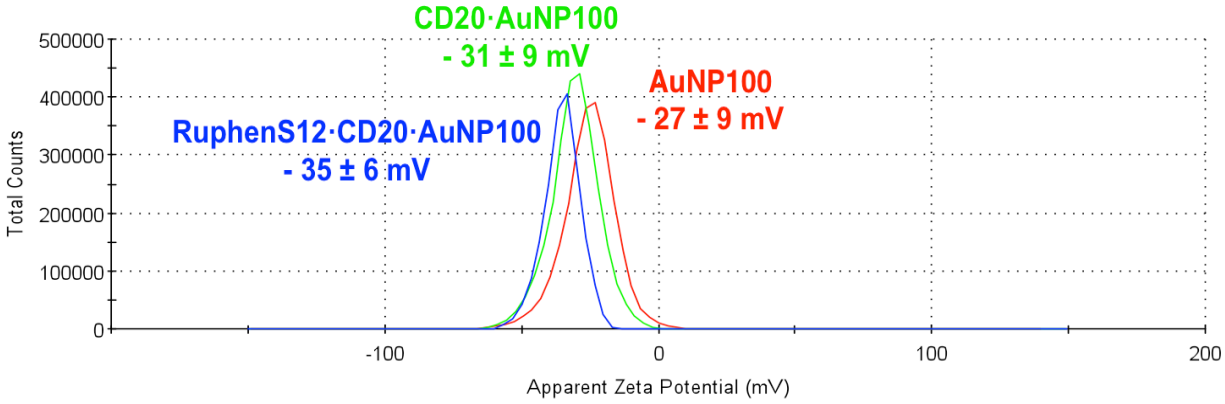


Figure 4-7. DLS zeta potential distributions of AuNP100, CD20·AuNP100 and RuphenS12·CD20·AuNP100.

Prior to proceeding with experimental studies in cells, photophysical characterization of RuphenS12·CD20·AuNP100 was performed to confirm that the ruthenium complex retains its characteristic luminescence properties upon attachment to the surface of AuNPs. The RuphenS12 complex in water shows absorption within the UV-Vis region, with an intense high-energy absorption band at 260 nm that is assigned to LC based transitions and a lower energy band between 400 and 500 nm, which based on previous assignments is assigned to singlet MLCT transitions[46] (Figure 4-8). Upon excitation of the RuphenS12 complex in water at 488 nm, a broad emission peak with λ_{max} at 630 nm is observed, which is attributed to contributions from triplet MLCT transitions.

Excitation of RuphenS12·CD20·AuNP100 at 488 nm indicates that the ruthenium functionalized AuNPs are emissive with a λ_{max} at 635 nm, showing a 5 nm shift from the maximum emission of the RuphenS12 complex in water (Figure 4-8). This could be attributed to the presence of the CD20 antibody and changes in the surrounding environment of the ruthenium complex when attached to the gold surface[46, 91]. The excitation spectrum of the ruthenium and CD20 coated AuNPs displayed the characteristic SPR bands of the RuphenS12 complex, confirming that the luminescent complex retains its photophysical properties when attached to the gold surface (Figure 4-8). The strong emission displayed by RuphenS12·CD20·AuNP100 when excited at 488 nm indicates the suitability of the modified nanoparticles to be used for FACS and confocal luminescence microscopy.

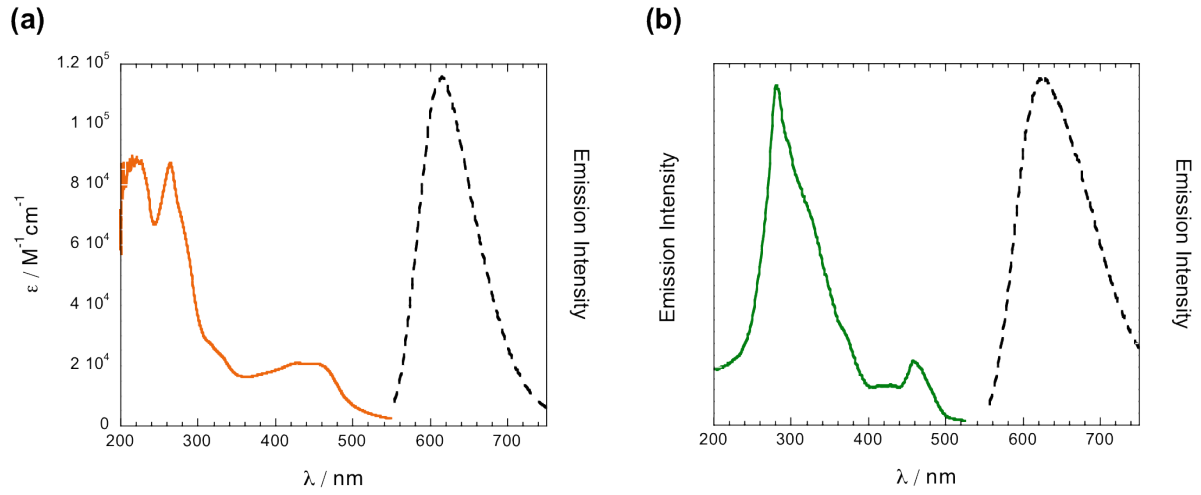


Figure 4-8. Phtophysical characterisation of RuphenS12 and RuphenS12·CD20·AuNP100 in water. (a) UV-Vis absorption spectrum (solid line) and emission spectrum (dashed line) of 30 µM RuphenS12 in water, λ_{exc}= 488 nm. (b) Excitation spectrum (solid line) and emission spectrum (dashed line of 100 pM RuphenS12·CD20·AuNP100 in water, λ_{exc}= 488 nm and λ_{em}= 635 nm.

4.3.3 Cellular uptake of RuphenS12·CD20·AuNP100 in CD20 positive cells by FACS

In order to evaluate the ability of the luminescent nanoparticles to serve as a nanoparticle- based cell-mediated delivery system for theranostic purposes, the cellular uptake efficacy of RuphenS12·CD20·AuNP100 was evaluated in CD20 expressing cells. The cellular uptake of the ruthenium and antibody coated AuNPs was evaluated by FACS and histogram analysis was performed using the PE-Texas Red filter, blue laser with λ_{exc} at 488 nm and $\lambda_{em} > 600$ nm.

Initially, the cellular uptake of RuphenS12·CD20·AuNP100 was evaluated in two CD20 positive cells lines, Karpas 422, a B-cell non-Hodgkin's lymphoma cell line, and SU-DHL-4, a Diffuse large B-cell lymphoma (DLBCL) cell line. For both cell lines, the cellular uptake efficacy of the ruthenium and CD20 coated AuNPs was assessed through comparing the increase in fluorescence intensity of the treated cells against the cells treated with negative controls (Control – H_2O, AuNP100 and CD20·AuNP100) (Figure 4-9). The cells were treated with 10 pM of the AuNP100 samples for 24 hours. Histogram analysis revealed that treatment with RuphenS12·CD20·AuNP100 results to a significant increase in the fluorescence intensity of CD20 expressing cells, suggesting the highly efficient cellular uptake of the antibody and ruthenium functionalized AuNPs. When comparing the increase in the fluorescence intensity between the two cell lines, it is evident that the uptake of RuphenS12·CD20·AuNP100 is higher in Karpas 422 than SU-DHL-4 cells, as the fold increase in MFI in Karpas 422 cells is 4.8, while in SU-DHL-4 cells is 3.4 (Figure 4-9).

According to literature, different B-cell lymphoma cell lines differ significantly in their sensitivity to CD20 targeting antibodies[92, 93]. Thus, the higher increase in MFI observed in Karpas 422 cells over SU-DHL-4 cells could be to attributed to the differences in the sensitivity of the two cell lines to RuphenS12·CD20·AuNP100. Karpas 422 cells have been previously reported to exhibit lower levels of CD20 expression when compared to other B-cell lymphoma cell lines, including SU-DHL-4[92]. In fact, SU-DHL-4 cell line expresses unusual high levels of CD20, thus exhibiting high sensitivity to anti-CD20 antibody targeting[94, 95].

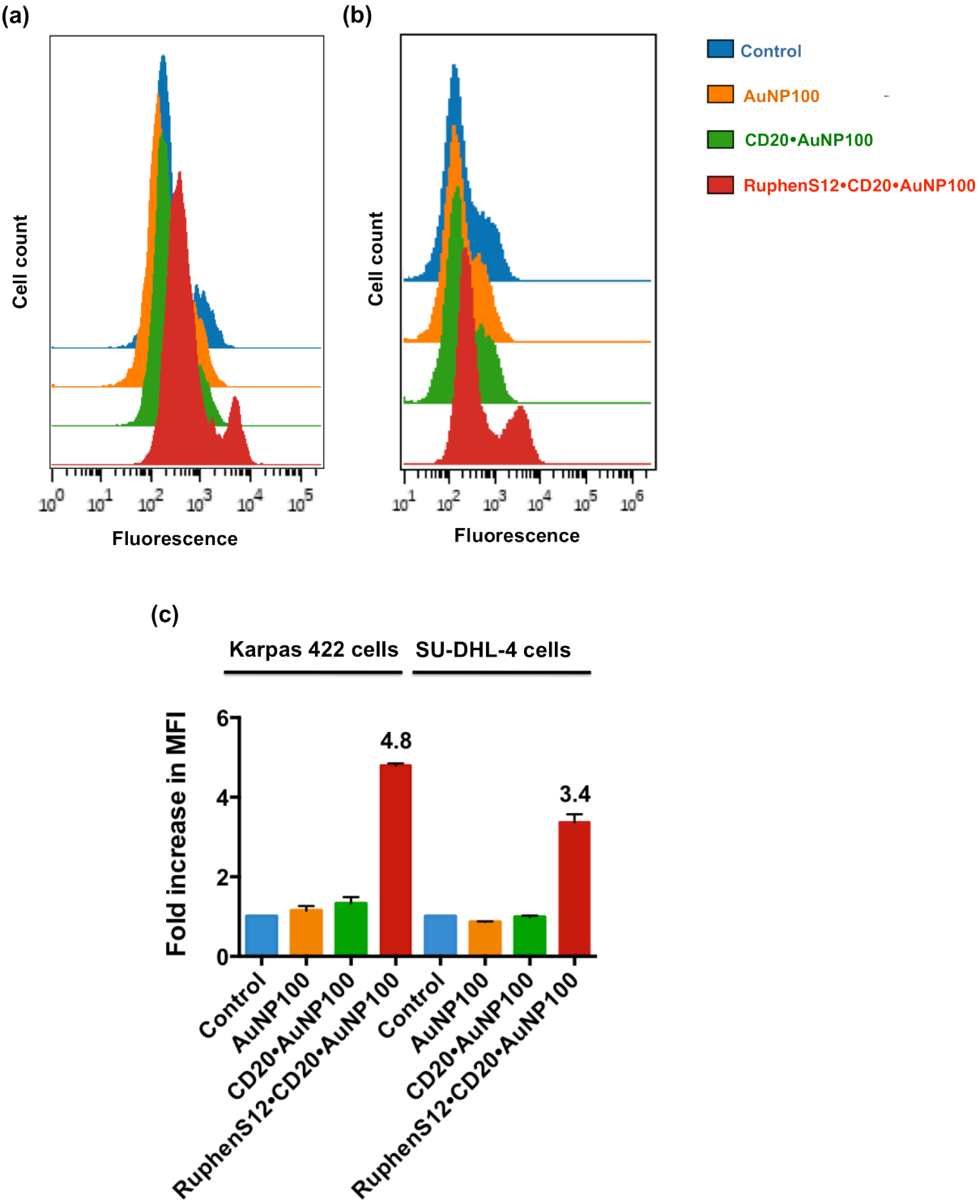


Figure 4-9. Cellular uptake efficacy in Karpas 422 and SU-DHL-4 cells by FACS analysis after treatment with 10 pM of AuNP100 samples for 24 h. λ_{exc}=488 nm and λ_{em}= >600 nm. (a) Histogram analysis after treatment of Karpas 422 cells with AuNP100, CD20·AuNP100 and RuphenS12·CD20·AuNP100. (b) Histogram analysis after treatment of SU-DHL-4 cells with AuNP100, CD20·AuNP100 and RuphenS12·CD20·AuNP100. (c) Fold increase in Mean Fluorescence Intensity (MFI) after treatment in Karpas 422 and SU-DHL-4 cells with 10 pM of AuNP100, CD20·AuNP100 and RuphenS12·CD20·AuNP100. The results are mean values ± SD of three independent experiments.

The higher expression of CD20 antigen on the surface of SU-DHL-4 cells would suggest a higher cellular uptake efficacy of RuphenS12·CD20·AuNP100 in SU-DHL-4 cells over Karpas 422 cells. However, the affinity of a monoclonal antibody against the same cell surface antigen present on different types of malignant cells often leads to the antibody exhibiting unique mechanisms of action and displaying different characteristics in *in vitro* and *in vivo* studies in different cell lines[96, 97].

The affinity of a targeting antibody to a cell surface antigen is the primary and most of the times, the only parameter that defines the efficient delivery of an antibody to the tumor site[96, 98-100]. Hence, the fact that RuphenS12·CD20·AuNP100 show higher cellular uptake in Karpas 422 cells could be attributed to the greater affinity and valence of the CD20 antibody on the gold surface towards the CD20 antigen expressed on the surface of Karpas 422 cells over SU-DHL-4 cells.

As discussed earlier in this chapter, in order to establish whether the attachment of the CD20 antibody to the surface of AuNPs improves the uptake and internalization of the nanoparticles in CD20 positive cells, the cellular uptake of RuphenS12·CD20·AuNP100 was compared to the uptake of RuphenS12·Z·AuNP100. The cellular uptake efficacy of RuphenS12·CD20·AuNP100 and RuphenS12·Z·AuNP100 was evaluated in Karpas 422 cells after treatment with 10 pM of the AuNP100 samples for 24 hours. The Karpas 422 cell line was chosen over the SU-DHL-4 cell line due to the higher increase observed in the fluorescence intensity after treatment with the ruthenium and CD20 coated AuNPs. When compared to the negative controls (Control – H_2O, CD20, AuNP100 and CD20·AuNP100), a significant increase was observed in the fluorescence intensity of the cells treated with both RuphenS12·CD20·AuNP100 and RuphenS12·Z·AuNP100, suggesting their highly efficient cellular uptake (Figure 4-10). However, treatment of the cells with RuphenS12·CD20·AuNP100 resulted to a 4.8 fold increase in MFI, while the cells treated with RuphenS12·Z·AuNP100 showed a 3.7 fold increase in MFI, indicating that the presence of the CD20 antibody on the gold surface improves the ability of the nanoparticles to penetrate the cell membrane and internalize in Karpas 422 cells.

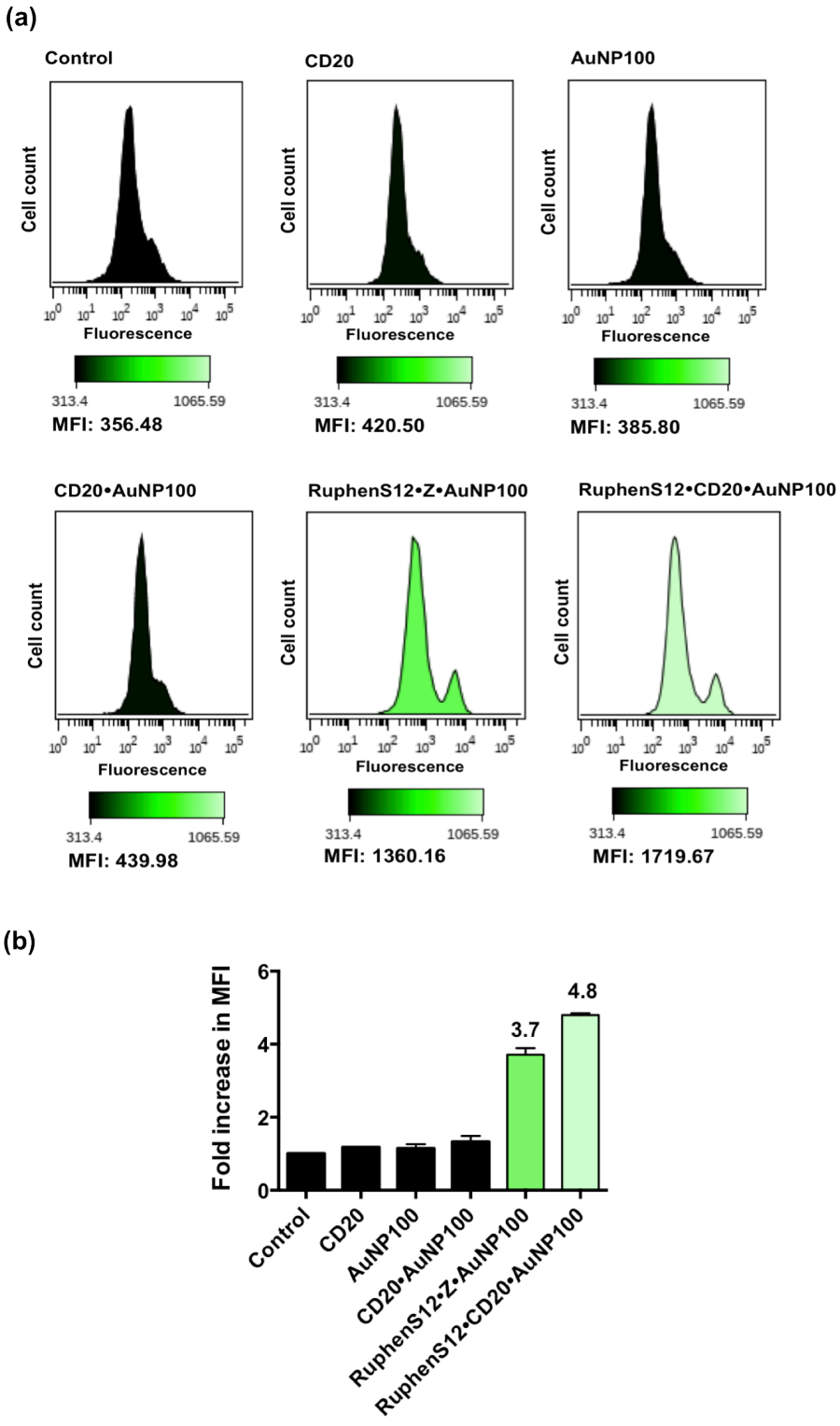


Figure 4-10. **Cellular uptake efficacy in Karpas 422 cells by FACS analysis after treatment with 10 pM of AuNP100 samples for 24 h. λ_{exc}=488 nm and λ_{em}= >600 nm. (a) Histogram analysis after treatment of Karpas 422 cells with CD20 and 10 pM of AuNP100, CD20·AuNP100, RuphenS12·Z·AuNP100 and RuphenS12·CD20·AuNP100. (b) Fold increase in Mean Fluorescence Intensity (MFI) after treatment in Karpas 422 cells with CD20, 10 pM of AuNP100, CD20·AuNP100, RuphenS12·Z·AuNP100 and RuphenS12·CD20·AuNP100. The results are mean values ± SD of three independent experiments.**

It has been previously reported that the cellular uptake of nanoparticles alters the complexity and granularity of the intracellular environment and thus, induces an increase in side scattering, which can be easily detected by flow cytometry[101, 102]. Therefore, besides histogram analysis, the cellular uptake and intracellular accumulation of the luminescent nanoparticles in Karpas 422 cells was also evaluated through side scatter (SSC) measurements of the treated cells (Figure 4-11). SSC was plotted against fluorescence to determine whether changes in the granularity of cells and uptake of the luminescent nanoparticles can be detected simultaneously. Similarly to histogram analysis, the cellular uptake of both RuphenS12·CD20·AuNP100 and RuphenS12·Z·AuNP100 in Karpas 422 cells was evident through the increase observed in the fluorescence intensity. However, the increase in side scattering was insignificant and thus, not conclusive. According to literature, changes in side scattering vary according to the size and complexity of nanoparticles[102]. More specifically, it has been reported that negatively charged and smaller than 200 nm nanoparticles cannot be detected by side scattering, as they do not change radically the intracellular granularity of cells[102-104]. Therefore, the fact that the luminescent nanoparticles did not induce an evident change in side scattering could be attributed to their electronegative surface charge and relatively small size.

Even though side scattering measurements did not provide further information on the uptake efficacy of the luminescent nanoparticles, the increase in fluorescence observed confirms the results presented earlier by histogram analysis. The significant increase detected in the fluorescence intensity of the cells after treatment with the ruthenium coated nanoparticles suggests that luminescent metal complexes can serve as detection probes to improve sensitivity in cellular uptake studies and thus, overcome current limitations and challenges in the nanomedicine field.

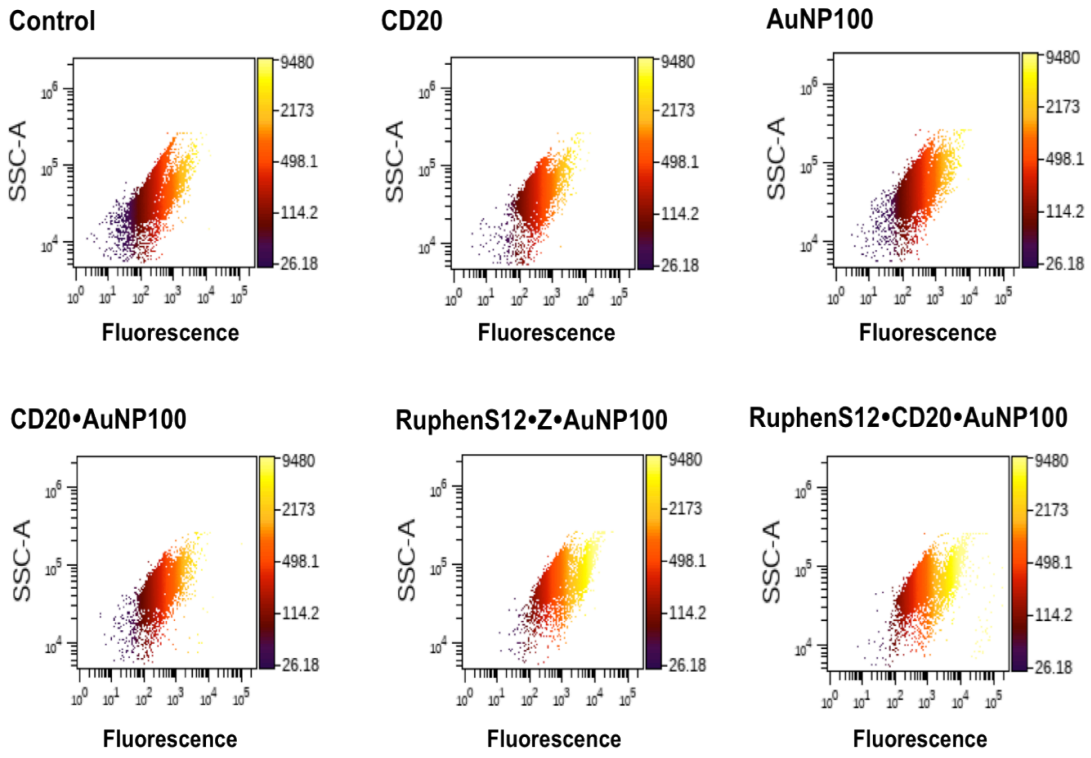


Figure 4-11. Cellular uptake efficacy in Karpas 422 cells as evaluated by flow cytometry after treatment with CD20 and 10 pM of AuNP100, CD20·AuNP100, RuphenS12·Z·AuNP100 and RuphenS12·CD20·AuNP100 for 24 h. Dot plots of side scatter (SSC) versus fluorescence, λ_{exc}=488 nm and λ_{em}= >600 nm.

4.3.4 Cellular uptake of RuphenS12·CD20·AuNP100 in Karpas 422 cells by Confocal Microscopy

The cellular uptake of RuphenS12·CD20·AuNP100 in Karpas 422 cells was further examined by confocal microscopy. After treatment of the cells for 24 hours with 10 pM of the antibody coated luminescent nanoparticles a high intensity luminescence signal from the ruthenium complex was detected. The presence of RuphenS12·CD20·AuNP100 within the intracellular environment was also confirmed by reflectance microscopy through scattering detection from the gold (Figure 4-12). Imaging analysis revealed co-localization between the signal from the luminescent complex and reflectance, confirming the presence of the ruthenium complex on the gold surface and the high stability of the luminescent nanoparticles within a biological environment.

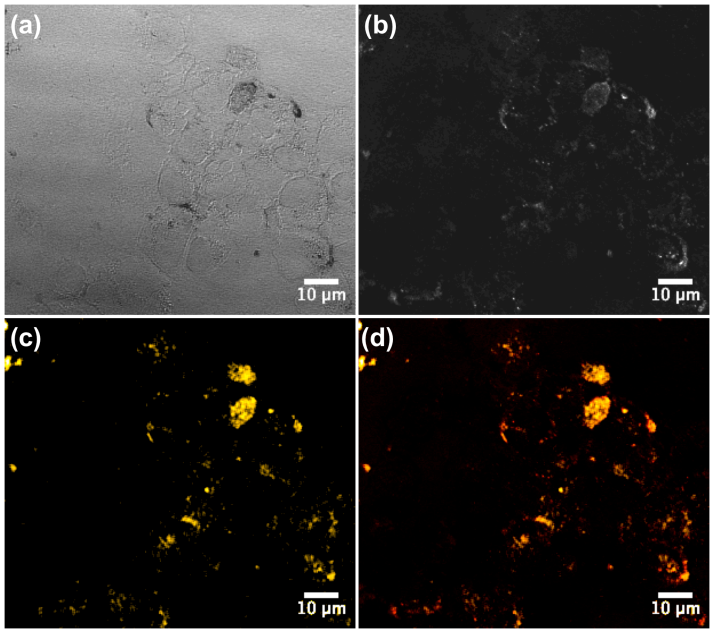


Figure 4-12. Confocal microscopy images of Karpas 422 cells after treatment with 10 pM RuphenS12·CD20·AuNP100 for 24 h (Scale bar: 10 µm). (a) Bright-field, (b) Reflectance (λ_{exc}=633 nm, λ_{em}=623-643 nm), (c) Ruthenium luminescence (λ_{exc}=488 nm, λ_{em}=600 nm-750 nm), (d) Overlay of (b) and (c) - red false colour has been applied to reflection image.

As discussed earlier in this chapter, the favourable light scattering properties of 100 nm AuNPs offer detection with reflectance microscopy, which can aid in interpreting whether after binding to antigens the modified nanoparticles remain attached to the extracellular receptors or undergo cellular internalization. Further imaging analysis of bright-field and reflectance microscopy in Karpas 422 cells after treatment with RuphenS12·CD20·AuNP100 revealed that the functionalized nanoparticles localize both within the intracellular environment and in the extracellular matrix, around the cell membrane (Figure 4-13). The presence of the ruthenium and CD20 coated AuNPs around the cell surface membrane indicates their affinity towards CD20 surface antigens expressed on the surface of Karpas 422 cells, and suggests that RuphenS12·CD20·AuNP100 internalize via receptor-mediated endocytosis rather than any other endocytotic pathways.

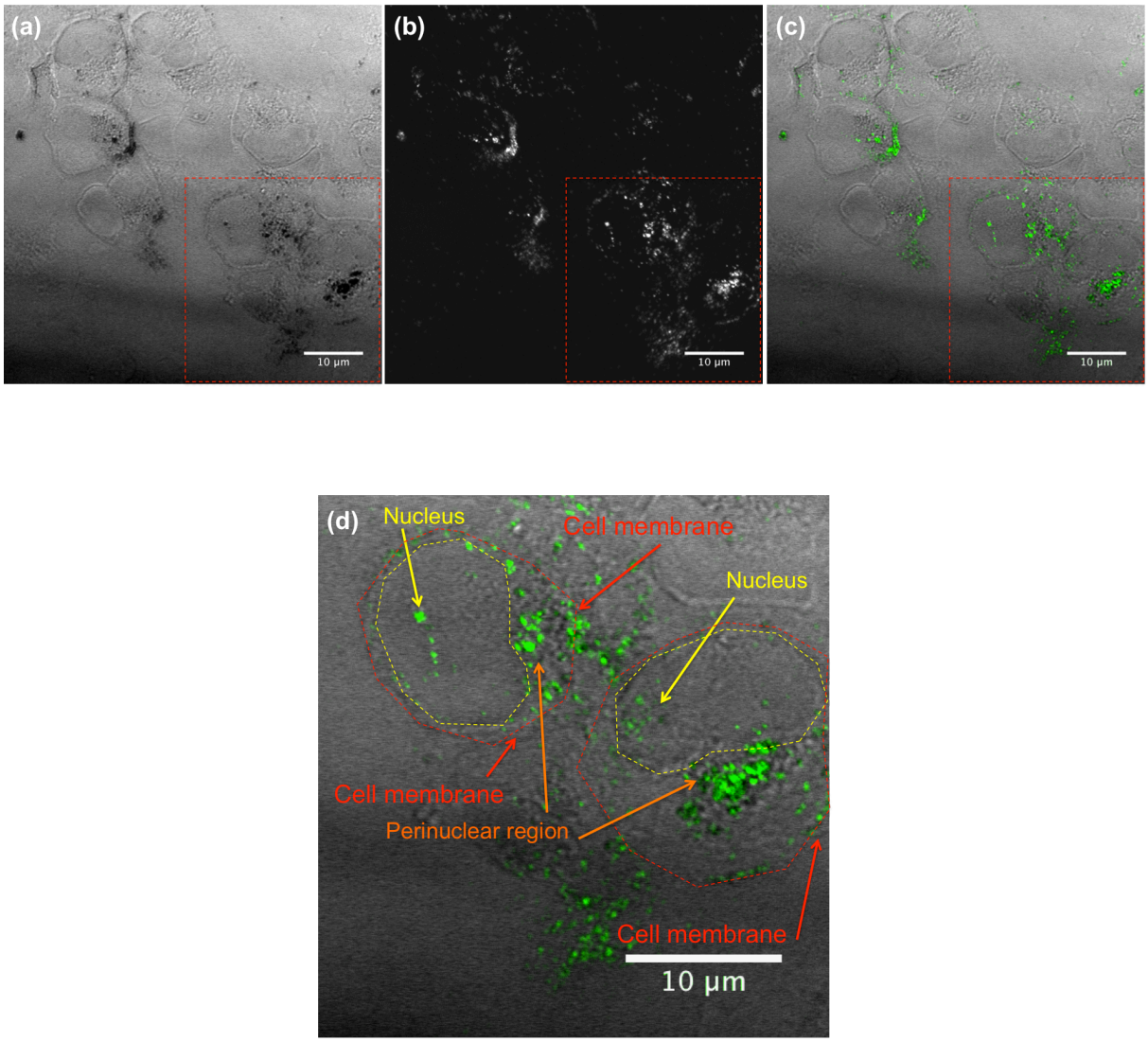


Figure 4-13. **Confocal microscopy images of Karpas 422 cells after treatment with 10 pM RuphenS12·CD20·AuNP100 for 24 h (Scale bar: 10 µm). (a) Bright-field, (b) Reflectance (λ_{exc}=633 nm, λ_{em}=623-643 nm), (c) Overlay of (a) and (b) - green false colour has been applied to reflection image, (d) Magnification of the red inset box.**

It was evident through imaging analysis that upon entry to the intracellular environment, RuphenS12·CD20·AuNP100 exhibit both perinuclear and nuclear localization in Karpas 422 cells. This could be attributed to the presence of the RuphenS12 complex on the gold surface, as luminescent ruthenium complexes have been previously reported to penetrate the nuclear membrane and interact with DNA and nuclear proteins[48, 105, 106]. Therefore, in order to further determine whether the presence of the RuphenS12 complex on the antibody coated AuNPs drives nuclear localization, confocal microscopy was performed in the presence of the nuclear stain 4′,6-diamidino-2-phenylindole, DAPI. Subcellular localization was evaluated both in Karpas 422 and SU-DHL-4 cells after treatment with 10 pM of RuphenS12·CD20·AuNP100 for 24 hours.

Imaging analysis In Karpas 422 and SU-DHL-4 cells stained with DAPI further confirmed that RuphenS12·CD20·AuNP100 undergo cellular internalization subsequent to bidning to CD20 antigens expressed on the cell surface membrane. In both cells lines co-localization between the signal from the luminescent complex and reflectance was observed, confirming the attachment of the ruthenium complex on the gold surface within the intracellular environment. Moreover, co-localization between DAPI and both the luminescent signal from the ruthenium complex and scattering from the AuNPs was also evident, suggesting that upon cellular entry, the functionalized nanoparticles can penetrate the nuclear envelope and localize within the nucleus (Figures 4-14 and 4-15). Imaging analysis of magnified cells further supports both nuclear and perinuclear clustering of the ruthenium and antibody modified AuNPs in both Karpas 422 and SU-DHL-4 cells (Figures 4-16 and 4-17).

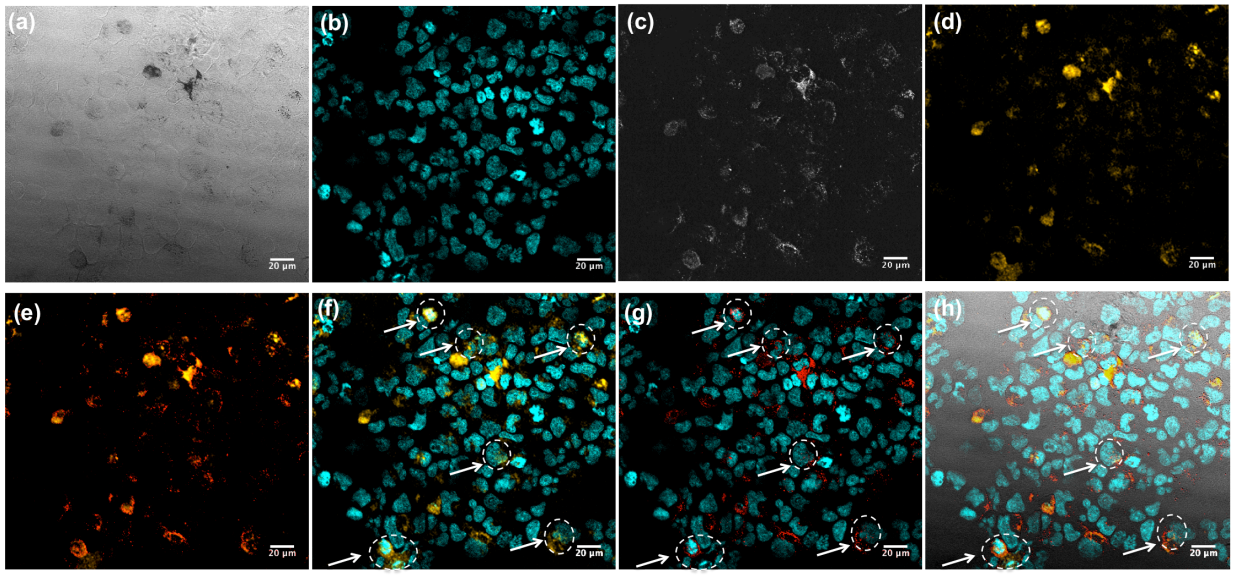


Figure 4-14. Confocal microscopy images of Karpas 422 cells after treatment with 10 pM RuphenS12·CD20·AuNP100 for 24 h (Scale bar: 20 µm). (a) Bright-field, (b) DAPI (λ_{exc}=405 nm, λ_{em}=410 nm-550 nm), (c) Reflectance (λ_{exc}=633 nm, λ_{em}=623-643 nm), (d) Ruthenium luminescence (λ_{exc}=488 nm, λ_{em}=600 nm-750 nm), (e) Overlay of (c) and (d) - red false colour has been applied to reflection image, (f) Overlay of (b) and (d), (g) Overlay of (b) and (c) - red false colour has been applied to reflection image, (h) Overlay of (a), (b) and (e).

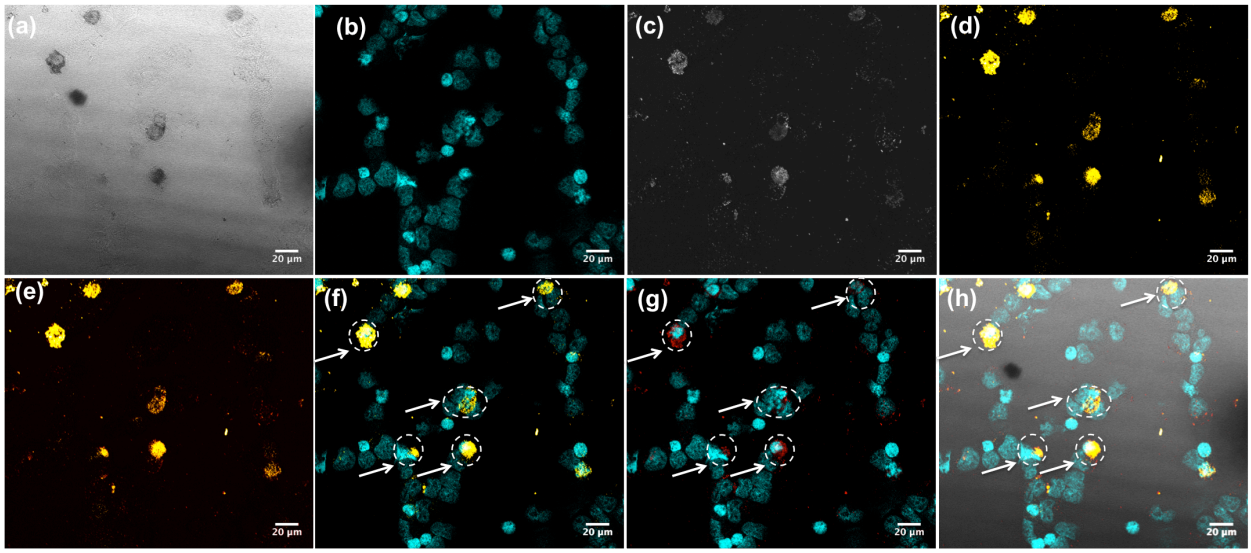


Figure 4-15. Confocal microscopy images of SU-DHL-4 cells after treatment with 10 pM RuphenS12·CD20·AuNP100 for 24 h (Scale bar: 20 µm). (a) Bright-field, (b) DAPI (λ_{exc}=405 nm, λ_{em}=410 nm-550 nm), (c) Reflectance (λ_{exc}=633 nm, λ_{em}=623-643 nm), (d) Ruthenium luminescence (λ_{exc}=488 nm, λ_{em}=600 nm-750 nm), (e) Overlay of (c) and (d) - red false colour has been applied to reflection image, (f) Overlay of (b) and (d), (g) Overlay of (b) and (c) - red false colour has been applied to reflection image, (h) Overlay of (a), (b) and (e).

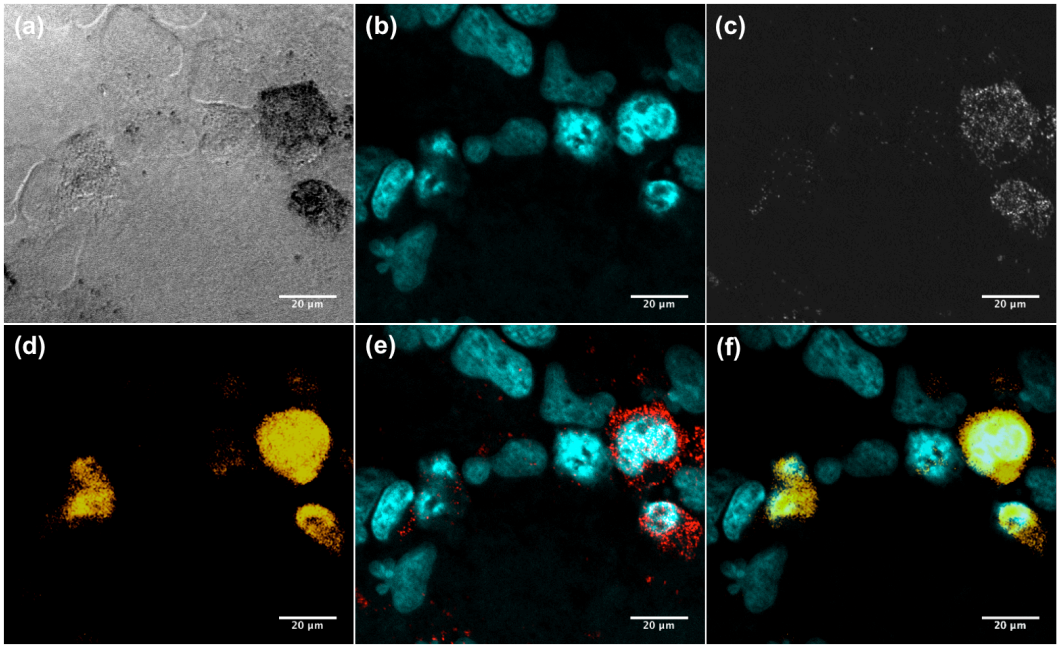


Figure 4-16. Confocal microscopy images of Karpas 422 cells after treatment with 10 pM RuphenS12·CD20·AuNP100 for 24 h (Scale bar: 20 µm). (a) Bright-field, (b) DAPI (λ_{exc}=405 nm, λ_{em}=410 nm-550 nm, (c) Reflectance (λ_{exc}=633 nm, λ_{em}=623-643 nm), (d) Ruthenium luminescence (λ_{exc}=488 nm, λ_{em}=600 nm-750 nm), (e) Overlay of (b) and (c) - red false colour has been applied to reflection image, (f) Overlay of (b) and (d).

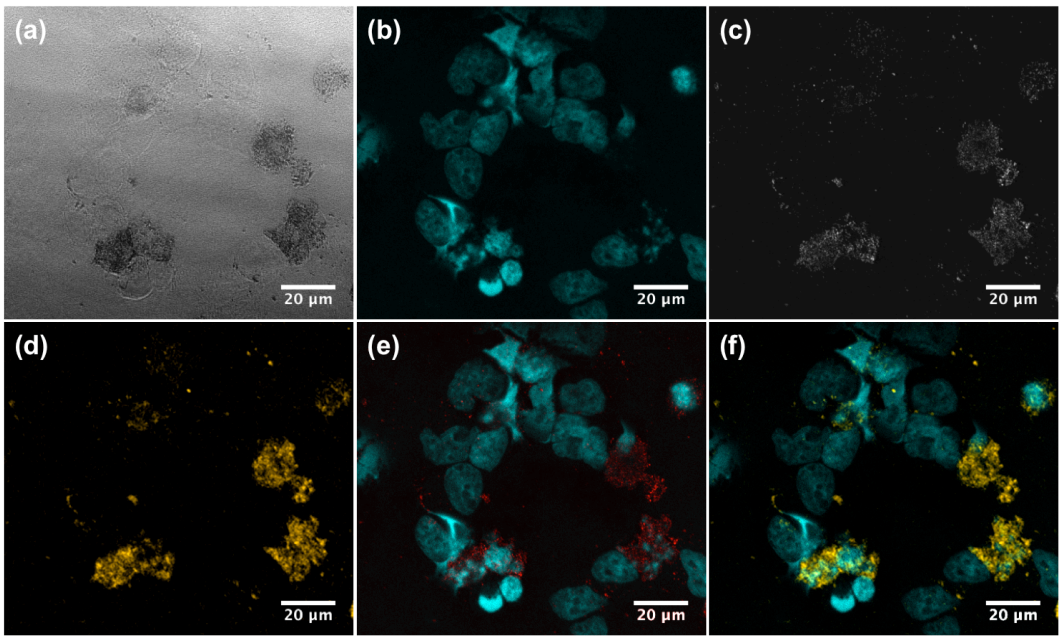


Figure 4-17. Confocal microscopy images of SU-DHL-4 cells after treatment with 10 pM RuphenS12·CD20·AuNP100 for 24 h (Scale bar: 20 µm). (a) Bright-field, (b) DAPI (λ_{exc}=405 nm, λ_{em}=410 nm-550 nm, (c) Reflectance (λ_{exc}=633 nm, λ_{em}=623-643 nm), (d) Ruthenium luminescence (λ_{exc}=488 nm, λ_{em}=600 nm-750 nm), (e) Overlay of (b) and (c) - red false colour has been applied to reflection image, (f) Overlay of (b) and (d).

When comparing the subcellular localization of RuphenS12·CD20·AuNP100 between the two cell lines, it was observed that confocal and reflectance microscopy in Karpas 422 cells showed small nanoparticle clusters in the perinuclear region and dense nanoparticle clusters inside the nucleus, while in SU-DHL-4 cells, imaging revealed dense nanoparticle clusters in the perinuclear space and smaller nanoparticle clusters within the nucleus. In Karpas 422 cells, the intensity of both the luminescent signal from the ruthenium complex and the gold scattering was significantly strong in the cells that showed nuclear uptake suggesting the high accumulation of RuphenS12·CD20·AuNP100 upon penetration of the nuclear membrane.

The lower nuclear uptake observed in SU-DHL-4 cells could be attributed to the relatively lower cellular uptake of RuphenS12·CD20·AuNP100 in SU-DHL-4 cells when compared to Kapras 422 cells, as evaluated by FACS analysis earlier in this chapter. Therefore, the results suggest that the highly efficient uptake of luminescent nanoparticles can improve drastically the bioavailability and accumulation of the luminescent complex within the intracellular environment, thus, providing more opportunities for more efficient subcellular localization[107, 108].

Even though the direct adsorption of the CD20 antibody to the surface of AuNPs allowed the development of functionalized nanoparticles with efficient uptake in CD20 expressing cells in culture, the random orientation of the antibody on the gold surface compromises the binding affinity of the antibody modified AuNPs in other biological specimens, such as sectioned tissues. It has been previously reported that when compared to random orientation, the controlled orientation of antibodies upon delivery to cancer cells can enhance significantly their antigen-binding affinity and thereby, improve drastically tumor uptake[82, 109]. Hence, the directional conjugation of antibodies to the surface of nanoparticles provides a promising approach to increase antibody-antigen binding activity and thus, improve selectivity and affinity in various types of biological samples.

4.3.5 Synthesis and characterization of AuNP

In order to achieve directional conjugation of a monoclonal antibody to the gold surface, synthesis of AuNPs was performed following a published protocol by Kumar et al.[37]. In brief, water-soluble, monodisperse naoparticles of about 18 nm in size (AuNP) were produced through the addition of a trisodium citrate solution to a boiling solution of chloroauric acid. Addition of the trisodium citrate changes the colour of the chloroauric acid to blue and then to deep red due to the increase induced in the size of nanoparticles through reduction of Au^{3+}.

After synthesis, the AuNPs were characterized by DLS, TEM and UV-Vis spectroscopy to confirm that the size and SPR band of the nanoparticles produced agree with the characterization of the nanoparticles described by the authors (Figure 4-18). The number and intensity distribution analysis of AuNP in water as measured by DLS suggest sizes of 15 ± 3 nm and 21 ± 6 nm (PDI=0.059), respectively. The size of AuNPs was further confirmed by analysis of TEM images, showing monodisperese nanoparticles with an average size of about 18 nm (n=20). UV-Vis spectroscopy of AuNP in water revealed the characteristic SPR band reported by the authors with a maximum, λ_{max} at 518 nm.

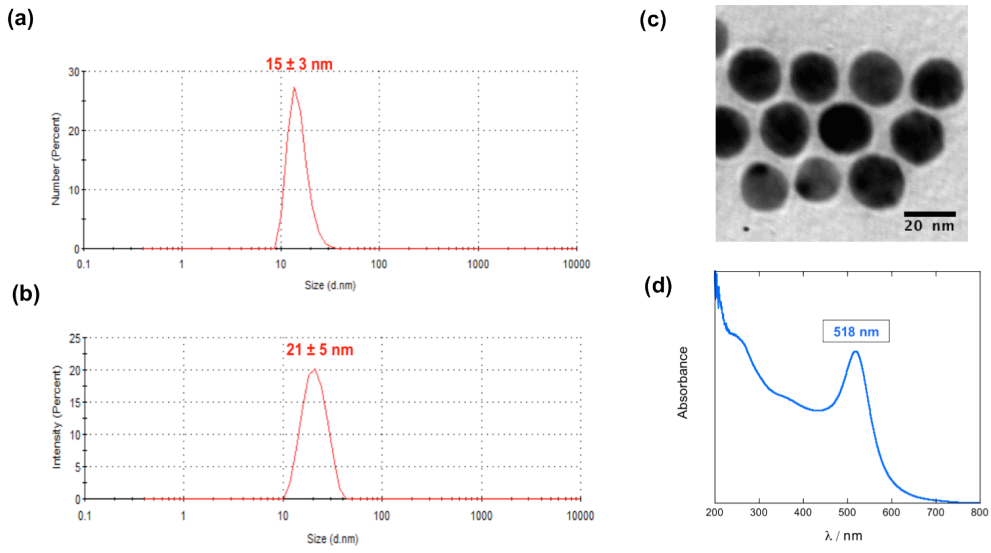


Figure 4-18. **(a) DLS number distribution of AuNP, (b) DLS intensity distribution of AuNP, (c) TEM image displaying the spherical nature of AuNP and a narrow size distribution (Scale bar= 20 nm). (d) UV-Vis absorbance of AuNP in water. The λ_{max} of the SPR band is 518 nm.**

4.3.6 Preparation of Rituximab with nanoparticle linker

For the directional attachment of monoclonal antibodies to the surface of nanoparticles, covalent strategies have been widely used in the presence of an intermediary linker[110, 111]. As discussed earlier in this chapter, binding orientation is crucial for maximizing the functional availability of a targeting antibody and improving binding affinity. The protocol described by Kumar et al. is based on directing the antigen-binding sites of the Fab region away from the gold surface using a conjugation linker, to maximise exposure and thus, increase the targeting availability of the antibody[37, 112, 113]. This can be achieved via the attachment of a heterofunctional linker to the non-targeting region (Fc region) of a glycosylated antibody, leaving the targeting Fab region unhindered. The heterofucntional linker that the authors used to form the antibody-linker complex is a PEG linker comprised of an amide-bonded adipic hydrazide for attachment to the Fc region of the antibody and an alkane chain terminating in dithiol tether for conjugation to the gold surface through a covalent thiol-gold bond[37, 114].

Therefore, in order to conjugate the glycosylated monoclonal CD20 antibody Rituximab, commercially available as Rituxan, to the surface of AuNPs, the antibody was initially attached to the hydrazide PEG-dithiol linker. Monoclonal antibodies that are glycosylated contain vicinal diol moieties on their Fc region, two hyrdroxyl groups (– OH), which can be oxidatively cleaved to yield aldehydes (– CH=O)[115]. The aldehyde moieties on the antibody act as important sites for payload attachment, as they can be linked with hydrazide-functionalized molecules[115]. The introduction of aldehydes on Rituximab was performed using sodium periodate ($NaIO_4$) as an oxidation reagent[37, 115]. The presence of the aldehydes was confirmed through a colorimetric test using the Purpald reagent[37] (Figure 4-19).

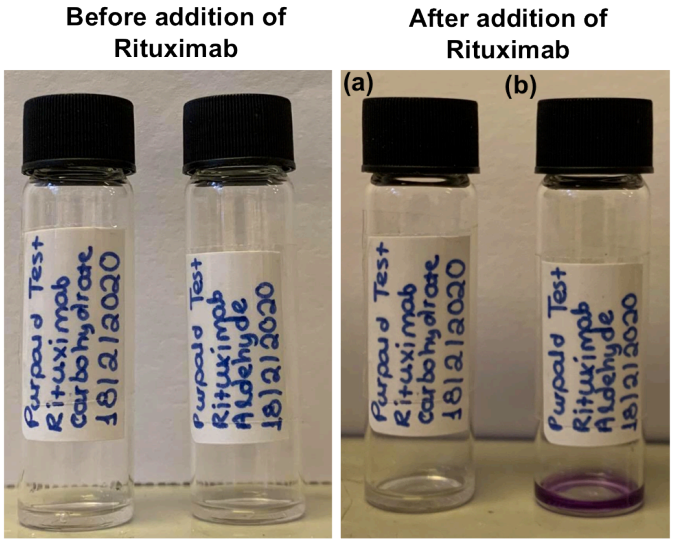


Figure 4-19. **Colorimetric assay using Purpald regaent to confirm the oxidation of the carbohydrate to aldehydes on Rituximab. (Left) Before addition of Rituximab (Right) After addition of Rituximab. (a) Rituximab with carbohydrate (b) Rituximab after oxidation of the carbohyrate to aldehydes.**

After the presence of the aldehydes on the antibody was confirmed, the hydrazide PEG-dithiol linker was added to form the antibody-linker complex (Rituximab-linker complex). The concentration of Rituximab in the antibody-linker complex was determined using UV-Vis spectroscopy and a known concentration of Rituximab (Figure 4-20).

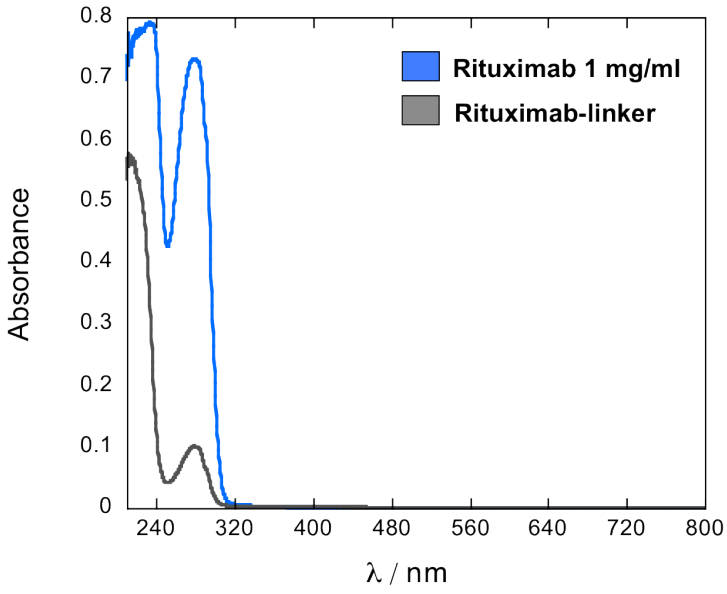


Figure 4-20. **UV-Vis absorption spectra of Rituximab (1 mg/ml) and Rituximab-linker in PBS.**

4.3.7 Conjugation of Rituximab-linker to AuNP

Following the published protocol by Kumar et al., the Rituximab-linker complex was added to AuNP solution (Rituximab-linker•AuNP) and the SPR was recorded to confirm attachment to the gold surface. However, UV-Vis spectroscopy revealed significant broadening and large shift in the SPR band of Rituximab-linker•AuNP, which are indicative of nanoparticle aggregation[116, 117] (Figure 4-21). This could be attributed to the larger size of Rituximab when compared to the relative small targeting antibodies used in the published protocol by Kumar et al., as attachment of larger molecules to the gold surface is more likely to compromise nanoparticle stability[79, 118].

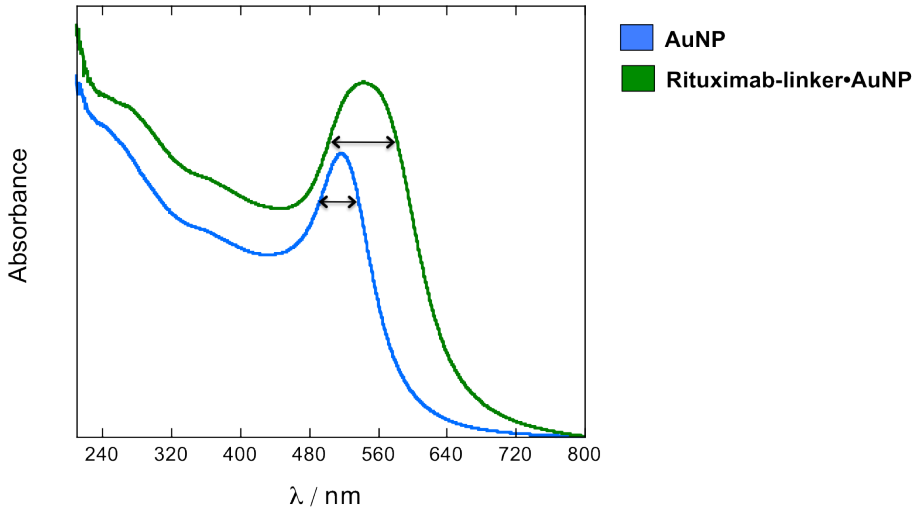


Figure 4-21. UV-Vis absorption spectra of AuNP and attempted attachment of Rituximab-linker to AuNP (Rituximab-linker•AuNP) in water. The broadening and large shift in the SPR band of Rituximab-linker•AuNP indicate nanoparticle aggregation.

Therefore, prior to conjugating the Rituximab-linker to the surface of AuNPs, the nanoparticles were coated with polyethylene glycol (PEG) to further stabilize the gold surface and prevent aggregation. Funtionalization of AuNPs with PEG has been previously reported to improve drastically their stability and eliminate toxicity in biological environments, which is essential for *in vitro* and *in vivo* biomedical applications[119, 120, 31]. The AuNPs were only coated partially with PEG to prevent saturation on the gold surface

and thus, allow attachment of the Rituximab-linker. The PEG coated nanoparticles were purified by centrifugation to produce PEG•AuNP. The PEG coating on the surface of AuNP resulted to a 2 nm shift in the SPR band, λ_{max}= 520 nm (Figure 4-22).

The Rituximab-linker complex was then titrated onto PEG•AuNP to determine the maximum amount that can be attached to the gold surface without inducing nanoparticle aggregation. Upon sequential addition of the Rituximab-linker complex to PEG•AuNP, a red shift was observed in the SPR band, confirming attachment to the gold surface (Figure 4-22). The final concentration of the antibody-linker complex chosen to coat PEG•AuNP was 2 µM, as addition of 3 µM induced broadening and a large red shift in the SPR band, which as discussed earlier are indicative of nanoparticle aggregation. Directional conjugation of the Rituximab-linker to the gold surface to produce Rituximab-linker•PEG•AuNP resulted to a further 3 nm shift in the SPR band, as λ_{max} shifted from 520 to 523 nm.

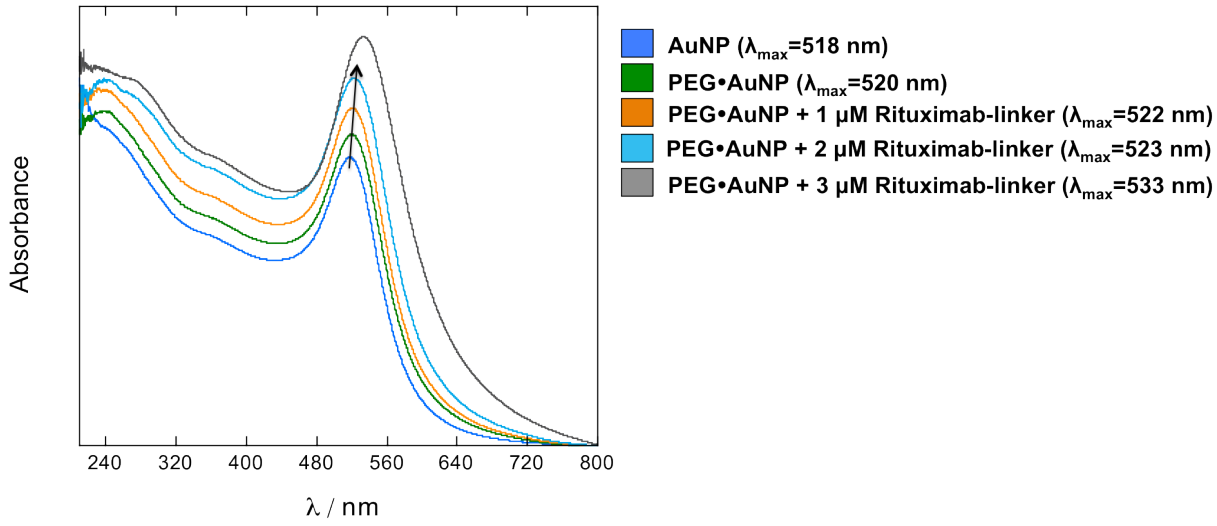


Figure 4-22. UV-Vis titration of Rituximab-linker complex (500 µM) in 2 µl aliquots into PEG•AuNP (1 nM) in water.

4.3.8 Conjugation of IrS1 to Rituximab-linker•PEG•AuNP

In order to evaluate the binding affinity of the antibody-conjugated nanoparticles in CD20 expressing biological samples by confocal microscopy, the luminescent cyclometalated iridium complex, IrS1, was attached to Rituximab-linker•PEG•AuNP. The synthesis and characterization of the IrS1 complex were carried out by Tasha Chauhan and Sarah Akponasa (School of Chemistry, University of Birmingham) (Appendix A – Scheme A-5, and Figure A-2). Photophysical characterization of the iridium complex validating its appropriatness for use in luminescence imaging is desribed in Chapter 2.

A stock solution of the IrS1 complex was prepared in methanol (1.17 mM) and added in 1 µl aliquots to 1 nM of Rituximab-linker•PEG•AuNP in water. The attachment of the luminescent complex to the surface of nanoparticles after each addition was confirmed through monitoring the shift in the SPR band using UV-Vis spectroscopy (Figure 4-23). The red shift in the SPR band allowed the maximum concentration of IrS1 that can be attached to the gold surface without inducing nanoparticle aggregation to be determined. Attachment of 7 µM of IrS1 to Rituximab-linker•PEG•AuNP resulted to a further 5 nm shift in the SPR band as λ_{max} was shifted from 523 to 528 nm. The luminescent antibody coated nanoparticles were then purified by centrifugation to produce IrS1•Rituximab-linker•PEG•AuNP. The SPR band of the isolated nanoaprticles did not change, indicating that both the luminescent complex and the antibody remain attached to the gold surface after purification (Figure 4-24).

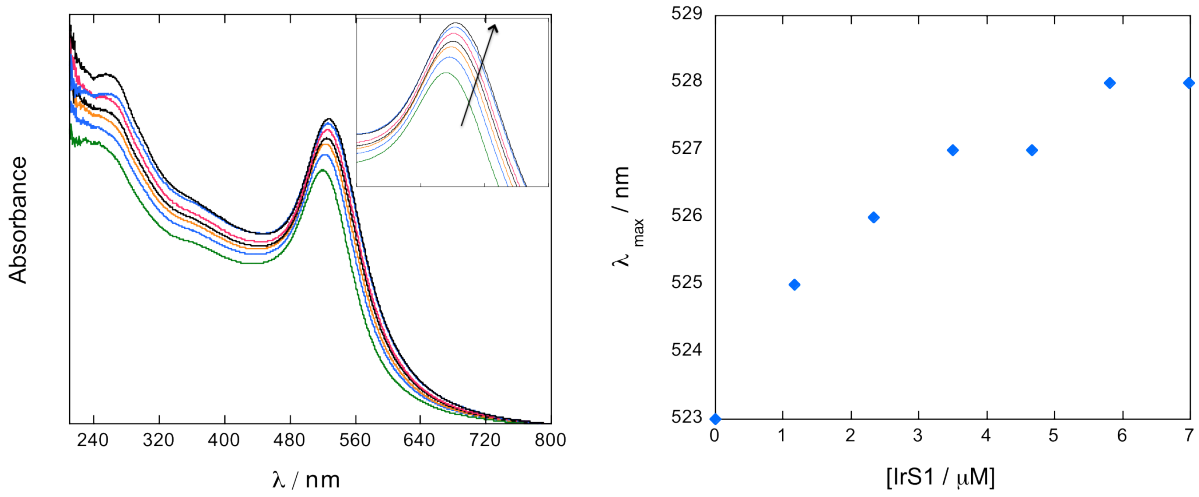


Figure 4-23. **(Left) UV-Vis titration of IrS1 (1.17 mM) in 1 µl aliquots to Rituximab-linker·PEG·AuNP in water (1 nM). (Right) The λ_{max} of the SPR band versus the concentration of the IrS1 complex added.**

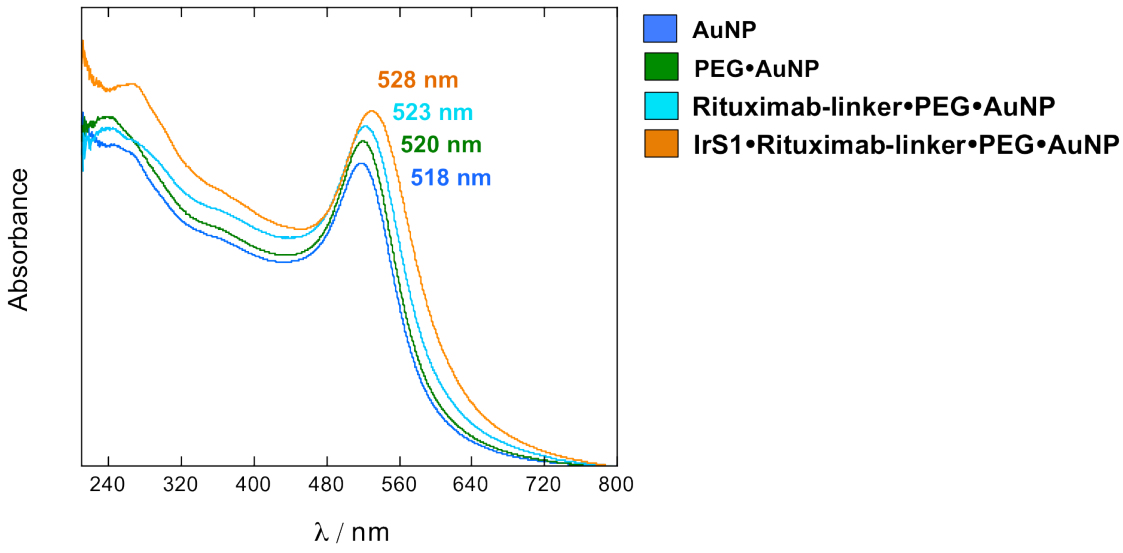


Figure 4-24. **UV-Vis absorption spectra of AuNP, PEG·AuNP, Rituximab-linker·PEG·AuNP and IrS1·Rituximab-linker·PEG·AuNP in water after purification.**

In order to determine whether the directional conjugation of the antibody to the gold surface improves the binding affinity of antibody conjugated AuNPs in CD20 positive specimens, luminescent nanoparticles in the absence of the Rituximab-linker complex were also prepared and used as the negative control. The IrS1 complex was added to PEG•AuNP (1 nM), and purification was performed by centrifugation to produce IrS1•PEG•AuNP (Figure 4-25). The concentration of the IrS1 complex used for the preparation of both IrS1•PEG•AuNP and IrS1•Rituximab-linker•PEG•AuNP was the same (7 μM), in order to make sure that the strength of the luminescence signal from the iridium complex will not influence the luminescence intensity during imaging. Attachment of 7 μM of the IrS1 complex to PEG•AuNP resulted to a further 3 nm shift in the SPR, λ_{max}=523 nm, confirming the presence of the luminescent complex on the gold suface.

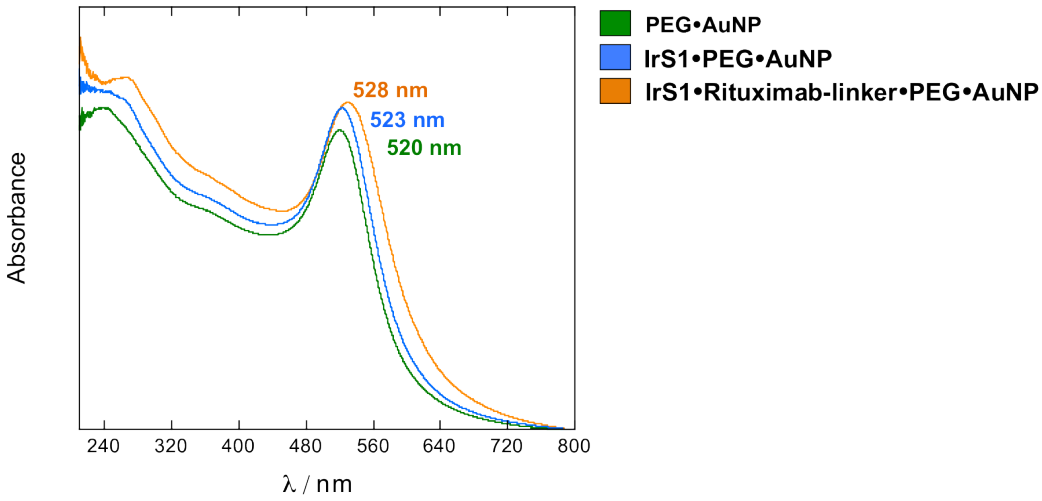


Figure 4-25. UV-Vis absorption spectra of PEG·AuNP, IrS1·PEG·AuNP and IrS1·Rituximab-linker·PEG·AuNP in water after purification.

4.3.9 Characterization of IrS1·Rituximab-linker·PEG·AuNP

The hydrodynamic diameter and zeta potential of IrS1·Rituximab-linker·PEG·AuNP were measured by DLS in order to evaluate the monodisperisty and stability of the functionalized nanoparticles (Figure 4-26) (DLS data are summarized in Table 4-3). When compared to PEG·AuNP, DLS measurements revealed higher intensity distributions for Rituximab-linker·PEG·AuNP and IrS1·Rituximab-linker·PEG·AuNP, indicating the presence of the Rituximab antibody on the gold surface. Upon conjugation of the antibody-linker to AuNPs, a relatively low PDI was maintained, which suggests that the modified AuNPs maintain their monodispersity upon functionalization. This was further confirmed by TEM, as imaging analysis of IrS1·Rituximab-linker·PEG·AuNP showed highly monodisperse and uniformly sized nanoparticles of about 18 nm in diameter (n=20) (Figure 4-27).

	Size by Number / nm	Size by Intensity / nm	Z-average / nm	ζ-potential / mV	PDI
AuNP	15 ± 3	21 ± 5	20	- 37 ± 9	0.059
PEG•AuNP	17 ± 5	37 ± 11	34	- 18 ± 5	0.088
IrS1•PEG•AuNP	19 ± 9	41 ± 15	37	- 46 ± 8	0.226
Rituximab-linker•PEG•AuNP	20 ± 8	42 ± 14	37	- 37 ± 8	0.129
IrS1•Rituximab-linker•PEG•AuNP	22 ± 10	43 ± 17	40	- 43 ± 9	0.242

Table 4-3. DLS for AuNP, PEG·AuNP, IrS1·PEG·AuNP, Rituximab-linker·PEG·AuNP and IrS1·Rituximab-linker·PEG·AuNP in water. Results indicate PDI, sizes by number and intensity (nm) and zeta potential data.

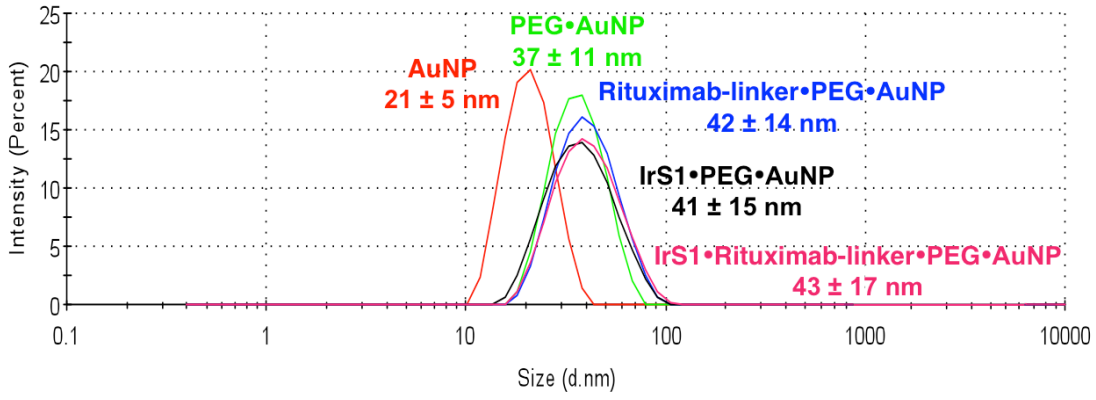


Figure 4-26. DLS Intensity distributions of AuNP, PEG·AuNP, IrS1·PEG·AuNP, Rituximab-linker·PEG·AuNP and IrS1·Rituximab-linker·PEG·AuNP.

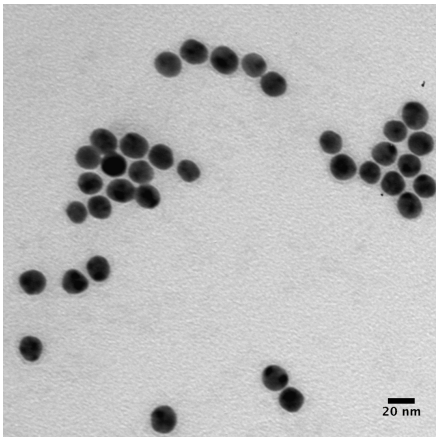


Figure 4-27. TEM image displaying the high monodispersity and spherical nature of IrS1·Rituximab-linker·PEG·AuNP (Scale bar= 20 nm).

What is more, attachment of the IrS1 complex to PEG·AuNP resulted to a small increase in the intensity distribution, confirming the presence of the luminescent complex on the gold surface. However, an increase in the intensity distribution was not evident after attachment of the IrS1 complex to Rituximab-linker·PEG·AuNP, which could be attributed to the fairly smaller size of the luminescent complex when compared to the size of the antibody. The fact that the luminescent complex is about 1 nm in length, while a monoclonal antibody like Rituximab is about 10 to 15 nm[76] suggests that attachment of the IrS1 to the antibody conjugated nanoparticles would not produce a further increase in the intensity distribution.

DLS zeta potential measurements revealed a considerable increase in the zeta potential upon coating of the gold surface with PEG, as AuNP and PEG·AuNP displayed an average surface charge of - 37 ± 9 mV and - 18 ± 5 mV, respectively (Figure 4-28) (DLS data are summarized in Table 4-3). The less electronegative surface charge of PEG·AuNP observed is consistent with literature, as functionalization of AuNPs with PEG has been previously reported to induce an increase in the zeta potential of citrate nanoparticles[121-123]. The presence of PEG on the gold surface reduces nanoparticle attractions through increasing the steric distance between them and promoting hydrophobicity via the formation of hydrogen bonds between ether repeats and the solvent[124, 125]. Furthermore,

zeta potential measurements indicated that both IrS1·PEG·AuNP and IrS1·Rituximab-linker·PEG·AuNP are highly electronegative with an average surface charge of - 46 ± 8 mV and - 43 ± 9 mV, respectively. The zeta potential of Rituximab-linker·PEG·AuNP was measured to be - 37 ± 8 mV, which is less negative than the zeta potential of IrS1·PEG·AuNP and IrS1·Rituximab-linker·PEG·AuNP, suggesting that the presence of the luminescent complex on the gold surface increases the electronegativity of the functionalized nanoparticles.

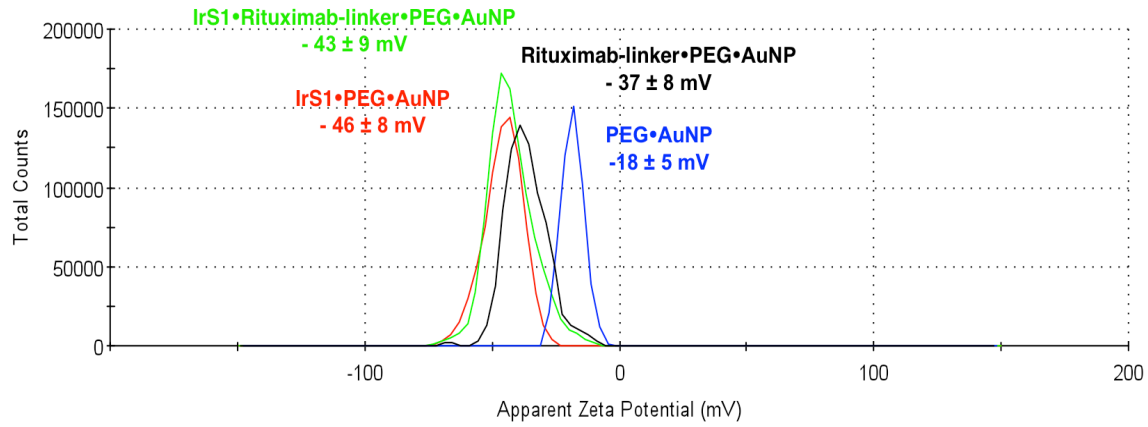


Figure 4-28. DLS zeta potential distributions of PEG·AuNP, IrS1·PEG·AuNP, Rituximab-linker·PEG·AuNP and IrS1·Rituximab-linker·PEG·AuNP.

Prior to proceeding with experimental studies in biological specimens, photophysical characterization of IrS1·Rituximab-linker·PEG·AuNP was performed in order to confirm that the IrS1 complex retains its characteristic luminescence properties upon attachment to the antibody conjugated AuNPs. Photophysical characterization of the IrS1 complex is described in Chapter 2. Upon excitation of IrS1·Rituximab-linker·PEG·AuNP at 405 nm, the functionalized nanoparticles are emissive with a λ_{max} at 600 nm, displaying a 20 nm shift from the maximum emission of the IrS1 complex in water (λ_{max}=580 nm) (Figure 4-29). This could be attributed to alterations in the surrounding environment of the complex induced by the presence of the PEG linker and the antibody. Previously published studies have reported red shifts in the emission of metal complexes of about 20 nm in the presence of PEG[126-128]. The excitation spectrum of IrS1·Rituximab-linker·PEG·AuNP

shows the characteristic SPR bands of the IrS1 complex, further confirming that the complex retains it photophysical properties when attached to the antibody modified AuNPs. The emission observed by IrS1·Rituximab-linker·PEG·AuNP upon excitation at 405 nm supports the appropriateness of the functionalized AuNPs to be used for imaging applications such as confocal luminescence microscopy.

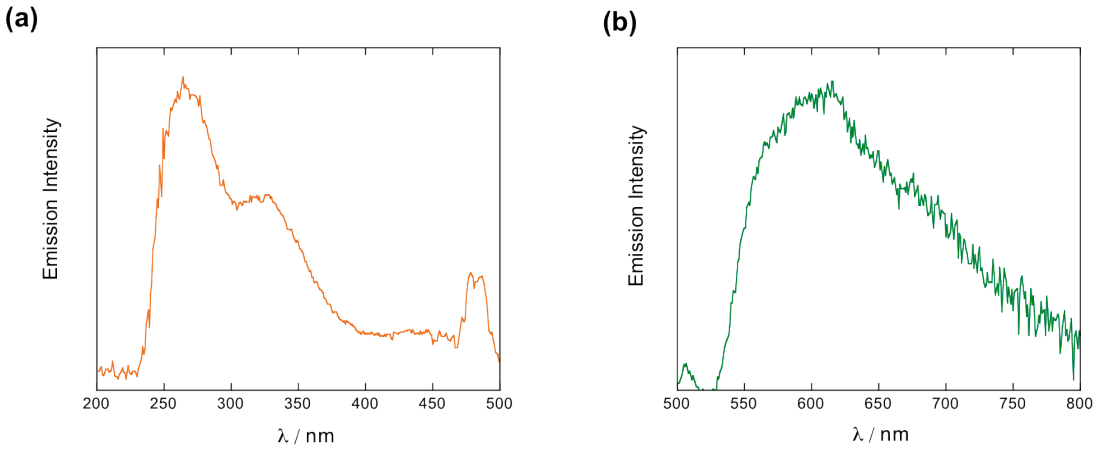


Figure 4-29. Phtophysical characterisation of IrS1·Rituximab-linker·PEG·AuNP in water. (a) Excitation spectrum of 1 nM IrS1·Rituximab-linker·PEG·AuNP, λ_{em}= 600 nm. (b) Emission spectrum of of 1 nM IrS1·Rituximab-linker·PEG·AuNP, λ_{exc}= 405 nm.

4.3.10 Gel electrophoresis to evaluate the size and surface charge of IrS1·Rituximab-linker·PEG·AuNP

The surface charge and environmental ionic conditions of functionalized nanoparticles impact their interaction with biological molecules and thus, determine their intracellular fate[129, 130]. Therefore, prior to proceeding with luminescence imaging in CD20 positive biological samples, the size and surface charge of IrS1·Rituximab-linker·PEG·AuNP were further evaluated by gel electrophoresis. Gel electrophoresis has been reported to be a highly effective tool for interpreting the stability of nanoparticles, as the mobility of

functionalized nanoparticles in a gel is determined both by their size and surface charge[77, 129, 131].

For the electrophoresis of the functionalized AuNP samples, an aqueous 1 % agarose gel was prepared and immersed in 0.5x TBE buffer. The percentage of the gel was chosen based on the size and the migration velocity of AuNPs[132, 133], while the TBE buffer was chosen as its low ionic strength and slightly alkaline pH can preclude nanoparticle aggregation[134-136].

The variation observed in the electrophoretic mobility of the different AuNP samples agrees with the DLS zeta potential measurements, discussed earlier in this chapter (Figure 4-30). The migration rate of the PEG coated nanoparticles towards the positive electrode was slower than the iridium coated AuNP samples. Even though PEG·AuNP possess a smaller hydrodynamic diameter when compared to the other AuNP samples, which would suggest faster migration rate, their relatively low electronegative surface charge hindered their movement in the agarose gel.

The iridium coated nanoparticles, IrS1·PEG·AuNP and IrS1·Rituximab-linker·PEG·AuNP, displayed faster migration rate towards the positive electrode than the other AuNP samples, which confirms their highly electronegative zeta potential observed by DLS. However, the migration distance of IrS1·Rituximab-linker·PEG·AuNP in the agarose gel was fairly shorter than the migration distance of IrS1·PEG·AuNP. The fact that both of the iridium coated AuNP samples exhibit the same average surface charge suggests that the shorter migration length of the Rituximab conjugated luminescent nanoparticles is attributed to their larger hydrodynamic diameter due to the presence of the antibody on the gold surface[136].

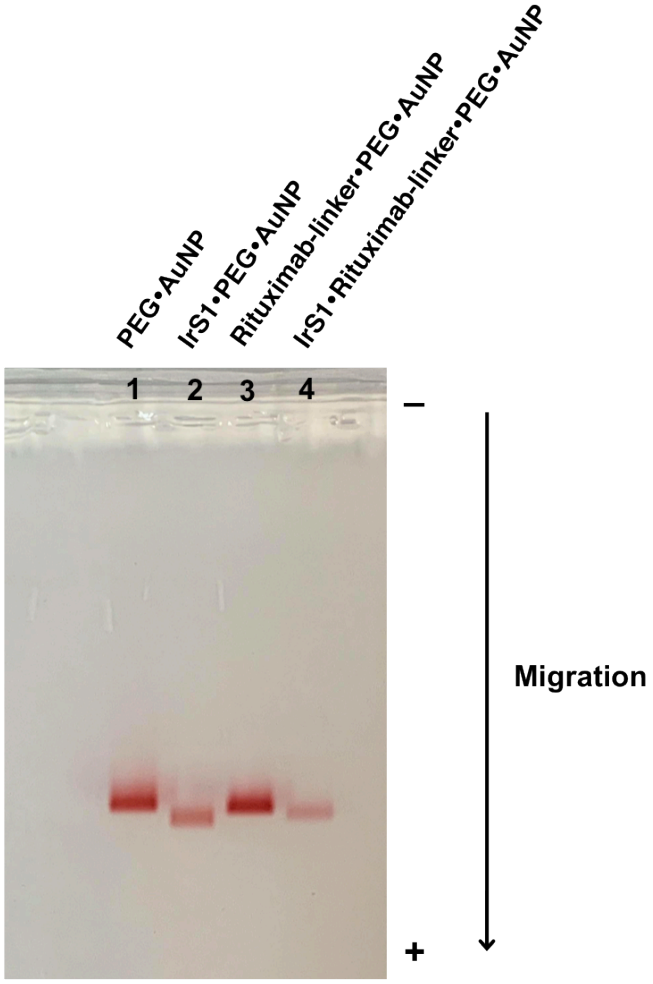


Figure 4-30. Gel electrophoresis of AuNP samples in a 1% agarose gel, run for 1 h at 100 V in 0.5x TBE. Lane 1: PEG·AuNP, Lane 2: IrS1·PEG·AuNP, Lane 3: Rituximab-linker·PEG·AuNP and Lane 4: IrS1·Rituximab-linker·PEG·AuNP.

The migration length of PEG·AuNP and Rituximab-linker·PEG·AuNP was fairly the same, which is more likely attributed to the increase in the hydrodynamic diameter and the increase in the electronegativity of Rituximab-linker·PEG·AuNP induced by the presence of the antibody on the surface of the nanoparticles (DLS data are summarized in Table 4-3). More specifically, based on their average surface charge, a longer migration distance towards the positive electrode should have been observed by Rituximab-linker·PEG·AuNP

when compared to PEG·AuNP. However, the conjugation of the antibody to the surface of AuNPs hinders further migration in the agarose gel as a result of the increase induced in the size of nanoparticles.

The results signify that gel electrophoresis is a powerful qualitative tool in the nanomedicine research field for evaluating the size, surface charge and stability of functionalized nanoparticles in physiological conditions.

4.3.11 Binding affinity of IrS1·Rituximab-linker·PEG·AuNP in tonsil tissue samples by Confocal luminescence microscopy

The binding affinity of IrS1·Rituximab-linker·PEG·AuNP was studied in fixed tonsil tissue samples, as the high expression of CD20 in tonsils makes them an ideal target for Rituximab based immunotherapies[137]. The tonsil specimens were treated with 1 nM of the luminescent antibody conjugated nanoparticles for 90 minutes and imaging was performed using confocal luminescence microscopy. Treatment of sectioned tonsil tissue specimens with IrS1·Rituximab-linker·PEG·AuNP resulted to a high intensity luminescence signal from the IrS1 complex during imaging, suggesting the highly efficient binding of the iridium and Rituximab functionalized nanoparticles against CD20 antigens expressed on the surface of tonsil B-cells. The strong binding of IrS1·Rituximab-linker·PEG·AuNP to cell surface receptors was evident in tonsil tissue sections from different patients (Figure 4-31).

The binding efficacy of IrS1·Rituximab-linker·PEG·AuNP in tonsil tissue specimens was also evaluated in the presence of the cell-permeant nuclear stain, NucRed Live 647 Reagent. In order to determine whether the directional conjugation of the Rituximab antibody on the gold surface is responsible for the strong binding observed, confocal luminescence microscopy was also performed in sectioned tonsil tissue after treatment with IrS1·PEG·AuNP, under the same conditions.

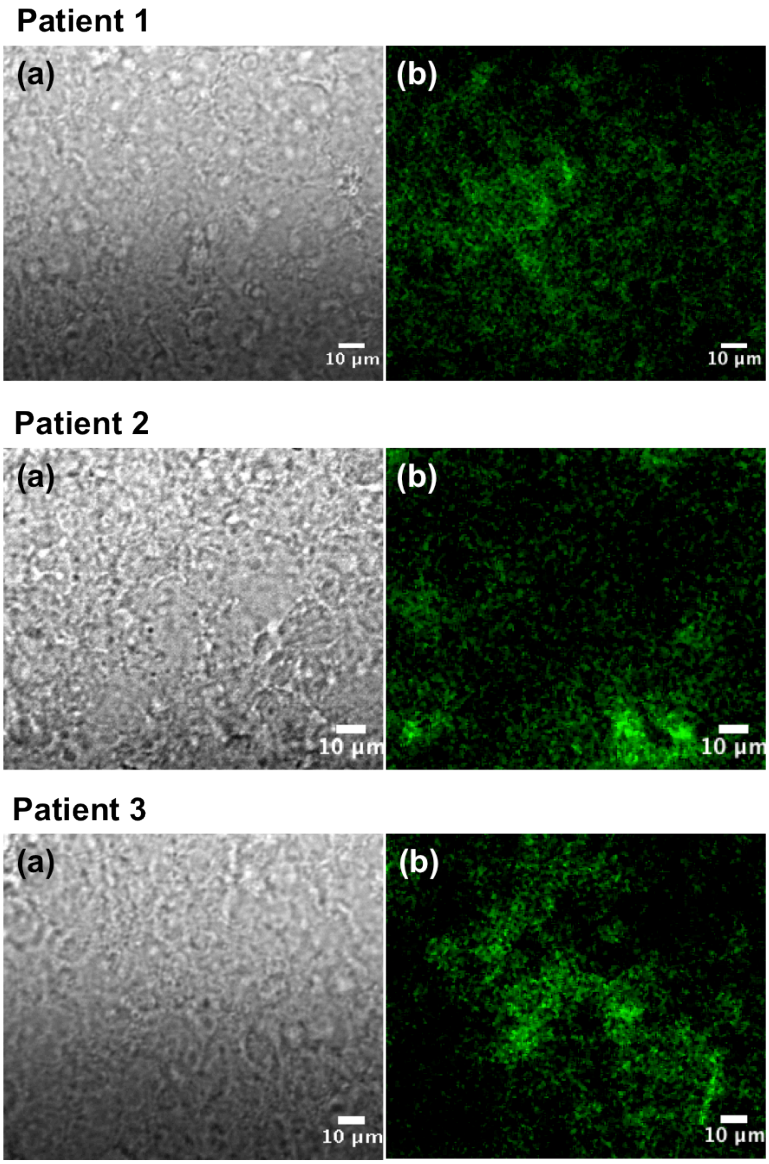


Figure 4-31. Confocal microscopy images of tonsil tissue sections after treatment with 1 nM IrS1·Rituximab-linker·PEG·AuNP for 90 min (Scale bar: 10 µm). (a) Bright-field and (b) Irirdium luminescence (λ_{exc}=405 nm, λ_{em}=550 nm-680 nm).

Luminescence imaging in tonsil slices treated with both IrS1·Rituximab-linker·PEG·AuNP and NucRed confirmed the highly efficient binding of the modified nanoparticles, as a strong luminescent signal was detected across the tissue section (Figure 4-32). Imaging analysis did not indicate any signs of co-localization between the luminescene signal of the iridium complex and the NucRed Live 647 stain.

The high binding affinity of the Rituximab conjugated AuNPs observed was not evident after treatment with IrS1·PEG·AuNP (Figure 4-33). In the sectioned tonsil tissue sample treated with IrS1·PEG·AuNP, the intensity of the luminescent signal from the iridium complex was significantly lower, proposing that the strong bidning of IrS1·Rituximab-linker·PEG·AuNP against tonsil B-cells is attributed to the presence of Rituximab on the gold surface.

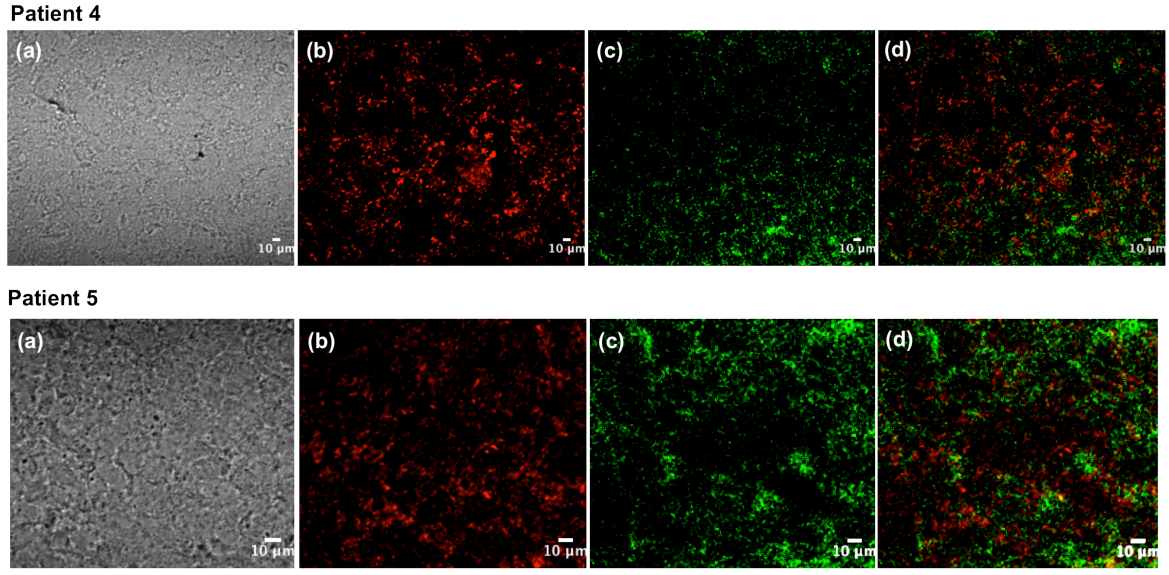


Figure 4-32. **Confocal microscopy images of tonsil tissue after treatment with 1 nM IrS1·Rituximab-linker·PEG·AuNP for 90 min (Scale bar: 10 µm). (a) Bright-field, (b) NucRed Live 647 (λ_{exc}=633 nm, λ_{em}=690 nm-800 nm), (c) Iridium luminescence (λ_{exc}=405 nm, λ_{em}=550 nm-680 nm) and (d) Overlay of (b) and (c).**

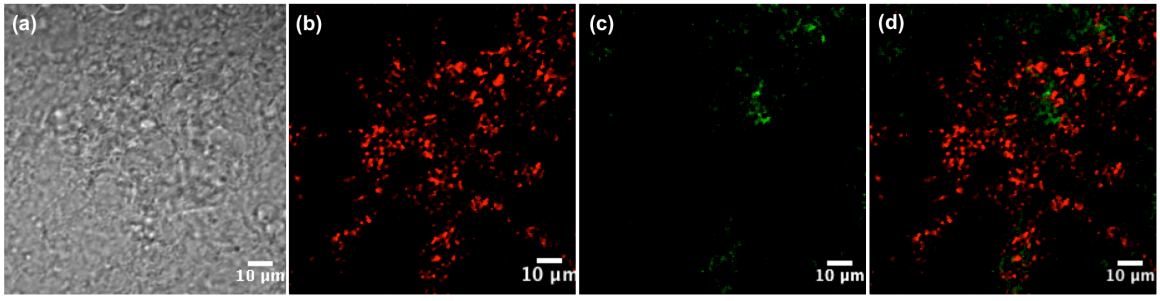


Figure 4-33. **Confocal microscopy images of tonsil tissue after treatment with 1 nM IrS1·PEG·AuNP for 90 min (Scale bar: 10 µm). (a) Bright-field, (b) NucRed Live 647 (λ_{exc}=633 nm, λ_{em}=690 nm-800 nm), (c) Iridium luminescence (λ_{exc}=405 nm, λ_{em}=550 nm-680 nm) and (d) Overlay of (b) and (c).**

The results suggest that the directional conjugation of Rituximab to the gold surface improves drastically the binding efficacy of nanoparticles against antigens, while the attachment of the luminescent complex allows visualisation of CD20 expressing cell subsets in sliced human tissue. The possibility of detecting and monitoring the CD20 expressing cells directly in tissue specimens using functionalized nanoparticles provides opportunities for the development of novel, innovative theranostic interventions for identifying tumor biomarkers *in vivo*.

4.4 Conclusion

In this chapter, luminescent gold nanoparticles were functionalized with the monoclonal antibody CD20 in order to improve binding affinity and cellular uptake in CD20 expressing malignant B-cells. Preliminary studies were performed in B-cell lymphoma cell lines using 100 nm AuNPs modified with CD20 and the luminescent ruthenium complex RuphenS12. The successful attachment of both the monoclonal antibody and the ruthenium complex to the gold surface was confirmed through monitoring the characteristic SPR band of the AuNPs and by DLS size and zeta potential measurements. More specifically, the direct adsorption of the CD20 antibody and the attachment of the ruthenium complex to AuNP100 resulted to a red shift in the SPR band of the nanoparticles, while DLS measurements revealed an increase in the intensity distribution, indicating the presence of the antibody and RuphenS12 on the gold surface. Moreover, zeta potential measurements indicated an increase in the electronegativity of the antibody functionalized AuNPs in water, suggesting their low cytotoxicity in normal cells and high stability in aqueous solutions, thereby, validating their appropriateness for use in biological environments.

The ability of the luminescent antibody coated AuNPs to enter CD20 expressing cells was initially evaluated in Karpas 422 and SU-DHL-4 cells using FACS and confocal microscopy. FACS analysis demonstrated a higher uptake of RuphenS12·CD20·AuNP100 in Karpas 422 cells over SU-DHL-4 cells, which was attributed to the higher binding affinity and valence of the CD20 antibody on the surface of the nanoparticles against the CD20 antigen receptors on the surface of Karpas 422 cells. The highly efficient internalization of the ruthenium and CD20 coated nanoparticles in Karpas 422 cells was also evident by both confocal luminescence and reflectance microscopy, as high nuclear accumulation of RuphenS12·CD20·AuNP100 was observed. The fact that the luminescent nanoparticles showed lower nuclear uptake in SU-DHL-4 as evaluated by confocal microscopy suggests that the improved cellular entry of RuphenS12·CD20·AuNP100 observed in Karpas 422 cells enhances drastically the bioavailability of the ruthenium complex within the intracellular environment, thus, promoting more efficient subcellular localization.

What is more, the cellular uptake of the luminescent nanoparticles in CD20 expressing cells was evaluated both in the presence and absence of the CD20 antibody from the surface of the AuNPs. After treatment of Karpas 422 cells with RuphenS12·CD20·AuNP100 and RuphenS12·Z·AuNP10 under the same conditions, FACS analysis revealed a higher increase in the fluorescence intensity of the cells treated with the antibody coated nanoparticles, suggesting that the presence of the CD20 antibody on the surface of AuNP100 improves penetration of the cell membrane and thus, enhances cellular internalization in CD20 positive cells.

The ability of antibody functionalized nanoparticles to enhance the binding affinity of antibodies towards antigen receptors expressed on the surface of malignant cells was further examined in this chapter through the development of Rituximab modified AuNPs. The monoclonal CD20 antibody Rituximab, which is currently used in the clinic for the treatment of B-cell haematological malignancies, was conjugated to the surface of AuNPs in a controlled manner in order to evaluate whether the directional conjugation of antibodies to the gold surface enhances their antigen-binding affinity. The directional conjugation of Rituximab to AuNPs was achieved using an intermediary PEG linker. The Rituximab modified nanoparticles were further functionalized with the luminescent iridium complex IrS1, as its favorable photophysical properties allow improved detection in biological specimens.

The characterization of the iridium and Rituximab modified nanoparticles was performed through monitoring the SPR, DLS size and zeta potential measurements as well as gel electrophoresis. The presence of the luminescent complex and Rituximab on the gold surface was evident through both the red shift observed in the SPR band of the AuNPs and the increase produced in the DLS intensity distribution after functionalization. What is more, the conjugation of Rituximab and IrS1 to AuNPs induced an increase in the electronegative surface charge of the nanoparticles, which was evident both by DLS zeta potential measurements and gel electrophoresis.

The binding affinity of the luminescent Rituximab modified AuNPs in CD20 expressing tonsil tissue specimens was evaluated and compared to the binding affinity of luminescent AuNPs without Rituximab. Confocal luminescence imaging performed in tonsil tissue

samples revealed highly efficient binding of IrS1·Rituximab-linker·PEG·AuNP, as a strong luminescence signal from the iridium complex was observed across the tissue sections. This was not the case in sliced tonsil tissue treated with IrS1·PEG·AuNP, implying that the directional conjugation of Rituximab to AuNPs enhances radically the binding affinity against CD20 antigens expressed on the surface of tonsil B-cells.

Overall, the results presented in this chapter are indicative of the significantly improved valence and uptake efficacy of nanoparticles upon modification with monoclonal antibodies. Furthermore, the attachment of both CD20 and luminescent metal complexes to the gold surface provides opportunities for visualizing CD20 expressing cell subsets directly into tonsil tissue samples. The use of AuNPs to deliver monoclonal antibodies in cancer cells can improve drastically the characterization of the highly heterogeneous tumor microenvironment, through overcoming current limitations in the oncology field associated with the use of immunostaining. To conclude, the ability to detect and monitor CD20 positive cells directly in sectioned tissue specimens using confocal microscopy potentiates a promising approach for the development of innovative interventions for use in cancer theranostics, such as identification of tumor biomarkers *in vivo*.

4.5 Acknowledgments

I would like to acknowledge Dr Sunil Claire (School of Chemistry, University of Birmingham) for his assistance in the preparation of the ruthenium and CD20 functionalized nanoparticle samples. I wish to thank Dr Shani Osborne (School of Chemistry, University of Birmingham) for providing the RuphenS12 complex used in this chapter. Also, I would like to thank both Tasha Chauhan and Sara Akponasa (School of Chemistry, University of Birmingham) for providing the IrS1 complex.

I wish to thank Mr Paul Stanley (School of Metallurgy and Materials, University of Birmingham) for performing the TEM imaging of the nanoparticle samples. I would also like to pay my special regards to Dr Tracey Perry (Institute of Cancer and Genomic Sciences, University of Birmingham) for providing the Rituximab antibody and the sectioned tonsil tissue specimens used in this chapter. Finally, I would like to thank Dr Alessandro Di Maio (School of Biosciences, University of Birmingham) for his assistance in the imaging of the tonsil tissue samples.

4.6 Experimental

4.6.1 Synthesis of AuNP100

The synthesis of AuNP100 was performed using an adapted protocol, which is based on an improved method reported by Turkevich et al.[63, 64] and a published protocol by Ziegler et al.[65]. Prior to the nanoparticle synthesis, all glassware were washed with freshly prepared Aqua Regia ($HCl:HNO_3$, 3:1), then with deionised H_2O and dried in an oven at 80^oC overnight. The AuNP100 synthesis is carried out using a growth procedure through the addition of Au^{3+} salt and trisodium citrate to 13 nm AuNPs (AuNP13). The AuNP13 seeds are synthesized through citrate reduction and are grown into 25 nm AuNPs (AuNP25), then into 50 nm AuNPs (AuNP50) and finally, into 100 nm AuNPs (AuNP100) stabilized with citrate ions. The synthesis of AuNP13 and AuNP25 was performed as described in Chapter 6.

For the growth procedure of AuNP25 to AuNP100 three stock solutions were prepared: 2.5 mM $HAuCl_4 \cdot 3H_2O$ (49% by assay), 57.7 mM ascorbic acid and 34.4 mM trisodium citrate dihydrate, each reagent was dissolved in 50 ml of filtered miliQ H_2O. Initially, AuNP25 (9 ml, 0.65 nM) were added to 31 ml of miliQ H_2O and vigorously stirred (Total volume 40 ml). From the three stock solutions two fresh diluted solutions were prepared, a solution of 0.5 mM $HAuCl_4 \cdot 3H_2O$ and a solution of 2.9 mM ascorbic acid and 0.9 mM trisodium citrate dihydrate, each in 20 ml of filtered miliQ H_2O. The two diluted solutions were added dropwise simultaneously to the stirring solution via a peristaltic pump over approximately 20 minutes. The resultant solution was then refluxed for 30 minutes forming 80 pM AuNP50.

The AuNP50 (40 ml, 80 pM) were left to vigorously stirred. From the three stock solutions two fresh diluted solutions were prepared, a solution of 2 mM $HAuCl_4 \cdot 3H_2O$ and a solution of 12 mM ascorbic acid and 3.6 mM trisodium citrate dihydrate, each in 20 ml of filtered miliQ H_2O. The two solutions were added dropwise simultaneously to the stirring solution via a peristaltic pump over approximately 20 minutes. The resultant solution was then refluxed for 30 minutes forming 40 pM AuNP100. UV-Vis (H_2O) λ_{max}=552 nm (SPR).

Diameter = 76 ± 19 nm (DLS number distribution). Diameter = 101 ± 26 nm (DLS intensity distribution). Zeta potential = - 27 ± 9 mV (40 pM in miliQ H_2O).

4.6.2 Synthesis of RuphenS12

The synthesis and characterization of the RuphenS12 complex was performed by Dr. Shani Osborne (School of Chemistry, University of Birmingham). The synthesis and full characterization of the complex are described in Dr. Osborne's thesis (Appendix C – Scheme C-1 and Figure C-1).

4.6.3 Preparation of RuphenS12·CD20·AuNP100

Initially, 4 ml of AuNP100 of 40 pM were centrifuged twice at 13, 000 rpm for 90 seconds to remove excess ascorbic acid from nanoparticle synthesis. The supernatant after each centrifugation was discarded and the AuNP100 pellet was re-suspended in 1 ml of fresh filtered miliQ H_2O (AuNP100 + centrifugation). The centrifuged nanoparticles were then coated with 200 µl of the monoclonal antibody CD20 (Dako, Catalogue Number: M0775) and stirred for 20 minutes. The antibody coated AuNPs were centrifuged twice at 13, 000 rpm for 90 seconds to remove, excess, unbound antibody. The centrifuged nanoparticles were re-suspended in 1 ml of fresh miliQ H_2O to produce CD20·AuNP100 (Final concentration ~ 110 pM). UV-Vis (H_2O) λ_{max}=556 nm (SPR). Diameter = 78 ± 21 nm (DLS number distribution). Diameter = 118 ± 34 nm (DLS intensity distribution). Zeta potential = - 31 ± 9 mV (30 pM in miliQ H_2O).

The RuphenS12 complex (Stock solution concentration in methanol: 1 mM) was mixed with the CD20 antibody prior to attachment to the surface of AuNP100 – 10 µM of the ruthenium complex were added to 200 µl of the antibody and stirred for 20 minutes. The pre-mixed solution of RuphenS12 and CD20 was then added to 1 ml of AuNP100 after centrifugation (AuNP100 + centrifugation) and the nanoparticles were stirred for 20 minutes. The ruthenium and antibody coated AuNPs were centrifuged twice at 13, 000 rpm

for 90 seconds to remove, excess, unbound RuphenS12 and CD20. The centrifuged nanoparticles were re-suspended in 1 ml of fresh miliQ H_2O to produce RuphenS12·CD20·AuNP100 (Final concentration ~ 100 pM). UV-Vis (H_2O) λ_{max}=557 nm (SPR). Diameter = 79 ± 23 nm (DLS number distribution). Diameter = 123 ± 46 nm (DLS intensity distribution). Zeta potential = - 35 ± 6 mV (30 pM in miliQ H_2O).

4.6.4 Preparation of RuphenS12·Z·AuNP100

Firstly, 4 ml of AuNP100 (40 pM) were centrifuged twice at 13, 000 rpm for 90 seconds to remove excess ascorbic acid from nanoparticle synthesis. The supernatant after each centrifugation was discarded and the AuNP100 pellet was re-suspended in 1 ml of fresh filtered miliQ H_2O (AuNP100 + centrifugation). A fresh stock solution of 2.5 % Zonyl FSA (0.2 mM) (Sigma-Aldrich) was prepared in miliQ H_2O and filtered. In 1 ml of AuNP100 after centrifugation, 10 µl (2 µM) of the fluorinated surfactant were added and stirred for about 10 minutes. The surfactant coated AuNP100 were centrifuged twice at 13, 000 rpm for 90 seconds to remove excess zonyl. The nanoparticles were then re-suspended in 1 ml of fresh filtered miliQ H_2O to produce Z·AuNP100. The concentration of the RuphenS12 complex used to coat Z·AuNP100 is 10 µM. The same concentration of the ruthenium comlex was used to to coat both RuphenS12·Z·AuNP100 and RuphenS12·CD20·AuNP100, to make sure that the strength of the luminescent signal will not impact the cellular uptake studies by FACS. The ruthenium coated nanoparticles were purified by size exclusion chromatography using Sephadex G-10 to produce RuphenS12·Z·AuNP100. Diameter = 77 ± 22 nm (DLS number distribution). Diameter = 113 ± 38 nm (DLS intensity distribution). Zeta potential = - 37 ± 8 mV (30 pM in miliQ H_2O).

4.6.5 Cellular uptake by FACS

The cells were cultured in 60 mm dishes, $1x10^6$ cells per dish and the samples were added at a ratio of 1:10 (sample:culture media). The cellular uptake efficacy of the ruthenium and antibody coated AuNPs was evaluated after treatment of the cells with 10 pM of AuNP100, CD20·AuNP100 and RuphenS12·CD20·AuNP100 for 24 hours. After the treatment period was finished, the cells were collected into falcon tubes and centrifuged at 1000 rpm for 5 minutes. The supernatant was discarded and the cells were washed twice with sterile PBS, which was removed after each washing by centrifugation. The cell pellets were then re-suspended in 1 ml of PBS supplemented with 1% FBS and transferred to FACS tubes for analysis. Samples were run on LSR II Flow Cytometer (BD Biosciences, Oxford, UK) using the BD FACSDiva Software. Analysis was performed using FlowJo and Cytobank.

4.6.6 Cell imaging by Confocal microscopy

The cells were cultured in 60 mm dishes, $1x10^6$ cells per dish, and treated with RuphenS12·CD20·AuNP100 for 24 hours. The ruthenium and antibody coated AuNPs were added to the cells at a ratio of 1:10 (sample:culture media). After treatment with 10 pM of RuphenS12·CD20·AuNP100, the cells were collected and centrifuged at 1000 rpm for 5 minutes. The supernatant was discarded and the cells were washed twice with sterile PBS, which was removed after each washing by centrifugation. The cells were then re-suspended in PBS to form a cell suspension of $5x10^4$ cells per 100 µl.

For confocal microscopy, cytospins were prepared using the ThermoFisher Scientific Cytospin^{TM} 4 Cytocentrifuge. On each slide, 100 µl of the treated cell suspension were added and centrifuged at 1000 x g for 5 minutes. Centrifugation resulted to a monolayer of $5x10^4$ cells deposited on each slide. The cells were then fixed in 10% Formal Saline for 10 minutes and allowed to air-dry at room temperature (RT) overnight.

The fixed cells were then washed once with H_2O and twice with Trisbuffered saline containing 0.1 % Tween-20 (TBS-T). Finally, the cells were stained with DAPI (1 mg/ml) (Thermo Fisher Scientific) dissolved in PBS (1:1000) for 10 minutes and then washed twice with TBS-T for 5 minutes. A cover slip was mounted on each slide using the Permount mounting medium (Catalogue number: 17986-05) and the slides were kept at 4°C until imaging. The cells were imaged using the Leica SP2 inverted confocal microscope with a 63x/1.4 oil lens. Image analysis was performed using ImageJ 2.0.0 software.

4.6.7 Synthesis of AuNP

The synthesis of AuNP was performed following a published protocol by Kumar et al.[37]. Prior to the nanoparticle synthesis, all glassware were washed with freshly prepared Aqua Regia ($HCl:HNO_3$, 3:1), then with deionised H_2O and dried in an oven at 80°C overnight. Initially 8 mg of $HAuCl_4 \cdot 3H_2O$ (Sigma-Aldrich, Catalogue number: G4022) were dissolved in 100 ml of filtered miliQ H_2O (0.2 mM) and brought to reflux while stirring. Then 1.88 ml of trisodium citrate (38.5 mM) (Fisher Scientific, Catalogue number: S279) was added to the boiling solution and the resultant solution was refluxed for another 10 minutes to form 1 nM AuNP. UV-Vis (H_2O) λ_{max}=518 nm (SPR). Diameter = 15 ± 3 nm (DLS number distribution). Diameter = 21 ± 5 nm (DLS intensity distribution). Zeta potential = - 37 ± 9 mV (0.5 nM in miliQ H_2O).

4.6.8 Preparation of Rituximab-linker complex

The preparation of the Rituximab-linker complex was performed according to the published protocol by Kumar et al. used for the AuNP synthesis[37], with minor modifications. Initially, the hydroxyl groups on the glycosylated antibody were oxidatively cleaved to produce aldehydes in order to allow attachment of the PEG linker. A solution of 1 mg/ml of the glycosylated monoclonal antibody Rituximab (Roche – MabThera) in PBS was centrifuged at 7830 rpm for 15 minutes at 4°C. For centrifugation, 10K MWCO filter

tubes were used (Merck Millipore Amicon™ Ultra Centrifugal Filter Units). Then, 300 µl of 100 mM Na_2HPO_4 (pH 7.5) were added to the antibody in 2 aliquots (150 µl each addition), mixed well and centrifuged at 7830 rpm for 15 minutes at 4°C. The addition of 300 µl of 100 mM Na_2HPO_4 (pH 7.5) to the antibody was repeated, and again, centrifugation was performed under the same conditions. Afterwards, 100 µl of 100 mM Na_2HPO_4 were added to the antibody, followed by the addition of 10 µl of 100 mM $NaIO_4$ and mixed well. The antibody solution was incubated in the dark for 30 minutes at RT. The reaction was then quenched via the addition of 500 µl of PBS.

The presence of aldehydes was confirmed through the addition of the modified antibody to a freshly prepared Purpald solution. The solution was prepared through the addition of 10 mg of the purpald reagent (Sigma-Aldrich, CAS Number: 1750-12-5) into 1ml of 1 M NaOH. Then, 20 µl of the antibody were added to 60 µl of the purpald solution. The colour of the solution turned purple within a few minutes, confirming the presence of the aldehydes. Subsequently, 2 µl of 46.5 mM of the mPEG-thiol, 10-5 M 5000 MW linker (Shearwater Polymers) were added to the antibody and incubated at RT for 1 hour. The antibody-linker complex was then centrifuged at 7830 rpm for 15 minutes at 4°C and washed with 500 µl of PBS twice. The PBS was removed after washing with centrifugation. Finally, the antibody-linker complex was re-suspended in 500 µl of PBS and kept stored at 4°C.

4.6.9 Preparation of IrS1·Rituximab-linker·PEG·AuNP

Initially, a fresh solution of 1 mM PEG was prepared in filtered miliQ H_2O (Sigma-Aldrich, Catalogue number: P2263). In order to stabilise the gold surface prior to attaching the Rituximab-linker, 5 µM of PEG were added to 1 ml of AuNP (1 nM) and stirred for 20 minutes. The AuNP surface was only coated partially with PEG to prevent full coverage of the gold surface and thereby, allow conjugation of the Rituximab-linker. The PEG coated AuNPs were centrifuged twice at 10, 000 g for 30 minutes and were then re-suspended in 1 ml of filtered miliQ H_2O to produce PEG·AuNP (Final concentration ~ 1nM). UV-Vis

(H_2O) λ_{max}=520 nm (SPR). Diameter = 17 ± 5 nm (DLS number distribution). Diameter = 37 ± 11 nm (DLS intensity distribution). Zeta potential = - 18 ± 5 mV (0.5 nM in miliQ H_2O).

The Rituximab-linker complex (Stock solution in PBS: 0.5 mM) was titrated in 2 µl aliquots to an aqueous solution of 1 ml PEG·AuNP (1 nM), with stirring in between each addition. The maximum concentration of the antibody-linker that is required to reach saturation on the gold surface was determined through monitoring the red shift in SPR of AuNP by UV-Vis spectroscopy (Cary 5000 Spectrometer). The final concentration of the Rituximab-linker complex chosen to coat PEG·AuNP is 2 µM. Subsequent to adding the antibody-linker to PEG·AuNP, the nanoparticles were stirred for 20 minutes and then divided into two aliquots of 500 µl each and centrifuged at 10, 000 g for 5 minutes using 10k MWCO 0.5 ml ultrafiltration centrifugal units (Thermo Fisher Scientific, Catalogue number: 88513). The nanopartircles in the filter of each centrifugal unit were re-suspended into 500 µl of filtered miliQ H_2O and mixed together to produce Rituximab-linker·PEG·AuNP (Final concentration ~ 0.9 nM). UV-Vis (H_2O) λ_{max}=523 nm (SPR). Diameter = 20 ± 8 nm (DLS number distribution). Diameter = 42 ± 14 nm (DLS intensity distribution). Zeta potential = - 37 ± 8 mV (0.5 nM in miliQ H_2O).

A stock solution of the IrS1 complex was prepared (Stock solution concentration in methanol: 1.17 mM) and added in 1 µl aliquots to an aqueous solution of Rituximab-linker·PEG·AuNP with stirring in between each addition. The attachment of the IrS1 to the gold surface was confirmed via monitoring the red shift in the SPR of AuNP using UV-Vis spectroscopy (Cary 5000 Spectrometer). The maximum concentration of the IrS1 complex required to reach saturation on the gold surface was determined to be 7 µM. Therefore, 7 µM of IrS1 were added to 1 ml of Rituximab-linker·PEG·AuNP (1 nM) in 1 µl aliquots with 5 minute stirring between each addition. After the last addition, the nanoparticles were further stirred for 20 minutes and then divided into two aliquots of 500 µl each and centrifuged at 10, 000 g for 5 minutes using 10k MWCO 0.5 ml ultrafiltration centrifugal units. Finally, the modified AuNPs in the filter of each centrifugal unit were re-suspended into 500 µl of filtered miliQ H_2O and mixed together to produce IrS1·Rituximab-linker·PEG·AuNP (Final concentration ~ 0.7 nM). UV-Vis (H_2O) λ_{max}=528 nm (SPR).

Diameter = 22 ± 10 nm (DLS number distribution). Diameter = 43 ± 17 nm (DLS intensity distribution). Zeta potential = - 43 ± 9 mV (0.5 nM in miliQ H_2O).

4.6.10 Preparation of IrS1·PEG·AuNP

Prior to attaching the IrS1 complex, AuNPs were coated with PEG following the procedure described in Section 4.6.10 (PEG·AuNP). The concentration of IrS1 used to coat the surface of PEG·AuNP is 7 μM. In order to evaluate the binding affinity of IrS1·PEG·AuNP and IrS1·Rituximab-linker·PEG·AuNP towards CD20 expressing tonsil tissue specimens the same concentration of IrS1 was used for the preparation of the two nanoparticle samples to ensure that the strength of the luminescence signal will not affect interpretation of binding upon imaging by confocal luminescence microscopy. Therefore, 7 μM of IrS1 were added to 1 ml of PEG·AuNP (1 nM) in 1 μl aliquots with 5 minute stirring between each addition. After the last addition of the complex the nanoparticles were stirred for a further 20 minutes. Similarly to IrS1·Rituximab-linker·PEG·AuNP, the IrS1 and PEG coated AuNPs were isolated by centrifugation. The nanoparticles were divided into two aliquots of 500 μl each and centrifuged at 10, 000 g for 5 minutes using 10k MWCO 0.5 ml ultrafiltration centrifugal units. The iridium coated PEG·AuNPs in the filter of each centrifugal unit were re-suspended into 500 μl of filtered miliQ H_2O and mixed together to produce IrS1·PEG·AuNP (Final concentration ~ 0.8 nM). UV-Vis (H_2O) λ_{max}=523 nm (SPR). Diameter = 19 ± 9 nm (DLS number distribution). Diameter = 41 ± 15 nm (DLS intensity distribution). Zeta potential = - 46 ± 8 mV (0.5 nM in miliQ H_2O).

4.6.11 Gel Electrophoresis

Initially a 0.5 M EDTA buffer was prepared through dissolving 18.7 g of EDTA Disodium salt (Sigma-Aldrich, CAS number: 6381-92-6) in 80 ml of deionised H_2O while stirring. Then, 2 g of NaOH pellets (Fisher Scientific, CAS number: 1310-73-2) were added to adjust the pH of the buffer to 8.

A 5x TBE buffer with a pH of 8.3 was prepared through dissolving 27 g of Tris base (Sigma-Aldrich, CAS number: 77-86-1) and 13.75 g of Boric acid (Simga-Aldrich, CAS number: 10043-35-3) in 450 ml of deionised H_2O while stirring. Then, 10 ml of the 0.5 M EDTA buffer were added, and the volume was adjusted to 500 ml. The 0.5x TBE buffer (pH 8.3) was prepared by adding 100 ml of the 5x TBE buffer into 900 ml of deionised H_2O.

A 1% agarose gel (w/v) was prepared by adding 4 g of agarose in 400 ml of 0.5x TBE buffer. The agarose solution was heated in a microwave on high power for about 2 minutes. Every 30 seconds the solution was removed from the microwave and swirled gently to speed up the dissolving process. The agarose solution was then allowed to cool for a few minutes and swirled gently to dissipate air bubbles. Finally, the gel was poured into the casting tray prepared with 15-well combs and allowed to polymerize at RT for about 1 hour.

Prior to running the AuNPs on the agarose gel, 15 µl of 20 % glycerol were added to 15 µl of each nanoparticle sample (10 % glycerol in each AuNP sample). The addition of the glycerol was performed in order to enhance sample density and thereby, improve loading in the wells. The 1 % agarose gel was placed in the 0.5x TBE buffer and the AuNP samples were loaded and run at 100 V for 1 hour using the Electrophoresis Power Sypply-EPS 301 system. Photographic images of the AuNPs on the gel were taken immediately after electrophoresis.

4.6.12 Preparation of tonsil tissue specimens and imaging by confocal microscopy

The sectioned tonsil tissue specimens were provided by Dr. Tracey Perry (Institute of Cancer and Genomic Sciences, University of Birmingham). Initially, the citrate-antigen retrieval method was performed on the specimens in order to expose the CD20 antigens. The antigen retrieval buffer was prepared through the addition of 1.26 g of sodium citrate (VWR, CAS number: 6132-04-03) and 0.5 g citric cid (VWR, CAS number: 77-92-9) in 1 L of distilled H_2O. The pH of the buffer was adjusted to 6 using 0.1 M sodium hydroxide. The

citrate buffer was then heated in a microwave for 10 minutes at full power. The glass slides with the sectioned tonsil tissue samples were immersed into the citrate buffer and heated for 10 minutes at medium power and 10 minutes at low power. The slides were then cooled at 4°C for 15 minutes and washed under running tap water for 5 minutes.

After washing, a hydrophobic barrier was drawn around each tissue section using a 5 mm tip width Pap pen (Sigma-Aldrich) and conditioned using TBS-T for 10 minutes. In order to prevent non-specific binding of the antibody coated AuNPs, the tonsil tissue sections were blocked with 5x casein for 10 minutes in distilled H_2O (Vector Laboratories, Catalogue number: SP-5020-250). The AuNP samples (150 µl, 1 nM) were then added to the sectioned tissue and incubated at RT for 90 minutes. The slides were washed twice with TBS-T in order to remove unbound nanoparticles and then they were stained with NucRed Live 647 Reagent (1 mg/ml) (Thermo Fisher Scientific, Catalogue number: R37 106) diluted in PBS (1:1000) for 10 minutes. Finally, the tissue sections were washed twice with TBS-T for 5 minutes and a cover slip was mounted on each slide using the Permount mounting medium (Catalogue number: 17986-05). The slides were kept at 4°C until imaging. The tonsil tissue specimens were imaged using the Nikon A1R inverted confocal microscope with a 63x/1.4 oil lens. Image analysis was performed using ImageJ 2.0.0 software.

4.7. References

[1] Aguado, B. A., Grim, J. C., Rosales, A. M., Watson-Capps, J. J. & Anseth, Kr. S. 2018. Engineering precision biomaterials for personalized medicine. *Sci Transl Med,* 10**,** eaam8645.

[2] Mitchell, M. J., Billingsley, M. M., Haley, R. M., Wechsler, M. E., Peppas, N. A. & Langer, R. 2020. Engineering precision nanoparticles for drug delivery. *Nat Rev Drug Discov*.

[3] Van Der Meel, R., Sulheim, E., Shi, Y., Kiessling, F., Mulder, W. J. M. & Lammers, T. 2019. Smart cancer nanomedicine. *Nat Nanotechnol,* 14**,** 1007-1017.

[4] Yoo, C. & Park, Y. S. 2015. Companion diagnostics for the targeted therapy of gastric cancer. *World J Gastroenterol,* 21**,** 10948-10955.

[5] Geyer, C. E., Forster, J., Lindquist, D., Chan, S., Romieu, C. G., Pienkowski, T., Jagiello-Gruszfeld, A., Crown, J., Chan, A., Kaufman, B., Skarlos, D., Campone, M., Davidson, N., Berger, M., Oliva, C., Rubin, S. D., Stein, S. & Cameron, D. 2006. Lapatinib plus Capecitabine for HER2-Positive Advanced Breast Cancer. *N Engl J Med,* 355**,** 2733-2743.

[6] Cobleigh, M. A., Vogel, C. L., Tripathy, D., Robert, N. J., Scholl, S., Fehrenbacher, L., Wolter, J. M. Fau ., Paton, V. , Shak, S., Lieberman, G. & Slamon, D. J. Multinational study of the efficacy and safety of humanized anti-HER2 monoclonal antibody in women who have HER2-overexpressing metastatic breast cancer that has progressed after chemotherapy for metastatic disease. *J Clin Oncol,* 17**,** 2639-2648.

[7] Baselga, J., Cortés, J., Kim, S. B., Im, S. A., Hegg, R., Im, Y. H., Roman, L., Pedrini, J. L., Pienkowski, T., Knott, A., Clark, E., Benyunes, M. C., Ross, G. & Swain, S. M. 2011. Pertuzumab plus Trastuzumab plus Docetaxel for Metastatic Breast Cancer. *N Engl J Med,* 366**,** 109-119.

[8] Bang, Y. J., Van Cutsem, E., Feyereislova, A., Chung, H. C., Shen, L., Sawaki, A., Lordick, F., Ohtsu, A., Omuro, Y., Satoh, T., Aprile, G., Kulikov, E., Hill, J., Lehle, M., Rüschoff, J. & Kang, Y. K. 2010. Trastuzumab in combination with chemotherapy versus chemotherapy alone for treatment of HER2-positive advanced gastric or gastro-oesophageal junction cancer (ToGA): a phase 3, open-label, randomised controlled trial. *Lancet,* 376**,** 687-697.

[9] Kang, Y. K., Rha, S. Y., Tassone, P., Barriuso, J., Yu, R., Szado, T., Garg, A. & Bang, Y. J. 2014. A phase IIa dose-finding and safety study of first-line pertuzumab in combination with trastuzumab, capecitabine and cisplatin in patients with HER2-positive advanced gastric cancer. *Br J Cancer,* 111**,** 660-666.

[10] El-Sayed, A. & Kamel, M. 2020. Advances in nanomedical applications: diagnostic, therapeutic, immunization, and vaccine production. *Environ Sci Pollut Res,* 27**,** 19200-19213.

[11] Blanco, E., Shen, H. & Ferrari, M. 2015. Principles of nanoparticle design for overcoming biological barriers to drug delivery. *Nat Biotechnol,* 33**,** 941-951.

[12] Ensign, L. M., Cone, R. & Hanes, J. 2012. Oral drug delivery with polymeric nanoparticles: The gastrointestinal mucus barriers. *Adv Drug Deliv Rev,* 64**,** 557-570.

[13] Nag, O. K. & Delehanty, J. B. 2019. Active Cellular and Subcellular Targeting of Nanoparticles for Drug Delivery. *Pharmaceutics,* 11**,** 543.

[14] Scheetz, L., Park, K. S., Li, Q., Lowenstein, P. R., Castro, M. G., Schwendeman, A. & Moon, J. J. 2019. Engineering patient-specific cancer immunotherapies. *Nat Biomed Eng,* 3**,** 768-782.

[15] Park, K. 2013. Facing the truth about nanotechnology in drug delivery. *ACS nano,* 7**,** 7442-7447.

[16] Huang, L., Huang, J., Huang, J., Xue, H., Liang, Z., Wu, J. & Chen, C. 2020. Nanomedicine – a promising therapy for hematological malignancies. *Biomater Sci,* 8**,** 2376-2393.
[17] Billingsley, M. M., Riley, R. S. & Day, E. S. 2017. Antibody-nanoparticle conjugates to enhance the sensitivity of ELISA-based detection methods. *PLoS One,* 12**,** e0177592.
[18] Bates, D., Abraham, S., Campbell, M., Zehbe, I. & Curiel, L. 2014. Development and characterization of an antibody-labeled super-paramagnetic iron oxide contrast agent targeting prostate cancer cells for magnetic resonance imaging. *PLoS One,* 9**,** e97220.
[19] Gao, X., Cui, Y., Levenson, R. M., Chung, L. W. & Nie, S. 2004. In vivo cancer targeting and imaging with semiconductor quantum dots. *Nat Biotechnol,* 22**,** 969-976.
[20] Patra, J. K., Das, G. , Fraceto, L. F. , Campos, E. , Rodriguez-Torres, M. , Acosta-Torres, L. S. , Diaz-Torres, L. A. , Grillo, R. , Swamy, M. K. , Sharma, S. , Habtemariam, S. & Shin, H. S. 2018. Nano based drug delivery systems: recent developments and future prospects. *J Nanobiotechnol,* 16**,** 71.
[21] Haba, Y., Kojima, C., Harada, A., Ura, T., Horinaka, H. & Kono, K. 2007. Preparation of Poly(ethylene glycol)-Modified Poly(amido amine) Dendrimers Encapsulating Gold Nanoparticles and Their Heat-Generating Ability. *Langmuir,* 23**,** 5243-5246.
[22] Bai, X., Wang, Y., Song, Z., Feng, Y., Chen, Y., Zhang, D. & Feng, L. 2020. The Basic Properties of Gold Nanoparticles and their Applications in Tumor Diagnosis and Treatment. *Int J Mol Sci,* 21**,** 2480.
[23] Arvizo, R., Bhattacharya, R. & Mukherjee, P. 2010. Gold nanoparticles: opportunities and challenges in nanomedicine. *Expert opinion on drug delivery,* 7**,** 753-763.
[24] Yang, W., Liang, H., Ma, S., Wang, D. & Huang, J. 2019. Gold nanoparticle based photothermal therapy: Development and application for effective cancer treatment. *Sustainable Materials and Technologies,* 22**,** e00109.
[25] Rampado, R., Crotti, S., Caliceti, P., Pucciarelli, S. & Agostini, M. 2019. Nanovectors Design for Theranostic Applications in Colorectal Cancer. *J Oncol,* 2019**,** 2740923.
[26] Goddard, Z. R., Marín, M. J., Russell, D. A. & Searcey, M. 2020. Active targeting of gold nanoparticles as cancer therapeutics. *Chem Soc Rev,* 49**,** 8774-8789
[27] Popovtzer, A., Mizrachi, A., Motiei, M., Bragilovski, D., Lubimov, L., Levi, M., Hilly, O., Ben-Aharon, I. & Popovtzer, R. 2016. Actively targeted gold nanoparticles as novel radiosensitizer agents: an in vivo head and neck cancer model. *Nanoscale,* 8**,** 2678-2685.
[28] Yook, S., Cai, Z., Jeong, J. J., Lu, Y., Winnik, M. A., Pignol, J. P. & Reilly, R. M. 2020. Dual-Receptor-Targeted (DRT) Radiation Nanomedicine Labeled with 177Lu Is More Potent for Killing Human Breast Cancer Cells That Coexpress HER2 and EGFR Than Single-Receptor-Targeted (SRT) Radiation Nanomedicines. *Mol Pharmaceutics,* 17**,** 1226-1236.
[29] Patra, C. R., Bhattacharya, R., Wang, E., Katarya, A., Lau, J. S., Dutta, S., Muders, M., Wang, S., Buhrow, S. A., Safgren, S. L., Yaszemski, M. J., Reid, J. M., Ames, M. M., Mukherjee, P. & Mukhopadhyay, D. 2008. Targeted Delivery of Gemcitabine to Pancreatic Adenocarcinoma Using Cetuximab as a Targeting Agent. *Cancer Res,* 68**,** 1970-1978.
[30] Tummala, S., Kumar, M. N. S. & Pindiprolu, S. K. 2016. Improved anti-tumor activity of oxaliplatin by encapsulating in anti-DR5 targeted gold nanoparticles. *Drug Deliv,* 23**,** 3505-3519.
[31] Spadavecchia, J., Movia, D., Moore, C., Maguire, C. M., Moustaoui, H., Casale, S., Volkov, Y. & Prina-Mello, A. 2016. Targeted polyethylene glycol gold nanoparticles for the treatment of pancreatic cancer: from synthesis to proof-of-concept in vitro studies. *Int J Nanomedicine,* 11**,** 791-822.

[32] Das, A., Soehnlen, E., Woods, S., Hegde, R., Henry, A., Gericke, A. & Basu, S. 2011. VEGFR-2 targeted cellular delivery of doxorubicin by gold nanoparticles for potential antiangiogenic therapy. *J Nanopart Res,* 13**,** 6283-6290.
[33] Jazayeri, M. H., Amani, H., Pourfatollah, A. A., Pazoki-Toroudi, H. & Sedighimoghaddam, B. 2016. Various methods of gold nanoparticles (GNPs) conjugation to antibodies. *Sensing and Bio-Sensing Research,* 9**,** 17-22.
[34] Oliveira, J. P., Prado, A. R., Keijok, W. J., Antunes, P. W. P., Yapuchura, E. R. & Guimarães, M. C. C. 2019. Impact of conjugation strategies for targeting of antibodies in gold nanoparticles for ultrasensitive detection of 17β-estradiol. *Sci Rep,* 9**,** 13859.
[35] Yu, M. K., Park, J. & Jon, S. 2012. Targeting strategies for multifunctional nanoparticles in cancer imaging and therapy. *Theranostics,* 2**,** 3-44.
[36] Juan, A. , Cimas, F. J., Bravo, I. , Pandiella, A., Ocaña, A. & Alonso-Moreno, C. 2020. An Overview of Antibody Conjugated Polymeric Nanoparticles for Breast Cancer Therapy. LID - 10.3390/pharmaceutics12090802 [doi] LID - 802. *Pharmaceutics,* 25**,** 802.
[37] Kumar, S., Aaron, J. & Sokolov, K. 2008. Directional conjugation of antibodies to nanoparticles for synthesis of multiplexed optical contrast agents with both delivery and targeting moieties. *Nat Protoc,* 3**,** 314-320.
[38] Alconcel, S. N. S., Baas, A. S. & Maynard, H. D. 2011. FDA-approved poly(ethylene glycol)–protein conjugate drugs. *Polym Chem,* 2**,** 1442-1448.
[39] Hoang Thi, T. T., Pilkington, E. H., Nguyen, D. H., Lee, J. S., Park, K. D. & Truong, N. P. 2020. The Importance of Poly(ethylene glycol) Alternatives for Overcoming PEG Immunogenicity in Drug Delivery and Bioconjugation. *Polymers,* 12**,** 298.
[40] Suk, J. S., Xu, Q., Kim, N., Hanes, J. & Ensign, L. M. 2016. PEGylation as a strategy for improving nanoparticle-based drug and gene delivery. *Adv Drug Deliv Rev,* 99**,** 28-51.
[41] Nieto, C., Vega, M. A. & Martín Del Valle, E. M. 2020. Trastuzumab: More than a Guide in HER2-Positive Cancer Nanomedicine. *Nanomaterials,* 10**,** 1674.
[42] Kubota, T., Kuroda, S., Kanaya, N., Morihiro, T., Aoyama, K., Kakiuchi, Y., Kikuchi, S., Nishizaki, M., Kagawa, S., Tazawa, H. & Fujiwara, T. 2018. HER2-targeted gold nanoparticles potentially overcome resistance to trastuzumab in gastric cancer. *Nanomedicine: NBM,* 14**,** 1919-1929.
[43] Emami, F., Banstola, A., Vatanara, A., Lee, S., Kim, J. O., Jeong, J. H. & Yook, S. 2019. Doxorubicin and Anti-PD-L1 Antibody Conjugated Gold Nanoparticles for Colorectal Cancer Photochemotherapy. *Mol Pharmaceutics,* 16**,** 1184-1199.
[44] Dey, P., Blakey, I. & Stone, N. 2020. Diagnostic prospects and preclinical development of optical technologies using gold nanostructure contrast agents to boost endogenous tissue contrast. *Chem Sci,* 11**,** 8671-8685.
[45] Wu, Y., Ali, M. R. K., Chen, K., Fang, N. & El-Sayed, M. A. 2019. Gold nanoparticles in biological optical imaging. *Nano Today,* 24**,** 120-140.
[46] Osborne, S. A. M. & Pikramenou, Z. 2015. Highly luminescent gold nanoparticles: effect of ruthenium distance for nanoprobes with enhanced lifetimes. *Faraday Discussions,* 185**,** 219-231.
[47] King, Siobhan M., Claire, Sunil, Teixeira, Rodolfo I., Dosumu, Abiola N., Carrod, Andrew J., Dehghani, Hamid, Hannon, Michael J., Ward, Andrew D., Bicknell, Roy, Botchway, Stanley W., Hodges, Nikolas J. & Pikramenou, Zoe 2018. Iridium Nanoparticles for Multichannel Luminescence Lifetime Imaging, Mapping Localization in Live Cancer Cells. *J Am Chem Soc,* 140**,** 10242-10249.

[48] Rogers, N. J., Claire, S., Harris, R. M., Farabi, S., Zikeli, G., Styles, I. B., Hodges, N. J. & Pikramenou, Z. 2014. High coating of Ru(II) complexes on gold nanoparticles for single particle luminescence imaging in cells. *Chem Commun* 50**,** 617-619.
[49] Rogers, N. J., Jeffery, H. C., Claire, S., Lewis, D. J., Zikeli, G., Hodges, N. J., Egginton, S., Nash, G. B. & Pikramenou, Z. 2017. Tailoring iridium luminescence and gold nanoparticle size for imaging of microvascular blood flow. *Nanomedicine (Lond),* 12**,** 2725-2740.
[50] Klein, C., Jamois, C. & Nielsen, T. 2020. Anti-CD20 treatment for B-cell malignancies: current status and future directions. *Expert Opin Biol Ther***,** 1-21.
[51] Pavlasova, G. & Mraz, M. 2020. The regulation and function of CD20: an "enigma" of B-cell biology and targeted therapy. *Haematologica,* 105**,** 1494-1506.
[52] Boross, P. & Leusen, J. H. W. 2012. Mechanisms of action of CD20 antibodies. *Am J Cancer Res,* 2**,** 676-690.
[53] Oflazoglu, E. & Audoly, L. P. 2010. Evolution of anti-CD20 monoclonal antibody therapeutics in oncology. *mAbs,* 2**,** 14-19.
[54] Manshouri, T., Do, K., Wang, X., Giles, F. J., O'brien, S. M., Saffer, H., Thomas, D., Jilani, I., Kantarjian, H. M., Keating, M. J. & Albitar, M. 2003. Circulating CD20 is detectable in the plasma of patients with chronic lymphocytic leukemia and is of prognostic significance. *Blood,* 101**,** 2507-2513.
[55] Lim, S. H., Beers, S. A., French, R. R., Johnson, P. W. M., Glennie, M. J. & Cragg, M. S. 2010. Anti-CD20 monoclonal antibodies: historical and future perspectives. *Haematologica,* 95**,** 135-143.
[56] Khashayar, P., Amoabediny, G., Larijani, B., Hosseini, M. & Vanfleteren, J. 2017. Fabrication and Verification of Conjugated AuNP-Antibody Nanoprobe for Sensitivity Improvement in Electrochemical Biosensors. *Sci Rep,* 7**,** 16070-16070.
[57] Plosker, G. L. & Figgitt, D. P. 2003. Rituximab: a review of its use in non-Hodgkin's lymphoma and chronic lymphocytic leukaemia. *Drugs,* 63**,** 803-843.
[58] Leget, G. A. & Czuczman, M. S. 1998. Use of rituximab, the new FDA-approved antibody. *Curr Opin Oncol,* 10**,** 548-551.
[59] Huang, X. & El-Sayed, M. A. 2010. Gold nanoparticles: Optical properties and implementations in cancer diagnosis and photothermal therapy. *J Adv Res,* 1**,** 13-28.
[60] Jain, P. K., Lee, K. S., El-Sayed, I. H. & El-Sayed, M. A. 2006. Calculated Absorption and Scattering Properties of Gold Nanoparticles of Different Size, Shape, and Composition: Applications in Biological Imaging and Biomedicine. *J Phys Chem B,* 110**,** 7238-7248.
[61] Yao, S., Zhu, Y. & Chen, L. 2013. Advances in targeting cell surface signalling molecules for immune modulation. *Nat Rev Drug Discov,* 12**,** 130-146.
[62] Bournazos, S., Wang, T. T., Dahan, R., Maamary, J. & Ravetch, J. V. 2017. Signaling by Antibodies: Recent Progress. *Annu Rev Immunol,* 35**,** 285-311.
[63] Turkevich, J., Stevenson, P. C. & Hillier, J. 1951. A Study of the Nucleation and Growth Processes in the Synthesis of Colloidal Gold. *Discuss Faraday Soc,* 11**,** 55-75.
[64] Schulz, F., Homolka, T., Bastus, N. G., Puntes, V., Weller, H. & Vossmeyer, T. 2014. Little adjustments significantly improve the Turkevich synthesis of gold nanoparticles. *Langmuir,* 30**,** 10779-10784.
[65] Ziegler, C. & Eychmuller, A. 2011. Seeded Growth Synthesis of Uniform Gold Nanoparticles with Diameters of 15-300 nm. *J Phys Chem C,* 115**,** 4502-4506.
[66] Park, J. W. & Shumaker-Parry, J. S. 2014. Structural study of citrate layers on gold nanoparticles: role of intermolecular interactions in stabilizing nanoparticles. *J Am Chem Soc,* 136**,** 1907-1921.

[67] Ivanov, M. R., Bednar, H. R. & Haes, A. J. 2009. Investigations of the mechanism of gold nanoparticle stability and surface functionalization in capillary electrophoresis. *ACS nano,* 3**,** 386-394.
[68] Mustafaoglu, N., Kiziltepe, T. & Bilgicer, B. 2017. Site-specific conjugation of an antibody on a gold nanoparticle surface for one-step diagnosis of prostate specific antigen with dynamic light scattering. *Nanoscale,* 9**,** 8684-8694.
[69] Thobhani, S., Attree, S., Boyd, R., Kumarswami, N., Noble, J., Szymanski, M. & Porter, R. A. 2010. Bioconjugation and characterisation of gold colloid-labelled proteins. *J Immunol Methods,* 356**,** 60-69.
[70] Yoshimoto, K., Nishio, M., Sugasawa, H. & Nagasaki, Y. 2010. Direct Observation of Adsorption-Induced Inactivation of Antibody Fragments Surrounded by Mixed-PEG Layer on a Gold Surface. *J Am Chem Soc,* 132**,** 7982-7989.
[71] Cruz, E. & Kayser, V. 2019. Synthesis and Enhanced Cellular Uptake In Vitro of Anti-HER2 Multifunctional Gold Nanoparticles. *Cancers,* 11**,** 870.
[72] Zhang, R., Qin, X., Kong, F., Chen, P. & Pan, G. 2019. Improving cellular uptake of therapeutic entities through interaction with components of cell membrane. *Drug Deliv,* 26**,** 328-342.
[73] Mahmoud, M. A., Chamanzar, M., Adibi, A. & El-Sayed, M. A. 2012. Effect of the Dielectric Constant of the Surrounding Medium and the Substrate on the Surface Plasmon Resonance Spectrum and Sensitivity Factors of Highly Symmetric Systems: Silver Nanocubes. *J Am Chem Soc,* 134**,** 6434-6442.
[74] Ferreira De Macedo, E., Ducatti Formaggio, D. M., Salles Santos, N. & Batista Tada, D. 2017. Gold Nanoparticles Used as Protein Scavengers Enhance Surface Plasmon Resonance Signal. *Sensors (Basel),* 17**,** 2765.
[75] Yeow, N., Tabor, R. F. & Garnier, G. 2017. Mapping the distribution of specific antibody interaction forces on individual red blood cells. *Sci Rep,* 7**,** 41956.
[76] Tan, Y. H., Liu, M., Nolting, B., Go, J. G., Gervay-Hague, J. & Liu, G. 2008. A nanoengineering approach for investigation and regulation of protein immobilization. *ACS nano,* 2**,** 2374-2384.
[77] Rasmussen, M. K., Pedersen, J. N. & Marie, R. 2020. Size and surface charge characterization of nanoparticles with a salt gradient. *Nat Commun,* 11**,** 2337.
[78] Alvarez-Puebla, R. A., Arceo, E., Goulet, P. J. G., Garrido, J. J. & Aroca, R. F. 2005. Role of Nanoparticle Surface Charge in Surface-Enhanced Raman Scattering. *J Phys Chem B,* 109**,** 3787-3792.
[79] Busch, R. T., Karim, F., Weis, J., Sun, Y., Zhao, C. & Vasquez, E. S. 2019. Optimization and Structural Stability of Gold Nanoparticle-Antibody Bioconjugates. *ACS omega,* 4**,** 15269-15279.
[80] Tan, G., Kantner, K., Zhang, Q., Soliman, M. G., Del Pino, P., Parak, W. J., Onur, M. A., Valdeperez, D., Rejman, J. & Pelaz, B. 2015. Conjugation of Polymer-Coated Gold Nanoparticles with Antibodies-Synthesis and Characterization. *Nanomaterials (Basel),* 5**,** 1297-1316.
[81] Lizoń, A., Wytrwal-Sarna, M., Gajewska, M. & Drożdż, R. 2019. Silver Nanoparticle-Based Assay for the Detection of Immunoglobulin Free Light Chains. *Materials (Basel),* 12**,** 2981.
[82] Tam, J. O., De Puig, H., Yen, C. W., Bosch, I., Gómez-Márquez, J., Clavet, C., Hamad-Schifferli, K. & Gehrke, L. 2017. A comparison of nanoparticle-antibody conjugation strategies in sandwich immunoassays. *J Immunoassay immunochem,* 38**,** 355-377.

[83] Tang, X., Xie, C., Jiang, Z., Li, A., Cai, S., Hou, C., Wang, J., Liang, Y. & Ma, D. 2018. Rituximab (anti-CD20)-modified AZD-2014-encapsulated nanoparticles killing of B lymphoma cells. *Artif Cells Nanomed Biotechnol,* 46**,** 1063-1073.
[84] Sheriff, S., Silverton, E. W., Padlan, E. A., Cohen, G. H., Smith-Gill, S. J., Finzel, B. C. & Davies, D. R. 1987. Three-dimensional structure of an antibody-antigen complex. *Proc Natl Acad Sci U S A,* 84**,** 8075.
[85] Sukhanova, A., Bozrova, S., Sokolov, P., Berestovoy, M., Karaulov, A. & Nabiev, I. 2018. Dependence of Nanoparticle Toxicity on Their Physical and Chemical Properties. *Nanoscale Res Lett,* 13**,** 44-44.
[86] Fröhlich, E. 2012. The role of surface charge in cellular uptake and cytotoxicity of medical nanoparticles. *Int J Nanomedicine,* 7**,** 5577-5591.
[87] Liu, Y., Li, W., Lao, F., Liu, Y., Wang, L., Bai, R., Zhao, Y. & Chen, C. 2011. Intracellular dynamics of cationic and anionic polystyrene nanoparticles without direct interaction with mitotic spindle and chromosomes. *Biomaterials,* 32**,** 8291-8303.
[88] Sharma, B., Peetla, C., Adjei, I. M. & Labhasetwar, V. 2013. Selective biophysical interactions of surface modified nanoparticles with cancer cell lipids improve tumor targeting and gene therapy. *Cancer Lett,* 334**,** 228-236.
[89] Jeon, S., Clavadetscher, J., Lee, D. K., Chankeshwara, S. V., Bradley, M. & Cho, W. S. 2018. Surface Charge-Dependent Cellular Uptake of Polystyrene Nanoparticles. *Nanomaterials (Basel),* 8**,** 1028.
[90] Khine, Y. Y., Callari, M., Lu, H. & Stenzel, M. H. 2016. Direct Correlation Between Zeta Potential and Cellular Uptake of Poly(methacrylic acid) Post-Modified with Guanidinium Functionalities. *Macromol Chem Phys,* 217**,** 2302-2309.
[91] Adams, S. J., Lewis, D. J., Preece, J. A. & Pikramenou, Z. 2014. Luminescent gold surfaces for sensing and imaging: patterning of transition metal probes. *ACS Appl Mater Interfaces,* 6**,** 11598-11608.
[92] Golay, J., Zaffaroni, L., Vaccari, T., Lazzari, M., Borleri, G. M., Bernasconi, S., Tedesco, F., Rambaldi, A. & Introna, M. 2000. Biologic response of B lymphoma cells to anti-CD20 monoclonal antibody rituximab in vitro: CD55 and CD59 regulate complement-mediated cell lysis. *Blood,* 95**,** 3900-3908.
[93] Di Gaetano, N., Xiao, Y., Erba, E., Bassan, R., Rambaldi, A., Golay, J. & Introna, M. 2001. Synergism between fludarabine and rituximab revealed in a follicular lymphoma cell line resistant to the cytotoxic activity of either drug alone. *Br J Haematol,* 114**,** 800-809.
[94] Teeling, J. L., French, R. R., Cragg, M. S., Van Den Brakel, J., Pluyter, M., Huang, H., Chan, C., Parren, P. W. H. I., Hack, C. E., Dechant, M., Valerius, T., Van De Winkel, J. G. J. & Glennie, M. J. 2004. Characterization of new human CD20 monoclonal antibodies with potent cytolytic activity against non-Hodgkin lymphomas. *Blood,* 104**,** 1793-1800.
[95] Franke, A., Niederfellner, G. J., Klein, C. & Burtscher, H. 2011. Antibodies against CD20 or B-cell receptor induce similar transcription patterns in human lymphoma cell lines. *PloS one,* 6**,** e16596-e16596.
[96] Glatt, D. M., Beckford Vera, D. R., Parrott, M. C., Luft, J. C., Benhabbour, S. R. & Mumper, R. J. 2016. The Interplay of Antigen Affinity, Internalization, and Pharmacokinetics on CD44-Positive Tumor Targeting of Monoclonal Antibodies. *Mol Pharmaceutics,* 13**,** 1894-1903.
[97] Shim, H. 2011. One target, different effects: a comparison of distinct therapeutic antibodies against the same targets. *Exp Mol Med,* 43**,** 539-549.

[98] Adams, G. P., Schier, R., Marshall, K., Wolf, E. J., Mccall, A. M., Marks, J. D. & Weiner, L. M. 1998. Increased Affinity Leads to Improved Selective Tumor Delivery of Single-Chain Fv Antibodies. *Cancer Res,* 58**,** 485.

[99] Adams, G. P., Tai, M. S., Mccartney, J. E., Marks, J. D., Stafford, W. F., Houston, L. L., Huston, J. S. & Weiner, L. M. 2006. Avidity-Mediated Enhancement of In vivo Tumor Targeting by Single-Chain Fv Dimers. *Clin Cancer Res,* 12**,** 1599.

[100] Muchekehu, R., Liu, D., Horn, M., Campbell, L., Del Rosario, J., Bacica, M., Moskowitz, H., Osothprarop, T., Dirksen, A., Doppalapudi, V., Kaspar, A., Pirie-Shepherd, S. R. & Coronella, J. 2013. The Effect of Molecular Weight, PK, and Valency on Tumor Biodistribution and Efficacy of Antibody-Based Drugs. *Transl Oncol,* 6**,** 562-572.

[101] Choi, S. Y., N., Yang, Jeon, S. K. & Yoon, T. H. 2014. Semi-quantitative estimation of cellular SiO2 nanoparticles using flow cytometry combined with X-ray fluorescence measurements. *Cytometry Part A,* 85**,** 771-780.

[102] Shin, H., Kwak, M., Lee, T. G. & Lee, J. Y. 2020. Quantifying the level of nanoparticle uptake in mammalian cells using flow cytometry. *Nanoscale,* 12**,** 15743-15751.

[103] Van Der Pol, E., De Rond, L., Coumans, F. A. W., Gool, E. L., Böing, A. N., Sturk, A., Nieuwland, R. & Van Leeuwen, T. G. 2018. Absolute sizing and label-free identification of extracellular vesicles by flow cytometry. *Nanomedicine: Nanotechnology, Biology and Medicine,* 14**,** 801-810.

[104] Zucker, R. M., Ortenzio, J. N. & Boyes, W. K. 2016. Characterization, detection, and counting of metal nanoparticles using flow cytometry. *Cytometry A,* 89**,** 169-183.

[105] Shum, J., Leung, P. K. K. & Lo, K. K. W. 2019. Luminescent Ruthenium(II) Polypyridine Complexes for a Wide Variety of Biomolecular and Cellular Applications. *Inorg Chem,* 58**,** 2231-2247.

[106] Blackmore, L., Moriarty, R., Dolan, C., Adamson, K., Forster, R. J., Devocelle, M. & Keyes, T. E. 2013. Peptide directed transmembrane transport and nuclear localization of Ru(ii) polypyridyl complexes in mammalian cells. *Chem Commun,* 49**,** 2658-2660.

[107] Hoang, B., Ekdawi, S. N., Reilly, R. M. & Allen, C. 2013. Active Targeting of Block Copolymer Micelles with Trastuzumab Fab Fragments and Nuclear Localization Signal Leads to Increased Tumor Uptake and Nuclear Localization in HER2-Overexpressing Xenografts. *Mol Pharmaceutics,* 10**,** 4229-4241.

[108] Mateus, A., Treyer, A., Wegler, C., Karlgren, M., Matsson, P. & Artursson, P. 2017. Intracellular drug bioavailability: a new predictor of system dependent drug disposition. *Sci Rep,* 7**,** 43047.

[109] Tajima, N., Takai, M. & Ishihara, K. 2011. Significance of Antibody Orientation Unraveled: Well-Oriented Antibodies Recorded High Binding Affinity. *Anal Chem,* 83**,** 1969-1976.

[110] Arruebo, M., Valladares, M., & González-Fernández, A. 2009. Antibody-Conjugated Nanoparticles for Biomedical Applications. *J Nanomater,* 2009**,** 1-24.

[111] Bird, R. E., Hardman, K. D., Jacobson, J. W., Johnson, S., Kaufman, B. M., Lee, S. M., Lee, T., Pope, S. H., Riordan, G. S. & Whitlow, M. 1988. Single-chain antigen-binding proteins. *Science,* 242**,** 423-426.

[112] Aaron, J. S., Oh, J., Larson, T. A., Kumar, S., Milner, T. E. & Sokolov, K. V. 2006. Increased optical contrast in imaging of epidermal growth factor receptor using magnetically actuated hybrid gold/iron oxide nanoparticles. *Opt Express,* 14**,** 12930-12943.

[113] Kumar, S., Harrison, N., Richards-Kortum, R. & Sokolov, K. 2007. Plasmonic Nanosensors for Imaging Intracellular Biomarkers in Live Cells. *Nano Lett,* 7**,** 1338-1343.

[114] Spangler, B. D. & Tyler, B. J. 1999. Capture agents for a quartz crystal microbalance-continuous flow biosensor: functionalized self-assembled monolayers on gold. *Anal Chim Acta,* 399**,** 51-62.
[115] Wang, L. X., Tong, X., Li, C., Giddens, J. P. & Li, T. 2019. Glycoengineering of Antibodies for Modulating Functions. *Annu Rev Biochem,* 88**,** 433-459.
[116] Gary, R., Carbone, G., Petriashvili, G., De Santo, M. P. & Barberi, R. 2016. Detection of Gold Nanoparticles Aggregation Growth Induced by Nucleic Acid through Laser Scanning Confocal Microscopy. *Sensors (Basel),* 16**,** 258-258.
[117] Gao, Q., Zheng, Y., Song, C., Lu, L. Q., Tian, X. K. & Xu, A. W. 2013. Selective and sensitive colorimetric detection of copper ions based on anti-aggregation of the glutathione-induced aggregated gold nanoparticles and its application for determining sulfide anions. *RSC Adv,* 3**,** 21424-21430.
[118] Miranda-Hernández, M. P., López-Morales, C. A., Ramírez-Ibáñez, N. D., Piña-Lara, N., Pérez, Nestor O., Molina-Pérez, A., Revilla-Beltri, J., Flores-Ortiz, L. F. & Medina-Rivero, E. 2015. Assessment of Physicochemical Properties of Rituximab Related to Its Immunomodulatory Activity. *J Immunol Res,* 2015**,** 910763.
[119] Zhang, J., Mou, L. & Jiang, X. 2020. Surface chemistry of gold nanoparticles for health-related applications. *Chem Sci,* 11**,** 923-936.
[120] Chen, T. Y., Chen, M. R., Liu, S. W., Lin, J. Y., Yang, Y. T., Huang, H. Y., Chen, J. K., Yang, C. S. & Lin, K. M. 2020. Assessment of Polyethylene Glycol-Coated Gold Nanoparticle Toxicity and Inflammation In Vivo Using NF-κB Reporter Mice. *Int J Mol Sci,* 21.
[121] Rahme, K., Nolan, M. T., Doody, T., Mcglacken, G. P., Morris, M. A., O'driscoll, C. & Holmes, J. D. 2013. Highly stable PEGylated gold nanoparticles in water: applications in biology and catalysis. *RSC Adv,* 3**,** 21016-21024.
[122] Manson, J., Kumar, D., Meenan, B. J. & Dixon, D. 2011. Polyethylene glycol functionalized gold nanoparticles: the influence of capping density on stability in various media. *Gold Bull,* 44**,** 99-105.
[123] Lipka, J., Semmler-Behnke, M., Sperling, R. A., Wenk, A., Takenaka, S., Schleh, C., Kissel, T., Parak, W. J. & Kreyling, W. G. 2010. Biodistribution of PEG-modified gold nanoparticles following intratracheal instillation and intravenous injection. *Biomaterials,* 31**,** 6574-6581.
[124] Lee, H. 2020. Molecular Simulations of PEGylated Biomolecules, Liposomes, and Nanoparticles for Drug Delivery Applications. *Pharmaceutics,* 12**,** 533.
[125] Jokerst, J. V., Lobovkina, T., Zare, R. N. & Gambhir, S. S. 2011. Nanoparticle PEGylation for imaging and therapy. *Nanomedicine (Lond),* 6**,** 715-728.
[126] Alam, P., Climent, C., Alemany, P. & Laskar, I. R. 2019. "Aggregation-induced emission" of transition metal compounds: Design, mechanistic insights, and applications. *J. Photochem. Photobiol. C,* 41**,** 100317.
[127] Zheng, J., Zhou, C., Yu, M. & Liu, J. 2012. Different sized luminescent gold nanoparticles. *Nanoscale,* 4**,** 4073-4083.
[128] Li, S. P. Y., Shum, J. & Lo, K. K. W. 2019. Iridium(iii) polypyridine complexes with a disulfide linker as biological sensors and cytotoxic agents. *Dalton Trans,* 48**,** 9692-9702.
[129] Park, S. & Hamad-Schifferli, K. 2008. Evaluation of Hydrodynamic Size and Zeta-Potential of Surface-Modified Au Nanoparticle-DNA Conjugates via Ferguson Analysis. *J Phys Chem C,* 112**,** 7611-7616.
[130] Han, G., Martin, C. T. & Rotello, V. M. 2006. Stability of gold nanoparticle-bound DNA toward biological, physical, and chemical agents. *Chem Biol Drug Des,* 67**,** 78-82.

[131] Hanauer, M., Pierrat, S., Zins, I., Lotz, A. & Sönnichsen, C. 2007. Separation of Nanoparticles by Gel Electrophoresis According to Size and Shape. *Nano Lett,* 7**,** 2881-2885.
[132] Pellegrino, T., Sperling, R. A., Alivisatos, A. P. & Parak, W. J. 2007. Gel electrophoresis of gold-DNA nanoconjugates. *J Biomed Biotechnol,* 2007**,** 26796-26796.
[133] Kim, S., Wark, A. W. & Lee, H. J. 2016. Gel electrophoretic analysis of differently shaped interacting and non-interacting bioconjugated nanoparticles. *RSC Adv,* 6**,** 109613-109619.
[134] Guerrini, L., Alvarez-Puebla, R. A. & Pazos-Perez, N. 2018. Surface Modifications of Nanoparticles for Stability in Biological Fluids. *Materials,* 11**,** 1154.
[135] Kim, J. Y., B., Kim H. & Jang, D. J. 2013. Electrophoretic separation of gold nanoparticles according to bifunctional molecules-induced charge and size. *Electrophoresis,* 34**,** 911-916.
[136] Cavadas, M. A. S., Monopoli, M. P., Cunha, C. S. E., Prudêncio, M., Pereira, E., Lynch, I., Dawson, K. A. & Franco, R. 2016. Unravelling Malaria Antigen Binding to Antibody-Gold Nanoparticle Conjugates. *Part Part Syst Charact,* 33**,** 906-915.
[137] Withers, D. R., Fiorini, C., Fischer, R. T., Ettinger, R., Lipsky, P. E. & Grammer, A. C. 2007. T cell-dependent survival of CD20+ and CD20- plasma cells in human secondary lymphoid tissue. *Blood,* 109**,** 4856-4864.

5. General conclusions and Future work

In this thesis, the development of novel, luminescent AuNPs for improved detection and localization in cancer cells is presented. The distinctive luminescent properties of transition metal complexes, along with their ability to penetrate the cell membrane, make them popular agents for various biomedical applications. However, their successful use as imaging and targeting moieties is often hindered by imprecise cellular localization and induced cellular toxicity. The inability of metal complexes to reach intracellular targets is mainly attributed to their poor aqueous solubility, which reduces systematic bioavailability in the cellular environment. Recent advances in nanotechnology offer countless opportunities for the development of nanoparticle-based systems to improve the bioavailability and site-specific delivery of theranostic complexes in biological systems.

The results presented in this thesis support that the use of AuNPs as a vehicle to deliver luminescent complexes in cancer cells is a promising approach to overcome the aforementioned challenges. In the first study described (Chapter 2), a cyclometalated iridium complex, IrS1, was used to functionalize the surface of surfactant coated nanoparticles in order to promote improved localization in mitochondrial structures and induce selective targeting of cancer cells. Photophysical characterization of the IrS1 coated AuNPs suggested that the complex retains its luminescence properties upon attachment to the gold surface. Through detecting the strong luminescence signal of the iridium complex in treated cells, the highly efficient uptake of the functionalized nanoparticles was observed. Live cell imaging revealed a stronger luminescence signal in the cells treated with the IrS1 modified AuNPs, when compared to the cells treated with the iridium complex in solution, indicating the enhanced uptake and bioavailability of the complex in the intracellular environment. The improved localization of the IrS1 complex in mitochondria in cancer cells when delivered attached to the gold scaffold was also evident through imaging analysis.

Interestingly, elemental analysis by ICP-MS suggested the preference of the luminescent nanoparticles for localizing in mitochondria in cancer cells, but not in normal cells. The selectivity of the luminescent AuNPs for inducing mitochondrial dysfunction in cancer cells was supported by the higher generation of intracellular ROS levels observed in cancer over normal cells.

The results provide evidence that the use AuNPs to deliver the IrS1 complex in the intracellular space promotes the efficient accumulation of the complex within mitochondrial structures. The site-specific delivery of the luminescent AuNPs in malignant cells presents a promising approach for overcoming off-target toxicity and adverse side effects associated with the use of conventional cancer therapies.

It would be interesting to further interpret the mechanism by which the luminescent nanoparticles target mitochondria in cancer cells, while sparing normal cells. For instance, elevation of ROS levels by exogenous inducers has been previously linked to the downregulation of the anti-apoptotic protein Bcl-2, which is localized on the outer membrane of mitochondria[1]. In malignant cells, overexpression of the Bcl-2 protein delays apoptosis through arresting the cells in the G0 phase of the cell cycle, while in normal cells expression of Bcl-2 is usually restricted.

Therefore, it is possible that mitochondrial dysfunction observed in cancer cells after treatment with the iridium coated AuNPs is attributed to interactions between the luminescent complex and proteins that regulate mitochondrial dynamics in malignant cells. The ability of the IrS1 coated AuNPs to interact with cellular proteins was described in Chapter 2, through monitoring conformational changes in the structure of BSA upon addition of the luminescent nanoparticles, using CD spectroscopy. Hence, with regards to future work, it would be worth checking the expression levels of mitochondrial proteins after treatment with the luminescent nanoparticles in malignant and normal cells lines, to evaluate deregulation of mitochondrial proteins involved in carcinogenesis.

What is more, in order to further evaluate the elevated ROS levels and selective targeting of mitochondria observed in cancer cells, mitochondrial function could be investigated through measuring the oxygen consumption rate after treatment with the IrS1

functionalized nanoparticles. Through monitoring the oxygen consumption rate after the sequential addition of different mitochondrial respiratory inhibitors further information can be derived on the induced mitochondrial dysfunction observed in cancer cells and hence, interpret how the differences in the phenotype, metabolic pathways and signaling between malignant and healthy cells contribute to the cancer selective targeting presented by the IrS1 coated AuNPs[2, 3].

The ability of AuNPs to improve the delivery of luminescent complexes in cells and guide efficient subcellular localization was further supported through the work presented in the second study of this thesis (Chapter 3). The cellular uptake and localization of an iridium complex with a dodecyl chain incorporated on the phenylpyridine ligand, IrC_{12}, were evaluated upon conjugation of the complex to the surface of surfactant modified AuNPs. Live cell imaging after treatment with the IrC_{12} coated AuNPs revealed a strong luminescence signal from the iridium complex in the nucleus and cytoplasm of the cells. The ability of the IrC_{12} complex to penetrate the nuclear membrane when attached to the gold scaffold was not evident upon treatment of the cells with the IrC_{12} complex in solution, suggesting that the use of AuNPs improves drastically the bioavailability of the complex within the intracellular space and promotes efficient subcellular localization. Elemental analysis by ICP-MS further confirmed the high accumulation of the iridium coated AuNPs in the nucleus, as a higher number of nanoparticles was detected in the nucleus, when compared to cytosol and mitochondria.

Similarly to the IrS1 modified AuNPs, the IrC_{12} coated nanoparticles revealed strong binding to BSA, suggesting that the luminescent complex can successfully interact with cellular proteins. The highly efficient accumulation of the IrC_{12} coated AuNPs in the nucleus along with the ability of the complex to interact with proteins provides opportunities for monitoring biomolecular interactions with nuclear proteins, such as chromatin, in *in vivo* models using multimodal imaging.

Due to the efficient localization of the IrC_{12} coated AuNPs in the nucleus it would be interesting to further investigate the ability of the luminescent complex to interact with DNA. The successful binding of luminescent nanoprobes to DNA offers possibilities for the development of anti-cancer agents with improved therapeutic efficacy that can be used for

real-time monitoring of the treatment process at a subcellular level. The ability of the IrC_{12} functionalized nanoparticles to interact with DNA could be evaluated using CD spectroscopy and gel electrophoresis.

Subsequent to evaluating the interaction of the IrC_{12} coated AuNPs with DNA, it would be worth further investigating their potential to induce DNA damage in malignant cells. Platinum based compounds, including cisplatin, oxaliplatin and carboplatin, have been widely used in the oncology field for the treatment of various types of cancer such as ovarian, lung, bladder and testicular cancer. The ability of such compounds to interact with DNA and induce damage leads to inhibition of DNA replication, transcription, cell cycle arrest and apoptosis[4, 5]. However, their successful use in the clinic is limited, as they are highly associated with drug resistance and off-target toxicity, leading to severe adverse side effects including hepatotoxicity, ototoxicity, gastrointestinal disorders and reduced immunity to infections[6]. Therefore, the nuclear localization of the IrC_{12} functionalized AuNPs in cancer cells makes them an ideal candidate for overcoming the limitations of conventional platinum chemotherapeutic drugs, since the improved delivery of the iridium complex upon attachment to the gold scaffold can eliminate off-target toxicity and hence, enhance the therapeutic outcome. DNA damage, both in cancer and normal cells, after treatment with the IrC_{12} functionalized nanoparticles could be studied using the comet assay, polymerase chain reaction (PCR) and gel electrophoresis.

In the final study of this thesis (Chapter 4), luminescent AuNPs were used to improve the binding affinity and uptake of monoclonal antibodies in malignant cells. Preliminary studies involved the direct adsorption of the monoclonal CD20 antibody to AuNPs, resulting to random antibody orientation on the gold surface. The antibody modified AuNPs were further functionalized with a ruthenium complex, RuphenS12, to allow improved detection in cells. The highly efficient cellular uptake of the antibody modified AuNPs in CD20 expressing cells was observed using flow cytometry and confocal microscopy. The localization of the antibody modified AuNPs in the intracellular environment was evident by both confocal luminescence and reflectance microscopy. The presence of the RuphenS12 complex on the gold surface allowed accumulation of the luminescent nanoparticles within the nucleus and perinuclear region.

Further studies were performed to evaluate the binding affinity of antibody conjugated AuNPs against CD20 antigens expressed in sectioned biological specimens. The monoclonal CD20 antibody Rituximab was conjugated to the surface of AuNPs in a controlled manner using an intermediary PEG linker to induce improved binding to CD20 antigens. The antibody conjugated AuNPs were further functionalized using the luminescent iridium complex, IrS1 in order to allow detection. Confocal luminescence imaging revealed the efficient binding of the luminescent antibody conjugated nanoparticles, as the luminescent signal of the iridium complex was detectable across the sectioned specimens. The results presented in this study suggested the improved affinity and uptake efficacy of antibody modified AuNPs both in cells and sectioned tonsil tissue specimens. The use of luminescent antibody modified nanoparticles offers improved characterization of the highly heterogeneous tumor microenvironment, through overcoming the limitations of conventional immunostaining methods. The attachment of luminescent complexes to the antibody modified AuNPs allows cell subsets to be detected directly in sectioned specimens using luminescence imaging, offering opportunities for the improved identification of tumor biomarkers both in biological specimens and *in vivo*.

Even though both of the methods employed to modify AuNPs with monoclonal antibodies revealed enhanced uptake and binding affinity, it would be interesting to compare the two approaches through quantifying the binding affinity of the antibody modified AuNPs. The direct adsorption of antibodies allows high antibody concentrations to be loaded onto the gold surface, however the affinity towards antigens is often compromised, as the random orientation of antibodies reduces the number of binding sites available. On the other hand, the directional conjugation of antibodies to AuNPs, allows relatively low antibody concentrations to be loaded on the gold surface, however, all antibody-antigen binding sites are available. Therefore, future work would include the quantification of the binding affinity of each method to further establish the improved antibody valency offered via the directional conjugation of antibodies to AuNPs. For the purposes of this work, the ELISA assay could be employed.

Even though cancer is a leading cause of death worldwide, early detection has been reported to improve drastically patient survival rate[7]. However, the high complexity and heterogeneity of tumors, along with the low abundance of biomarkers in patients' samples present some of the major challenges of detecting cancer at an early stage[8]. Within the past decade, advancements in high-throughout profiling techniques have allowed identification of tumor biomarkers in biological specimens, aiming to improve clinical diagnosis, patient prognosis and determine treatment regimen[9, 10]. However, the successful use of such technologies in the clinic is often compromised by their weak specificity and sensitivity[10].

As discussed in Chapter 4, the directional conjugation of antibodies to the surface of AuNPs improves the affinity towards antigens and hence, enhances detection sensitivity in biological specimens, as all antibody-antigen binding sites are available. Therefore, future work would include the directional conjugation method used for the attachment of Rituximab to AuNPs to examine the possibility of incorporating multiple monoclonal antibodies on the gold surface in order to detect different biomarkers in tissue samples simultaneously. The large surface area offered by AuNPs provides opportunities for attaching multiple antibodies to the gold surface at the same time, which aids in probing the highly heterogeneous tumor microenvironment. The multifunctionalization of AuNPs with several antibodies, along with the enhanced sensitivity offered by the directional conjugation of the antibodies to the gold surface can overcome the limitations of the diagnostic tools currently used in the clinic and promote detection at an early stage of the disease to improve drastically patient prognosis.

References:

[1] Rajina, S., Kim, W. J., Shim, J. H., Chun, K. S., Joo, S. H., Shin, H. K., Lee, S. Y. & Choi, J. S. Isolinderalactone Induces Cell Death via Mitochondrial Superoxide- and STAT3-Mediated Pathways in Human Ovarian Cancer Cells. *Int J Mol Sci,* 21**,** 7530.

[2] Connolly, N. M. C., Theurey, P., Adam-Vizi, V., Bazan, N. G., Bernardi, P., Bolaños, J. P., Culmsee, C., Dawson, V. L., Deshmukh, M., Duchen, M. R., Düssmann, H., Fiskum, G., Galindo, M. F., Hardingham, G. E., Hardwick, J. M., Jekabsons, M. B., Jonas, E. A., Jordán, J., Lipton, S. A., Manfredi, G., Mattson, M. P., Mclaughlin, B., Methner, A., Murphy, A. N., Murphy, M. P., Nicholls, D. G., Polster, B. M., Pozzan, T., Rizzuto, R., Satrústegui, J., Slack, Ruth S., Swanson, R. A., Swerdlow, R. H., Will, Y., Ying, Z., Joselin, A., Gioran, A., Moreira Pinho, C., Watters, O., Salvucci, M., Llorente-Folch, I., Park, D. S., Bano, D., Ankarcrona, M., Pizzo, P. & Prehn, J. H. M. 2018. Guidelines on experimental methods to assess mitochondrial dysfunction in cellular models of neurodegenerative diseases. *Cell Death Differ,* 25**,** 542-572.

[3] Muller, B., Lewis, N., Adeniyi, T., Leese, H. J., Brison, D. R. & Sturmey, R. G. 2019. Application of extracellular flux analysis for determining mitochondrial function in mammalian oocytes and early embryos. *Sci Rep,* 9**,** 16778.

[4] Dasari, S. & Tchounwou, P. B. 2014. Cisplatin in cancer therapy: molecular mechanisms of action. *Eur J Pharmacol,* 740**,** 364-378.

[5] Sazonova, E. V., Kopeina, G. S., Imyanitov, E. N. & Zhivotovsky, B. 2021. Platinum drugs and taxanes: can we overcome resistance? *Cell Death Discov,* 7.

[6] Oun, R., Moussa, Y. E. & Wheate, N. J. 2018. The side effects of platinum-based chemotherapy drugs: a review for chemists. *Dalton Trans,* 47**,** 6645-6653.

[7] Chinen, A. B., Guan, C. M., Ferrer, J. R., Barnaby, S. N., Merkel, T. J. & Mirkin, C. A. 2015. Nanoparticle Probes for the Detection of Cancer Biomarkers, Cells, and Tissues by Fluorescence. *Chem Rev,* 115**,** 10530-10574.

[8] Bhawal, R., Oberg, A. L., Zhang, S. & Kohli, M. 2020. Challenges and Opportunities in Clinical Applications of Blood-Based Proteomics in Cancer. *Cancers,* 12**,** 2428.

[9] Zubair, M., Wang, S. & Ali, N. 2021. Advanced Approaches to Breast Cancer Classification and Diagnosis. *Front Pharmacol,* 11**,** 2487.

[10] Tang, Y., Qiao, G., Xu, E., Xuan, Y., Liao, M. & Yin, G. 2017. Biomarkers for early diagnosis, prognosis, prediction, and recurrence monitoring of non-small cell lung cancer. *OncoTargets Ther,* 10**,** 4527-4534.

6. General Experimental

6.1 Synthesis of AuNP25

Synthesis of AuNPs was performed using an adapted protocol, which is based on an improved method by Turkevich et al.[2, 3] and a previously published protocol by Ziegler et al.[4]. Prior to the synthesis, all glassware were washed with freshly made Aqua Regia (HCl:HNO_3, 3:1), then with deionised H_2O and dried in an oven at 80ºC overnight. Initially, 13 nm AuNPs were synthesized, which were then grown into 25 nm AuNPs. For the synthesis of the 13 nm AuNPs, a solution of trisodium citrate dihydrate (60.6 mg, 0.21 mmol), citric acid (13.3 mg, 0.07 mmol) and ethylenediaminetetraacetic acid (EDTA) (1 mg, 0.003 mmol) was prepared in 100 ml of filtered miliQ H_2O and it was brought to reflux while vigorously stirring for 15 minutes at 150°C. After refluxing, a gold chloride trihydrate solution ($HAuCl_4 \cdot 3H_2O$ – 49% by assay) (8 mg, 0.02 mmol) prepared in 25 ml of miliQ H_2O was rapidly added and refluxed for another 15 minutes. Then, the heat was turned off to allow the solution to cool to room temperature, forming 2.3 nM AuNP13. UV-Vis (H_2O) λ_{max} = 518 nm (SPR). Diameter = 13 ± 3 nm (DLS number distribution). Diameter = 19 ± 5 nm (DLS intensity distribution). Zeta potential = - 41 ± 10 mV (1 nM in miliQ H_2O).

For the synthesis of AuNP25, three stock solutions were prepared, each in 50 ml of filtered miliQ H_2O: 2.5 mM $HAuCl_4 \cdot 3H_2O$ (49% by assay), 57.7 mM ascorbic acid and 34.4 mM trisodium citrate dihydrate. Then, 34 ml of 2.3 nM AuNP13 were diluted to 40 ml using filtered miliQ H_2O and stirred vigorously. From the three stock solutions, two fresh diluted solutions were prepared, a solution of 0.5 mM $HAuCl_4 \cdot 3H_2O$ and a solution of 2.9 mM ascorbic acid with 0.9 mM trisodium citrate dihydrate, each in 20 ml of filtered miliQ H_2O. The two solutions were then added simultaneously to the diluted AuNP13 solution via a peristaltic pump (over approximately 20 minutes). The resultant solution was then refluxed for 30 minutes at 150°C, forming a solution of 0.65 nM AuNP25 (Appendix D-1). UV-Vis (H_2O) λ_{max} = 519 nm (SPR). Diameter = 24 ± 6 nm (DLS number distribution). Diameter = 34 ± 9 nm (DLS intensity distribution). Zeta potential = - 25 ± 8 mV (1 nM in miliQ H_2O).

6.2 Photophysical Characterization

UV-Vis spectroscopy was carried out on Cary 5000 spectrometer using a 1 cm path length quartz cuvette. UV-Vis spectra were collected at room temperature. Samples were run at a 300 nm min^{-1} acquisition rate.

Both the emission and excitation spectra were recorded using Edinburgh Instruments FLS920 spectrometer with a 450 W Xenon lamp used as the illumination source. The detection system used incorporated an R928 visible Hamamatsu photomultiplier tube (PMT). The emission monochromator was fitted with a grating blazed at 500 nm. The data were recorded using the F900 spectrometer analysis software. Measurements were performed using 1 cm path quartz cuvettes with four transparent sides. Appropriate long-pass filters were employed upon recording in order to eliminate scattering. The excitation and emission spectra recorded were corrected for lamp instrument response and PMT response, respectively.

Luminescence lifetime measurements were carried out on Edinburgh Instruments using an EPL – 376 nm laser as the excitation source. Lifetimes were fitted using the Edinburgh Instruments F900 FAST software, with an error of ± 10%. Luminescence lifetime measurements were performed using a 1 cm path length quartz cuvette with four transparent sides and appropriate long-pass filters to reduce scattering.

6.3 Dynamic Light Scattering (DLS) and Zeta Potential measurements

Dynamic light scattering (DLS) size and Zeta potential measurements were performed using a Zetasizer nano ZSP, manufactured by Malvern. DLS size analysis measurements were recorded using a 1 cm disposable cuvette and zeta potential measurements were recorded using a folded capillary cell. The measurements were recorded using a standard operating procedure (SOP) with the following settings; Refractive index: 1.33, Absorption: 1.00, Dispersant: Water, Temperature: 25 ºC, Cell: DTS0012 disposable cuvette (Size measurements) and DTS1060 folded capillary cell (Zeta potential measurements).

Prior to recording the measurements, the instrument was left to equilibrate at 25 ºC for 120 seconds. For DLS size, 5 measurements were recorded with 15 runs in each measurement. For zeta potential, 10 measurements were recorded with 100 runs in each measurement. Both for DLS size and zeta potential measurements the average was presented.

6.4 Circular Diachroism (CD) Spectroscopy

Circular dichroism (CD) spectroscopy was performed on a Jasco J-810 spectropolarimeter using a 1 cm path length quartz cuvette. CD spectra were recorded at an internal temperature of 22˚C. A stock solution of 0.1 µM BSA (Sigma-Aldrich) was prepared in miliQ H_2O. Solutions of iridium complexes were prepared at 100 µM in miliQ H_2O. Solutions of the IrS1 and IrC_{12} coated nanoparticles were prepared in miliQ H_2O at 2 and 4 nM, respectively. The parameters of the instrument were set to: time constant – 0.5 s, scan speed – 100 nm/mn, bandwidth – 1 nm, device sensitivity – standard (100 mdeg). The CD spectra for the interaction of BSA with iridium complexes were recorded from 185 to 500 nm and for the interaction of BSA with the iridium coated nanoparticles from 185 to 700 nm. The scans were repeated three times for each spectrum.

6.5 Preparation of nanoparticle samples for TEM

TEM was used to characterize the size of both citrate and functionalized nanoparticles. For each nanoparticle sample 10 µl (AuNP25 samples: 2 nM, AuNP100 samples: 50 pM) were added to a 200-mesh formvar-coated copper TEM grid and left to dry overnight. Transmission electron miscroscopy was performed in the Department of Materials and Metallurgy and the images were acquired on Jeol 1400 Ex Bio TEM.

6.6 Cell Culture conditions

6.6.1 HeLa and HEK293 cell lines

HeLa (Catalogue number: 93021013), Human cervical cancer cell line and HEK293 (Catalogue number: 85120602), Human Embryonic Kidney 293 cell line, were cultured using DMEM media (Gibco®-Thermo Fisher Scientific) that was supplemented with 10% Fetal Bovine Serum (FBS) (Gibco®-Thermo Fisher Scientific) and 1% Penicillin Streptomycin (Pen Strep) (Gibco®-Thermo Fisher Scientific). The cells were grown as a monolayer culture in vented cap T75 flasks and were kept at all times at 37°C in a humidified atmosphere (5% CO_2).

6.6.2 Karpas 422 and SU-DHL-4 cell lines

Karpas 422 (Catalog number: HTL99023), B-cell non-Hodgkin's lymphoma cell line and SU-DHL-4 (Catalog number: CRL-2957), Diffuse large B-cell lymphoma cell line, were cultured using RPMI1640 media (Gibco®-Thermo Fisher Scientific) supplemented with 10% FBS (Gibco®-Thermo Fisher Scientific) and 1% Penicillin Streptomycin (Pen Strep) (Gibco®-Thermo Fisher Scientific). The cell lines were cultured in suspension in vented T75 flasks and were kept at all times at 37°C in a humidified atmosphere (5% CO2).

6.7 References

[1] Rajina, S., Kim, W. J., Shim, J. H., Chun, K. S., Joo, S. H., Shin, H. K., Lee, S. Y. & Choi, J. S. Isolinderalactone Induces Cell Death via Mitochondrial Superoxide- and STAT3-Mediated Pathways in Human Ovarian Cancer Cells. *Int J Mol Sci,* 21**,** 7530.

[2] Turkevich, J., Stevenson, P. C. & Hillier, J. 1951. A Study of the Nucleation and Growth Processes in the Synthesis of Colloidal Gold. *Discuss Faraday Soc,* 11**,** 55-75.

[3] Schulz, F., Homolka, T., Bastus, N. G., Puntes, V., Weller, H. & Vossmeyer, T. 2014. Little adjustments significantly improve the Turkevich synthesis of gold nanoparticles. *Langmuir,* 30**,** 10779-10784.

[4] Ziegler, C. & Eychmuller, A. 2011. Seeded Growth Synthesis of Uniform Gold Nanoparticles with Diameters of 15-300 nm. *J Phys Chem C,* 115**,** 4502-4506.

Appendix A

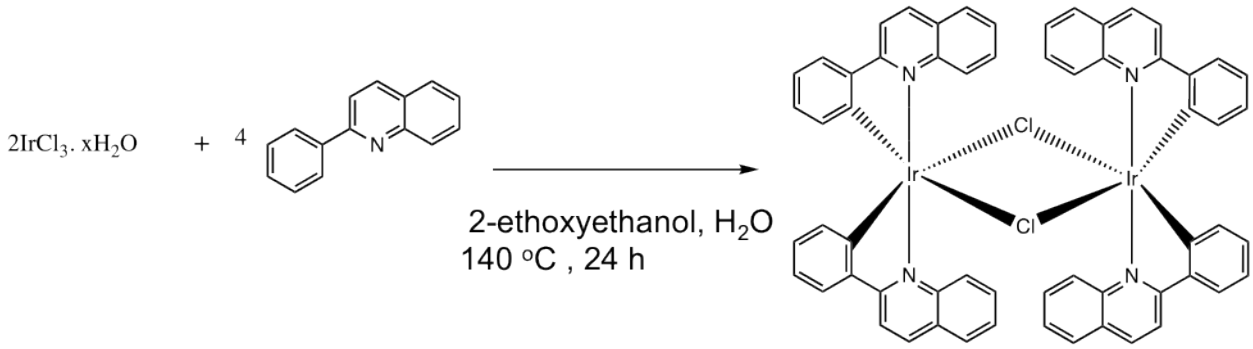
Synthesis of Ir1 and IrS1

Starting materials were purchased from Fisher Scientific, Alfa Aesar and Sigma Aldrich/Merck.

The synthesis and characterization of Ir1 and IrS1 were carried out by Tasha Chauhan and Sarah Akponasa (School of Chemistry, University of Birmingham).

Synthesis of $[Ir(pq)_2Cl]_2$ dimer

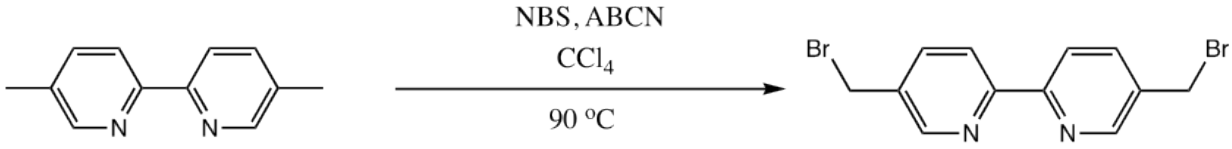
Synthesis was performed using a modified published protocol by Chen et al.[1]. $IrCl_3 \bullet xH_2O$ (0.39 g, 1.0 mmol) and 2-phenylquinoline (0.51 g, 2.5 mmol) were dissolved together in 2-ethoxyethanol (30 mL) and water (10 mL) and brought to reflux at 140 ^oC for 24 hours with continuous stirring. A colour change from dark brown to red-brown was observed. The mixture was cooled to room temperature and the precipitate was washed with MeOH (60 mL) and acetone (60 mL). The solvent was removed from the filtrates *in vacuo* and the dark-orange solid was dissolved in DCM (80 mL), washed with HCl (0.1 M, 3 x 20 mL) and dried using Mg_2SO_4. The solvent was removed and the solid was dissolved in a minimal volume of DCM. Then, hexane was added to induce precipitation and the solvents were removed *in vacuo* to yield the final dark orange solid. (410 mg, 0.3 mmol, 50%). λ_{max} (MeCN)/nm (ε/$dm^3mol^{-1}cm^{-1}$), 259 (110100), 279 (68600), 323 (32900), 337 (30000) and 418 (6 100); δH (400 MHz; CD_2Cl_2) 7.50 – 7.59 (6 H, m, H-h,m,l), 7.63 (2 H, t, *J* = 7.5, H-d), 7.80 (2H, t, *J* = 7.7, H-c), 7.93 (2 H, d, *J* = 8.1, H-n), 7.97 (2 H, d, *J* = 8.6, H-k), 8.23 (2 H, d, *J* = 7.5, H-e), 8.23 (2 H, d, *J* = 7.7, H-b), 8.41 (2 H, d, *J* = 8.8, H-g); MS $(ES)^+$ *m/z*: 1238 $(M\text{-}Cl)^+$.



Scheme A-1. Schematic of the synthesis of $[Ir(pq)_2Cl]_2$.

Synthesis of 5,5'-Bis(bromomethyl)-2,2'-bipyridine

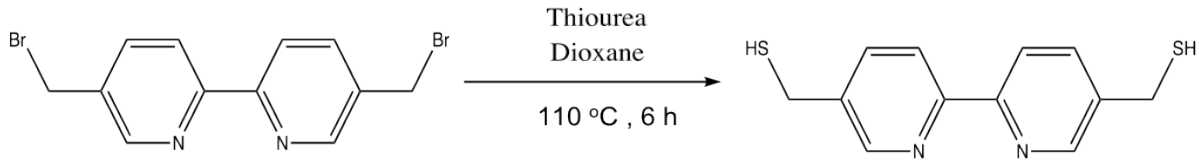
The synthesis of 5,5'-Bis(bromomethyl)-2,2'-bipyridine was performed using a published protocol by Bertoncello et al.[2]. A solution of 5,5'-dimethyl-2-2'-bipyridine (0.57 g, 3.09 mmol), 1,1'-azobis(cyclohexanecarbonitrile) (ABCN) (0.08 g, 0.29 mmol) and N-bromosuccinimide (NBS) (2.90 g, 16.3 mmol) were stirred together in dry CCl_4 (50 mL) and brought to reflux at 90 ^oC, while monitoring using TLC (silica gel, DCM:MeOH, 1:1). A colour change from cloudy white to cloudy yellow was observed. The solution was then hot filtered and the solvent was removed *in vacuo.* The solid was dissolved in DCM (100 mL) and washed with a solution of $Na_2S_2O_3$ (23.72 g, 0.5 M, 2 x 150 mL). The aqueous phase was then washed with DCM (5 x 50 mL). The solvent from the combined DCM phases was removed *in vacuo* to yield a pale yellow solid (1.9 g). The solid was recrystallized from hot DCM, yielding a white solid powder (219.12 mg, 0.6 mmol, 21%). δH (300 MHz; $CDCl_3$) 4.54 (4 H, s, H-7), 7.86 (2 H, dd, J = 8.2, 2.4, H-4), 8.40 (2 H, dd, J = 8.2, 0.8, H-3), 8.68 (2 H, dd, J = 2.4, 0.8, H-6); δC (101 MHz; $CDCl_3$) 29.7 (C-7), 121.3 (C-3), 134.0 (C-5), 137.8 (C-4), 149.5 (C-6), 155.6 (C-2); MS $(ASAP)^+$ *m/z*: 343 $(M+H)^+$.



Scheme A-2. Schematic of the synthesis of 5,5'-Bis(bromomethyl)-2,2'-bipyridine.

Synthesis of 5,5′-Bis(mercaptomethyl)-2,2′-bipyridine

5,5′-Bis(mercaptomethyl)-2,2′-bipyridine was synthesized using a modified protocol by Bertoncello et al.[2]. 5,5'-Bis(bromomethyl)-2,2'-bipyridine (105.7 mg, 0.3 mmol) and thiourea (65 mg, 0.9 mmol) were stirred together in dry dioxane (30 mL) and brought to reflux at 110 °C for 3 hours. A colour change was observed from cloudy white to cloudy yellow. NaOH (40 mg, 1 mmol) in degassed water (5 mL) was added and the mixture was refluxed for a further 3 hours. A colour change was observed from pale yellow to clear yellow. The solvent was removed *in vacuo*, producing a pale yellow solid. Degassed acidified water (30 mL, pH ~ 4, HCl) was then added and the aqueous phase was extracted using DCM (5 x 20 mL). The combined DCM phases were extracted and the solvent was removed *in vacuo* to yield the final yellow solid (51.4 mg, 0.2 mmol, 67%). δH (300 MHz; $CDCl_3$) 3.81 (4 H, s, H-7), 7.80 (2 H, dd, J = 8.2, 2.4, H-4), 8.35 (2 H, d, J = 8.2, H-3), 8.61 (2 H, d, J = 2.4, H-6); MS $(ASAP)^+$ *m/z*: 249 $(M+H)^+$.



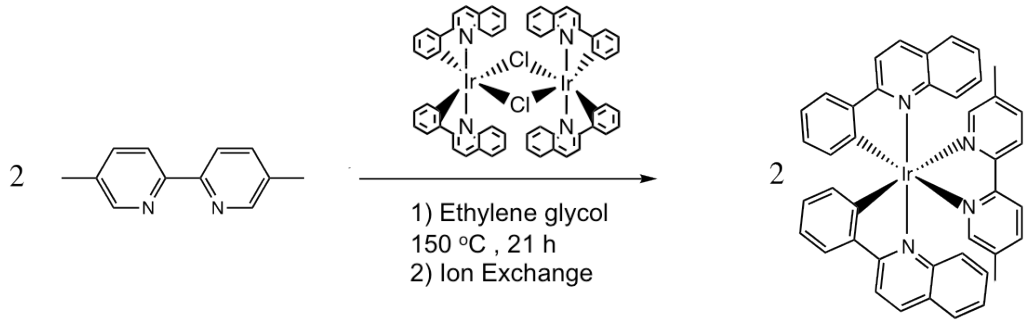
Scheme A-3. Schematic of the synthesis of 5,5′-Bis(mercaptomethyl)-2,2′-bipyridine.

Synthesis of $[Ir(2\text{-}pq)_2bpy]PF_6$

Synthesis was performed using a modified method by Slinker et al.[3]. Initially, $[Ir(2\text{-}pq)_2Cl]_2$ (66.4 mg, 0.05 mmol) and 5,5'-dimethyl-2-2'-bipyridine (25 mg, 0.14 mmol) were stirred together in ethylene glycol (6.5 mL) and brought to reflux at 150 ^oC for 21 hours. H_2O (20 mL) and concentrated NH_4PF_6 in MeOH were then added until the orange precipitate stopped forming. The mixture was then cooled (0 – 5 ^oC), filtered and washed with H_2O. Purification was performed by column chromatography (aluminium oxide, DCM/MeOH, 99:1) to yield the final orange solid (30.6 mg, 0.033 mmol, 32%). λ_{max} (MeOH)/nm (ε/$dm^3mol^{-1}cm^{-1}$) 260 (11600), 280 (10800), 313 (6500), 334 (5500) and 438 (1100); ν_{max}/cm^{-1} 833 (PF_6 asymmetric stretch), 564 (symmetric stretch); δH (400 MHz; Acetone) 2.26 (3 H, s, C***H*****$_3$**), 6.57 (1 H, ddd, *J* = 7.7, 1.2, 0.5, H-n), 6.83 (1 H, ddd, *J* = 7.7, 7.2, 1.3, H-m), 7.08 – 7.21 (2 H, m, H-b,l), 7.40 – 7.49 (2 H, m, H-c,e), 7.85 – 7.95 (2 H, m, H-4,d), 8.10 (1 H, dd, *J* = 2.1, 0.7, H-6), 8.19 – 8.28 (2 H, m, H-3,k), 8.48 – 8.56 (2 H, m, H-g,h); MS $(ES)^+$ *m/z*: 785 $(M\text{-}PF6)^+$.

Ion Exchange of $[Ir(2\text{-}pq)_2bpy]PF_6$ to form $[Ir(2\text{-}pq)_2bpy]Cl$ (Ir1)

Ion exchange of $[Ir(2\text{-}pq)_2bpy]PF_6^+$ to $[Ir(2\text{-}pq)2bpy]Cl^-$ (Ir1) was performed to produce a stock solution of Ir1 of ~1 mM concentration in MeOH. Two spatulas of Dowex (1 x 8 200-400 mesh) were added in deionised H_2O (30 mL) and the pH was lowered to 1 using HCl (10%). The suspension was then stirred for 1 hour. The Dowex was filtered in vaccum and washed with deionised water (~ 30 mL). The Dowex was then re-suspended in MeOH (30 mL) and left to stir for about 1 hour. A solution of $[Ir(2\text{-}pq)_2bpy]PF_6$ (5 mg in 5 mL of MeOH) was then added and the mixture was stirred for a further 2 hours. The Dowex was then filtered, and the resin was washed with MeOH. The solution was dried to yield the final yellow solid.



Scheme A-4. Schematic of the synthesis of [Ir(2-pq)$_2$bpy]Cl (Ir1).

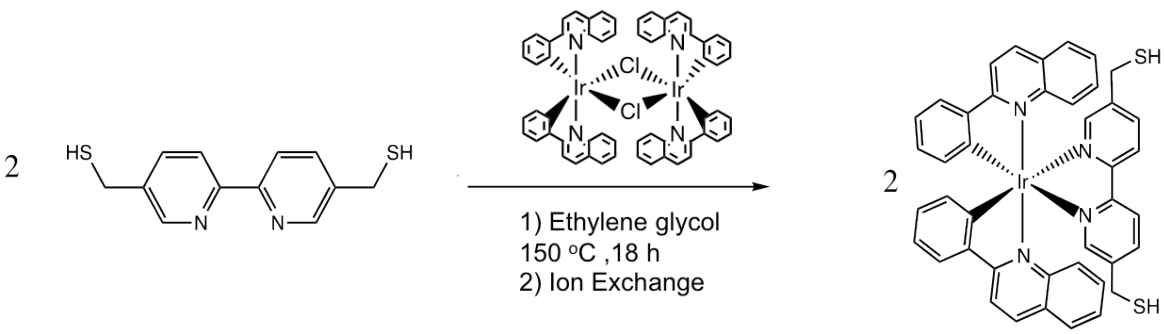
.

Synthesis of [Ir(2-pq)$_2$bpySH]PF$_6$

Synthesis was carried out using a modified method by Slinker et al.[3] [Ir(2-pq)$_2$Cl]$_2$ (92.15 mg, 0.07 mmol) and 5,5′-Bis(mercaptomethyl)-2,2′-bipyridine (51.4 mg, 0.21 mmol) were stirred in ethylene glycol (6.5 mL) and brought to reflux at 150 °C for 18 hours. Then, H_2O (20 mL) and concentrated NH_4PF_6 in MeOH were added until the orange precipitate stopped forming. The mixture was then cooled (0 – 5 °C), filtered and washed with H_2O. The final orange-yellow product was washed with chloroform and dried. (32.81 mg, 0.03 mmol, 23%). λ_{max} (MeOH)/nm (ε/dm^{3}mol^{-1}cm^{-1}), 260 (18800), 315 (11000), and 435 (1800); λ_{max} (H_2O)/nm (ε/dm^{3}mol^{-1}cm^{-1}), 260 (14800), 315 (8300), and 435 (1400); ν_{max}/cm^{-1} 828 (PF_6 asymmetric stretch), 559 (symmetric stretch); δH (400 MHz; Acetone) 2.29 (1 H, t, *J* = 8.4, S***H***), 3.75 (2 H, qd, *J* = 14.4, 8.5, **CH$_2$**), 6.56 (1 H, d, *J* = 7.8, H-n), 6.81 (1 H, ddd, *J* = 7.5, 7.4, 1.3, H-m), 7.09 (1 H, ddd, *J* = 8.7, 6.9, 1.6, H-c), 7.17 (1 H, ddd, *J* = 7.5, 6.9, 1.2, H-l), 7.36 – 7.49 (2 H, m, H-b,d), 7.87 (1 H, dd, *J* = 8.0, 1.4 , H-e), 8.00 (1 H, d, *J* = 2.1, H-4), 8.20 – 8.26 (2 H, m, H-k,3), 8.36 (1H, d, *J* = 2.1, H-6), 8.45 – 8.53 (2 H, m, H-h,g); MS (ES)$^+$ *m/z*: 849 (M-PF6)$^+$.

Ion Exchange of $[Ir(2\text{-}pq)_2bpySH]PF_6$ to form $[Ir(2\text{-}pq)_2bpySH]Cl$ (IrS1)

Ion exchange of $[Ir(2\text{-}pq)_2bpySH]PF6^+$ to $[Ir(2\text{-}pq)2bpySH]Cl^-$ was performed to produce a stock solution of IrS1 of ~1 mM in MeOH. Two spatulas of Dowex (1 x 8 200-400 mesh) were added in deionised H_2O (30 mL) and the pH was lowered to 1 using HCl (10%). The suspension was then stirred for 1 hour. The Dowex was filtered in vaccum and washed with deionised water (~ 30 mL). The Dowex was re-suspended in MeOH (30 mL) and stirred for about 1 hour. A solution of $[Ir(2\text{-}pq)_2bpySH]PF_6$ (5 mg in 5mL of MeOH) was added and the mixture was stirred for a further 2 hours. The Dowex was then filtered, and the resin was washed with MeOH. The solution was dried, to yield the final yellow solid.



Scheme A-5. Schematic of the synthesis of $[Ir(2\text{-}pq)_2bpySH]Cl$ (IrS1).

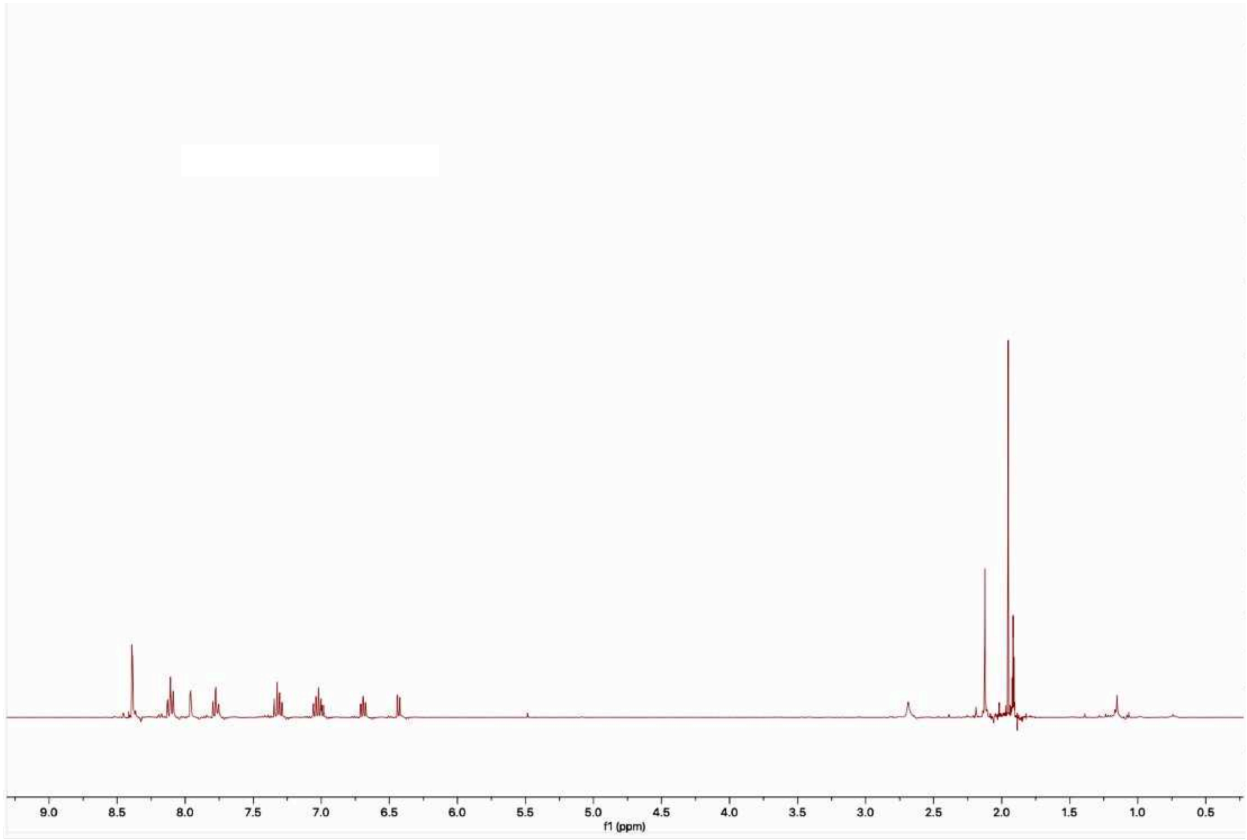


Figure A-1. ^{1}H NMR of Ir1 (acetone-d_6).

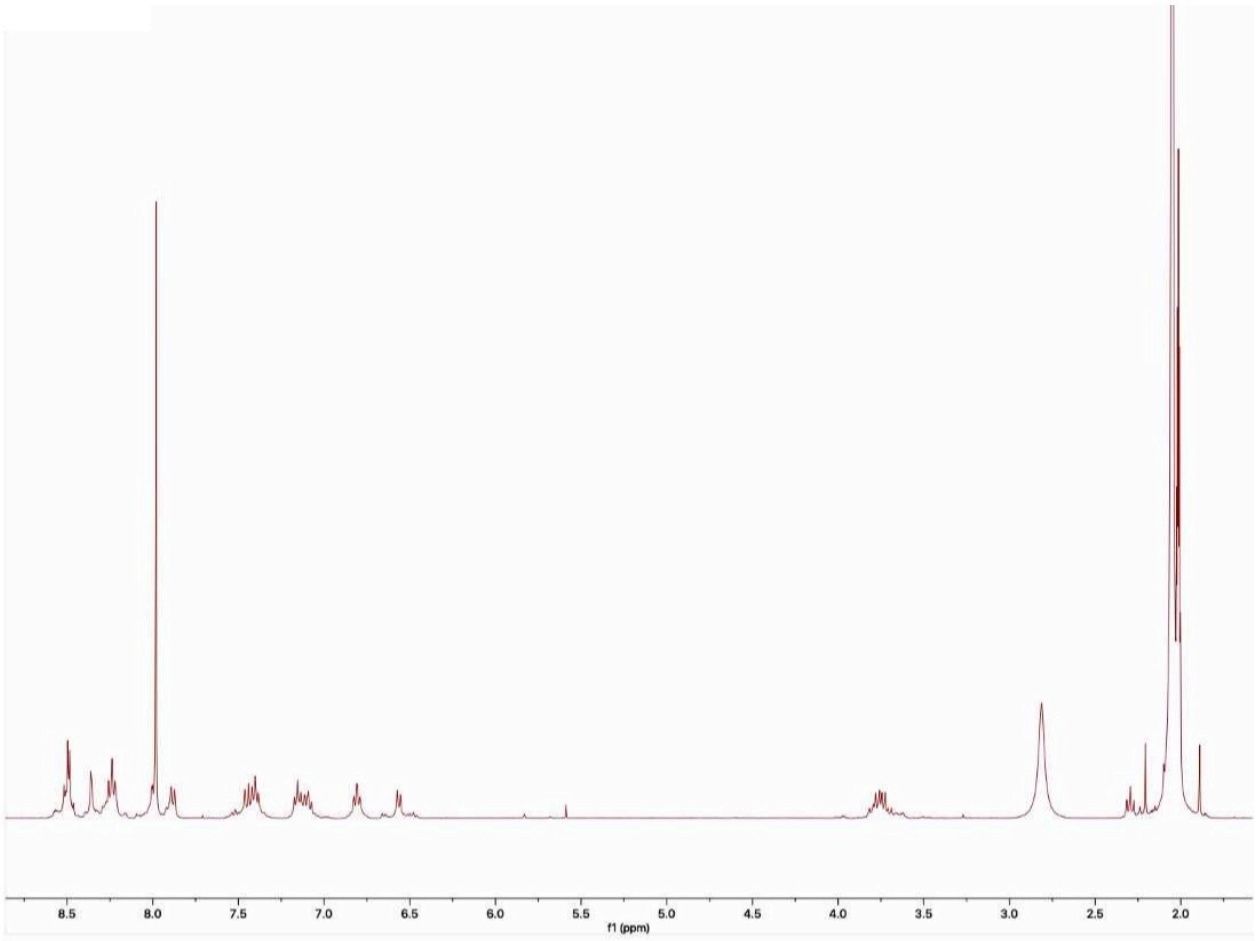


Figure A-2. ^{1}H NMR of IrS1 (acetone-d_6).

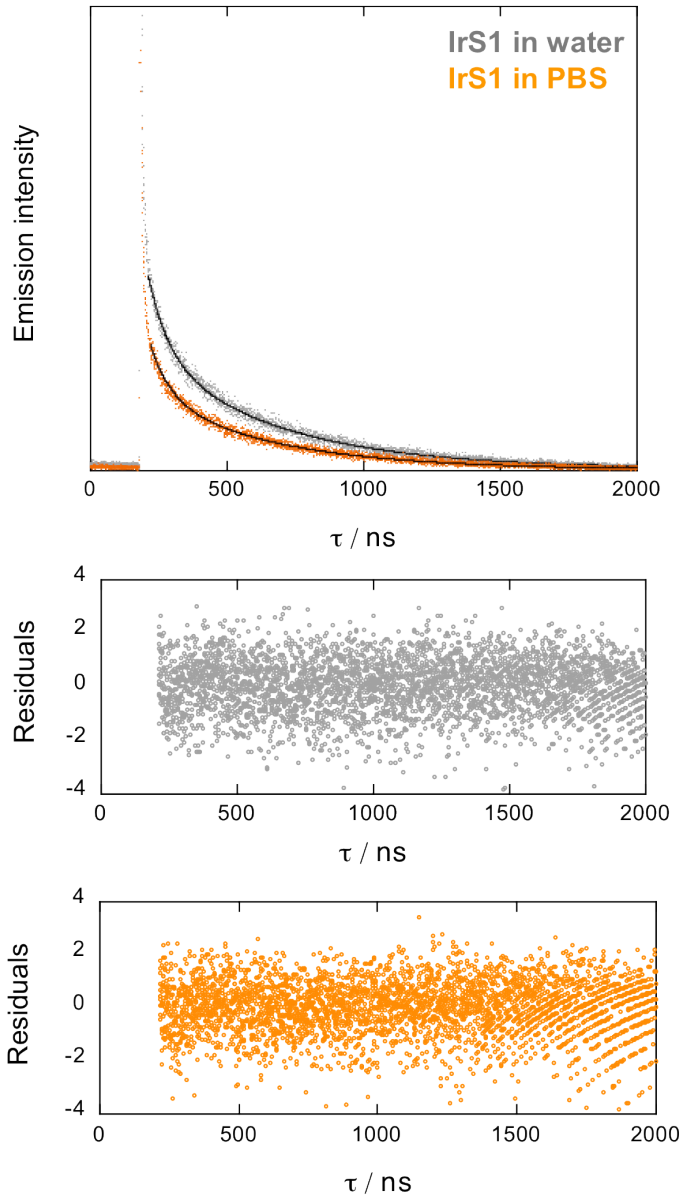


Figure A-3. Fitted luminescence lifetime decays of IrS1 in water and PBS, λ_{exc}=376 nm and λ_{det}=580 nm. Lifetimes of IrS1 in water and PBS were fitted with a χ^2 value of 1.07 and 1.09, respectively.

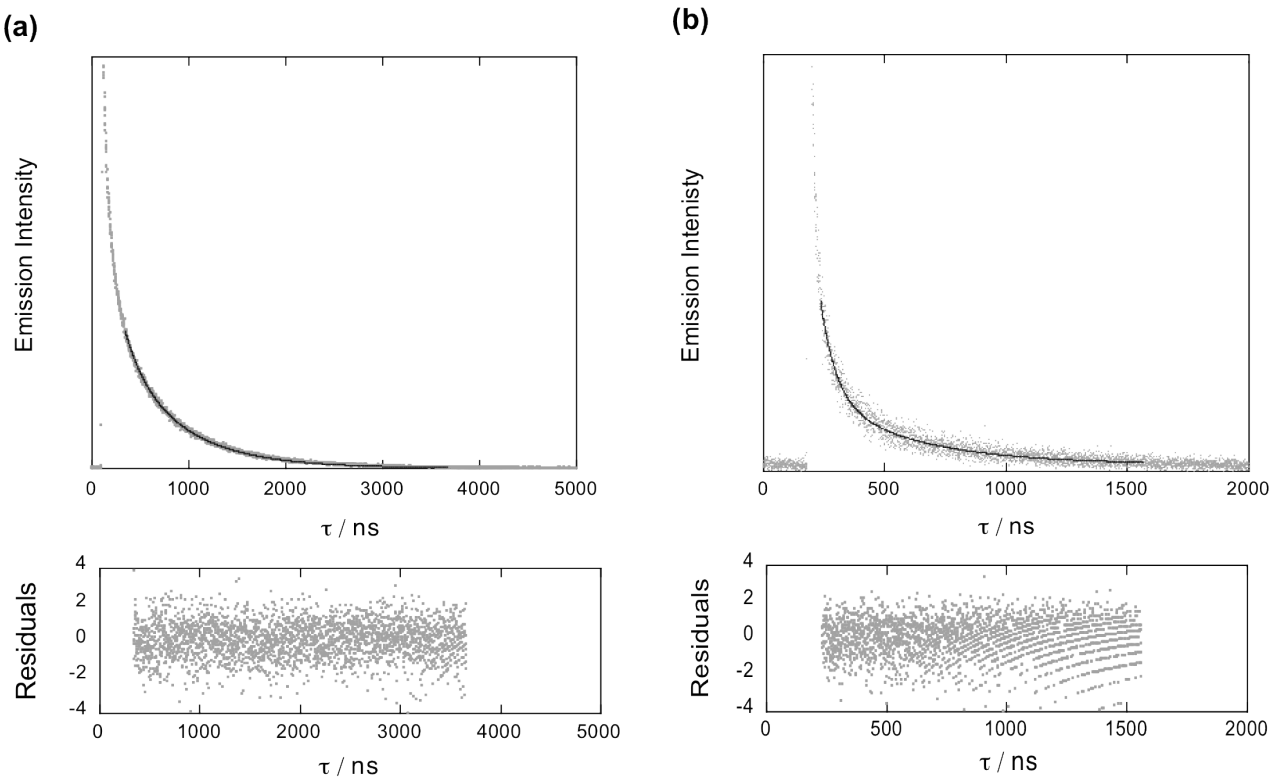


Figure A-4. (a) Fitted luminescence lifetime decay of Ir1 in water, λ_{exc}=376 nm and λ_{det}=580 nm. Lifetime was fitted with a χ^2 value of 1.04. (b) Fitted luminescence lifetime decay of IrS1·Z·AuNP25 in water, λ_{exc}=376 nm and λ_{det}=585 nm. Lifetime was fitted with a χ^2 value of 1.19.

References

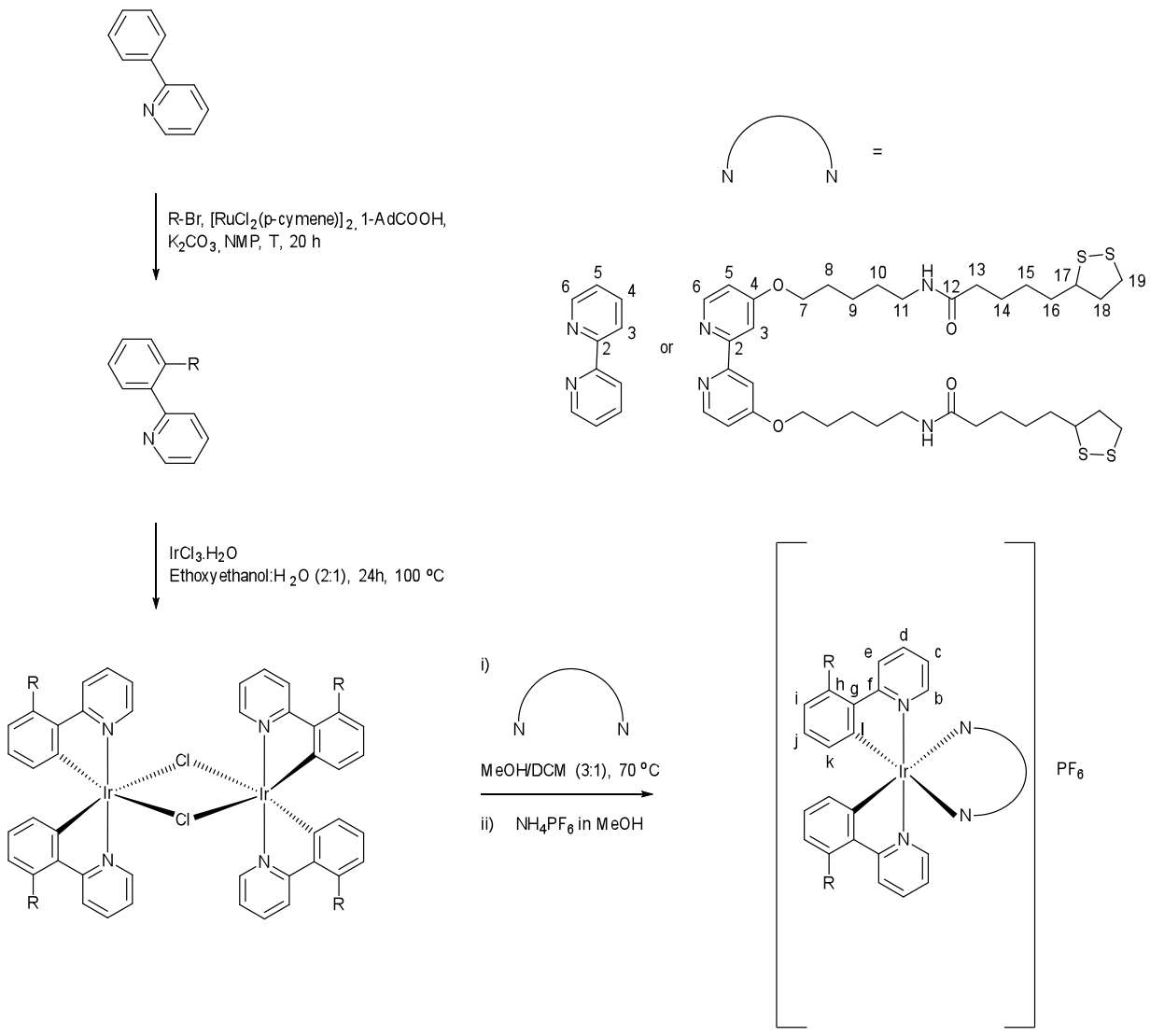
[1] Chen, Y., Qiao, L., Ji, L. & Chao, H. 2014. Phosphorescent iridium(III) complexes as multicolor probes for specific mitochondrial imaging and tracking. *Biomaterials,* 35**,** 2-13.

[2] Bertoncello, P., Kefalas, E. T., Pikramenou, Z., Unwin, P. R. & Forster, R. J. 2006. Adsorption dynamics and electrochemical and photophysical properties of thiolated ruthenium 2,2'-bipyridine monolayers. *J Phys Chem B,* 110**,** 10063-10069.

[3] Slinker, J. D., Gorodetsky, A. A., Lowry, M. S., Wang, J., Parker, S., Rohl, R., Bernhard, S. & Malliaras, G. G. 2004. Efficient yellow electroluminescence from a single layer of a cyclometalated iridium complex. *J Am Chem Soc,* 126**,** 2763-2767.

Appendix B

The synthesis and characterization of IrC_{12} and $IrC_{12}bpy$ were performed by Andrew Carrod (School of Chemistry, University of Birmingham). For the experimental work described in Chapter 3, the hexafluorophosphate salt was converted to chloride via Dowex ion exchange.



Scheme B-1. Synthetic scheme for IrC_{12} and $IrC_{12}bpy$. The final structure is the general structure for the iridium complexes, where R=dodecyl.

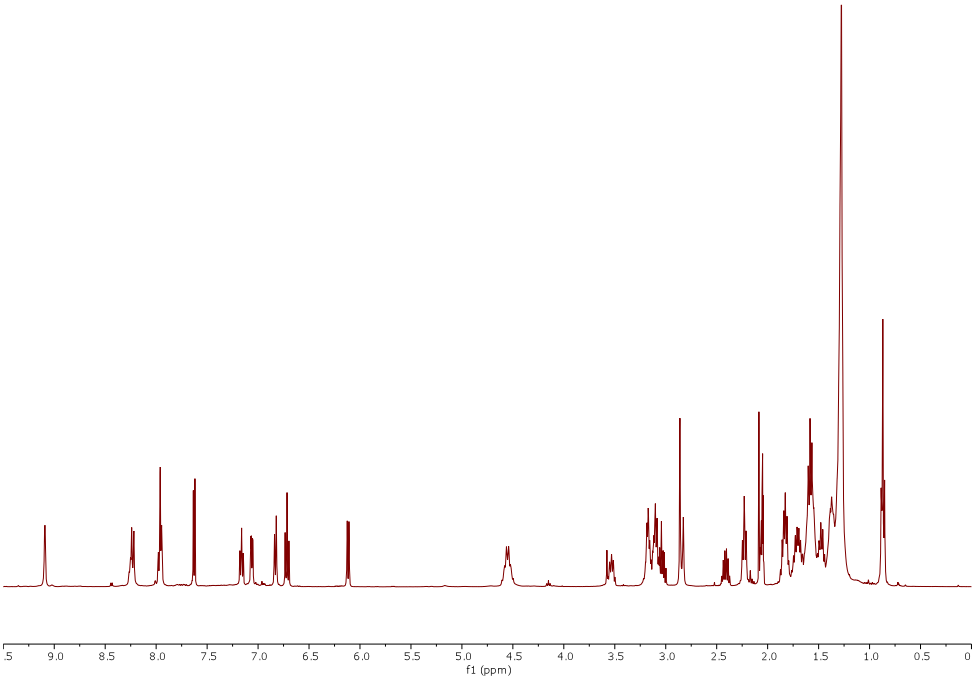


Figure B-1. ^{1}H NMR of IrC_{12} (acetone-d_6).

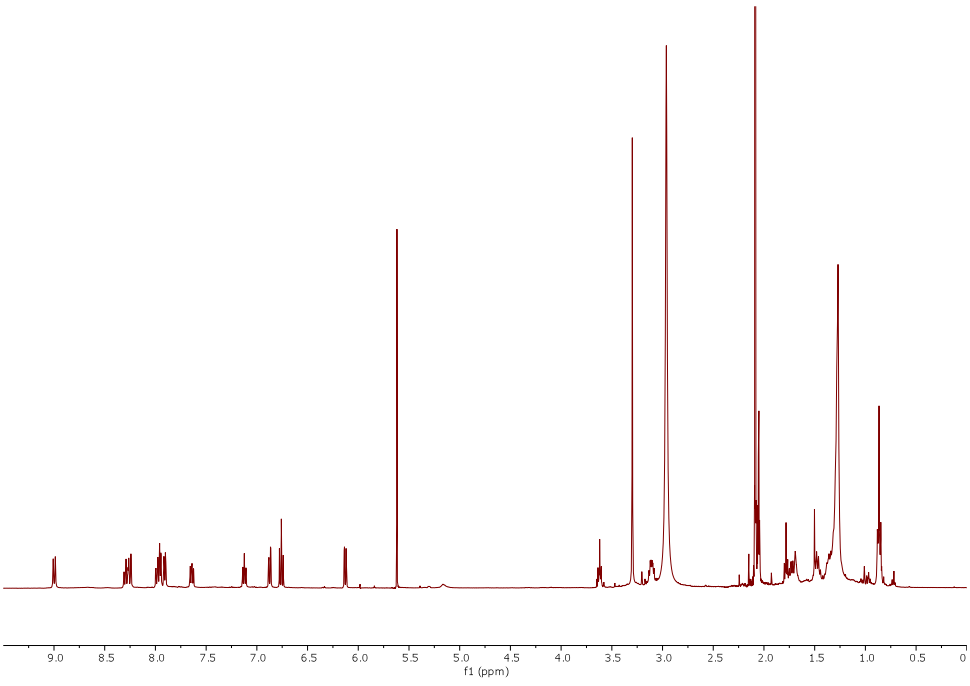


Figure B-2. ^{1}H NMR of IrC_{12}bpy in (acetone-d_6).

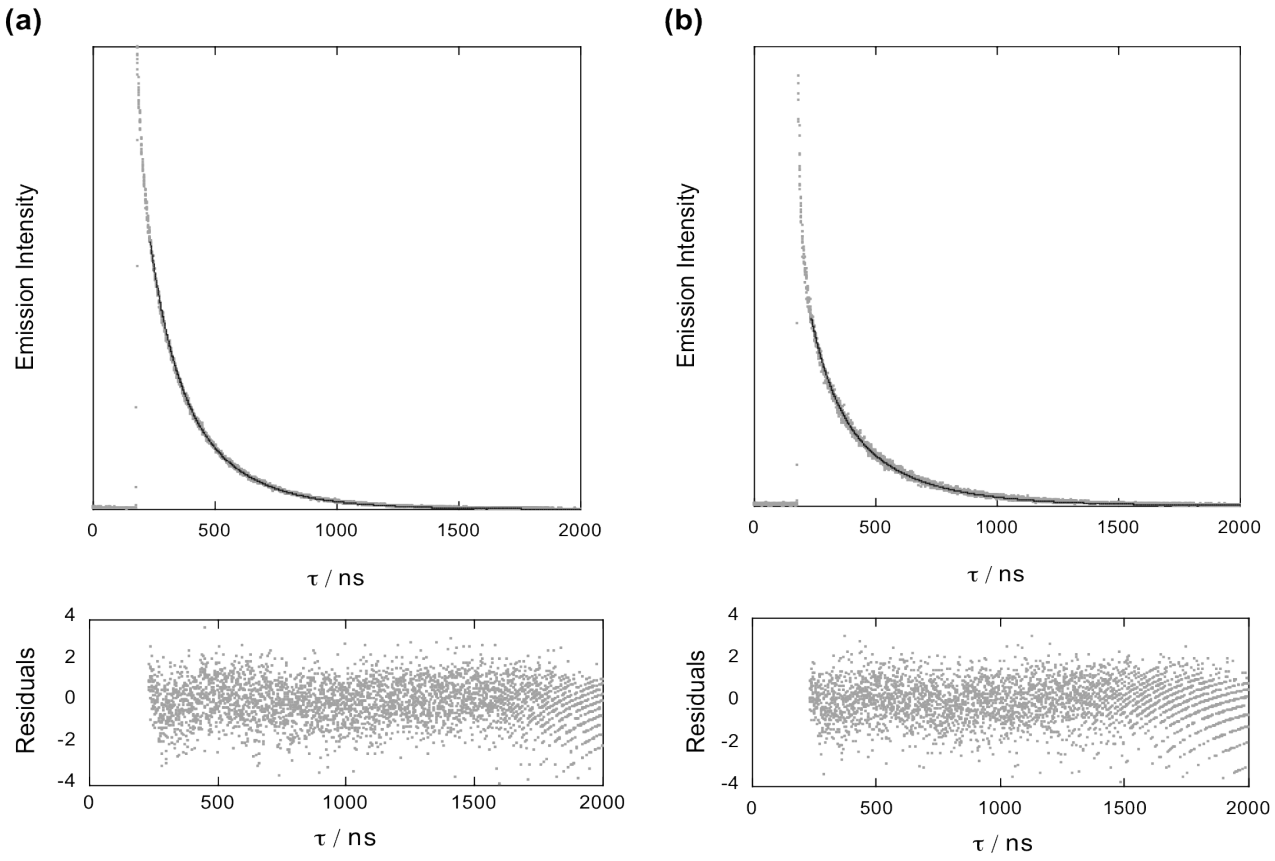


Figure B-3. (a) Fitted luminescence lifetime decay of IrC_{12} in water, λ_{exc}=376 nm and λ_{det}=585 nm. Lifetime was fitted with a χ^2 value of 1.06. (b) Fitted luminescence lifetime decay of IrC_{12}·Z·AuNP25 in water, λ_{exc}=376 nm and λ_{det}=595 nm. Lifetime was fitted with a χ^2 value of 1.04.

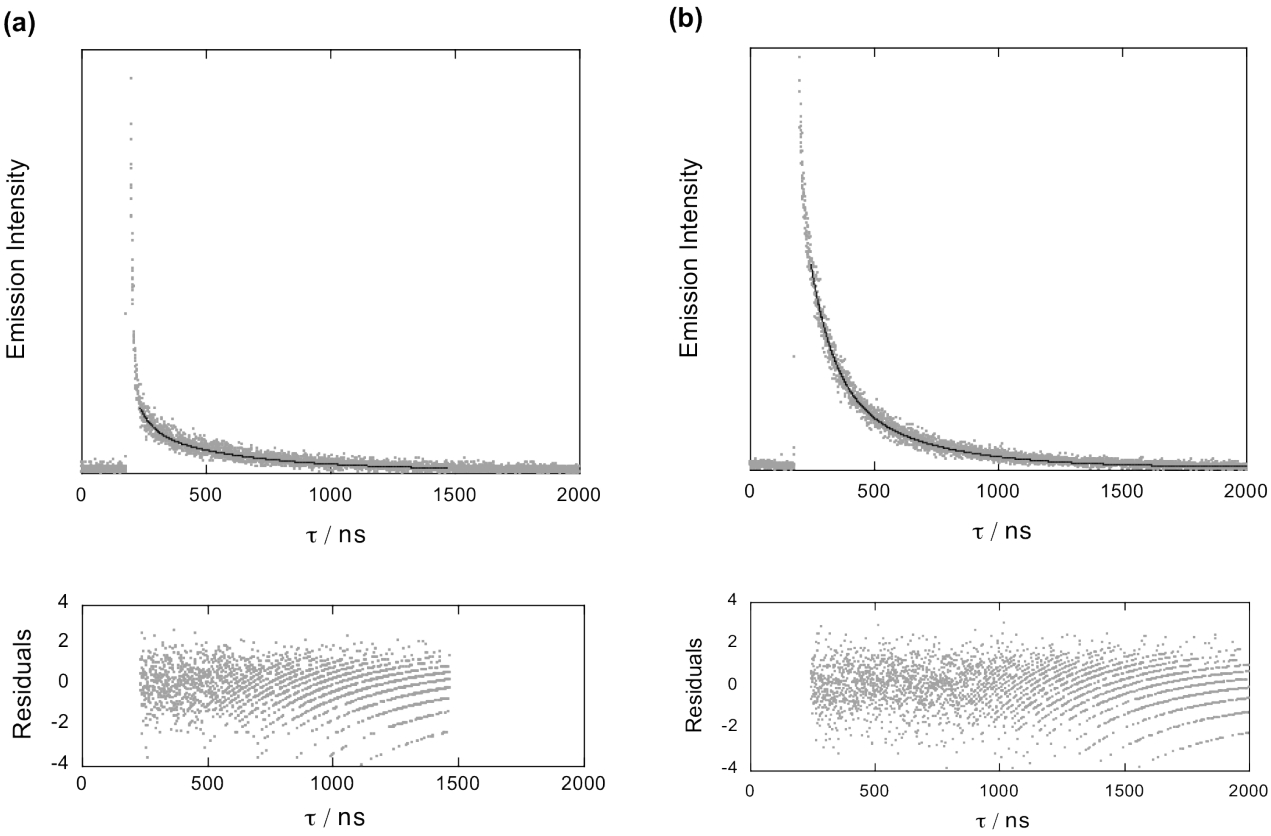
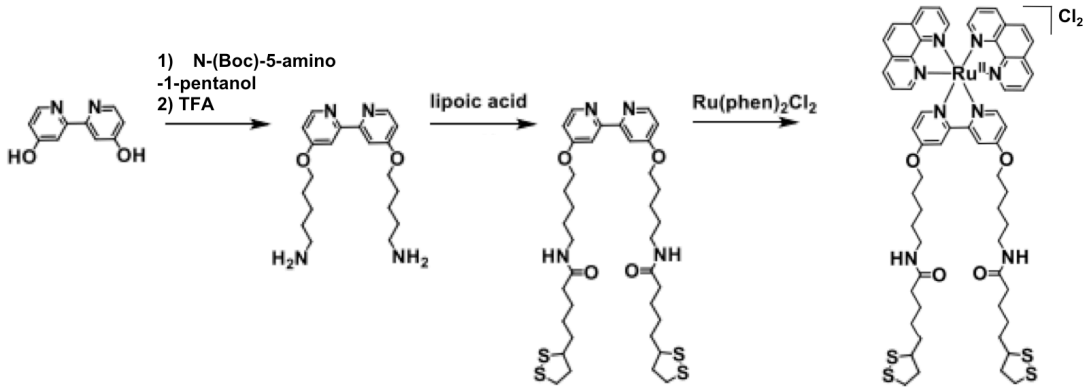


Figure B-4. (a) Fitted luminescence lifetime decay of IrC_{12} in HeLa cells, λ_{exc}=376 nm and λ_{det}=585 nm. Lifetime was fitted with a χ^2 value of 1.11. (b) Fitted luminescence lifetime decay of IrC_{12}·Z·AuNP25 in HeLa cells, λ_{exc}=376 nm and λ_{det}=595 nm. Lifetime was fitted with a χ^2 value of 1.21.

Appendix C

The synthesis and characterization of the RuphenS12 complex were performed by Dr. Shani Osborne (School of Chemistry, University of Birmingham). The synthetic scheme and ^{1}H NMR for RuphenS12 were adapted from Dr Osborne's thesis.



Scheme C-1. Schematic of the synthesis of RuphenS12.

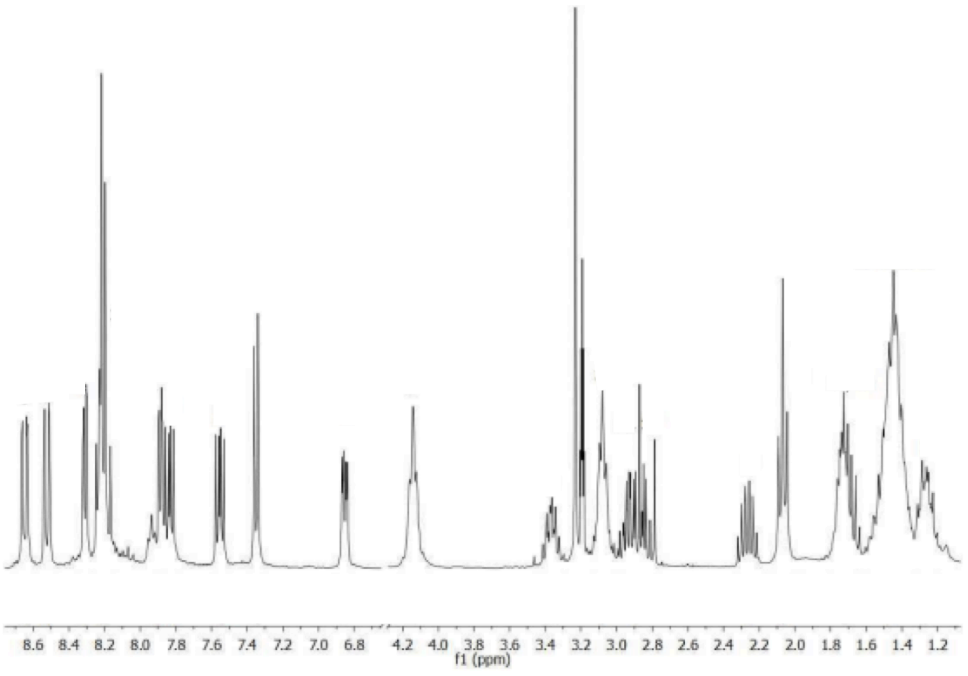


Figure C-1. ^{1}H NMR of RuphenS12 (δ_4-CD_3OD).

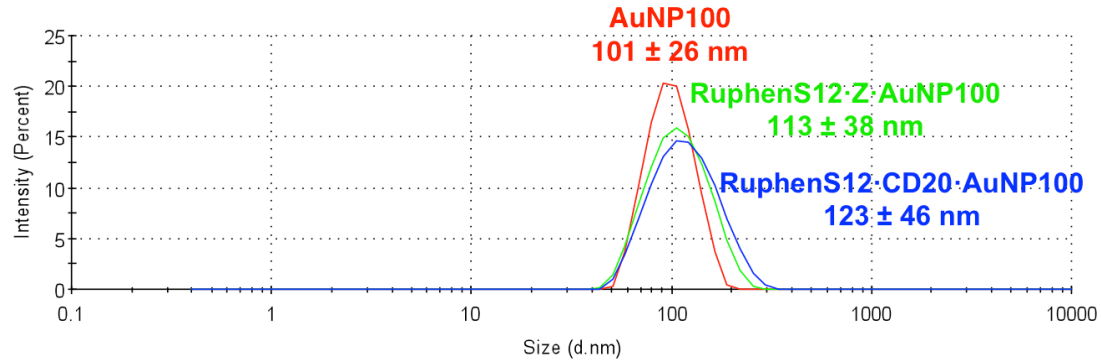


Figure C-2. DLS intensity distributions of AuNP100, RuphenS12·Z·AuNP100 and RuphenS12·CD20·AuNP100.

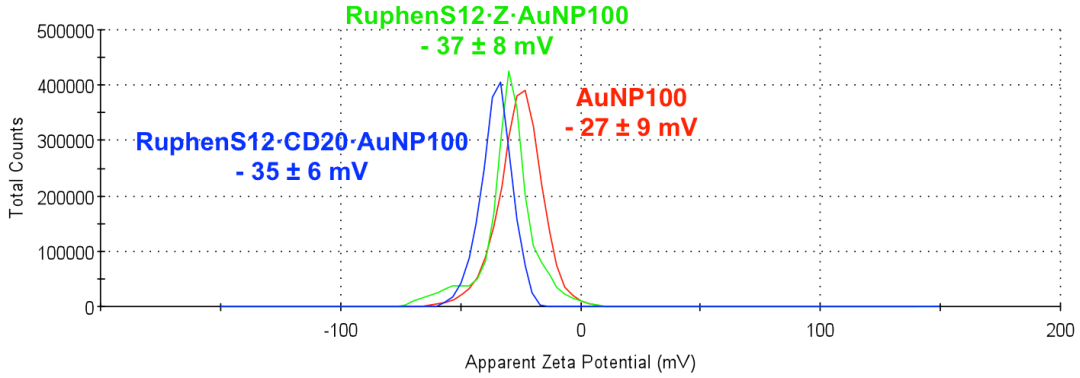


Figure C-3. DLS zeta potential distributions of AuNP100, RuphenS12·Z·AuNP100 and RuphenS12·CD20·AuNP100.

Appendix D

Calculations

D-1 Concentration of AuNP25

Formula used to calculate concentration[1]:

$$C = \frac{m_{i,Au}}{N \times V \times Mr}$$

How the formula is derived:

Assuming that AuNPs are spheres and that atoms are packed in a uniform face-centred cubic crystalline structure[2]:

Volume of a sphere (v)

$$v = \frac{4}{3}\pi R^3 = \frac{1}{6}\pi D^3$$

(D) – Diameter

(R) - Radius

Density of gold (ρ)

$$\rho = \frac{m}{v} = \frac{n \times Mr}{v}$$

(The density of gold is ρ_{gold} = 19.32 g cm^{-3} [2])

Number of moles (n)

$$n = \frac{\rho \times v}{Mr} = \frac{\rho \times \pi D^3}{6 \times Mr}$$

(The Mr of gold is 196.96657 g mol^{-1})

To convert from moles (n) to number of atoms (N) → Multiply by Avogadro's constant N_A= 6.022140857 × 10^{23} mol^{-1}

$$N = \frac{\rho \times \pi D^3}{6 \times Mr} \times N_A$$

In order to define the number of atoms per nanoparticle of size D (nm):

→ Convert the ρ_{gold} from g cm^{-3} to g nm^{-3} and then use the formula to calculate (N)

$$N = \frac{\rho \times \pi D^3}{6 \times Mr} \times N_A = \frac{19.32 \times 10^{-21} \text{g nm}^{-3} \times \pi \times D^3}{6 \times 196.96657 \text{ g mol}^{-1}} \times 6.022140857 \times 10^{23} \text{ mol}^{-1}$$

$$\therefore N = 30.89685812 \times D^3$$

For the concentration (C), the number of moles (n) of gold nanoparticles per unit volume (V) in the gold colloid is determined[1].

The total number of gold nanoparticles (N_{NP}) is defined as the number of moles (n) of gold nanoparticles multiplied by the Avogadro's constant N_A.

N_{NP}= n x N_A

Therefore, since $C = \frac{n}{V}$ then, $C = \frac{n}{V} = \frac{N_{NP}}{V \times N_A}$

The total number of gold nanoparticles (N_{NP}) can also be defined as the number of gold atoms N_{atoms} in the solution divided by the number of gold atoms per nanoparticle (N).

Thus, since $N_{NP} = \frac{N_{atoms}}{N}$ then, $C = \frac{N_{NP}}{V \times N_A} = \frac{N_{atoms}}{N \times V \times N_A}$

The total number of gold atoms in solution (N_{atoms}) can be determined using the amount of gold used in the reaction ($m_{i,Au}$) and assuming that 100% of that amount has been successfully converted into gold nanoparticles.

Number of moles of gold used in the reaction ($n_{i,Au}$) $$n_{i,Au} = \frac{m_{i,Au}}{Mr}$$

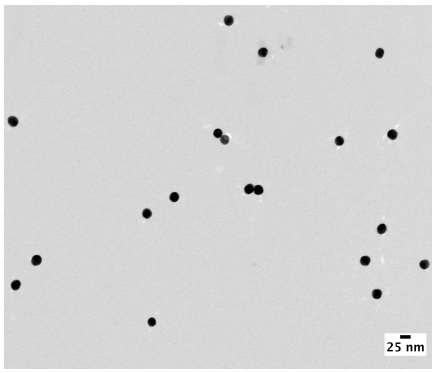
To convert from moles ($n_{i,Au}$) to number of atoms (N_{atoms}) → Multiply by Avogadro's constant N_A= 6.022140857 × 10^{23} mol^{-1}

$$N_{atoms} = n_{i,Au} \times N_A = \frac{m_{i,Au} \times N_A}{Mr}$$

Finally, by incorporating the above equation into the C equation, $C = \frac{N_{atoms}}{N \times V \times N_A}$, the concentration after synthesis can be calculated using:

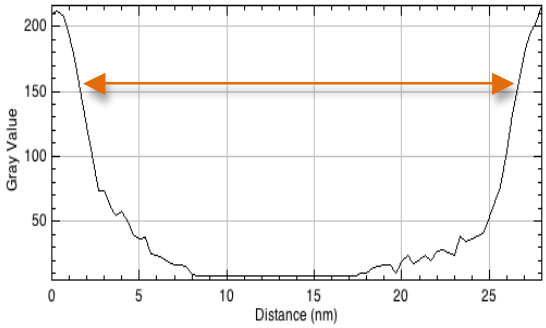
$$C = \frac{N_{atoms}}{N \times V \times N_A} = \frac{m_{i,Au} \times N_A}{N \times V \times N_A \times Mr} \rightarrow \boxed{C = \frac{m_{i,Au}}{N \times V \times Mr}}$$

For AuNP25:



→ TEM image of AuNP25 is used to define the size of D (nm) by getting an average of 15 nanoparticles. (n=15)

ImageJ software is used for size analysis to determine *D*:



27 – 2 = 25

D = 25 nm

Therefore, to calculate *N*:

$$N = \frac{\rho \times \pi D^3}{6 \times Mr} \times N_A = \frac{19.32 \times 10^{-21} \text{g nm}^{-3} \times \pi \times D^3}{6 \times 196.96657 \text{ g mol}^{-1}} \times 6.022140857 \times 10^{23} \text{ mol}^{-1}$$

$$\therefore N = 30.89685812 \times D^3$$

N = 30.89685812 x $(25)^3$ = 482763

For the AuNP25 synthesis the amount of gold used can be calculated:

$HAuCl_4 \cdot 3H_2O$ – 49% by assay as stated by manufacturer. (Sigma-Aldrich ACS Reagent, CAS Number: 16961-25-4)

→ 34 ml of AuNP13 are used + 6 ml of H_2O (For AuNP13 – 8 mg of gold are used in total volume of 125 ml. Therefore, in 34 ml there is 2.176 mg of gold.

→ Then a gold solution of 0.5 mM $HAuCl_4 \cdot 3H_2O$ in 20 ml of H_2O (8 mg of gold) is made up and used in the AuNP25 synthesis.

→ Therefore, total amount of gold used in the AuNP25 synthesis is 10.2mg (2.176mg from AuNP13 and 8 mg from AuNP25 synthesis).

→ Total volume in AuNP25 synthesis is 80 ml.

Therefore, to calculate the concentration of AuNP25 after synthesis:

$$C = \frac{m_{i,Au}}{N \times V \times Mr}$$

$$C = \frac{0.49 \text{ x } 10.176 \text{ x } 10^{-3} \text{ g}}{482763 \text{ x } 0.080 \text{ L x } 196.96657 \text{ g mol}^{-1}} = 6.5 \text{ x } 10^{-10} \text{ M} = 0.65\text{nM}$$

D-2 Number of metal complexes per AuNP25 by ICP-MS

To calculate the number of metal complexes per nanoparticle:

→ The ratio of metal complex (M) to gold (Au), which is derived from elemental analysis by ICP-MS, is initially calculated and it is then multiplied by the number of Au atoms found in one gold nanoparticle.

For ICP-MS analysis of gold nanoparticles coated with a metal complex two dilutions of the modified nanoparticles are used:

1. 1:200 (For Au value)
2. 1:1 (For M value)

For IrS1•Z•AuNP25:

Number of atoms per AuNP25: **482763** (Calculations are shown in D1)

Au [ppb]	M [ppb]	Au [ppb] x 200	M [ppb] / Au [ppb]	M / Au x number of Au atoms in 1 nanoparticle
18.525	19.802	3705	0.005345	2580

2 580 IrS1 complexes per AuNP25

D-3 Number of AuNPs per cell by ICP-MS

The concentration of gold (Au) detected by ICP-MS in the treated cells is used to derive the total number of AuNPs, which is then divided by the total number of cells digested for elemental analysis.

For IrS1•Z•AuNP25 in HeLa cells:

Concentrations of Au detected by ICP-MS and number of cells digested for analysis after treatment with IrS1•Z•AuNP25 for 24 hours (Experiment performed in triplicate):

	Number of cells
1. 1047.388 ppb	2120000
2. 1069.166 ppb	2105000
3. 1146.020 pbb	2260000

In order to calculate total number of nanoparticles in cells:

→ Firstly, the mass of Au was calculated using the concentration detected by ICP-MS and the volume of the digested sample:

(ppb = μg / L)

(Volume of each sample used for ICP-MS is 5 ml)

1. $0.001047388 \times (5\times10^{-3}) \rightarrow 5.237\times10^{-6}$ g
2. $0.001069166 \times (5\times10^{-3}) \rightarrow 5.346\times10^{-6}$ g
3. $0.001146020 \times (5\times10^{-3}) \rightarrow 5.730\times10^{-6}$ g

→ Then, Au mass was converted to moles to determine the number of Au atoms in the cells:

(Mr of Au is 196.96657 g mol^{-1})

(Avogadro's constant= 6.022140857 × 10^{23} mol^{-1})

1. 5.237x10^{-6} / 197 → 2.658x10^{-8} x 6.022140857 × 10^{23} → 1.601x10^{16} atoms
2. 5.346x10^{-6} / 197 → 2.714x10^{-8} x 6.022140857 × 10^{23} → 1.601x10^{16} atoms
3. 5.730x10^{-6} / 197 → 2.909x10^{-8} x 6.022140857 × 10^{23} → 1.752x10^{16} atoms

→ Finally, the total number of AuNPs in each sample is calculated and divided by the number of cells:

Number of atoms per AuNP25 **482763** (Calculations are shown in D1)

1. 1.601x10^{16} / 482763 → 33161169674 / 2120000 → 15642
2. 1.601x10^{16} / 482763 → 33850679152 / 2105000 → 16081
3. 1.752x10^{16} / 482763 → 36283940306 / 2260000 → 16054

Average= 15925

Therefore, there are about 16 000 AuNPs per cell.

References:

[1] Shang, J. & Gao, X. 2014. Nanoparticle counting: towards accurate determination of the molar concentration. *Chem Soc Rev,* 43**,** 7267-7278.

[2] Carney, R. P., Kim, J. Y., Qian, H., Jin, R., Mehenni, H., Stellacci, F. & Bakr, O. M. 2011. Determination of nanoparticle size distribution together with density or molecular weight by 2D analytical ultracentrifugation. *Nat Commun,* 2**,** 335.

Appendix E - Copyright Permissions

Type of content	Source	Copyright holder	Permission requested on	Permission	Permission note
Figure 1-2	Nel et al.[1]	Springer Nature	8/02/2021	YES	Copyright permission was granted via the Copyright Clearance Center's RightsLink service (License number: 5004311105427)
Figure 1-3	Dykman and Khlebtsov[2]	Elsevier	8/02/2021	YES	Copyright permission was granted via the Copyright Clearance Center's RightsLink service (License number: 5004320877474)
Figure 1-6	Wang et al.[3]	American Chemical Society	8/02/2021	YES	Copyright permission was granted via the Copyright Clearance Center's RightsLink service
Figure 1-9	Donahue et al.[4]	Elsevier	8/02/2021	YES	Copyright permission was granted via the Copyright Clearance Center's RightsLink service (License number: 5004460514432)
Figure 1-10	Vats et al.[5]	MDPI, Basil, Switzerland	8/02/2021	YES	This is an open access article, distributed under the terms and conditions of the Creative Commons Attribution license (http://creativecommons.org/licenses /by/4.0/)
Figure 1-11	Rogers et al.[6]	Royal Society of Chemistry	9/02/2021	YES	Copyright permission was granted via the Copyright Clearance Center's Marketplace™ (License order ID: 1096346-1)
Figure 1-12	King et al.[7]	American Chemical Society	9/02/2021	YES	Copyright permission was granted via the Copyright Clearance Center's RightsLink service
Figure 1-14	Patra et al.[8]	American Association for Cancer Research	9/02/2021	YES	Copyright permission was granted from the American Association for Cancer Research. No license required
Figure 2-2	Zamora et al.[9]	Elsevier	7/3/2021	YES	Copyright permission was granted via the Copyright Clearance Center's RightsLink service (License number: 5023791238247)

References:

[1] Nel, A. E., Madler, L., Velegol, D., Xia, T., Hoek, E. M., Somasundaran, P., Klaessig, F., Castranova, V. & Thompson, M. 2009. Understanding biophysicochemical interactions at the nano-bio interface. *Nat Mater,* 8**,** 543-557.

[2] Dykman, L. & Khlebtsov, N. 2012. Gold nanoparticles in biomedical applications: recent advances and perspectives. *Chem Soc Rev,* 41**,** 2256-2282.

[3] Wang, F., Wang, Y. C., Dou, S., Xiong, M. H., Sun, T. M. & Wang, J. 2011. Doxorubicin-Tethered Responsive Gold Nanoparticles Facilitate Intracellular Drug Delivery for Overcoming Multidrug Resistance in Cancer Cells. *ACS Nano,* 5**,** 3679-3692.

[4] Donahue, N. D., Acar, H. & Wilhelm, S. 2019. Concepts of nanoparticle cellular uptake, intracellular trafficking, and kinetics in nanomedicine. *Adv Drug Deliv Rev,* 143**,** 68-96.

[5] Vats, M. , Mishra, S. K. , Baghini, M. S. , Chauhan, D. S. , Srivastava, R. & De, A. 2017. Near Infrared Fluorescence Imaging in Nano-Therapeutics and Photo-Thermal Evaluation. *Int J Mol Sci,* 18**,** 924.

[6] Rogers, N. J., Claire, S., Harris, R. M., Farabi, S., Zikeli, G., Styles, I. B., Hodges, N. J. & Pikramenou, Z. 2014. High coating of Ru(II) complexes on gold nanoparticles for single particle luminescence imaging in cells. *Chem Commun* 50**,** 617-619.

[7] King, Siobhan M., Claire, Sunil, Teixeira, Rodolfo I., Dosumu, Abiola N., Carrod, Andrew J., Dehghani, Hamid, Hannon, Michael J., Ward, Andrew D., Bicknell, Roy, Botchway, Stanley W., Hodges, Nikolas J. & Pikramenou, Zoe 2018. Iridium Nanoparticles for Multichannel Luminescence Lifetime Imaging, Mapping Localization in Live Cancer Cells. *J Am Chem Soc,* 140**,** 10242-10249.

[8] Patra, C. R., Bhattacharya, R., Wang, E., Katarya, A., Lau, J. S., Dutta, S., Muders, M., Wang, S., Buhrow, S. A., Safgren, S. L., Yaszemski, M. J., Reid, J. M., Ames, M. M., Mukherjee, P. & Mukhopadhyay, D. 2008. Targeted Delivery of Gemcitabine to Pancreatic Adenocarcinoma Using Cetuximab as a Targeting Agent. *Cancer Res,* 68**,** 1970-1978.

[9] Zamora, A., Vigueras, G., Rodríguez, V., Santana, M. D. & Ruiz, J. 2018. Cyclometalated iridium(III) luminescent complexes in therapy and phototherapy. *Coord Chem Rev,* 360**,** 34-76.

Conferences and Presentations:

• Poster presentation at the Photochemistry Meeting held by the Royal Society of Chemistry in Birmingham, UK in September 2017.

• Poster and flash presentation at the PG Symposium of the School of Chemistry at the University of Birmingham in June 2018.

• Poster and video presentation at EuroBIC conference in Birmingham, UK , August 2018. – Won Runner-up prize for video presentation.

• Oral presentation at the 10^{th} International Conference of Nanomedicine in Sydney, Australia , June 2019. – Received Oral presentation prize.

• Oral presentation at the RSLC Seminar at the University of Birmingham, UK, August 2019. – Won best Oral presentation.